Assessment of Short Circuit Power and Protection Systems for Future Low Inertia Power Systems.

Jia, Jundi

Publication date:
2018

Document Version
Publisher's PDF, also known as Version of record

Citation (APA):
Jia, J. (2018). Assessment of Short Circuit Power and Protection Systems for Future Low Inertia Power Systems. Technical University of Denmark, Department of Electrical Engineering.

Technical University of Denmark

Jundi Jia

Assessment of Short Circuit Power and Protection Systems for Future Low Inertia Power Systems

PhD thesis, July 2018
Kongens Lyngby, Denmark

Center for Electric Power and Energy
Department of Electrical Engineering

DANMARKS TEKNISKE UNIVERSITET
Center for Electric Power and Energy (CEE)
DTU Electrical Engineering

Assessment of Short Circuit Power and Protection Systems for Future Low Inertia Power Systems

Vurdering af Kortslutningseffekt og Beskyttelsessystemer til Fremtidige Lav Inerti Elsystemer

PhD Thesis, by Jundi Jia

Supervisors:
Associate Professor Guangya Yang, Technical University of Denmark
Associate Professor Arne Hejde Nielsen, Technical University of Denmark
Engineer Peter Rønne-Hansen, Siemens A/S, Denmark

DTU - Technical University of Denmark, Kongens Lyngby - July 2018

Assessment of Short Circuit Power and Protection Systems for Future Low Inertia Power Systems

This thesis was prepared by:
Jundi Jia

Supervisors:
Associate Professor Guangya Yang, Technical University of Denmark
Associate Professor Arne Hejde Nielsen, Technical University of Denmark
Engineer Peter Rønne-Hansen, Siemens A/S, Denmark

Dissertation Examination Committee:
Senior Researcher Henrik W. Binder (chairman)
Department of Electrical Engineering, Technical University of Denmark, Denmark

Professor Jian Sun
Department of Electrical, Computer, and Systems Engineering, Rensselaer Polytechnic Institute, USA

Professor Campbell Booth
Department of Electronic and Electrical Engineering, University of Strathclyde, UK

Center for Electric Power and Energy (CEE)
DTU Electrical Engineering
Elektrovej, Bygning 325
DK-2800 Kgs. Lyngby
Denmark

http://www.cee.elektro.dtu.dk

Release date:	31st July, 2018
Edition:	Final
Class:	Internal
Field:	Electrical Engineering, Electric Power System
Remarks:	The dissertation is presented to the Department of Electrical Engineering of the Technical University of Denmark in partial fulfillment of the requirements for the degree of Doctor of Philosophy.

Preface

This thesis is prepared at the Department of Electrical Engineering of the Technical University of Denmark in partial fulfillment of the requirements for acquiring the degree of Doctor of Philosophy in Engineering. The Ph.D. project was funded by the Danish ForskEL project "Synchronous Condenser APPlication in Low Inertia Systems (SCAPP)", grant no. 12196, funded by PSO (Public Service Obligation), administrated by Energinet.

This dissertation summarizes the work carried out by the author during his Ph.D. project. It started on 1st August 2015, and it was completed on 31st July 2018. During this period, he was hired by the Technical University of Denmark as a Ph.D. student at the Center for Electric Power and Energy (CEE).

The thesis is composed of 6 chapters based on 8 scientific publications, 7 of which have been peer-reviewed and published, whereas the remaining one is currently under review.

Jundi Jia
31st July, 2018

Acknowledgements

Three years could be long when you just start this journey and count how many milestones you have to reach. Three years could also be short when you nearly approach the destination and realize that it has been so far the best time of your life.

First of all, I would like to express my sincerest gratitude to my supervisors Guangya Yang and Arne Hejde Nielsen for the consistent guidance. The constructive feedback, insightful criticism, and unwavering support have made this dissertation reach its present level. Guangya has particularly shed light upon my research through the years. I have been feeling very blessed to have you as my supervisor.

Special acknowledgment is given to my supervisor, an experienced protection engineer, Peter Rønne-Hansen from Siemens A/S, Denmark, for material providing, knowledge sharing, and good times working together. I am also thankful to the engineer Peter Højaard Jensen, project managers Peter Weinreich-Jensen and Bo Johansson from Siemens, for your support to the SCAPP project. I would like to thank the Danish transmission system operator Energinet for providing data and suggestions on system modeling.

From September 2017 to January 2018 I had the pleasure to do my external research stay with the Transmission and Grid Integration Group at the National Wind Technology Center (NWTC) in the National Renewable Energy Laboratory (NREL), Boulder, Colorado, USA. I enjoyed very much working at NWTC and the surrounding wild nature. I would like to thank my hosts, Eduard Muljadi, and Vahan Gevorgian, for your warm welcome, inspiring discussions and valuable suggestions.

I would also to express my thankfulness to my colleagues at CEE for the knowledge, encouragement, friendship and the time spent together after work. It has been a great pleasure to work with all these smart people. Besides, I would like to thank all my friends in Denmark, Sweden, China and all over the world. The friendship never changes even though we have been geographically separated. I am grateful to my landlord Svend Jørgen Skotte and his family. The relationship we have built has made me feel as if I were staying at home.

Last but not least, my parents have always been standing behind me and been supportive. Thank you for your patience, understanding, and love.

Jundi Jia

Kongens Lyngby, Denmark, July, 2018

Table of Contents

Abstract

With the proliferated renewable energy integration and the gradual retirement of conventional generation units, power systems are experiencing significant changes in regard to the generation mix. The conventional power plants comprise large synchronous generators that naturally provide instantaneous short circuit power. The high short circuit current is of crucial importance to activate the protective relays. In contrast, renewable-based generations typically interface with the grids through power converters, whose short circuit contribution can be significantly different from that of synchronous generators both in the quality and the quantity. This Ph.D. work, as part of the Danish project "Synchronous Condenser Application in Low Inertia System (SCAPP) ", concerns the assessment of short circuit power and protection systems for future low inertia power systems.

Voltage source converters are widely utilized in the renewable energy integration. To characterize the short circuit power for future low inertia power systems, a comparison on the short circuit response between synchronous sources and voltage source converters was carried out considering the converter peak current limit and the reactive power support capability. The short circuit response of voltage source converters is significantly different from that of the synchronous sources, especially during grid unbalanced faults. For voltage source converters, the conventional synchronous reference frame control only in positive-sequence can result in distorted voltage and current outputs, and uncontrollable converter peak current. This indicates that it is necessary for voltage source converters to have current control loops in both positive- and negative-sequence.

Base on the instantaneous power theory, the dual-sequence current control strategies of voltage source converters under grid unbalanced faults were reviewed aiming at the short circuit power provision. They were classified into two groups, namely power-characteristic-oriented control strategy, and voltage-support-oriented control strategy, in terms of the properties that are being directly controlled. The review also covered the inner current controllers and the design of the converter peak current limit. Through various simulations and discussions, the short circuit power from voltage source converters can be characterized by the different combinations of the positive- and negative-sequence powers. In addition, the dual-sequence current controls were extended to microgrids as a case study to examine the short circuit power in a system with 100% penetration of renewable energy.

To investigate the challenges brought by low inertia power systems to protection systems, a hardware-in-the-loop test platform was created integrating power system real-time simulations and protective relays into a closed loop. The platform is able to automate the relay testing under different scenarios through the bi-directional communication between Real Time Digital Simulator and MATLAB. On the transmission level, the performances of distance relays installed at a voltage source converter substation and protecting the neighboring line were explored through hardware-in-the-loop tests. It was revealed that the measuring error caused by the fault resistance will be enlarged in low inertia power systems. The occurrence of underreach and overreach problems become unpredictable due to the low short circuit current level and the non-conventional short circuit power characteristics.

Synchronous condensers, as synchronous machines in principle, have the advantage of short circuit contribution. An investigation on the combined effect of voltage source converters and synchronous condensers was carried out considering the diverse dual-sequence current controls. It focused on the aspects of the combined short circuit current, the voltage at the point of common coupling, the DC-side voltage and the system frequency response during faults. In particular, it was verified through hardware-in-the-loop tests under various scenarios that the associated short circuit current interaction could jeopardize the reliability of distance relays. The investigation was concluded with suggestions on selecting the dual-sequence current control strategies when incorporating synchronous condensers.

In order to analytically perform the fault analysis, a static fault analysis method was developed and verified taking the short circuit contribution from voltage source converters and their dual-sequence current controls into account. The method was used to help explain a phenomenon, which has not been revealed in the literature, that the system may not have a stable response under unbalanced faults due to the negative-sequence reactive power injection. The developed fault analysis method helps to understand the impact of the short circuit contribution from voltage source converters on low inertia power systems. With the proposed method, the optimal sizes and locations of synchronous condensers for the western Danish power system of a future scenario were investigated through optimizations. The allocation results indicated that there is a need of more synchronous condensers for future low inertia power systems to maintain the system short circuit ratios.

Resumé

Energisystemer undergår store forandringer i produktion af energi, som skyldes at vedvarende energikilder erstatter fossile brændsler i større omfang. De traditionelle kraftværker består af store synkrongeneratorer som øjeblikkeligt leverer kortslutningseffekt, hvor den høje kortslutningsstrøm har en stor indflydelse i at aktivere beskyttelsesrelæer. I modsætning til synkrongeneratorer varierer kortlustningsbidraget både i kvalitet og mængde for vedvarende energikilder, som er koblet til elsystemet gennem effektomformere. Denne ph.d.-afhandling, som er tilknyttet det danske forskiningsprojekt "Synchronous Condenser Application in Low Inertia System (SCAPP)", handler om evalueringen af kortslutningseffekt og beskyttelsessystemer for fremtidige lav inerti energisystemer.

Spændingskilde konvertere er i stor udstrækning anvendt i integreringen af vedvarende energikilder. For at karakterisere kortslutsningseffekten for fremtidige lav inerti energisystemer, blev der udført en sammeligning af kortslutningsreaktionen mellem synkronmaskiner og spændingskilde konvertere, hvor konverter spidsstrømsgrænsen og reaktiv effekt support kapabiliteten var betragtet. Kortslutningsreaktionen af spændingskilde konvertere er markant anderledes sammenlignet med synkronmaskiner, og endnu mere når usymmetriske netfejl opstår. For spændingskilde konvertere kan den traditionelle synkronmaskine reference kontrol model i positiv sekvens, resultere i forvrænget spænding og strøm ydelse og ustyrlig konverter spidsstrømme. Dette indikerer nødvendigheden for spændingskilde konvertere, at betragte både positiv og negativsekvens i lukket-sløjfe strømkontrol.

Dobbelt-sekvens strømkontrolstrategier af spændingskilde konvertere under usymmetriske netfejl, baseret på øjeblikkelig effekt teori, blev undersøgt med fokus på at anskaffe kortslutningseffekt. Kontrolstrategierne blev kategoriseret i henholdsvis effekt-karakteristik-orienteret kontrol strategi og spændings-support-orienteret kontrol strategi, i forhold til de egenskaber som kan direkte kontrolleres. Undersøgelsen omfattede også de indre strømkontroller og designet af konverter spidsstrømsgrænse. I gennem adskillige simuleringer og diskussioner, kan kortslutningseffekten fra spændingskilde konvertere karakteriseres af forskellige kombinationer af positiv og negativsekvens effekter. Yderligere blev dobbelt-sekvens strømkontrolstrategierne udvidet til microgrids, som et forsøg på at studere kortslutningseffekten i et energisystem med 100% vedvarende energi.

En hardware-i-sløjfen platform, som bruger real-tids simuleringer og beskyttelsesrelæer i en lukket sløjfe, blev bygget for at undersøge udfordringerne et lav inerti system forårsager til beskyttelsessystemet. Platformen er i stand til at automatisere relæ-undersøgelser under forskellige scenarier gennem bi-direktionel kommunikaion mellem Real Time Digital Simulator og MATLAB. Ydeevnen af afstandsrelæer installeret på en spændsingskilde konverter omformerstation og beskyttelse af de nærliggende linjer, blev undersøgt på transmissionsniveauet ved hjælp af hardware-i-sløjfe undersøgelser. Det blev opdaget at målingsfejlen forårsaget af fejlmodstanden bliver større for lav inerti systemer. Forekomsten af under -og overrækkevidde problemer bliver uforudsigelige på grund af lave kortslutningsstrømme og utraditionelle karakteristikker af kortslutningseffekten.

Synkronkompensatorer, som fungerer ligesom en synkronmaskine, har den fordel at de bidrager til kortslutningseffekten. Det kombinerede bidrag af spændingskilde konvertere og synkronkompensatorer blev undersøgt med fokus på forskellige dobbelt-sekvens strømkontrolstrategier. Undersøgelsen fokuserede på de kombinerede aspekter af kortslutningsstrømmen, spændingen ved leveringspunktet, spændingen ved jævnstrømssiden og systemfrekvensresponset under fejl. Det blev bekræftet ved hjælp af hardware-i-sløjfe undersøgelser for forskellige scenarier, at den tilhørende vekselvirkning af kortslutningsstrømmen kan påvirke driftssikkerheden af afstandsrelæer. Undersøgelsen blev konkluderet med forslag til at vælge dobbelt-sekvens strømkontrolstrategier, som omfatter synkronkompensatorer.

For at udføre analytisk fejlanalyse, blev en statisk fejlanalyse metode udviklet og bekræftet, som betragter kortslutningsbidraget fra spændingskilde konverter og deres dobbelt-sekvens strømkontrol. Metoden blev brugt til at redegøre for et fænomen, som ikke er blevet opdaget i litteraturen. Det blev bemærket at systemet muligvis ikke har en stabil reaktion under ubalancerede fejl, som skyldes leveringen af negativ-sekvens reaktiv effekt. Den udviklede fejlanalyse metode bidrager med, at forstå indflydelsen af kortslutningseffekten fra spændingskilde konvertere i lav inerti energisystemer. Med den foreslåaet metode, blev den optimale størrelse og beliggenhed af synkronkompensatorer for det vestlige danske energisystem for et fremtidigt scenarie undersøgt ved hjælp af optimering. Allokeringsresultaterne indikerede at der er brug for synkronkompensatorer i fremtidige lav inerti energisystemer, for at opretholde kortslutningsrationen for systemet.

Acronyms

AVR Automatic Voltage Regulator

CT Current Transformer

DER Distributed Energy Resource

DG Distributed Generation

DK1 Western Danish Power System

DSOGI Dual Second Order Generalized Integrator

EMTP Electromagnetic Transients Program

EU European Union

FPNSPC Flexible Positive- and Negative-Sequence Power Control

FOPC Flexible Oscillating Power Control

FRT Fault Ride Through

GA Genetic Algorithm

GTAO Gigabit Transceiver Analogue Output Card

GTDI Gigabit Transceiver Digital Input Card

HIL Hardware-in-the-Loop

HVDC High Voltage Direct Current

ICT Information and Communications Technology

IP Internet Protocol

KCL Kirchhoff's Current Law

KVL Kirchhoff's Voltage Law

LCC-HVDC Line Commutated Converter based HVDC

MINLP Mixed-Integer Non-Linear Programming

NLP Non-Linear Programming

PCC Point of Common Coupling

PI Proportional-Integral

PLL Phase-Locked Loop

PMU Phasor Measurement Unit

PR Proportional-Resonant

PSS Power System Stabilizer

PV Photovoltaic

PWM Pulse Width Modulation

RE Renewable Energy

RES Renewable Energy Sources

RMS Root Mean Square

RoCoF Rate of Change of Frequency

RTDS Real Time Digital Simulator

SC Synchronous Condenser

SCAPP Synchronous Condenser Application in Low Inertia Systems

SCR Short Circuit Ratio

SG Synchronous Generator

SRF Synchronous Reference Frame

STATCOM Static Synchronous Compensator

SVC Static Var Compensator

TCP Transmission Control Protocol

TCP/IP Transmission Control Protocol/Internet Protocol

TSO Transmission System Operator

VSC Voltage Source Converter

VSC-HVDC Voltage Source Converter based HVDC

VT Voltage Transformer

List of Figures

List of Tables

CHAPTER 1

Introduction

1.1 Background

In the past decade, an increasing attention has been paid to the integration of Renewable Energy (RE) into power systems as a concern of the world-wide climate change and the growing electricity demand. It is reported that around two-thirds of all anthropogenic greenhouse gas emissions are oriented from the energy sector due to the use of fossil fuels [3]. Geothermal power plants and hydropower plants have already existed for decades. Their development is typically restricted to the geographic characteristics and the natural environments. With the progress of the technology and the reduction of the cost, wind and solar power are becoming the main Renewable Energy Sources (RES). High Voltage Direct Current (HVDC) transmission systems have been used world-widely since the 1950s because of their advantages on long-distance transmission, asynchronous interconnections, lower losses, etc [4]. In recent years, Voltage Source Converter based HVDC (VSC-HVDC) connection has become a new trend for the integration of offshore wind farms [5].

As one of the leading counties in RE integration, Denmark has set energy strategies aiming to increase the share of RE to 50% by 2030, and in the long term to realize the energy supply based on 100% RE by 2050, thus eliminating the dependency of fossil fuels [6, 7]. Figure 1.1 [1] shows the existing grid of Denmark at the end of 2017. Currently, Denmark has multiple HVDC transmission connections to the neighboring countries (e.g. Sweden, Norway, Germany) and several large offshore and wind farms (e.g. Anholt, Horns Rev A, B, C) connected to the transmission system. According to the Danish Transmission System Operator (TSO) Energinet, the HVDC connections to the Netherlands (COBRAcable), to the United Kingdom (Viking Link), and the two near-shore wind farms (Vesterhav Nord and Vesterhav Syd) are expected to be in commission in 2019, 2022, and 2020 respectively [8, 9]. In the long term, the Danish power system will gradually transform into the one shown in Fig. 1.2.

In order to achieve a 100% renewable-based power system, the conventional fossil-fuel-based power plants will be cycled offline and gradually phased out. These power plants usually have large synchronous generators, whose unique characteristics have served as the basis of planning and operating power systems since the inception of electric machinery [10]. However, wind power plants, Photovoltaic (PV) power plants, and HVDC transmission systems interface with the grid through power converters, which means the power system will experience significant changes in regard to the generation mix.

Synchronous generators and power converters are substantially different from each other. Synchronous generators induce the voltage across the stator winding through the rotating magnetic field produced by the rotating rotor. Their active power is regulated through controlling the mechanical input torque on the turbine shaft, while reactive power is regulated through controlling the excitation current performed by the Automatic Voltage Regulator (AVR). In contrast, power

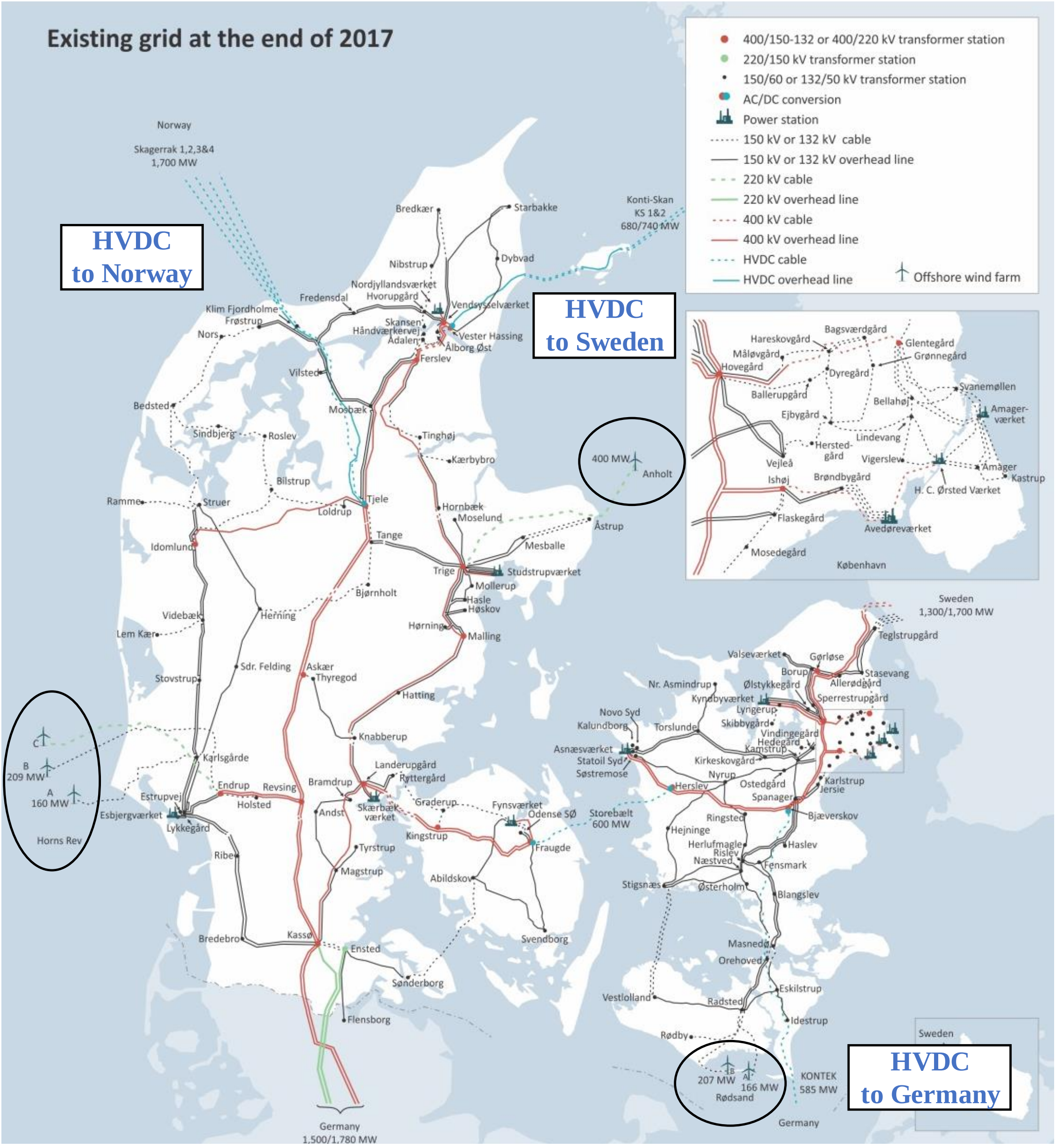

Figure 1.1: Existing grid of Denmark at the end of 2017 [1]

converters are electronic and do not possess the physical properties of synchronous generators. On the one hand, RE such as wind power and solar power are intermittent and indispatchable relying on the weather conditions. To accommodate the associated uncertainties, the operation of the power system requires a greater flexibility. On the other hand, the operation of power converters and their response subject to disturbances are determined by the control systems rather than their physical properties. Therefore, the transition to a 100% renewable-based power system will bring up a variety of challenges [10, 11, 12].

1.1.1 Problem and motivation

The impact of converters on a power system is not significant when they only constitute a small portion of the total generation. However, with the proliferation of RE integration and HVDC

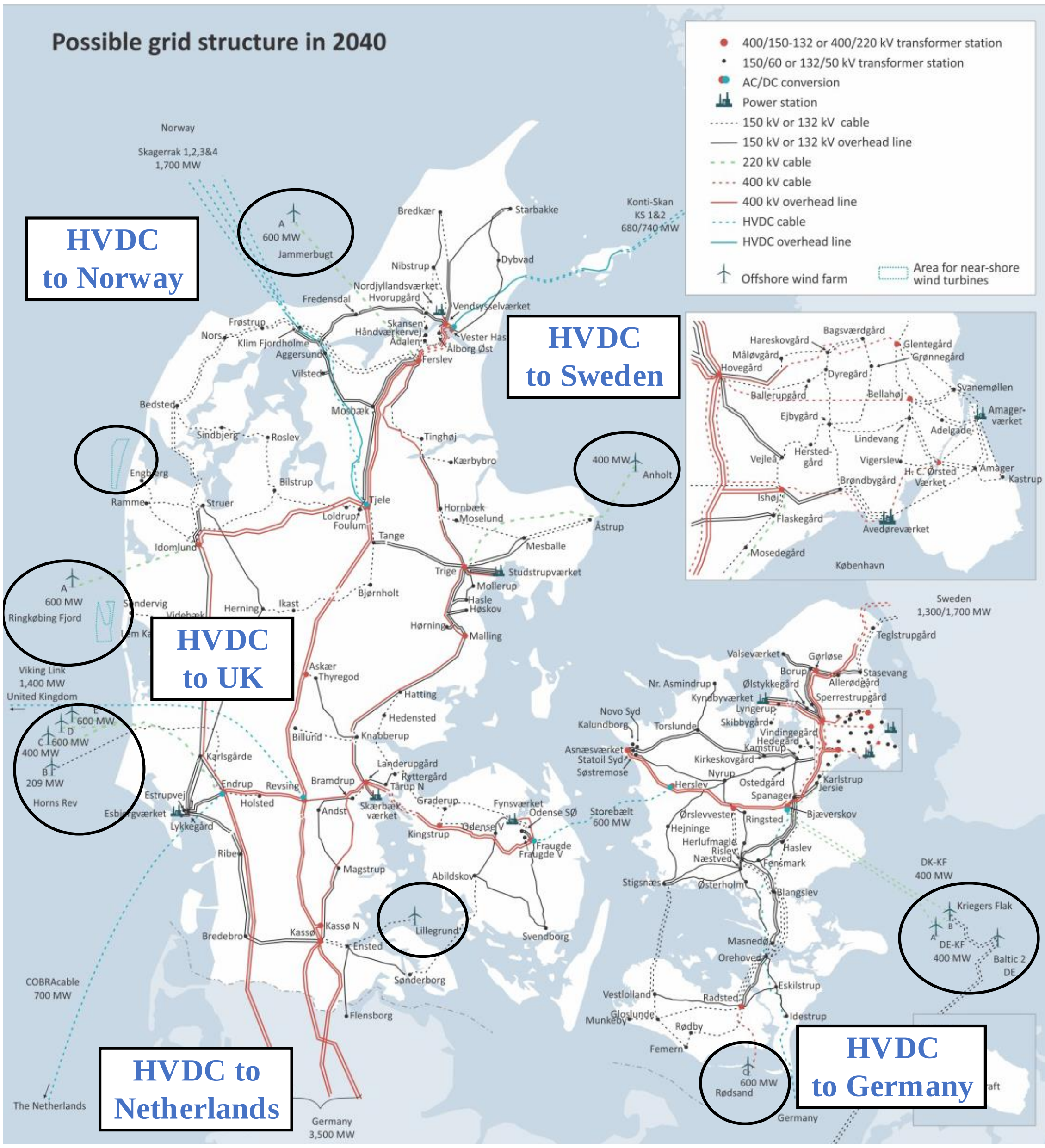

Figure 1.2: Possible grid structure of Denmark in 2040 [1]

transmission systems, the number of converter-interfaced generations and transmissions can be more than 50% of the total rated power of a system at any time, thus forming a converter-dominated power system [10].

First of all, conventional power plants are dispatchable in that their supply can be adjusted accordingly to meet the demand. In contrast, RE is characterized by variability and uncertainty, which can result in situations when the load-generation balance cannot be maintained. In order to tackle this challenge, a variety of solutions has been proposed such as the deployment of energy storage, demand response, advanced RE and load forecasting, etc.

Secondly, synchronous generators can provide a number of ancillary services to support the grid operation. Even though renewable-based generations, as well as HVDC transmission systems, can also be controlled to provide some of the services, converters are physically different from synchronous generators. The system frequency and voltage are the two key properties should be maintained. They are typically regulated by the controllers of each synchronous generator.

Synchronous generators usually have large rotating shafts, on which the stored kinetic energy adds inertia to the system. During the system disturbances, kinetic energy can either be released from or be stored on the shaft. Inertia is a crucial feature of the rotating synchronous generators and helps a system to render frequency deviations. A system with higher inertia is less prone to frequency changes. With AVR and Power System Stabilizer (PSS), synchronous generators have the ability to remain in synchronism after being subject to a disturbance, which is referred to rotor angle stability. It is the ability to maintain the equilibrium between mechanical torque and electromagnetic torque of each machine [13]. The synchronizing torque and the damping torque produced by synchronous generators are crucial for remaining the synchronism and damping the low-frequency oscillations. In contrast, power converters do not have any rotating mass directly coupled with the grid. The lack of synchronous generators in converter-dominated power systems can drastically change frequency characteristics, challenging the frequency control and the system operation in low inertia power systems.

Synchronous generators are able to regulate their reactive power to provide voltage support. The AVR system adjusts the excitation to keep their terminal voltage stable. Converter-interfaced generations and transmissions are also able to regulate voltage and their control system is even faster than the conventional AVR of synchronous generators. However, due to the limited semiconductor overload capability, the voltage regulation service of a converter tends to occupy the current margin for active power delivery. As a result, converters have limited voltage regulation capability. On the other hand, the faster dynamics may also create unexpected couplings and invalidate the control approaches based on time-scale separations [11].

Thirdly, synchronous generators are natural voltage sources, which are able to provide fast short circuit power injections during voltage dips. The accompanied significant amount of short circuit current is of particular importance to activate the protective relays under fault conditions. The relays rely on the short circuit current to distinguish the fault conditions from the normal conditions, and to identify the type of the faults. In contrast, converter-interfaced generations and transmissions do not provide short circuit power naturally. The converters manage their power outputs through controlling the on/off status of the semiconductors. The short circuit power is governed by their control systems and the magnitude of the short circuit current is restricted due to the limited semiconductor overload capability [14]. Therefore, the quality and quantity of the short circuit power in a renewable-based power system can be significantly different from that of a conventional power system. How a converter should react to different type of faults is still under open discussion.

The protective relays are typically designed based on the characteristics of the conventional power systems with synchronous generators being the main source of short circuit power. The addition of converter-interfaced generations and transmissions brings up increasing challenges to the protection system. For example, due to the low system inertia, the greater Rate of Change of Frequency (RoCoF) impacted the frequency tracking of the digital relays, which resulted in the misoperation of 8 relays and caused the South Australia blackout in September 2016 [15]. Besides the reduced short circuit current level, being controllable is another crucial feature of the short circuit power from converters. This means the converters do not have unique short circuit response as the control system can be designed in various ways. Therefore, power system protection and power electronic controls will be strongly correlated with each other in converter-based systems, which makes the evaluation and design of protective relays even more challenging. Possible malfunctions of different types of protection schemes have been recognized in [12, 16, 17, 18]. However, detailed investigation through tests is lacking for each protection scheme. It is necessary to explore and find out, in which way and to what extent the relays are affected.

The increasing converter-interfaced generations and transmissions not only cause a reduced short circuit current level, but also weaken the system short circuit strength [12]. The most prevalent type of converters for wind power plants, PV power plants, and HVDC transmission systems is grid-following converters. With the presumption of "strong" conditions, grid-following converters follow the local voltage and frequency to inject a certain amount of power. In contrast, the "weak grid" conditions can lead to a variety of problems such as instability of converter control loops, inaccuracy of the Phase-Locked Loop (PLL), inapplicability of the traditional anti-islanding techniques. Therefore, the concept of grid-forming converters (a type of converters being able to regulate the voltage and frequency) [19] as well as virtual synchronous machines (a type of converters emulating the dynamics of synchronous machines) [20, 21] have been proposed. However, there are still many challenges to deal with before their application in transmission systems, such as their compatibility with the existing synchronous generators, their coordination among themselves, the reliability of the source on the DC-side, etc.

Last but not least, with the changes in system mechanisms and properties, the conventional analytical methods for power system analysis such as stability assessment and fault analysis based on synchronous generators may become insufficient. To perform power system analysis, two research approaches are particularly adopted: theory-based method and simulation-based method. Since the response of converter-interfaced generations and transmissions depends on the control system and the control system can vary significantly, how the converters should be modeled for different types of studies is still under open discussion. It can be anticipated that power electronics control and power system analysis will become increasingly correlated with each other during the transition to a 100% renewable-based power system.

To guarantee a smooth transition of the power system from the conventional synchronous-generator-based one to the future renewable-based one, several projects are conducted world-widely to deal with the related technical challenges. The European Union (EU)-funded project "Massive Integration of Power Electronic Devices (MIGRATE)" under the framework of Horizon 2020 focuses on safeguarding the grid stability, improving the control systems of power electronic devices, and operating the system at 100% penetration of converter-interfaced generators [22]. Another EU project "RESERVE" focuses on the high-level vision of the possible scenarios, the development of new Information and Communications Technology (ICT) infrastructures, the business models, etc. for the transition to a 100% renewable-based power system. In Norway, the project "Prosmart" aims to improve the classical power system relaying with communication technology for a better handling of faults and reduced risks of blackouts [23]. The project "Operation of Low-inertia Power Systems" from the UK gives attention to the system dynamic performances, Phasor Measurement Unit (PMU) data analysis and developing control algorithms for operating systems with high penetrations of non-synchronous infeed [24].

1.1.2 Synchronous condensers

A Synchronous Condenser (SC) is in principle a synchronous machine without a prime mover [25]. During the start-up phase, the rotor of the SC can be driven to the synchronous speed by a frequency-controlled electric motor or a starting frequency converter [26]. After the synchronous speed is reached, the field is supplied by the exciter and then the SC can be connected to the grid once the synchronism check is performed. Since there is no mechanical torque provided to the shaft, an SC cannot provide sustaining active power.

Depending on the excitation level performed by the AVR, an SC can provide/absorb reactive power to/from the grid, thus being able to provide essential dynamic voltage support during normal operation. Similar to an Synchronous Generator (SG), an SC is in nature a voltage source capable of providing fast short circuit power injection when there is a short circuit in the grid. As a result, SCs can help increase the system short circuit current level, which is valuable for activating the protection devices, operating systems with high shares of converter-interfaced generations and transmissions, and stabilizing the grids during emergency situations. In addition, as a rotating device directly coupled with the grid, an SC is able to inherently provide inertia response. During the frequency deviation, kinetic energy can be either released from or stored in the rotational shaft of the SC, which naturally counteracts the frequency changes during disturbances. Therefore, SCs are able to provide both voltage and frequency support to the system.

1.1.3 SCAPP project

The Danish project “Synchronous Condenser Application in Low Inertia Systems (SCAPP)” [27] sees the challenges mainly in two aspects due to the different operation principles between synchronous machines and converters. The project sees SC as a critical component to secure power systems under the transition from a synchronous-generator-based one to a future converter-based one. As discussed above, the voltage and frequency characteristics of a future low inertia power system can be significantly changed due to the retirement of SGs and the integration of RE. The dynamic behavior of the system subject to short circuits or load-generation imbalance may also deviate considerably from those of a conventional power system. Therefore, systematic investigations are needed to quantify the impacts and provide solutions to secure the power system operation. Considering the benefits of SCs, it can be anticipated that SCs can play a crucial role in the future converter-based power system. Even though there have been successful experiences with the application of SCs world-widely (e.g. Bjæverskov in Denmark and Talega in USA [26]), detailed studies considering SCs’ incorporation with the services provided to renewable-based systems, the advances in SCs with respect to different designs, the interactions between SCs and power converters, various cases studies in a real-time environment, and experimental validations with hardware are still needed for a better application of SCs.

The SCAPP project aims to investigate the characteristics of a renewable-based power system in terms of voltage and frequency during transients, namely short-circuit power and system inertia. The system of analysis will be developed from the current western Danish power system, looking towards a future scenario with 100% renewable energy supply. Protective relays, as well as the control systems of SCs will be tested and validated through Hardware-in-the-Loop (HIL) tests. The project also aims to determine the optimal design and control settings of SCs for renewable-based systems to improve the reliability of protection systems and to enhance the system security.

1.1.4 Focus of the Ph.D project

This Ph.D. project is the second work package of the SCAPP project, mainly focusing on:

- Electro-magnetic modeling of the future converter-based Danish power systems with different types of converter-interfaced generations and transmissions.
- Short circuit power characterization of low inertia power systems.
- Assessment of distance protection performances in low inertia power systems considering the impacts from large wind farms and HVDC transmission systems.
- Evaluation of the effect of synchronous condensers on different system properties.
- Optimal allocation of synchronous condensers in terms of the number, size, and location for short circuit power improvement.

1.2 State of the art

This section discusses the state of the art related to this Ph.D project in terms of five aspects. They are grid requirements, Voltage Source Converter (VSC) controls for short circuit power provision, fault analysis, distance protection evaluation, and synchronous condenser applications.

1.2.1 Grid requirements

With an increase in the number and capacity of renewable-based generations integrated to high-voltage transmission systems through power converters, the TSOs in many countries have imposed strict requirements on converter-interfaced generations and transmissions in terms of grid codes. This requires converter-based generations not only to stay connected to the grid during disturbances but also to provide ancillary services like conventional power plants to help safeguard the grid operation.

Under grid fault conditions, a voltage drop will propagate across large geographical areas around the fault location. In the past, converter-interfaced generations such as wind power plants and PV power plants are allowed to be disconnected from the grid during the faults. However, when converter-interfaced generations constitute a considerate part of the network generation, their disconnection poses threats to the security of supply of power systems. Therefore, converter-interfaced generations (power park modules [28]) and HVDC transmission systems are required to have Fault Ride Through (FRT) capability within the EU [28, 29]. The requirement comes in the form of the lower limit of a voltage-against-time profile at the Point of Common Coupling (PCC), whose parameters on voltage and time are usually decided on a national level [30]. An example of the Danish FRT requirement on wind power plants connected to over 100 kV or with a power output above 1.5 MW is given in Fig. 1.3, according to which wind power plants are only allowed to be disconnected from the grid when the voltage drops into Area C [2].

Conventional power plants are able to provide fast short circuit power injection during faults. This is of great importance not only to the grid voltage support but also to the activation of protective relays. Therefore, large wind and PV power plants as well as HVDC transmission systems are required to have the capability to provide fast fault current at the PCC [2, 29, 31, 32]. Corresponding to Fig. 1.3, Fig. 1.4 presents the reactive current injection requirement in Denmark, where a wind power plant connected to over 100 kV or with a power output above 1.5 MW must provide additional reactive current accordingly when the voltage drops into Area B. Table. 1.1 summarizes the reactive current injection requirements for large wind power plants in some EU countries based

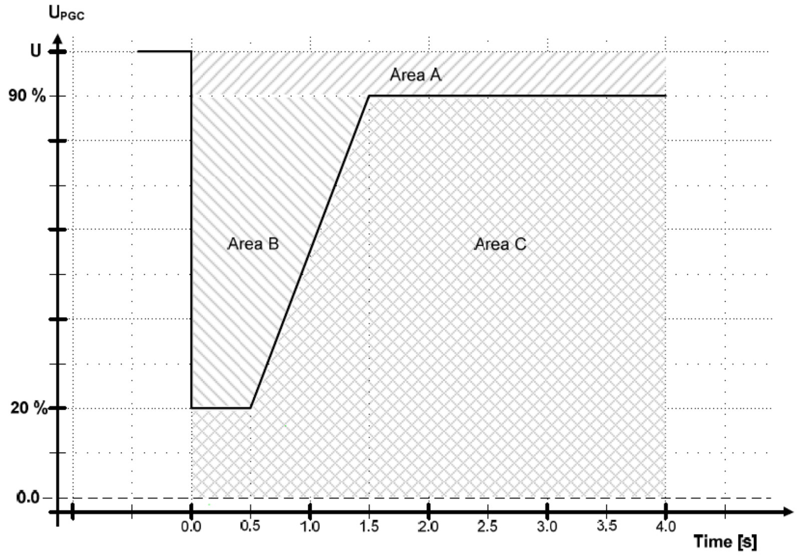

Figure 1.3: Voltage dip tolerance requirements for wind power plants connected to over 100 kV or with a power output above 1.5 MW [2]

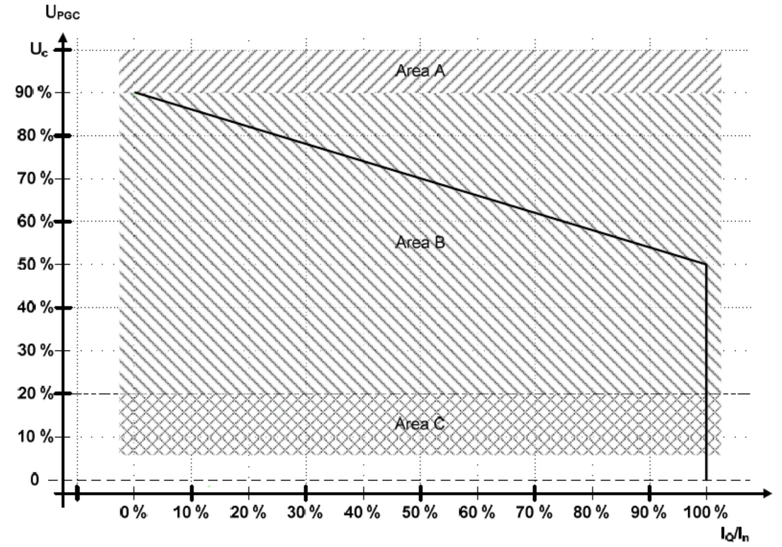

Figure 1.4: Requirements for the delivery of added reactive current during voltage dips for wind power plants connected to over 100 kV or with a power output above 1.5 MW [2]

on [2, 30, 32, 33, 34, 35, 35, 36, 37, 38]. For example, Germany enforces additional reactive current injection in terms of positive-sequence amounting to at least 2% of the rated current for each 1% voltage dip. The current should reach 90% of the steady-state value within 50 ms.

However, there still exist uncertainties in the existing grid codes such as the priority between active and reactive current [39], how the reactive current should be measurend and calculated, and how the rising time is defined. In addition, the current grid codes generally lack specific statements regarding grid unbalanced faults. According to [29], system operators may specify a requirement for HVDC transmission systems to inject unbalanced current in the case of unbalanced faults in the future. Therefore, how a converter should be controlled for short circuit power provision is still under open discussion.

Table 1.1: Reactive current injection requirements for wind power plants in Europe

Country	**Current Type**	**Character**	**Rising Time (ms)**	**Amount**
Denmark [2]	-	Additional	100	At least 2% injection for 1% PCC voltage reduction
Germany [32, 36]	Pos.seq	Additional	50 (90%)	At least 2% injection for 1% PCC voltage reduction
Ireland [37]	-	-	100 (90%)	At least proportional to the voltage dip
Spain [32, 38]	Pos.seq	Absolute	150	3%, 0.75% or 0.5% injection for 1% PCC voltage reduction (depending on voltage-dip level)
UK [35]	-	-	-	Maximum reactive current without exceeding the transient rating limits

1.2.2 VSC controls for short circuit power provision

VSC is widely utilized in RE integration such as Type-IV wind power plants, PV power plants, and HVDC transmission systems due to the control flexibility. They can be controlled to provide short circuit power while riding through the grid faults. Their short circuit behavior under three-phase balanced faults is evaluated for Type-III and Type-IV wind generators in [40, 41, 42, 43] and for VSC-HVDC transmission systems in [44, 45, 46]. Since the negative-sequence components are not present during three-phase faults, the VSC control systems in these studies only need to act on the positive-sequence components.

However, if the same control system is used for unbalanced faults analysis, undesirable performances such as output voltage and current distortions can be observed. Therefore, a variety of studies [47, 48, 49, 50] has been performed to improve the short circuit response of VSCs under unbalanced faults. Song *et al.* [50] firstly proposes to control a VSC by two sets of current controllers under unbalanced faults, one for positive-sequence and one for negative-sequence. It is a common practice to set the negative-sequence current references to zero so that a VSC provides only positive-sequence short circuit current under unbalanced faults [40]. Based on this dual-sequence control concept and the developed instantaneous power theory [51], a variety of control strategies [52, 53, 54, 55] have been proposed in recent years focusing on the formulation of both positive- and negative-sequence current references, giving VSCs the capability to provide positive- and negative-sequence short circuit current simultaneously under grid unbalanced faults.

When doing dynamic simulations, it is inevitable to model VSCs together with the control systems. Comprehensive reviews regarding different control aspects of VSCs have been provided in [55, 56, 57, 58, 59]. The work in [56] focuses on the different current control techniques of VSCs under steady state, while the controller design is of interest in [57]. The VSC control structures in different reference frames are thoroughly reviewed in [58, 59], without illustrating the short circuit response of VSCs. With the focus on unbalanced faults, the work in [55] reviews various VSC control strategies. However, reactive power support from VSCs is not given much attention. In addition, one critical aspect of the VSC control techniques, converter peak current limit, has been left out. Due to the limited semiconductor overload capability, VSCs usually can only provide 1-2 p.u. short circuit current, which is significantly lower than that of synchronous machines.

Therefore, short circuit power characterization for VSCs considering converter peak current limit and reactive power support capability is still missing.

1.2.3 Fault analysis

For the purpose of static fault analysis, an SG is commonly modeled as an ideal voltage source behind an impedance whose value varies with time. The corresponding short circuit current can be classified into three characteristic periods: sub-transient, transient and steady-state. The fault analysis can be performed using either the complete method (the superposition method) [60, 61] or the developed international standards such as IEC 60909 [62]. However, converters have different physical properties and operation principles from SGs and their short circuit response is mainly governed by the control systems. The short circuit behavior can exhibit diverse characteristics depending on how the control systems are designed and the hardware's capability. This indicates that the conventional fault analysis method becomes inadequate with the presence of converters and thus dynamic simulations are commonly used.

From the system point of view, the impact of the negative-sequence short circuit current injection from VSCs on the grid have been investigated in [63, 64, 65] through dynamic simulations. These studies evaluate the impact of a single converter without extension to multiple VSCs. Even though dynamic simulations can provide accurate results and can exhibit transient behavior, they are not able to analytically perform the fault analysis and demand quite much work on the modeling. If the size of the system and the number of the converters increase, the modeling work can become extremely time-consuming. As a result, a variaty of studies [66, 67, 68, 69, 70, 71, 72, 73] attempt to include VSCs in the static fault analysis. However, a static fault analysis method considering both positive- and negative-sequence short circuit contributions from multiple VSCs is missing.

1.2.4 Distance protection evaluation

Renewable energy sources used to be integrated mainly in distribution networks in the form of Distributed Generation (DG). The existence of DGs transforms the distribution network into an active network that allows bi-directional power flows. With DGs' capability of contributing short circuit current, the fault current also becomes bidirectional in a distribution network, in which the fault current has conventionally been unidirectional. In addition, most of the DGs are interfaced with the network through VSCs, whose short circuit current is limited and has different characteristics from SGs. These changes can cause mis-coordination of overcurrent relays including protection blinding and sympathetic tripping [74]. These challenges have received much attention in recent years and a variety of solutions has been proposed [75, 76].

On the other hand, the ratings of renewable-based generations are increasing rapidly and many large wind farms as well as HVDC transmission systems up to the order of several hundred megawatts have been connected to the high-voltage transmission networks. This can also bring up challenges for the protection systems, such as transmission line protection using distance protection scheme.

Regarding three-phase balanced faults, the work in [17] analyses the potential impact of VSCs on distance protection, pointing out that the relays may refuse to trip when the fault current is insufficient and communication-aided approaches are necessary. However, the analysis is only based on theories without providing any test result. Li *et al.* [77] evaluates the distance relay performances with respect to different RE penetration levels, converter response time, output current ramp rates and fault current levels. The simulation results have shown that the response time of the relay can be significantly increased due to the presence of VSCs. In [78], the priority of active or reactive power injection from VSCs is concerned. The simulation results reveal that underreach problems can occur under resistive faults. The work in [79] discusses the effect of VSC-HVDC systems on the backup distance protection of adjacent lines through simulations. The described effect is actually a well-known phenomenon that can exist in any system and has already been tackled by protection engineers.

However, most of the faults in power systems are unbalanced faults and three-phase balanced faults rarely occur [80, 81]. Unbalanced faults are considered in [82, 83, 84, 85, 86], where the VSCs are controlled to provide only positive-sequence short circuit current. The work in [82] reports that the relay may mis-operate due to the lack of negative-sequence current. Hooshyar *et al.* [83] and Alam *et al*. [84] reveal that the distance relay cannot calculate impedance accurately during resistive faults and an algorithm based on communication for distance relay is proposed in [87]. In addition, all the studies mentioned above evaluate relay performances through only simulations. Nevertheless, the relay models in software are generally basic, without the procedures of signal processing or hardware responses. The models are not updated with the state-of-art functionalities from relay manufacturers and thus it can be difficult to discover potential protection problems. Even though testing on a real distance relay is performed in [85, 86], no work has considered VSCs' ability to provide negative-sequence short circuit current. In [88], the authors acknowledge that the negative-sequence short circuit current from VSCs may affect distance protections but without test results. Therefore, distance relay testing in converter-based power systems considering both positive- and negative-sequence short circuit current contributions from VSCs is missing.

1.2.5 Synchronous condenser applications

Synchronous condenser has been a well-known technology since the 1910s and was considered as an important shunt compensation device for long-distance high-voltage AC transmission at that time [89]. With the development of power electronic, Static Var Compensator (SVC) and Static Synchronous Compensator (STATCOM) started to gain popularity due to their lower costs and fewer maintenance requirements. As a result, less interest has been paid to SCs since then and their sale to support transmission ended abruptly. However, with the growing of RE integration and the development of synchronous machine technology, SCs' advantages over static devices in supporting grid operation have gained increasing attention in recent years.

The work in [89] states the performance characteristics of SCs and summarizes SCs' beneficial characteristics to the transmission grid. Several studies have been conducted illustrating the benefits of SC applications on voltage stability enhancement [90, 91], frequency stability improvement [92, 93, 94, 95, 96], and short circuit power contributions [90, 92, 93]. The dynamic responses of SCs under grid fault conditions are investigated in [93, 97] but unbalanced fault scenarios are left out. Nedd *et al.* [92] mentions that SCs can help address protection challenges in converter-based power systems but detailed studies are missing.

On the other hand, given the benefits of SC applications, the allocation of SCs in terms of locations and sizes has become a question both in academia and industry. For the purpose of voltage stability enhancement [98] and power quality improvement [99], the optimal location of SCs is investigated by comparing the simulation results. No optimization procedure is involved and hence only small-scale power systems are considered. The works in [100, 101] suggest that the refurbishment of conventional power plants to SCs can be a cost-effective solution. Marrazi *et al.* [102] presents an approach to allocating SCs for restoring system short circuit power. It requires a detailed power system model in PowerFactory to perform the fault analysis. However, it can be quite time-consuming to do the modeling for a larger power system. The results from [102] suggests that conventional power plants may not always serve as the best locations and newly installed SCs at the PCCs of converters can be anticipated. Therefore, it is necessary to investigate the cooperation of a VSC and an SC, and also to find a simple way to optimally decide the locations and sizes of SCs.

1.3 Contributions

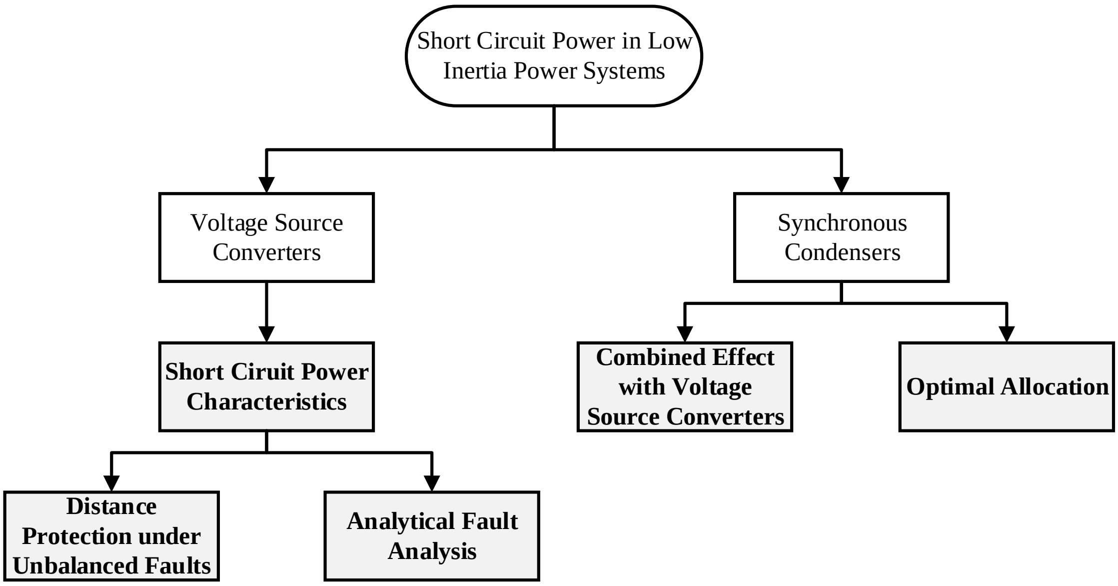

Figure 1.5: Overview of the research path

As discussed in Section 1.2, short circuit power issues in low inertia power systems have raised considerable attention in recent years and a variety of research work has been conducted. Voltage source converters and synchronous condensers can be regarded as the main sources of short circuit power in future low inertia power systems. However, there still exist certain gaps that need to be filled. They are illustrated in Figure 1.5 and further elaborated as below:

Voltage source converters

- *Short circuit power characteristics*: There exists a variety of control strategies of VSCs for short circuit power provision under grid unbalanced faults. The different strategies are developed based on specific control objectives and some of them are not sufficient or complete for short circuit power provision considering reactive power support capability and converter peak current limit. There lacks a unified approach to analyse the nature of and quantify the short circuit power from VSCs.
- *Distance protection under unbalanced faults*: The investigation on the potential impact of VSCs on distance protection is not sufficient. On the one hand, the basic relay models in different

power system simulation tools neither have the procedures of signal processing or hardware responses, nor the state-of-art functionalities. On the other hand, less attention has been given to unbalanced faults. The possible negative-sequence short circuit power contributions from VSCs are left unnoticed when it comes to relay testing.

- *Analytical fault analysis*: Simulation-based fault analysis is accurate and able to exhibit transient behavior, but it is difficult to be applied to large power systems with multiple converters and draw general conclusions analytically. For transmission systems, there lacks a static fault analysis method considering the presence of VSCs and their short circuit power in both positive- and negative-sequence. This makes it challenging to evaluate the impact of the short circuit power from VSCs on low inertia power systems.

Synchronous condensers

- *Combined effect with voltage source converters*: Synchronous condensers are well-known for their benefits on short circuit contributions. For a future converter-dominated power system, SCs are likely to be installed at the PCCs of VSC stations and hence introduce possible interactions between SCs and VSCs. What is the impact of SCs on different systems properties? Is there any negative impact? How should the VSCs be controlled under unbalanced faults for incorporating SCs? These questions require detailed and systematic research work.
- *Optimal allocation*: Synchronous condensers are able to improve the system short circuit strength. However, there lacks a simple approach to allocate SCs optimally in terms of the total cost, numbers, sizes and locations in low inertia power systems.

Therefore, the main contributions of this work to the assessment of short circuit power and protection systems for low inertia power systems are:

- *Characterising the short circuit power contributions from VSCs*: The short circuit power from VSCs is investigated and characterized in terms of different groups considering the reactive power support capability and the converter peak current limit. The characterization provides a unified manner to analyze the various control strategies of VSCs under grid unbalanced faults.
- *Identification of possible malfunctions of distance relays in low inertia power systems*: The HIL tests on distance protection reveals how the distance relay can be affected by the power electronics control in a converter-dominated system under unbalanced faults, and how an SC should help restore distance relay performances.
- *Development of a static fault analysis method considering short circuit power contributions from VSCs*: The proposed method accommodates VSCs' capability of simultaneous injection of short circuit power in positive- and negative-sequence. A new phenomenon is discovered that the system may not have a stable response under grid unbalanced faults in low inertia power systems. The phenomenon is mathematically investigated and explained by the developed method.

- *Provision of suggestions on selecting the control strategies of VSCs under unbalance faults for incorporating SCs*: The investigation on the combined effect of VSCs and SCs points out the disadvantages associated with certain control strategies, leading to the suggestions on selecting the control strategies for VSCs when incorporating an SC at the PCC.
- *Development of a simple method for the optimal allocation of SCs*: A simple optimization approach is developed to determine the number, size, and location of new SCs for Short Circuit Ratio (SCR) improvement. It uses the developed static fault analysis method and does not require detailed power system models in simulations.

This work also has the following contributions to the SCAPP project:

- *Development and validation of the future western Danish transmission power system in Real Time Digital Simulator (RTDS)*: The model includes detailed VSC-HVDC and Line Commutated Converter based HVDC (LCC-HVDC) transmission systems, Type-III and Type-IV wind farms and other electrical components. The system is validated by comparing the simulation results and the fault records subject to real short circuit events provided by the Danish TSO Energinet.
- *Development of a HIL test platform for distance and generator protective relays*: The test platform integrates RTDS models, communication interfaces, amplifiers and relays into a closed loop to achieve relay testing in real time. A Transmission Control Protocol/Internet Protocol (TCP/IP) link is established between RTDS and MATLAB. The bi-directional communication enables to automate the relay testing in different scenarios only through MATLAB scripts.

1.4 Thesis structure

This section introduces the thesis structure to help readers find the way through the thesis. The main results from this Ph.D. project are presented in separate scientific publications listed on page 15. The rest of the thesis is a representation of all the publications in a unified way. However, the publications may also be read independently of the thesis.

- *Chapter 1* firstly presents the background of the project with an introduction to synchronous condensers. The state of art of grid requirements, fault analysis, distance protection evaluation, and synchronous condenser applications are discussed. The chapter is concluded by a list of the contributions, the description of the thesis structure, and a list of the publications prepared throughout the project.
- *Chapter 2* presents the short circuit power characterization for synchronous sources and voltage source converters supported by various simulation results from RTDS. It illustrates the differences of the short circuit response between these two types of sources, and the undesirable performances of VSCs under grid unbalanced faults when using the conventional control method. Based on the instantaneous power theory, the dual-sequence current control strategies of grid-connected VSCs are reviewed and categorized into two different groups and their relationships are analyzed through a unified manner. The different control aspects of VSCs are also provided with a focus on the design of the converter peak current limit and the inner current controllers.

- *Chapter 3* firstly presents the modeling work of the western Danish power system and its validation. Then, the hardware-in-the-loop test platform developed through the project is introduced. The communication between RTDS and the external program MATLAB is established to automate the distance relay testing investigating the impact of the dual-sequence current control strategies of VSCs on distance protection. By connecting a synchronous condenser at the point of common coupling of a VSC-HVDC station, the interaction between synchronous condensers and VSC-based sources is explored through examining the combined short circuit current, the voltage at the point of common coupling, the DC-side voltage and the system frequency response during faults.

- *Chapter 4* develops an analytical static fault analysis method considering both positive- and negative-sequence short circuit currents from VSCs. The method is validated through real-time simulations. The method is used to help explain a phenomenon that the system does not have a stable response under grid unbalanced faults due to the injection of negative-sequence reactive power. Then, the fault analysis method is further applied to help optimally allocate synchronous condensers in terms of sizes and locations for a future western Danish power system.

- *Chapter 5* extends the use of the dual-sequence current control strategies of VSCs to a microgrid environment. As a case study of Chapter 2, the focus is given to the control of the grid-forming converter and investigates the short circuit power characteristics when the system is operating under 100 % penetration of renewable energy.

- *Chapter 6*: concludes the work done as well as the findings of the Ph.D. project, and provides some visions for the future work.

1.5 List of publications

The relevant publications throughout the project are listed as follows:

[Pub. A] **J. Jia**, G. Yang, A. H. Nielsen and P. Rønne-Hansen, "Impact of VSC Control Strategies and Incorporation of Synchronous Condensers on Distance Protection under Unbalanced Faults", *IEEE Transactions on Industrial Electronics*, vol. 66, no. 2, pp. 1108-1118, Feb. 2019, DOI: 10.1109/TIE.2018.2835389.

[Pub. B] **J. Jia**, G. Yang and A. H. Nielsen, "A Review on Grid-Connected Converter Control for Short-Circuit Power Provision Under Grid Unbalanced Faults", *IEEE Transactions on Power Delivery*, vol. 33, no. 2, pp. 649-661, Apr. 2018, DOI: 10.1109/TPWRD.2017.2682164.

[Pub. C] **J. Jia**, G. Yang and A. H. Nielsen, "Fault Analysis Method Considering Dual-Sequence Current Control of VSCs under Unbalanced Faults", *Energies*, vol. 11, no. 7, pp. 1-17, Jun. 2018, DOI: 10.3390/en11071660.

[Pub. D] **J. Jia**, G. Yang, A. H. Nielsen and Vahan Gevorgian, "Investigation on the Combined Effect of VSC-Based Sources and Synchronous Condensers under Grid Unbalanced Faults", submitted to *IEEE Transactions on Power Delivery*, under review.

[Pub. E] **J. Jia**, G. Yang, A. H. Nielsen and P. Rønne-Hansen, "Hardware-in-the-loop Tests on Distance Protection Considering VSC Fault-ride-through Control Strategies", *IET The Journal of Engineering*, vol. 2018, no. 15, pp. 824-829, Oct. 2018, presented at *The 14th International Conference on Developments in Power System Protection (DPSP)*, Belfast, Uk, 12-15 Mar. 2018, DOI: 10.1049/joe.2018.0248.

[Pub. F] **J. Jia**, G. Yang, A. H. Nielsen and P. Rønne-Hansen, "Investigation of Grid-Connected Voltage Source Converter Performance under Unbalanced Faults", in *Proceedings of IEEE PES Asia-Pacific Power and Energy Conference (APPEEC)*, pp. 609-613, Beijing, China, 25-28 Oct. 2016, DOI: 10.1109/APPEEC.2016.7779576.

[Pub. G] **J. Jia**, G. Yang, A. H. Nielsen, P. Weinreich-Jensen, Eduard Muljadi and Vahan Gevorgian, "Synchronous Condenser Allocation for Improving System Short Circuit Ratio", in *Proceedings of The 5th International Conference on Electric Power and Energy Conversion Systems (EPECS)*, pp. 1-5, Kitakyushu, Japan, 23-25 Apr. 2018, DOI: 10.1109/EPECS.2018.8443358.

[Pub. H] **J. Jia**, G. Yang, A. H. Nielsen and P. Rønne-Hansen, "Study of Control Strategies of Power Electronics during Faults in Microgrids", Chapter 7 in *Hybrid-Renewable Energy Systems in Microgrids Integration, Developments and Control*, Woodhead Publishing, Elsevier, pp. 109-146, Jun. 2018, DOI: 10.1016/B978-0-08-102493-5.00007-8.

The following publication has also been prepared during the Ph.D. study, but has been omitted from the thesis because it is not directly related to the primary objective.

[Pub. I] M. Sarkar, **J. Jia** and G. Yang, "Distance relay performance in future converter dominated power systems", in *Proceedings of The 12th IEEE PES PowerTech Conference*, Manchester, pp. 1-6, 18-22 Jun. 2017, DOI: 10.1109/PTC.2017.7981144.

CHAPTER 2

Short Circuit Power Characterization

This chapter presents the short circuit power characterization for synchronous sources and voltage source converters, which provides a basis and understanding for the subsequent studies in this dissertation. Firstly, the short circuit behavior of an SG, an SC, and a grid-connected VSC with conventional controls are compared under different types of faults. Next, given the undesirable responses of the VSC under unbalanced faults, the dual-sequence current control strategies of VSCs using the instantaneous power theory are reviewed. They are classified into two groups based on the properties being control directly, namely power-characteristic-oriented control strategy and voltage-support-oriented control strategy. The different control aspects of VSCs are also provided with a focus on the converter peak current limit and the inner current controllers. Finally, the relationship among different control strategies are analysed in an unified manner and the control objectives are discussed. The main results of this chapter were documented in [**Pub. A**], [**Pub. B**], [**Pub. D**] and [**Pub. F**].

2.1 Short circuit power from synchronous sources

2.1.1 Short circuit current calculation

Fault studies are an crucial part of power system analysis. Power system faults can be generally classified into three-phase balanced faults, and unbalanced faults which consist of single line-to-ground fault, line-to-line fault, and double line-to-groud fault [103]. The characteristics of the short circuit current mainly depend on the network configuration and the impedance of its components through which the short circuit current passes. In a conventional power system, SGs are the main sources of the short circuit current and the characteristics of the short circuit current can be illustrated by Fig. 2.1 [62]. The short circuit impedance of an SG under short circuit conditions is a time-varying quantity. For the purpose of fault studies, the corresponding short circuit current is typically classified into the subtransient period (the first few cycles), transient period (the next a few cycles), and steady-state period. In IEC 60909 [62], the initial symmetrical short circuit current $I_k^{''}$ and the initial symmetrical short circuit power $S_k^{''}$ are defined as:

$$I_k^{''} = \frac{cU_n}{\sqrt{3}Z_k} \tag{2.1}$$

$$S_k^{''} = \sqrt{3}U_n I_k^{''} \tag{2.2}$$

where U_n refers to the system nominal voltage; Z_k is the equivalent short circuit impedance of the system as seen from the fault location; c is a voltage factor takes the voltage variations into account. $S_k^{''}$ is a common measure of the strength of the system at a certain bus. A system with higher short circuit power is less prone to voltage deviation.

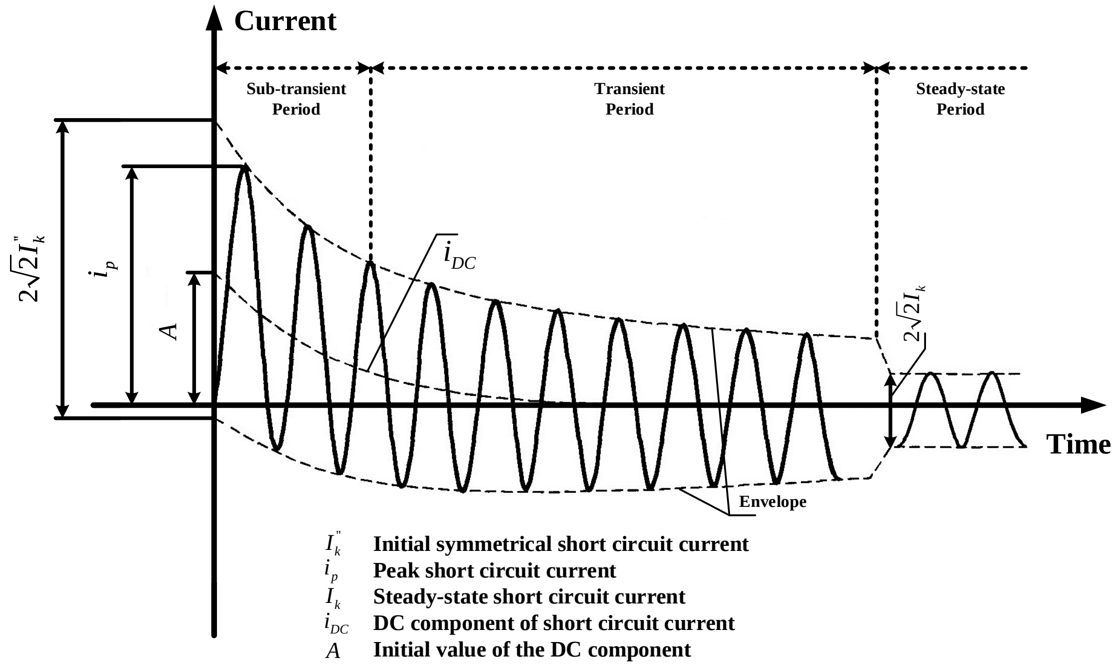

Figure 2.1: Schematic diagram of the short circuit current of a near-to-generator short circuit with decaying AC component

Regarding the three types of unbalanced faults, the initial short circuit current for single line-to-ground fault $I_{k1}^{''}$, for line-to-line fault $I_{k2}^{''}$, and for double line-to-ground fault $I_{kE2E}^{''}$ are calculated respectively according to [62]:

$$I_{k1}^{''} = \frac{\sqrt{3}cU_n}{Z_1 + Z_2 + Z_0} \tag{2.3}$$

$$I_{k2}^{''} = \frac{cU_n}{Z_1 + Z_2} \tag{2.4}$$

$$I_{kE2E}^{''} = \frac{\sqrt{3}cU_n Z_2}{Z_1 Z_2 + Z_1 Z_0 + Z_2 Z_0} \tag{2.5}$$

where Z_1, Z_2 and Z_0 represents the short circuit impedance as seen from the fault location in positive-, negative- and zero-sequence networks.

2.1.2 Short circuit current simulation

Electromagnetic Transients Program (EMTP) is a valuable tool for analysing the transient and dynamic behavior of power systems. It can provide supplements to the conventional fault studies and hand calculations. This section examines and compares the short circuit behavior of an SG and an SC through EMTP simulations with RTDS.

In Fig. 2.2, an SG or an SC with a rating of 250 MVA is connected to a grid through a 21/400 kV step-up transformer. The grid is modeled as a constant 400 kV voltage source behind an impedance of $32\angle 85°\Omega$. The SG and SC share the same parameters. Prior to the fault, both SG and SC are excited to exchange zero reactive power with grid and the SG delivers 250 MW active power. Subject to a three-phase balanced fault or an unbalanced fault on the high-voltage side, the three-phase voltage, the three-phase current and the power measured from the low-voltage

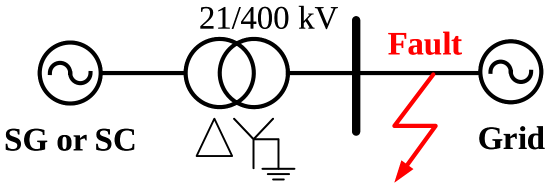

Figure 2.2: Single-line diagram of a simple system

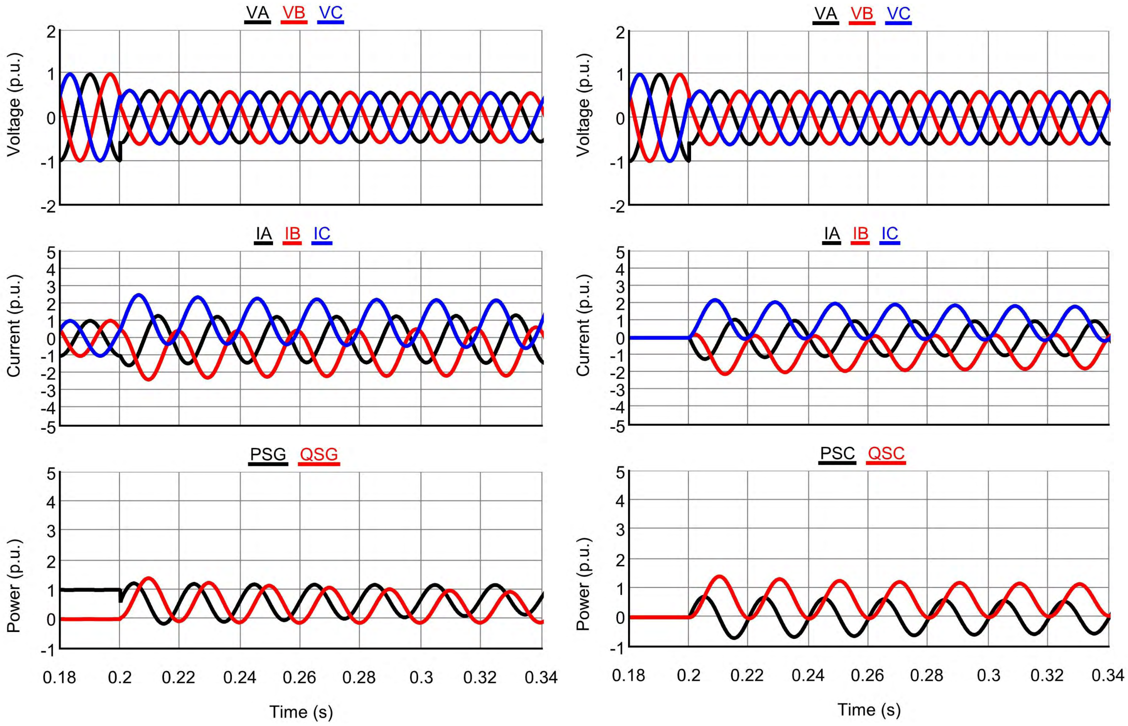

(a) SG (b) SC

Figure 2.3: Short circuit response of an SG and an SC under three-phase balanced faults

side (delta-winding side) are presented in Fig. 2.3 and Fig. 2.4 respectively. The short circuit response is given in terms of per unit values with $S_{base} = 250$ MVA, $V_{base} = \sqrt{2/3} \cdot 21$ kV, and $I_{base} = \sqrt{2/3} \cdot 250/21$ kA.

As a synchronous machine, the SC provides short circuit current conforming to the schematic diagram in Fig. 2.1. The magnitude of its short circuit current is within the same order as that of the SG. During the fault, both SG and SC naturally contribute a considerate amount of reactive power. The SC cannot provide sustaining active power but as a rotating machine, the SC provides inertia response resulting in its active power exchange with the grid.

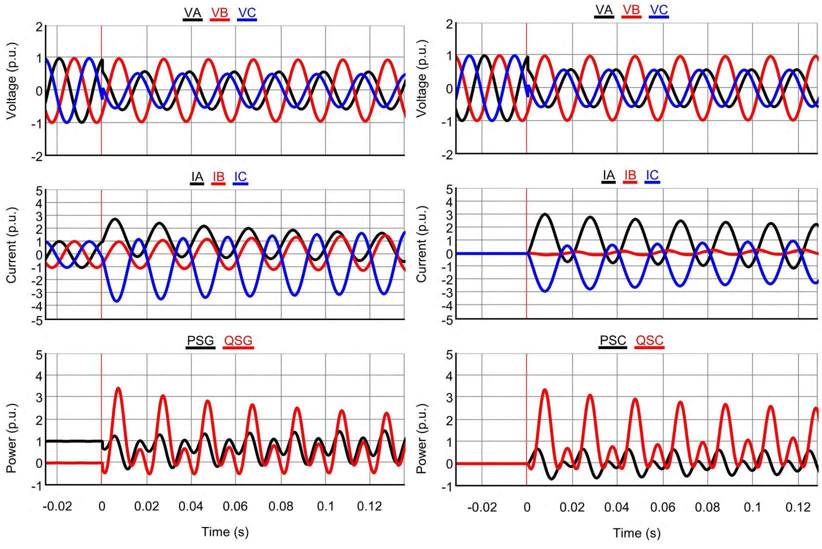

(a) SG, A-g fault (b) SC, A-g fault

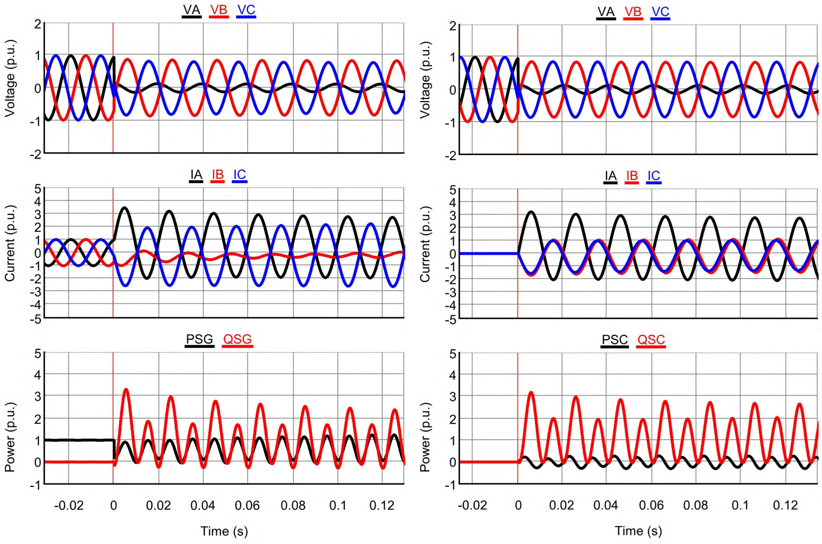

(c) SG, A-B fault (d) SC, A-B fault

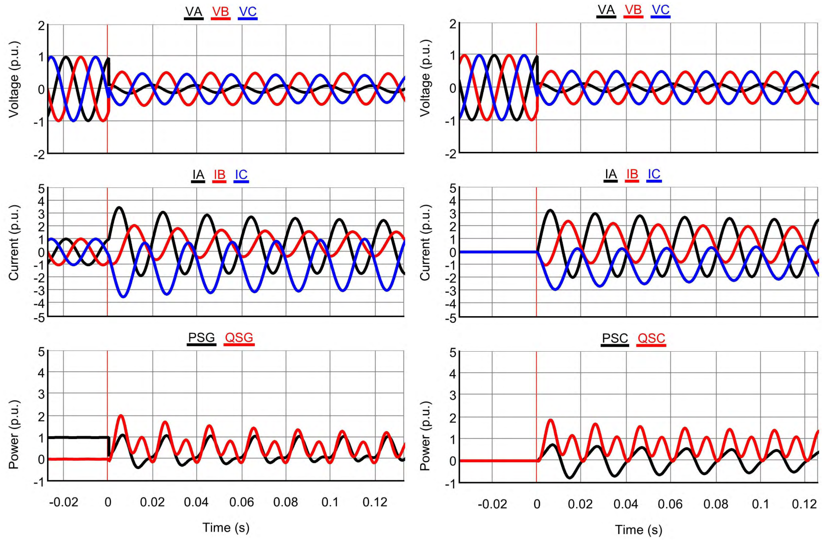

(e) SG, A-B-g fault (f) SC, A-B-g fault

Figure 2.4: Short circuit response of an SG and an SC under unbalanced faults

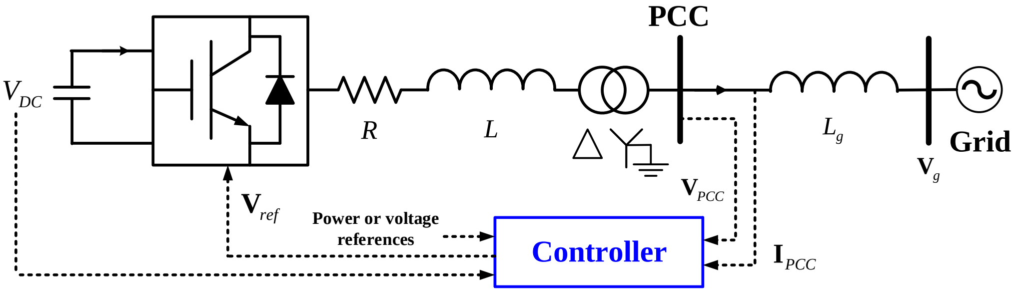

Figure 2.5: Configuration of a grid-connected VSC system

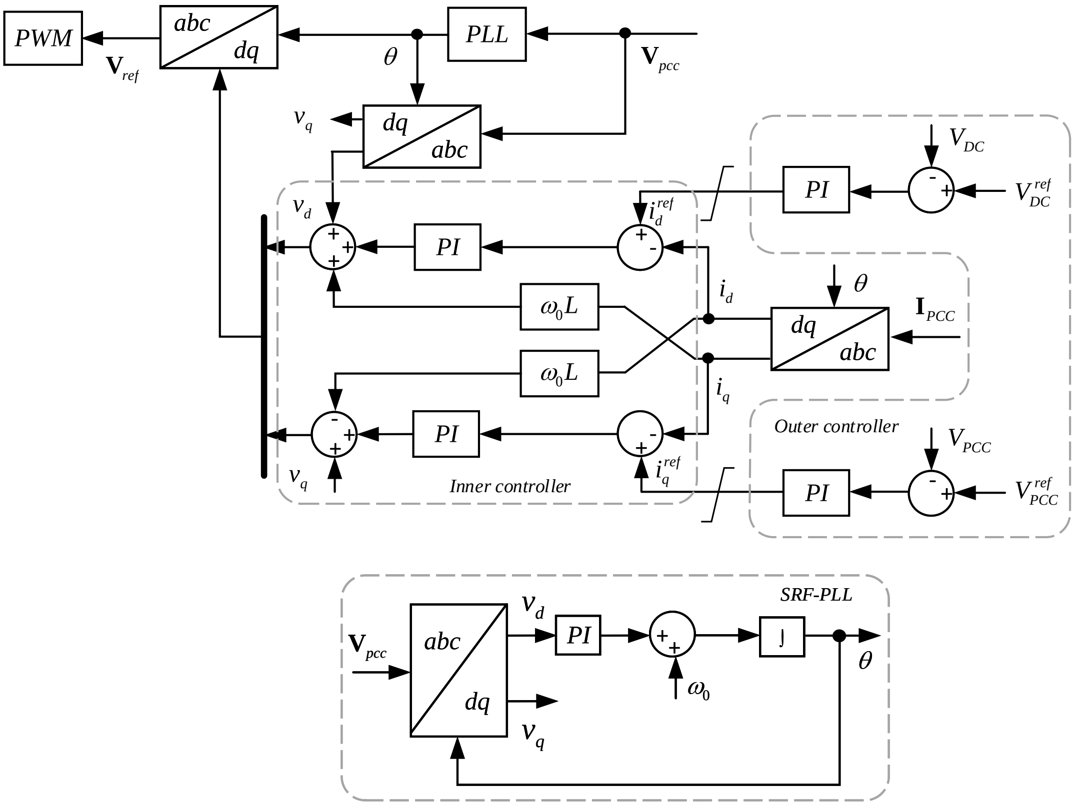

Figure 2.6: Control block diagram of a grid-connected VSC in SRF

2.2 Short circuit power from VSCs with conventional controls

In modern grid codes, VSC-based generation units and VSC-HVDC systems are required to have the capability to provide fast fault current during grid short circuit conditions [28, 29]. However, unlike synchronous machines, VSCs cannot provide short circuit power naturally and their short circuit response is mainly governed by the control systems.

Figure 2.5 shows a basic configuration of a grid-connected VSC system. The control system takes the PCC voltage, the PCC current, power or voltage references, and the DC-side voltage as inputs. The final outputs of the controller are a set of voltage references for the Pulse Width Modulation (PWM). Correspondingly, Fig. 2.6 presents the control block diagram of a conventional controller implemented in Synchronous Reference Frame (SRF) [104, 105, 106]. The SRF, which is commonly used in the industry [107], converts the three-phase voltage and current into a frame that rotates synchronously with the grid through Park Transformation, so that the three-phase time-varying signals are transformed into DC signals. The angle θ, provided by the PLL, is classically generated in a way so that v_q=0. Therefore, the output active and reactive powers at the PCC can be expressed by:

$$p = \frac{3}{2} v_d i_d \tag{2.6}$$

$$q = -\frac{3}{2} v_d i_q \tag{2.7}$$

which indicates that the active and reactive powers can be controlled by i_d and i_q, respectively.

Typically, for a current-controlled VSC system, the control system consists of a slower outer controller and a faster inner current controller. The outer controller regulates the DC side voltage, the AC side voltage, and the output powers at the PCC depending on the application. It generates current references for the inner current controller that regulates the converter current.

Firstly, the grid-connected VSC system in Fig 2.5 is simulated in RTDS with the conventional controls illustrated by Fig. 2.6. The VSC with the rating of 500 MVA interfaces with the grid through a 150/400 kV step-up transformer. The grid is modeled as a constant 400 kV voltage source behind an impedance of $32\angle 85°\Omega$. Prior to the fault, the VSC delivers 500 MW active power at the unity power factor. To provide reactive power support, the current reference i_q^{ref} during the fault is generated according to the grid code in Fig. 1.4. The short circuit response is given in per unit values with $S_{base} = 500$ MVA, $V_{base} = \sqrt{2/3} \cdot 150$ kV, and $I_{base} = \sqrt{2/3} \cdot 500/150$ kA. Considering the limited semiconductor overload capability, it is assumed that the VSC has a converter peak current limit at 1.2 p.u..

2.2.1 Three-phase balanced faults

Corresponding to a three-phase balanced fault on the high voltage side, Fig. 2.7(a) presents the short circuit response of the VSC when there is no converter current peak limit imposed. The VSC provides a set of balanced short circuit current during the fault. The active power remains the same as the pre-fault level and the reactive power increases to a certain level after some initial transients. The short circuit response with a 1.2 p.u. converter peak current limit is given in Fig. 2.7(b), where the reactive current injection is prioritized based on (2.8). The actual i_d^{ref} is decided by how much current margin is left after satisfying the reactive current injection. As a result, the active power from the VSC is curtailed during the fault to comply with the current limit. By comparing Fig. 2.7 with Fig. 2.3, it can be observed that the short circuit current from the VSC is restricted in the magnitude and its characteristic does not comply with the schematic diagram in Fig. 2.1 for synchronous sources.

$$i_{d,limit}^{ref} = \sqrt{(I_{max})^2 - (i_q^{ref})^2} \tag{2.8}$$

2.2.2 Unbalanced faults

With the same control technique and the converter peak current limit, Fig. 2.8 shows the short circuit response of the VSC subject to three different types of unbalanced faults on the high-voltage

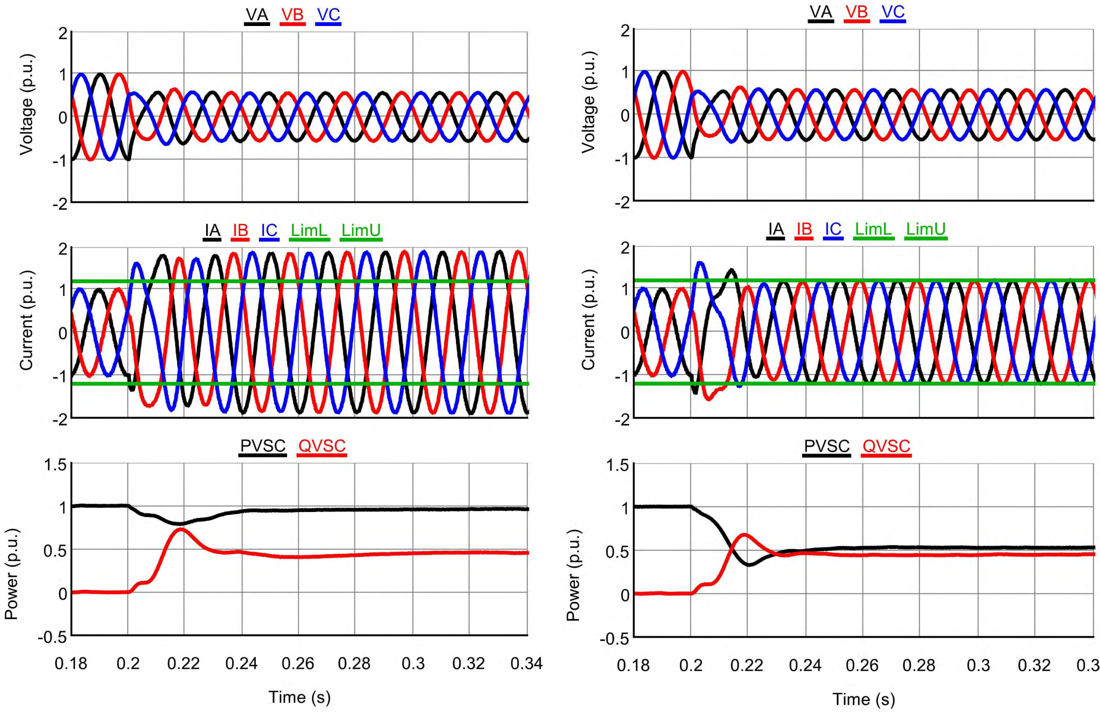

(a) Without converter current limit

(b) With converter current limit

Figure 2.7: Short circuit response of a grid-connected VSC under three-phase balanced faults

side at the zero time instant. For the A-g and A-B fault, the voltage exhibits undesirable distortions. The short circuit current is mixed with the third-order harmonics and the peak current is not within the pre-defined limit.

During unbalanced faults, negative-sequence components will appear at the PCC. For example, as shown in Fig. 2.9, a set of current can be represented by the superposition of the positive-sequence component $\mathbf{i}_{\alpha\beta}^{+}$ which rotates counter-clockwise, and the negative-sequence component $\mathbf{i}_{\alpha\beta}^{-}$ which rotates clockwise. The corresponding mathematical representation can be given by:

$$\mathbf{i}_{\alpha\beta} = \mathbf{i}_{\alpha\beta}^{+} + \mathbf{i}_{\alpha\beta}^{-} = I^{+}\begin{bmatrix}\cos(\omega t+\delta^{+})\\ \sin(\omega t+\delta^{+})\end{bmatrix} + I^{-}\begin{bmatrix}\cos(-\omega t+\delta^{-})\\ \sin(-\omega t+\delta^{-})\end{bmatrix} \tag{2.9}$$

where α and β represents the quantities expressed in the stationary reference frame. If the Park Transformation is applied to $\mathbf{i}_{\alpha\beta}$, there is:

$$\begin{bmatrix}i_d\\ i_q\end{bmatrix} = \begin{bmatrix}\cos(\omega t+\theta^{+}) & \sin(\omega t+\theta^{+})\\ -\sin(\omega t+\theta^{+}) & \cos(\omega t+\theta^{+})\end{bmatrix}\mathbf{i}_{\alpha\beta} = \underbrace{I^{+}\begin{bmatrix}\cos(\theta^{+}-\delta^{+})\\ -\sin(\theta^{+}-\delta^{+})\end{bmatrix}}_{DC\ terms} + \underbrace{I^{-}\begin{bmatrix}\cos(2\omega t+\theta^{+}-\delta^{-})\\ -\sin(2\omega t+\theta^{+}-\delta^{-})\end{bmatrix}}_{AC\ terms} \tag{2.10}$$

which indicates that there is a coupling between the positive- and negative-sequence networks when doing the Park Transformation under unbalanced conditions. This introduces AC terms into the inputs v_d, v_q, i_d and i_q for the control system in Fig. 2.6. As a result, as shown in Fig. 2.8, the current references under fault conditions are contaminated with AC terms. Due to the limited bandwidth, a Proportional-Integral (PI) controller is not able to track AC references without any steady-state error [50]. Therefore, the generated modulation waves for the PWM become non-sinusoidal and the VSC exhibits undesirable performances.

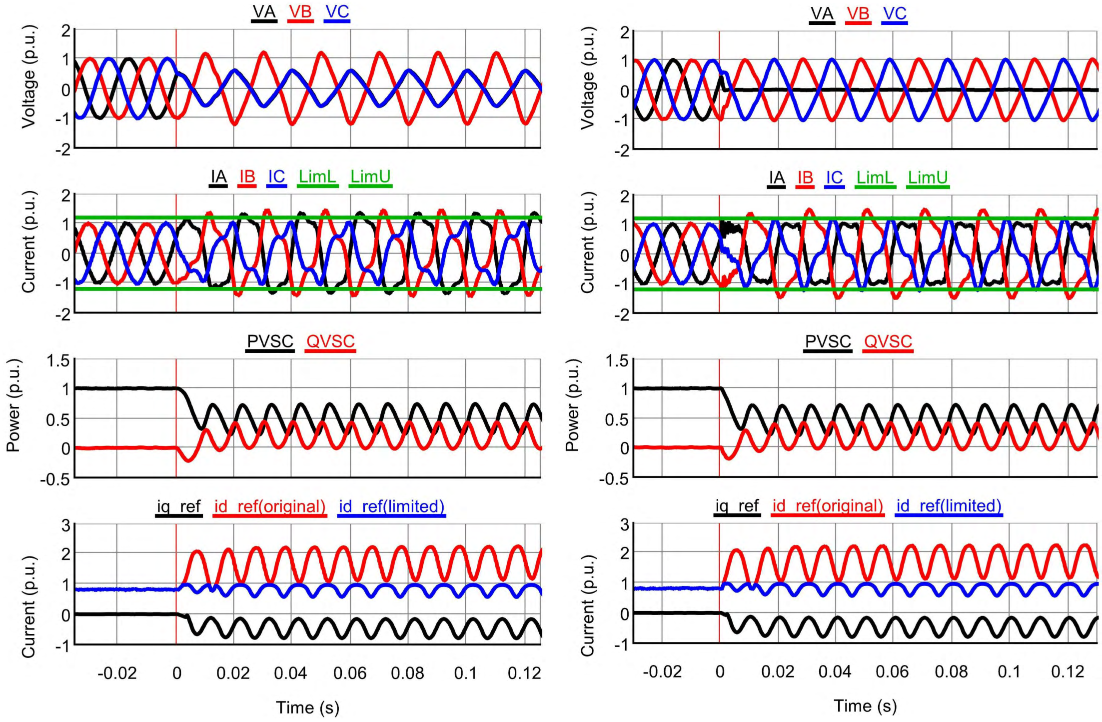

(a) A-g fault (b) A-B fault

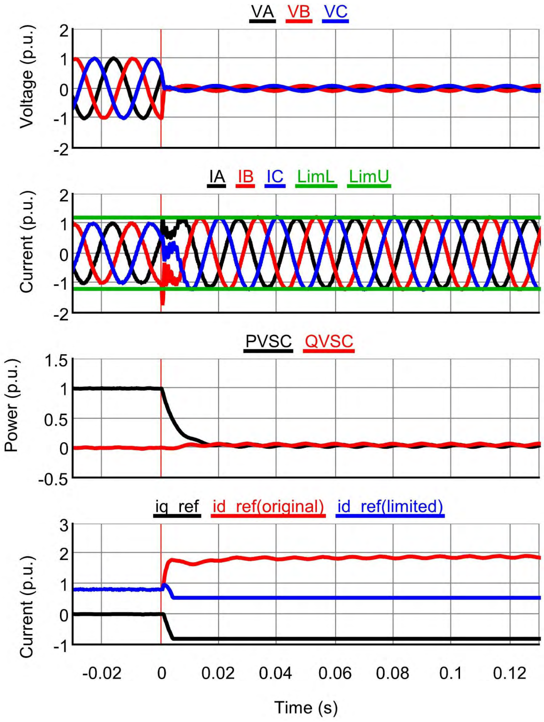

(c) A-B-g fault

Figure 2.8: Short circuit response of a grid-connected VSC under unbalanced faults with conventional controls

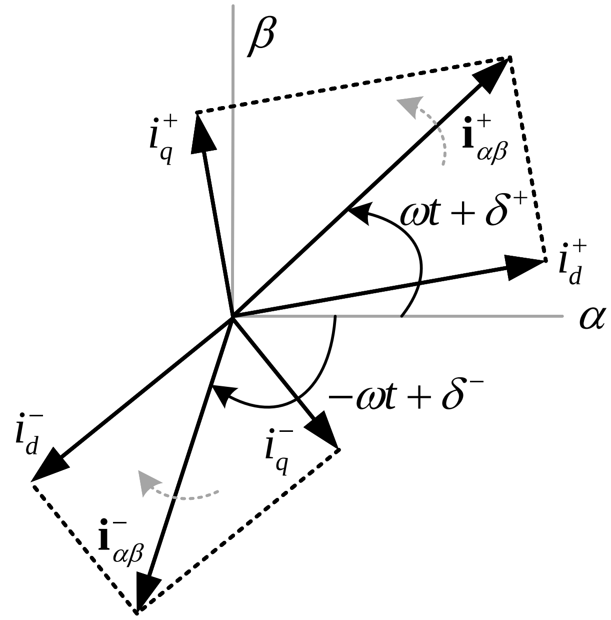

Figure 2.9: Phasor digram of the superposition of positive- and negative-sequence currents

Then, the controller is modified by using only the positive-sequence voltage and current as inputs. The current references i_d and i_q are filtered by notch filters to eliminate the AC terms. The corresponding VSC short circuit response is given in Fig. 2.10. For the same fault conditions, the voltage and current are free of distortions and exhibit sinusoidal waveforms. However, the converter peak current is still not within the pre-defined limit after the initial transients. The reason is that the controller in Fig. 2.6 is only implemented in the SRF for the positive-sequence component, leaving the negative-sequence current unregulated. This indicates that, the negative-sequence current from the VSC should be controlled properly.

2.3 Instantaneous power theory

The instantaneous power theory [51] presents a time-domain analysis of power in a three-phase electric circuit. It has been widely applied in designing controllers for power electronic devices due to its efficiency and flexibility. If the instantaneous voltage and current measured at the PCC are denoted by the vectors **v** and **i**, the instantaneous active and reactive powers are expressed by:

$$p = \mathbf{v} \cdot \mathbf{i} \tag{2.11}$$

$$q = \mathbf{v}_{\perp} \cdot \mathbf{i} \tag{2.12}$$

where "·" represents the doc product; $\mathbf{v}_{\perp}$ refers to a 90°-lagged version of the original vector. The definition given by (2.11)-(2.12) is valid in any reference frame [54]. When there is an unbalanced fault, the voltage and current can be considered as the superposition of the positive- and negative-sequence components:

$$\mathbf{v} = \mathbf{v}^+ + \mathbf{v}^- \tag{2.13}$$

$$\mathbf{v} = \mathbf{i}^+ + \mathbf{i}^- \tag{2.14}$$

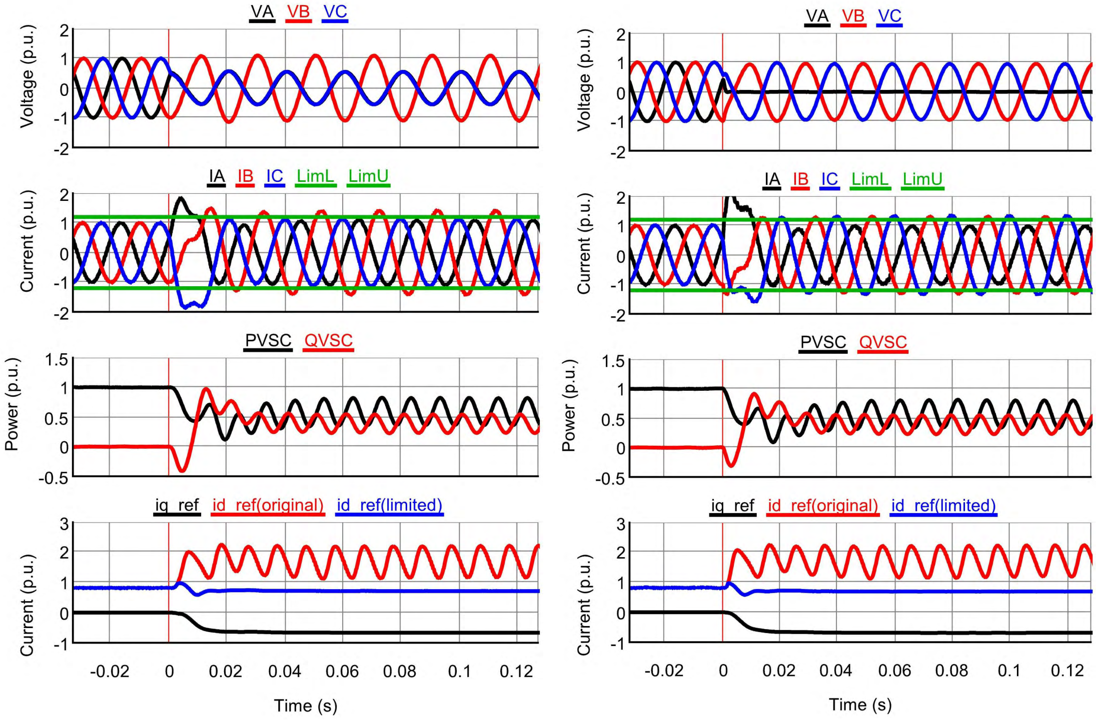

(a) A-g fault (b) A-B fault

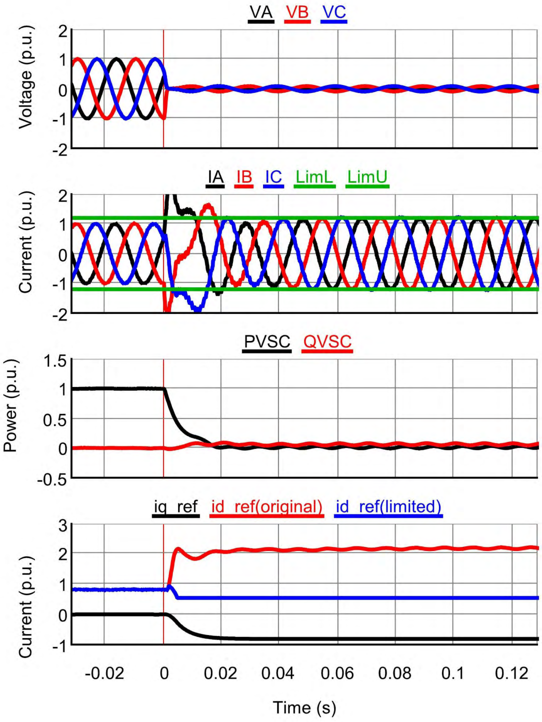

(c) A-B-g fault

Figure 2.10: Short circuit response of a grid-connected VSC under unbalanced faults with modified conventional controls

Therefore, with (2.13)-(2.14) substituted into (2.11)-(2.12) and further derivation considering only the fundamental frequency component [see Appendix A], the instantaneous active and reactive powers can be expanded as:

$$p = \overbrace{\underbrace{P^{+} + P^{-}}_{\mathbf{v}^{+}\cdot\mathbf{i}^{+}+\mathbf{v}^{-}\cdot\mathbf{i}^{-}}}^{\overline{P}} + \overbrace{\underbrace{P_{c2}\cos(2\omega t) + P_{s2}\sin(2\omega t)}_{\mathbf{v}^{+}\cdot\mathbf{i}^{-}+\mathbf{v}^{-}\cdot\mathbf{i}^{+}}}^{\widetilde{P}} \tag{2.15}$$

$$q = \overbrace{\underbrace{Q^{+} + Q^{-}}_{\mathbf{v}_{\perp}^{+}\cdot\mathbf{i}^{+}+\mathbf{v}_{\perp}^{-}\cdot\mathbf{i}^{-}}}^{\overline{Q}} + \overbrace{\underbrace{Q_{c2}\cos(2\omega t) + Q_{s2}\sin(2\omega t)}_{\mathbf{v}_{\perp}^{+}\cdot\mathbf{i}^{-}+\mathbf{v}_{\perp}^{-}\cdot\mathbf{i}^{+}}}^{\widetilde{Q}} \tag{2.16}$$

where $\overline{P}$ and $\overline{Q}$ are constant power terms that result from the interaction between the voltage and current from the same sequence. They consist of positive-sequence powers P^{+} and Q^{+}, and negative-sequence powers P^{-} and Q^{-}; $\widetilde{P}$ and $\widetilde{Q}$ are oscillating power terms that originate from the interaction between the voltage and current from different sequences. They are oscillating at twice fundamental frequency. If (2.15)-(2.16) are transformed into SRF through Park Transformation, the constant power terms and the magnitudes of the oscillating power terms can be expressed by:

$$\overline{P} = \frac{3}{2}(v_d^{+} i_d^{+} + v_q^{+} i_q^{+} + v_d^{-} i_d^{-} + v_q^{-} i_q^{-}) \tag{2.17}$$

$$P_{c2} = \frac{3}{2}(v_d^{-} i_d^{+} + v_q^{-} i_q^{+} + v_d^{+} i_d^{-} + v_q^{+} i_q^{-}) \tag{2.18}$$

$$P_{s2} = \frac{3}{2}(v_q^{-} i_d^{+} - v_d^{-} i_q^{+} - v_q^{+} i_d^{-} + v_d^{+} i_q^{-}) \tag{2.19}$$

$$\overline{Q} = \frac{3}{2}(v_q^{+} i_d^{+} - v_d^{+} i_q^{+} + v_q^{-} i_d^{-} - v_d^{-} i_q^{-}) \tag{2.20}$$

$$Q_{c2} = \frac{3}{2}(v_q^{-} i_d^{+} - v_d^{-} i_q^{+} + v_q^{+} i_d^{-} - v_d^{+} i_q^{-}) \tag{2.21}$$

$$Q_{s2} = \frac{3}{2}(-v_d^{-} i_d^{+} - v_q^{-} i_q^{+} + v_d^{+} i_d^{-} + v_q^{+} i_q^{-}) \tag{2.22}$$

where v_d^{+}, v_q^{+}, i_d^{+} and i_q^{+} are the positive-sequence voltage and current in SRF that rotates at the frequency ω; v_d^{-}, v_q^{-}, i_q^{+} and i_q^{-} are the negative-sequence voltage and current in SRF that rotates at the frequency $-\omega$. This indicates that, if the positive- and negative-sequence current are controlled simultaneously, the short circuit power from VSCs can exhibit various characteristics depending on how current references are formulated.

2.4 Short circuit power from VSCs with dual-sequence controls

With the help of the instantaneous power theory and the symmetrical component theory, the short circuit power from VSCs can be characterized by (2.15)–(2.22). The simultaneous control over the positive- and negative-sequence current enables VSCs to provide short circuit power in various ways and achieve different control objectives under unbalanced faults. This section focus on the short circuit response of a VSC with dual-sequence current controls under unbalanced faults.

2.4.1 Inner current controllers

For a current-controlled VSC, the inner current controller is a crucial part of the control system. It tracks the current references generated by the outer controller so that the VSC operates as desired. In general, the inner current controller can be implemented in three different reference frames.

Synchronous reference frame

Synchronous reference frame (SRF) control is also denoted as dq-control. The three-phase grid voltage and current are converted into a frame that rotates synchronously with the grid by Park Transformation. This enables the three-phase time-varying quantities to become DC signals in the SRF. The PI controller is typically used in SRF and its transfer function in Laplace-domain is:

$$G_{PI}(s) = K_p + \frac{K_i}{s} \tag{2.23}$$

where K_p, K_i are the proportional gain, and the integral gain respectively. It is able to track DC references without steady-state error. However, the PI controller has steady-state errors when regulating AC signals. Since the bandwidth of a PI controller cannot be extended easily, it does not give satisfactory performances with the conventional controls as shown in Section 2.2.2.

Since the 1990s, a considerable amount of work has been conducted to control VSCs under unbalanced conditions using dq-control. The very first work in [47] proposes to use PI controllers acting on the complete current in positive-sequence SRF. The negative-sequence current is compensated by adding a negative-sequence control variable to the voltage references for PWM. The work aims to minimize the DC-side oscillations and the distortions in AC current. The use of PI controller acting on complete currents has also been reported in [48] and [49]. The negative-sequence voltage is feed-forwarded to the voltage references in [48], so that the converter provides only positive-sequence current. In [49], the current references and the feed-forwarded grid voltages are modified by adding the negative-sequence components that have been transformed into positive-sequence SRF, in order to achieve constant active power provision. However, the steady-state error issue still exists in these methods and the converter cannot be controlled flexibly.

Song *et al.* [50] firstly proposes to use current controllers in dual-sequence. The method applies two sets of PI controllers as shown in Fig. 2.11, one regulating only positive-sequence current in positive-sequence SRF, and the other regulating only negative-sequence current in negative-sequence SRF. This allows the current in different sequences to be controlled as DC signals.

Stationary reference frame

Stationary reference frame control is also referred to $\alpha\beta$-control, which regulates current in the stationary two-phase frame. Figure 2.12 presents a general structure of the current controller for VSC application with dual-sequence current control. Proportional-Resonant (PR) controller is commonly used in the stationary reference frame with the transfer function:

$$G_{PR}(s) = K_p + \frac{K_i s}{s^2 + \omega_0^2} \tag{2.24}$$

where K_p, K_i are the proportional gain, and the integral gain respectively; ω_0 represents the resonant frequency. PR controller is able to track sinusoidal references without steady-state error. This controller has a high gain around ω_0, and K_i decides the bandwidth around ω_0 point [108]. This indicates that PR controller is frequency sensitive and it should be carefully designed considering the system frequency response. In [109], the PR controller is improved with the frequency-adaptive feature. The ω_0 is generated by a PLL rather than using the fundamental frequency.

To actively compensate for the higher order harmonics, a harmonic compensator given by:

$$G_h(s) = \sum_h \frac{K_{ih} s}{s^2 + (h \cdot \omega_0)^2} \tag{2.25}$$

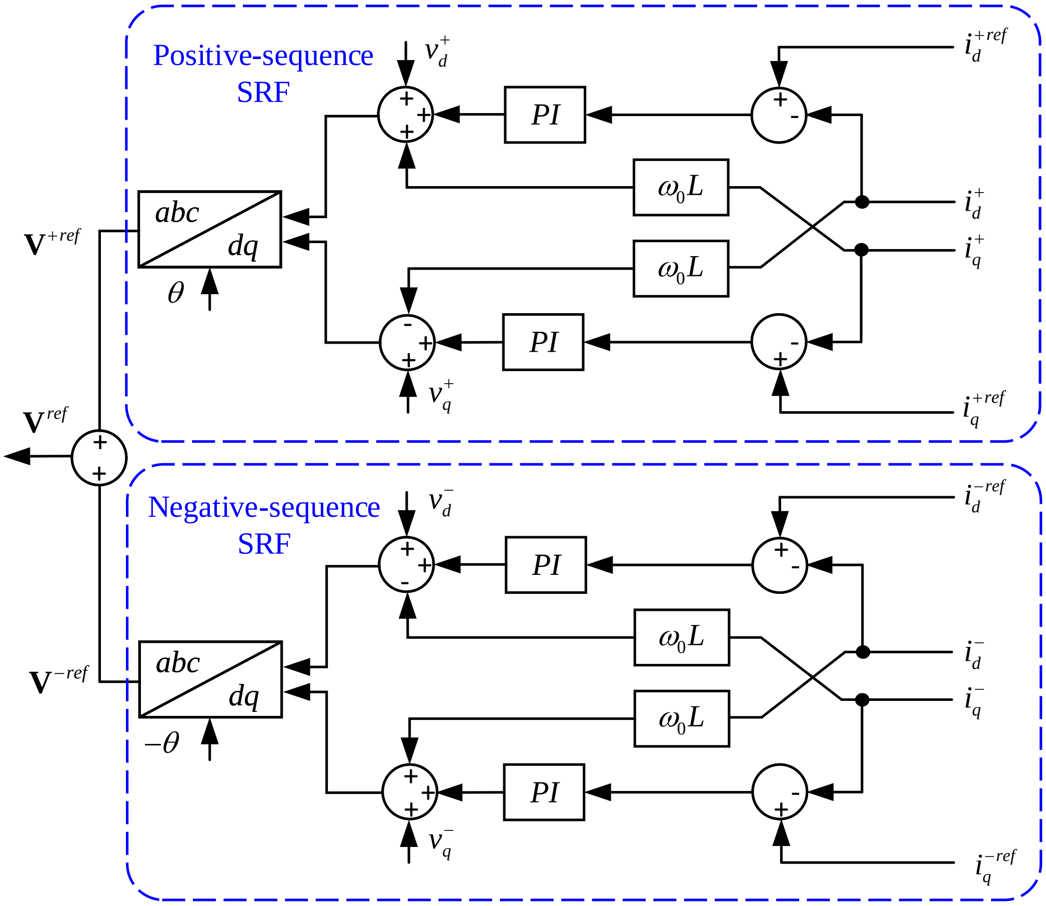

Figure 2.11: Inner current controller of a grid-connected VSC with dual-sequence current control in SRF

can also be cascaded in the current controller for the h-th order harmonics.

The work in [110] derives the equations for transforming the conventional PI controller to its equivalent PR controller. It firstly uses a low-pass filter to represent the ideal DC integrator of a PI controller, which gives the open-loop transfer function as:

$$G_{PI}(s) = K_p + \frac{K_i \omega_c}{s + \omega_c} \tag{2.26}$$

where ω_c is the lower breakpoint frequency of the transfer function. Then the equivalent PR controller of this approximated PI controller is given by [110]:

$$G_{PR}(s) = K_p + \frac{2K_i \omega_c s}{s^2 + 2\omega_c s + \omega_0^2} \tag{2.27}$$

The purpose of doing this is to consider that it may not be possible to have an ideal lossless resonant transfer function. In [110], it is also suggested that the value of ω_c should be chosen as small as possible if (2.27) must be used considering the stability issues.

Compared to four PI units needed in SRF control, only two PR units are required in the stationary reference frame control. Another advantage of the PR controller is the elimination of the necessity to have sequence current extraction as the PR controller is capable to regulate AC signals.

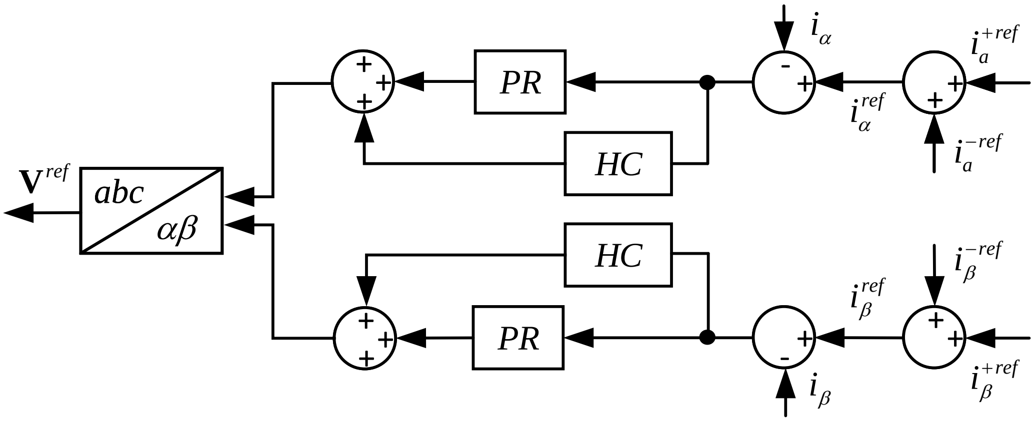

Figure 2.12: Inner current controller in stationary reference frame

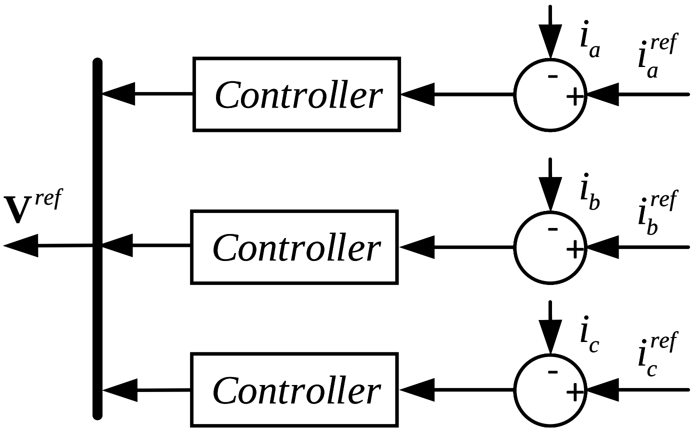

Figure 2.13: Inner current controller in natural reference frame

Natural reference frame

Natural reference frame control, as the name suggested, regulates the current in abc-frame. This means each phase has an individual current controller as shown in Fig. 2.13. For a neutral-isolated system, only two controllers are needed as the sum of the currents in two phases equals the negative of the current in the third phase based on Kirchhoff's Current Law (KCL). The natural reference frame control can still use the aforementioned PI and PR controllers. According to [111, 112], a PI controller can be transformed from dq-frame to abc-frame. However, the PI controller expressed in the natural reference frame is extremely complicated because of the coupling among the three phases. In contrast, it is more straightforward to use PR controllers because of their capability to track AC signals.

In recent years, digital controllers such as predictive deadbeat controllers [113, 114] and hysteresis controllers [115, 116] are gaining popularity with the rapid development of digital devices. It is more common to apply these controllers in the virtual flux-oriented and direct power control schemes rather than voltage-oriented current-controlled scheme. The review of these controllers is beyond the scope of this dissertation.

2.4.2 Power-characteristic-oriented control strategy

In (2.17)–(2.22), there exist six instantaneous power terms and four current variables (i_d^+, i_d^-, i_q^+ and i_q^-) that can be controlled. This means four out of six instantaneous power terms from a VSC can be freely decided by manipulating with the four current references. The control strategies in this section mainly focus on the control of power oscillations. Therefore, they are classified as power-characteristic-oriented control strategy in this dissertation.

Balanced current control

Balanced current control strategy is to inject a set of balanced sinusoidal short circuit current under grid unbalanced faults. It is the most commonly used dual-sequence current control strategy for VSCs [117, 118, 119, 120, 121]. In the following review, the current references are represented using the superposition of the positive- and negative-sequence components:

$$\mathbf{i}^{ref} = \mathbf{i}_P^{ref} + \mathbf{i}_Q^{ref} = (\mathbf{i}_P^{+,ref} + \mathbf{i}_P^{-ref}) + (\mathbf{i}_Q^{+,ref} + \mathbf{i}_Q^{-ref}) \tag{2.28}$$

where $\mathbf{i}_P^{ref}$ and $\mathbf{i}_Q^{ref}$ are the active and reactive current references respectively. They are valid in any reference frame. The balanced current control is achieved by setting the negative-sequence current references to zero so that:

$$\mathbf{i}_P^{ref} = \mathbf{i}_P^{+,ref} = \frac{P^{ref}}{|\mathbf{v}^+|^2}\mathbf{v}^+ \tag{2.29}$$

$$\mathbf{i}_Q^{ref} = \mathbf{i}_Q^{+,ref} = \frac{Q^{ref}}{|\mathbf{v}^+|^2}\mathbf{v}_\perp^+ \tag{2.30}$$

where P^{ref} and Q^{ref} are the active and reactive power references. They can be directly set based on calculations or generated through an outer controller. By substituting (2.29)–(2.30) into (2.15)–(2.16), the instantaneous powers at the PCC can be simplified as:

$$p = \underbrace{\mathbf{v}^+ \cdot \mathbf{i}_P^{+,ref}}_{\overline{P}} + \underbrace{\mathbf{v}^- \cdot \mathbf{i}_P^{+,ref}}_{\widetilde{P}} \tag{2.31}$$

$$q = \underbrace{\mathbf{v}_\perp^+ \cdot \mathbf{i}_Q^{+,ref}}_{\overline{Q}} + \underbrace{\mathbf{v}_\perp^- \cdot \mathbf{i}_Q^{+,ref}}_{\widetilde{Q}} \tag{2.32}$$

which indicates that both active and reactive powers will have oscillating power terms.

Constant active power control

This control strategy eliminates the oscillating term $\widetilde{P}$. This is realized by giving the current references as [50, 54, 122, 123]:

$$\mathbf{i}_P^{ref} = \frac{P^{ref}}{|\mathbf{v}^+|^2 - |\mathbf{v}^-|^2}(\mathbf{v}^+ - \mathbf{v}^-) \tag{2.33}$$

$$\mathbf{i}_Q^{ref} = \frac{Q^{ref}}{|\mathbf{v}^+|^2 - |\mathbf{v}^-|^2}(\mathbf{v}_\perp^+ - \mathbf{v}_\perp^-) \tag{2.34}$$

with which (2.15)–(2.16) is expanded as:

$$p = \underbrace{\mathbf{v}^+ \cdot \mathbf{i}_P^{+,ref} + \mathbf{v}^- \cdot \mathbf{i}_P^{-,ref}}_{\overline{P}} + \underbrace{\mathbf{v}^+ \cdot \mathbf{i}_Q^{-,ref} + \mathbf{v}^- \cdot \mathbf{i}_Q^{+,ref}}_{\widetilde{P}} \tag{2.35}$$

$$q = \underbrace{\mathbf{v}_\perp^+ \cdot \mathbf{i}_Q^{+,ref} + \mathbf{v}_\perp^- \cdot \mathbf{i}_Q^{-,ref}}_{\overline{Q}} + \underbrace{\mathbf{v}_\perp^+ \cdot \mathbf{i}_P^{-,ref} + \mathbf{v}_\perp^- \cdot \mathbf{i}_P^{+,ref}}_{\widetilde{Q}} \tag{2.36}$$

However, the existence of $\mathbf{i}_Q^{+,ref}$ and $\mathbf{i}_Q^{-,ref}$ contributes to the oscillations in the active power. The only way to eliminate $\widetilde{P}$ is to let Q^{ref} be zero. Therefore, with $Q^{ref} = 0$, (2.35)–(2.36) becomes:

$$p = \underbrace{\mathbf{v}^+ \cdot \mathbf{i}_P^{+,ref} + \mathbf{v}^- \cdot \mathbf{i}_P^{-,ref}}_{\overline{P}} \tag{2.37}$$

$$q = \underbrace{\mathbf{v}_\perp^+ \cdot \mathbf{i}_P^{-,ref} + \mathbf{v}_\perp^- \cdot \mathbf{i}_P^{+,ref}}_{\widetilde{Q}} \tag{2.38}$$

which gives a constant active power and an oscillating reactive power with the zero average value. However, the VSC cannot provide reactive power support with the reactive power reference set to zero. Therefore, the works in [120, 124, 125, 126] modify the reactive current reference (2.34) as:

$$\mathbf{i}_Q^{ref} = \frac{Q^{ref}}{|\mathbf{v}^+|^2 + |\mathbf{v}^-|^2}(\mathbf{v}_\perp^+ + \mathbf{v}_\perp^-) \tag{2.39}$$

In this way, the instantaneous powers can be finally expressed by (2.37) and (2.36) when using the current references (2.33) and (2.39). The oscillation-free active power and reactive power support can be achieved at the same time. This also means that a set of unbalanced short circuit current is injected from the VSC, and the reactive power has oscillations at twice fundamental frequency.

Constant reactive power control

Similarly, constant reactive power control [127, 128] deploys current references (2.33)–(2.34) with $P^{ref} = 0$ because the existence of $\mathbf{i}_P^{+,ref}$ and $\mathbf{i}_P^{-,ref}$ contributes to $\widetilde{Q}$ in (2.36). As a result, the instantaneous powers (2.35)–(2.36) become:

$$p = \underbrace{\mathbf{v}^+ \cdot \mathbf{i}_Q^{-,ref} + \mathbf{v}^- \cdot \mathbf{i}_Q^{+,ref}}_{\widetilde{P}} \tag{2.40}$$

$$q = \underbrace{\mathbf{v}_\perp^+ \cdot \mathbf{i}_Q^{+,ref} + \mathbf{v}_\perp^- \cdot \mathbf{i}_Q^{-,ref}}_{\overline{Q}} \tag{2.41}$$

This leads to a constant reactive power and active power with oscillations at twice fundamental frequency. However, the VSC loses the ability to deliver active power in this case. Therefore, the active power references (2.33) is modified as [129]:

$$\mathbf{i}_P^{ref} = \frac{P^{ref}}{|\mathbf{v}^+|^2 + |\mathbf{v}^-|^2}(\mathbf{v}^+ + \mathbf{v}^-) \tag{2.42}$$

The instantaneous active and reactive powers become (2.35) and (2.41) respectively with the current references (2.42) and (2.34). This also means a set of unbalance short circuit current is injected from the VSC.

Constant Active-Reactive Power Control

Constant active-reactive power control achieves oscillation-free active power and oscillation-free reactive power simultaneously. The corresponding current references are [53, 54, 122]:

$$\mathbf{i}_P^{ref} = \frac{P^{ref}}{|\mathbf{v}|^2}\mathbf{v} \tag{2.43}$$

$$\mathbf{i}_Q^{ref} = \frac{Q^{ref}}{|\mathbf{v}|^2}\mathbf{v}_\perp \tag{2.44}$$

Therefore, the instantaneous powers at the PCC are simplified as:

$$p = \underbrace{\mathbf{v}^{+} \cdot \mathbf{i}_P^{ref}}_{\overline{P}} = P^{ref} \tag{2.45}$$

$$q = \underbrace{\mathbf{v}_{\perp}^{+} \cdot \mathbf{i}_Q^{ref}}_{\overline{Q}} = Q^{ref} \tag{2.46}$$

This enables the highest degree of control over the instantaneous powers because the output powers are strictly equal to the references. However, the term $|\mathbf{v}|$ in the denominator of (2.43)–(2.44) will oscillate at twice fundamental frequency under unbalanced conditions. This leads to the non-sinusoidal short circuit current similar to Fig. 2.8.

Flexible Oscillating Power Control (FOPC)

To achieve a compromise among the balanced current control, constant active power control, and constant reactive power control, flexible scalars k_p and k_q that can be adjusted within a specific range are involved in the formulation of the current references [122, 129, 130, 131]:

$$\mathbf{i}_P^{ref} = \frac{P^{ref}}{|\mathbf{v}^+|^2 + k_p |\mathbf{v}^-|^2}(\mathbf{v}^+ + k_p \mathbf{v}^-) \tag{2.47}$$

$$\mathbf{i}_Q^{ref} = \frac{Q^{ref}}{|\mathbf{v}^+|^2 + k_q |\mathbf{v}^-|^2}(\mathbf{v}_{\perp}^+ + k_q \mathbf{v}_{\perp}^-) \tag{2.48}$$

By substituting (2.47)–(2.48) into (2.15)–(2.16), the constant power terms $\overline{P}$ and $\overline{Q}$ are equal to P^{ref} and Q^{ref} respectively. The oscillating power terms $\widetilde{P}$ and $\widetilde{Q}$ become:

$$\widetilde{P} = \underbrace{\frac{(1 + k_p)P^{ref}}{|\mathbf{v}^+|^2 + k_p |\mathbf{v}^-|^2}\mathbf{v}^+\mathbf{v}^-}_{\widetilde{P_p}} + \underbrace{\frac{(1 - k_q)Q^{ref}}{|\mathbf{v}^+|^2 + k_q |\mathbf{v}^-|^2}\mathbf{v}_{\perp}^+\mathbf{v}^-}_{\widetilde{P_q}} \tag{2.49}$$

$$\widetilde{Q} = \underbrace{\frac{(1 + k_q)Q^{ref}}{|\mathbf{v}^+|^2 + k_q |\mathbf{v}^-|^2}\mathbf{v}_{\perp}^+\mathbf{v}_{\perp}^-}_{\widetilde{Q_q}} + \underbrace{\frac{(1 - k_p)P^{ref}}{|\mathbf{v}^+|^2 + k_p |\mathbf{v}^-|^2}\mathbf{v}^+\mathbf{v}_{\perp}^-}_{\widetilde{Q_p}} \tag{2.50}$$

where $\widetilde{P_p}$ and $\widetilde{Q_p}$ denote the oscillating power terms due to the active power injection while $\widetilde{P_q}$ and $\widetilde{Q_q}$ are oscillating power terms due to the reactive power injection. Equation (2.49)–(2.50) indicates that the oscillating power terms can be flexibly controlled using different values of k_p and k_q. If the relationship of the two flexible scalars are chosen as $k_p = -k_q = k$ $(-1 \leq k \leq 1)$, $k = -1$ yields constant active power control and $k = 1$ results in constant reactive power control. When $k = 0$, it is equivalent to balanced current control. Selecting other values of k enables a compromise among theses three most representaive secenarios. Therefore, FOPC is a group of different control strategies with their current references formulated in a more general way. It is worth mentioning here that the flexible scalars k_p and k_q can also have other values or relationships [131], or generated based on other control objectives.

The grid-connected VSC system shown in 2.5 is simulated in RTDS with FOPC. The control system is implemented according to Fig. 2.11. The Dual Second Order Generalized Integrator (DSOGI)-PLL [132] shown in Fig. 2.14 is used to extract the positive- and negative-sequence voltages, and to estimate the phase angle of the positive-sequence voltage. The sequence current extractor in Fig. 2.15 [133] separates the positive-sequence current from the negative-sequence current.

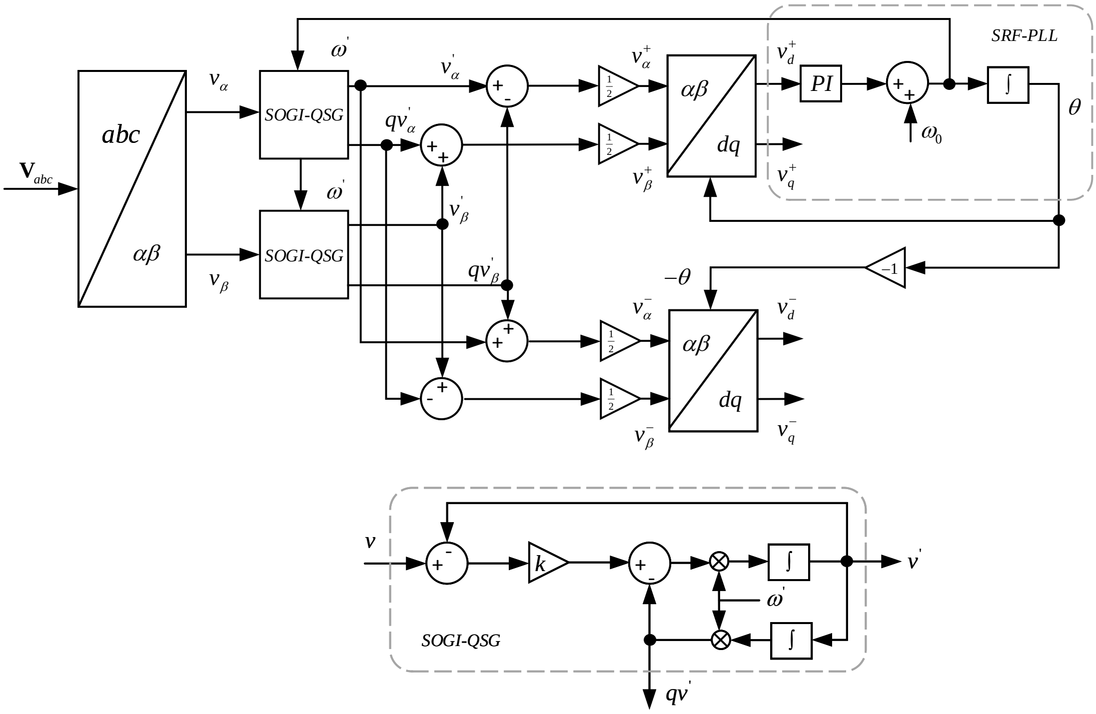

Figure 2.14: Control block diagram of DSOGI-PLL

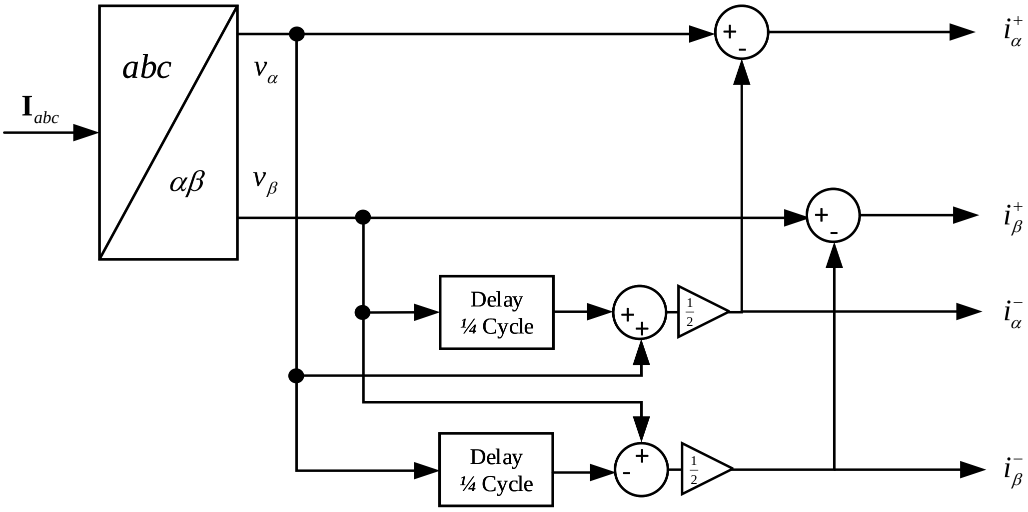

Figure 2.15: Control block diagram of sequence current extractor

As an example, Fig. 2.16 presents the short circuit response of the VSC, as well as the sequence voltages measured at the PCC regarding an A-g fault at the high voltage side. The fault occurs at zero time instant and lasts for 0.5 seconds. In order to illustrate the differences among the control strategies, the value of k is decreased from 1 to -1 with a -0.5 step every 0.1 seconds since 0.1 second time instant. Therefore, Fig. 2.16 integrates five different VSC short circuit responses, including constant reactive power (0-0.1 second), balanced current (0.2-0.3 second) and constant active power (0.4-0.5 second). The responses are significantly different from each other and from SG and SC. The voltage and current during the fault are free of distortions due to the dual-sequence current controls.

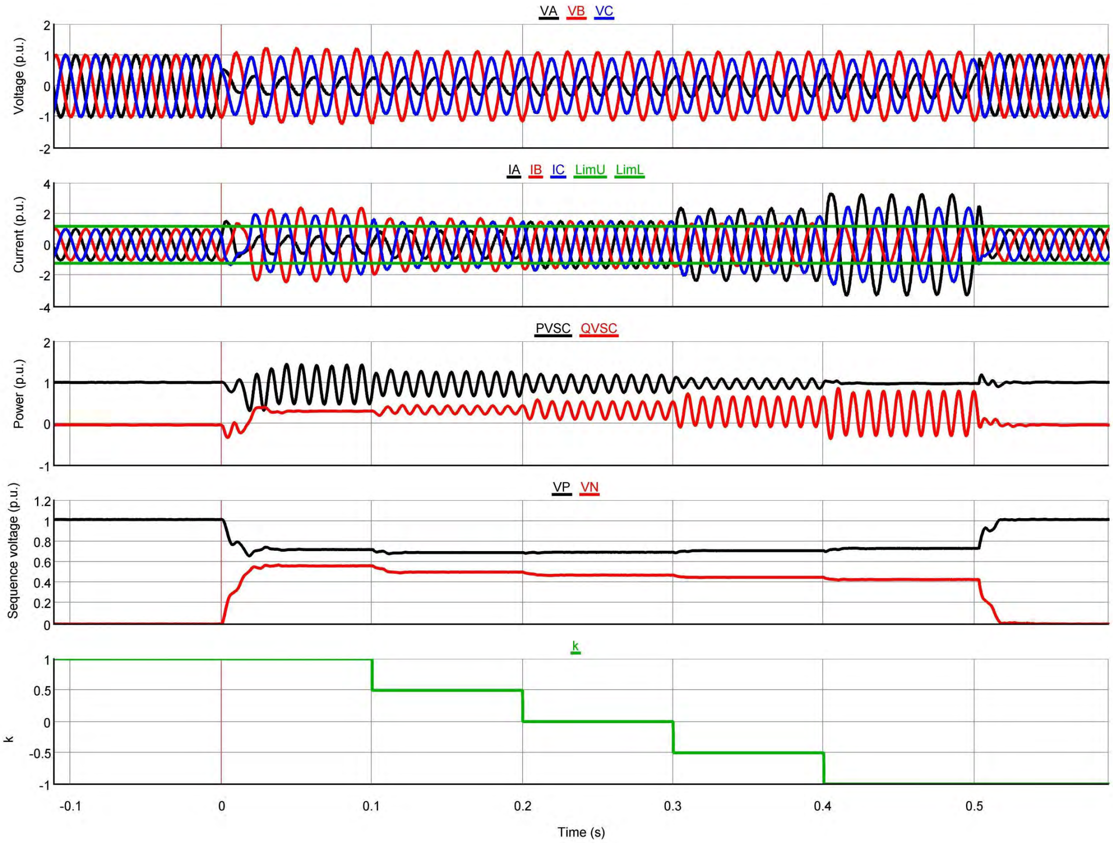

Figure 2.16: Short circuit response of a grid-connected VSC under A-g faults using FOPC without converter current limit

With k changing from 1 to -1, oscillations in active power are gradually reduced but this gives rise to the oscillations in reactive power. The positive-sequence voltage of the PCC is gradually increased and the negative-sequence voltage is gradually attenuated. When the converter peak current limit is not considered, it can be observed that balanced current control gives the lowest peak current. The negative-sequence current injection helps increase the short circuit current level.

2.4.3 Voltage-support-oriented control strategy

As shown in (2.15)–(2.22), the constant power terms consist of positive-sequence powers and negative-sequence powers. The control strategies reviewed in this section mainly deal with the relative relationship between the positive- and negative-sequence powers, which directly affect the positive- and negative-sequence voltages at the PCC. Therefore, they are classified as voltage-support-oriented control strategy in this dissertation.

Voltage support concept

Figure 2.17 illustrates a simplified power system as seen from the PCC. The mathematical relationship between the PCC voltage $\mathbf{v}$ and grid voltage $\mathbf{v}_g$ is defined by:

$$\mathbf{v} = \mathbf{v}_g + R_g\mathbf{i} + L_g\frac{\mathrm{d}\mathbf{i}}{\mathrm{d}t} \tag{2.51}$$

which can be split into (2.52)–(2.53) in terms of the magnitudes of the symmetrical components if the resistance R_g is ignored [see Appendix B]:

$$\left|\mathbf{v}^+\right| = \left|\mathbf{v}_g^+\right| + \omega L_g \left|\mathbf{i}_Q^+\right| \tag{2.52}$$

$$\left|\mathbf{v}^-\right| = \left|\mathbf{v}_g^-\right| - \omega L_g \left|\mathbf{i}_Q^-\right| \tag{2.53}$$

Equation (2.52)–(2.53) indicates that the positive-sequence PCC voltage can be boosted by injecting positive-sequence reactive current, while the negative-sequence PCC voltage can be mitigated by injecting negative-sequence reactive current. In (2.15)–(2.16), the sequence powers are defined as:

$$P^+ = \mathbf{v}^+ \cdot \mathbf{i}_P^+ \tag{2.54}$$

$$P^- = \mathbf{v}^- \cdot \mathbf{i}_P^- \tag{2.55}$$

$$Q^+ = \mathbf{v}_\perp^+ \cdot \mathbf{i}_Q^+ \tag{2.56}$$

$$Q^- = \mathbf{v}_\perp^- \cdot \mathbf{i}_Q^- \tag{2.57}$$

which suggests that grid voltage support can be realized in two different aspects. The injection of Q^+ ($Q^+ > 0$) raises the PCC voltage equally in each phase with respect to $\left|\mathbf{v}_g^+\right|$. On the other hand, The injection of Q^- ($Q^- > 0$) helps compensate for the voltage unbalance at the PCC.

For low-voltage distribution grids, the network impedance is more resistive rather than inductive. The voltage support concept explained by (2.52)–(2.53) become insufficient [134]. If the grid inductance L_g is ignored rather than R_g, there are:

$$\left|\mathbf{v}^+\right| = \left|\mathbf{v}_g^+\right| + R_g \left|\mathbf{i}_P^+\right| \tag{2.58}$$

$$\left|\mathbf{v}^-\right| = \left|\mathbf{v}_g^-\right| + R_g \left|\mathbf{i}_P^-\right| \tag{2.59}$$

which indicates that the injection of P^+ ($P^+ > 0$) helps increase the positive-sequence voltage at the PCC. The reduction of P^- helps compensate for the voltage unbalance for a resistive network.

Therefore, another group of VSC control strategies under unbalanced is developed based the voltage support concept. It is featured by controlling the relative relationship between the positive- and negative-sequence powers.

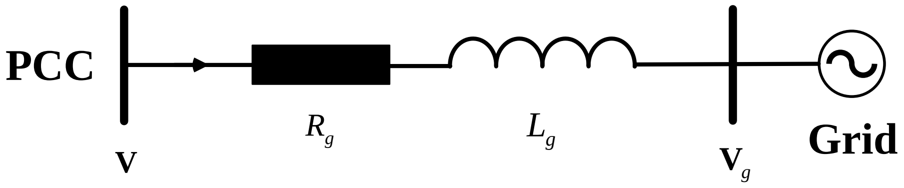

Figure 2.17: A Simplified power system as seen from the PCC

Semi-flexible positive- and negative-sequence power control

In [135, 136, 137, 138], the reactive current reference contains a flexible scalar k_q as:

$$\mathbf{i}_Q^{ref} = \frac{k_q \mathbf{v}_\perp^+ + (1-k_q)\mathbf{v}_\perp^-}{k_q \left|\mathbf{v}^+\right|^2 + (1-k_q)\left|\mathbf{v}^-\right|^2} Q^{ref} \tag{2.60}$$

This concept can also be extended to the active current reference in the same manner:

$$\mathbf{i}_P^{ref} = \frac{k_p \mathbf{v}^+ + (1-k_p)\mathbf{v}^-}{k_p \left|\mathbf{v}^+\right|^2 + (1-k_p)\left|\mathbf{v}^-\right|^2} P^{ref} \tag{2.61}$$

By substituting (2.60)–(2.61) into (2.15)–(2.16), the instantaneous powers at the PCC become:

$$\begin{aligned} p =& \underbrace{\frac{k_p P^{ref}}{k_p \left|\mathbf{v}^+\right|^2 + (1-k_p)\left|\mathbf{v}^-\right|^2} \cdot \left|\mathbf{v}^+\right|^2}_{P^+} + \underbrace{\frac{(1-k_p) P^{ref}}{k_p \left|\mathbf{v}^+\right|^2 + (1-k_p)\left|\mathbf{v}^-\right|^2} \cdot \left|\mathbf{v}^-\right|^2}_{P^-} \\ & + \underbrace{\frac{P^{ref}}{k_p \left|\mathbf{v}^+\right|^2 + (1-k_p)\left|\mathbf{v}^-\right|^2} \cdot \mathbf{v}^+\mathbf{v}^-}_{\widetilde{P_p}} + \underbrace{\frac{(2k_q-1) Q^{ref}}{k_p \left|\mathbf{v}^+\right|^2 + (1-k_p)\left|\mathbf{v}^-\right|^2} \cdot \mathbf{v}_\perp^+\mathbf{v}^-}_{\widetilde{P_q}} \end{aligned} \tag{2.62}$$

$$\begin{aligned} q =& \underbrace{\frac{k_q Q^{ref}}{k_q \left|\mathbf{v}^+\right|^2 + (1-k_q)\left|\mathbf{v}^-\right|^2} \cdot \left|\mathbf{v}_\perp^+\right|^2}_{Q^+} + \underbrace{\frac{(1-k_q) Q^{ref}}{k_q \left|\mathbf{v}^+\right|^2 + (1-k_q)\left|\mathbf{v}^-\right|^2} \cdot \left|\mathbf{v}_\perp^-\right|^2}_{Q^-} \\ & + \underbrace{\frac{Q^{ref}}{k_q \left|\mathbf{v}^+\right|^2 + (1-k_q)\left|\mathbf{v}^-\right|^2} \cdot \mathbf{v}_\perp^+\mathbf{v}_\perp^-}_{\widetilde{Q_q}} + \underbrace{\frac{(2k_p-1) P^{ref}}{k_q \left|\mathbf{v}^+\right|^2 + (1-k_q)\left|\mathbf{v}^-\right|^2} \cdot \mathbf{v}^+\mathbf{v}_\perp^-}_{\widetilde{Q_p}} \end{aligned} \tag{2.63}$$

Then the relative relationship between the positive- and negative-sequence powers is:

$$\frac{P^+}{P^-} = \frac{k_p}{1-k_p} \cdot \frac{\left|\mathbf{v}^+\right|^2}{\left|\mathbf{v}^-\right|^2} \tag{2.64}$$

$$\frac{Q^+}{Q^-} = \frac{k_q}{1-k_q} \cdot \frac{\left|\mathbf{v}_\perp^+\right|^2}{\left|\mathbf{v}_\perp^-\right|^2} \tag{2.65}$$

This indicates that, the relative relationship between the positive- and negative-sequence powers is decided by not only the values of the flexible scalars, but also the grid conditions during the fault, which is the reason why this group of control strategies is named as "semi-flexible" in this dissertation. When $k_q = 1$, only positive-sequence reactive power is injected, being independent of the fault conditions. When $k_q = 0$, only negative-sequence reactive power is injected. The same relation also applies to k_p with regard to active power.

Flexible Positive- and Negative-Sequence Power Control (FPNSPC)

The flexible scalars k_p and k_q can also be involved in the current references as [139, 140, 141, 142]:

$$\mathbf{i}_P^{ref} = k_p \frac{P^{ref}}{\left|\mathbf{v}^+\right|^2}\mathbf{v}^+ + (1-k_p)\frac{P^{ref}}{\left|\mathbf{v}^-\right|^2}\mathbf{v}^- \tag{2.66}$$

$$\mathbf{i}_Q^{ref} = k_q \frac{Q^{ref}}{\left|\mathbf{v}^+\right|^2}\mathbf{v}_\perp^+ + (1-k_q)\frac{Q^{ref}}{\left|\mathbf{v}^-\right|^2}\mathbf{v}_\perp^- \tag{2.67}$$

By substituting (2.66)–(2.67) into (2.15)–(2.16), the instantaneous powers can be further expressed by:

$$\begin{aligned} p =& \underbrace{\frac{k_p P^{ref}}{|\mathbf{v}^+|^2} \cdot \left|\mathbf{v}^+\right|^2}_{P^+} + \underbrace{\frac{(1-k_p) P^{ref}}{|\mathbf{v}^-|^2} \cdot \left|\mathbf{v}^-\right|^2}_{P^-} \\ &+ \underbrace{\left(\frac{k_p P^{ref}}{|\mathbf{v}^+|^2} + \frac{(1-k_p) P^{ref}}{|\mathbf{v}^-|^2}\right) \mathbf{v}^+ \cdot \mathbf{v}^-}_{\widetilde{P_p}} + \underbrace{\left(\frac{k_q Q^{ref}}{|\mathbf{v}^+|^2} - \frac{(1-k_q) Q^{ref}}{|\mathbf{v}^-|^2}\right) \mathbf{v}_\perp^+ \cdot \mathbf{v}^-}_{\widetilde{P_q}} \end{aligned} \tag{2.68}$$

$$\begin{aligned} q =& \underbrace{\frac{k_q Q^{ref}}{|\mathbf{v}^+|^2} \cdot \left|\mathbf{v}_\perp^+\right|^2}_{Q^+} + \underbrace{\frac{(1-k_q) Q^{ref}}{|\mathbf{v}^-|^2} \cdot \left|\mathbf{v}_\perp^-\right|^2}_{Q^-} \\ &+ \underbrace{\left(\frac{k_q Q^{ref}}{|\mathbf{v}^+|^2} + \frac{(1-k_q) Q^{ref}}{|\mathbf{v}^-|^2}\right) \mathbf{v}_\perp^+ \cdot \mathbf{v}_\perp^-}_{\widetilde{Q_q}} + \underbrace{\left(\frac{k_p P^{ref}}{|\mathbf{v}^+|^2} - \frac{(1-k_p) P^{ref}}{|\mathbf{v}^-|^2}\right) \cdot \mathbf{v}^+ \mathbf{v}_\perp^-}_{\widetilde{Q_p}} \end{aligned} \tag{2.69}$$

Therefore, the relative relationship between the positive- and negative-sequence powers becomes:

$$\frac{P^+}{P^-} = \frac{k_p}{1-k_p} \tag{2.70}$$

$$\frac{Q^+}{Q^-} = \frac{k_q}{1-k_q} \tag{2.71}$$

This realizes a direct control over the relative amount of the sequence powers since it is determined only by k_p and k_q, regardless of the fault conditions. This is the reason why this group of control strategies is named as "flexible" rather than "semi-flexible" in this dissertation.

The system shown in Fig. 2.5 is simulated in RTDS with FPNSPC. For example, Fig. 2.18–2.19 presents the short circuit response of the VSC, as well as the sequence voltages measured at the PCC regarding an A-B fault at the high voltage side. The fault occurs at zero time instant and lasts for 0.5 seconds. In Fig. 2.18, the value of k_q is increased from 0 to 1 with a 0.25 step every 0.1 seconds since 0.1 second time instant. It integrates five different VSC responses in terms of the relative relationship between Q^+ and Q^-. With k_q changing from 0 to 1, the share of Q^+ in the injected reactive power increases from 0% to 100%. During this procedure, both positive- and negative sequence voltages are boosted.

In Fig. 2.19, the value of k_p is varied during the fault instead of k_q. With k_p changing from 0 to 1, the share of P^+ in the injected active power increases from 0% to 100%. Since the system is an inductive grid, the variation on sequence active powers has no notable effect on the sequence voltages. With the converter peak current limit not considered, the injection of negative-sequence current helps increase the short circuit current level.

2.4.4 Converter peak current limit

Overview

The current flowing through converters should be restricted in each individual phase due to the limited semiconductor overload capability. Under fault conditions, the controls of the VSCs may push the converter current to a dangerously high value, which may lead to the block or an

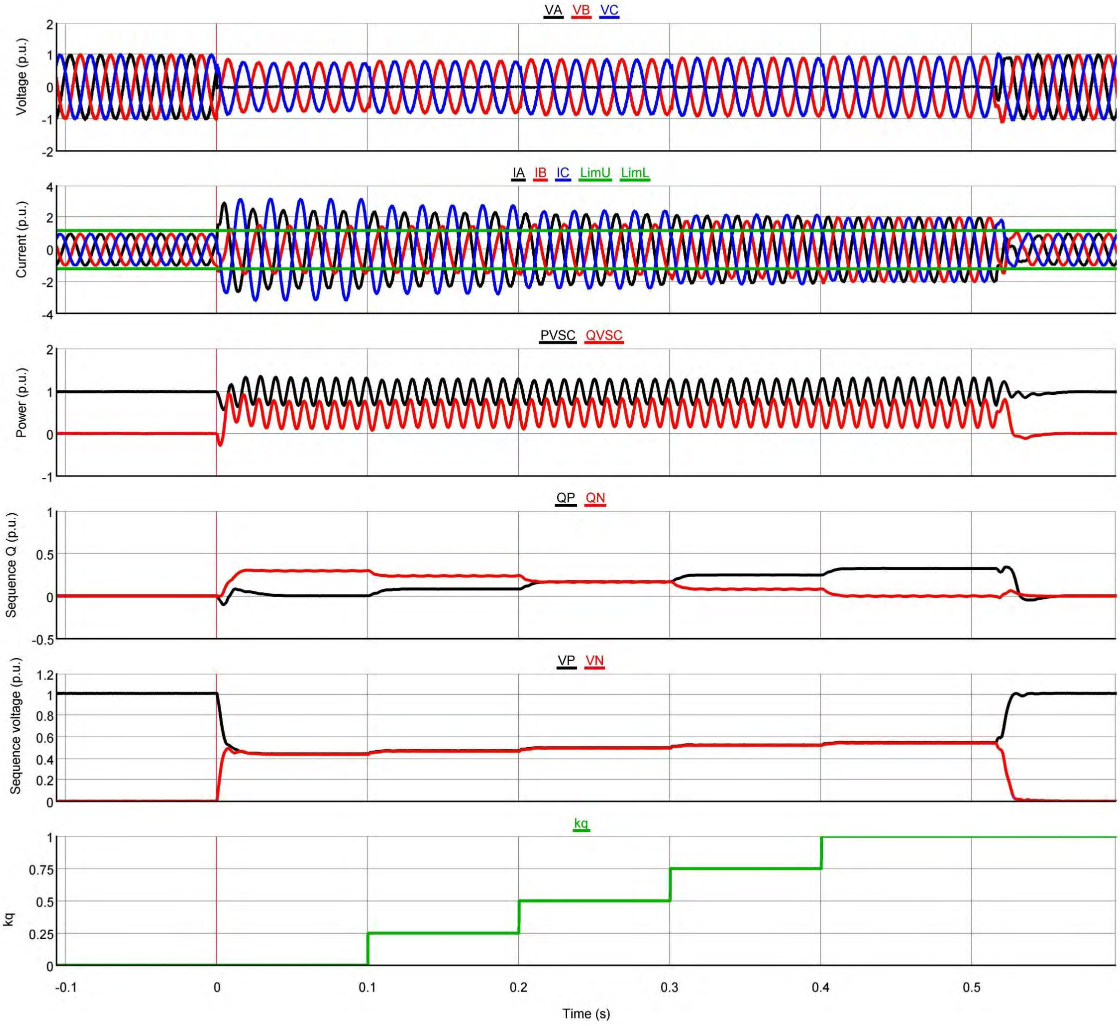

Figure 2.18: Short circuit response of a grid-connected VSC under A-B faults using FPNSPC for reactive power without converter current limit

undesirable disconnection of the converter. For a three-phase balanced fault, the short circuit current from a VSC does not contain any negative-sequence component ideally. This makes the design of converter peak current limit straightforward with (2.8), if reactive current injection takes the priority. The maximum permitted value of i_d can be determined as long as the peak current limit I_{max} and the reactive current i_q are given [143, 144]. Under unbalanced faults, (2.8) is still valid if balanced current control is adopted, as the negative-sequence current is always regulated to be zero. However, the converter peak current limit method becomes more complicated if negative-sequence current is injected under unbalanced faults.

It is suggested in [54, 145] that, the converter peak current limit should be specifically analyzed for each control strategy because of the different current references. The works in [123, 125, 126, 146] focus on constant active power control. The peak current limit comes in the form of limiting the active power reference without considering reactive power support capability.

The maximum magitidue among the three-phase currents under unbalanced conditions is derived for constant active power control and constant reactive power control in [128]. Then the maximum reactive power that can be injected without exceeding the converter peak current limit can be

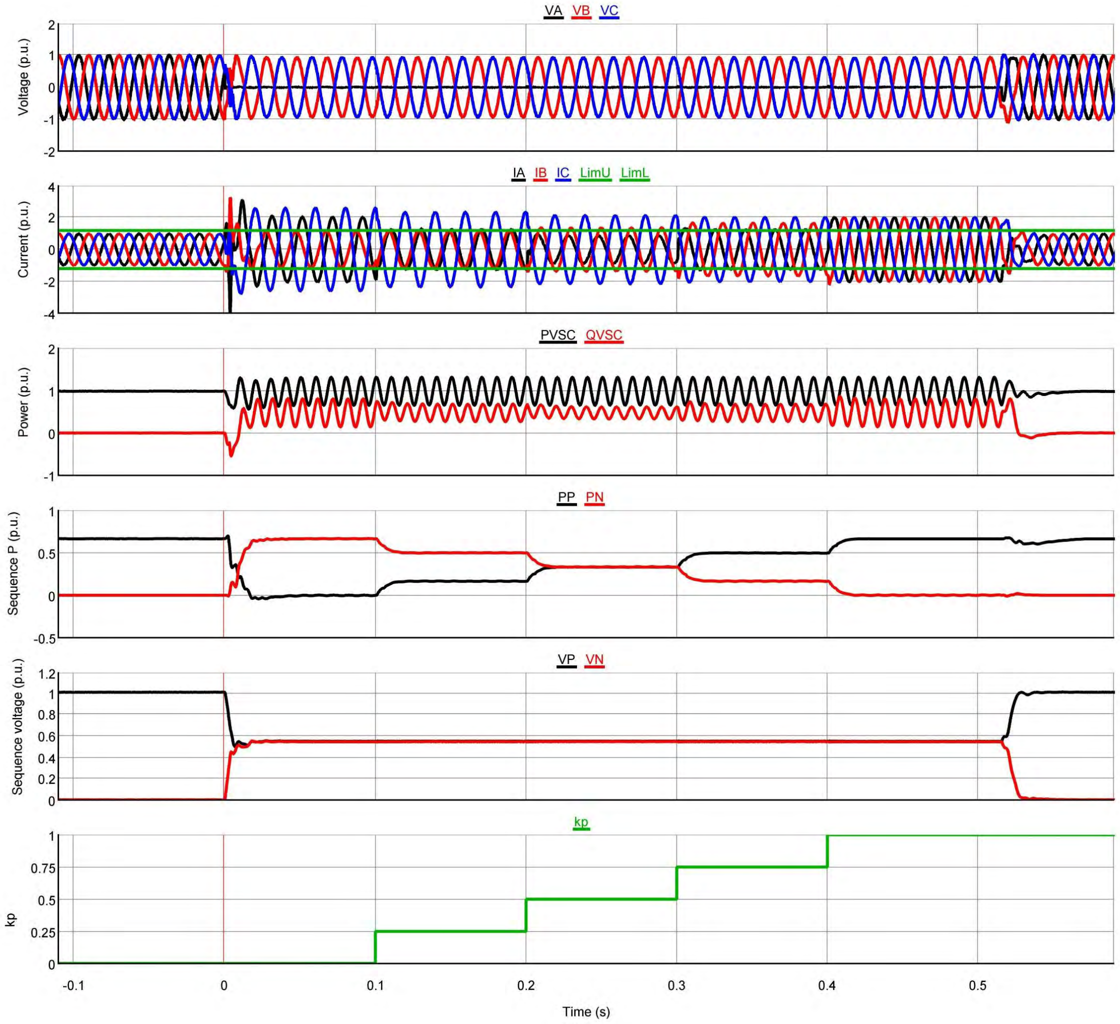

Figure 2.19: Short circuit response of a grid-connected VSC under A-B faults using FPNSPC for active power without converter current limit

determined. The work in [147] restricts the reactive power reference taking the converter peak current limit, the upper voltage limit, and the DC-side voltage limit into account at the same time. It is acknowledged in [148] that, one single converter is not enough to compensate for the voltage unbalance or recover the voltage to the nominal level. This is because the capacity of a single converter is quite small compared to rest of the grid. The required reactive current can be extremely high to achieve the desired phase voltage regulation. In [148], the magnitude of the current in each phase I_m $(m = a, b, c)$ is mathematically calculated using the on-line measurements of other quantities. The saturated reactive power Q_s^+ and Q_s^- are obtained by multiplying the scale factor $I_{max}/\max\{I_m\}$ to the desired Q^+ and Q^-. Finally, two selectors are used to determine the final reactive power reference:

$$Q^{+ref} = \min\{Q_s^+, Q^+\} \tag{2.72}$$

$$Q^{-ref} = \min\{Q_s^-, Q^-\} \tag{2.73}$$

This guarantees that the current in each individual phase is restricted. If Q_s^+ or Q_s^- is selected in (2.72)–(2.73), the corresponding phase-voltage regulation will not be accomplished any more. With semi-FPNSPC appiled in [138], $\max\{I_m\}$ is derived as a function of Q^{ref} and k_q. The permitted reactive power Q_{max} without violating the converter peak current can be determined by solving $\max\{I_a, I_b, I_c\} = I_{max}$ once I_{max} is provided. However, the methods mentioned above are only applicable if the active power reference is set to zero.

The above-reviewed methods are not sufficient when active power and reactive powers are injected simultaneously using the dual-sequence current controls. The superposition of the active and reactive current will raise the current in certain phases above the limit during different time periods within one cycle. The study in [136], with flexible control over the sequence reactive power, analyses the magnitude of the current in each phase with the superposition of the positive-sequence active power and reactive power from both sequences. Considering the use of FPNSPC, the work in [149] mathematically calculates the magnitude of the current in each individual phase. It is graphically explained in [144] that, which phase has the highest current under the fault varies with different fault conditions. The dual-sequence current control strategies under unbalanced faults are generally developed based on certain control objectives. The realization of these objectives may violate the converter peak current limit. This indicates that the desired control objectives have to be compromised, or the output powers have to be reduced whenever the current in any phase reaches its limit.

Flexible positive- and negative-sequence power control

The current ellipse theory presented in [54] provides a theoretical background for analysing the magnitudes of a set of unbalanced currents. With the application of FPNSPC, the peak current in each individual phase can be represented by [54, 139]:

$$\hat{I_m}^2 = (I_{pL} \cos\gamma_m - I_{qL} \sin\gamma_m)^2 + (I_{qS} \cos\gamma_m + I_{pS} \sin\gamma_m)^2, m \subset (a, b, c) \tag{2.74}$$

$$I_{pL} = P^{ref}\left(\frac{k_p}{|\mathbf{v}^+|} + \frac{1-k_p}{|\mathbf{v}^-|}\right),\ I_{pS} = P^{ref}\left(\frac{k_p}{|\mathbf{v}^+|} - \frac{1-k_p}{|\mathbf{v}^-|}\right) \tag{2.75}$$

$$I_{qL} = Q^{ref}\left(\frac{k_q}{|\mathbf{v}_\perp^+|} + \frac{1-k_q}{|\mathbf{v}_\perp^-|}\right),\ I_{qS} = Q^{ref}\left(\frac{k_q}{|\mathbf{v}_\perp^+|} - \frac{1-k_q}{|\mathbf{v}_\perp^-|}\right) \tag{2.76}$$

$$\gamma_a = \frac{|\phi^+| - |\phi^-|}{2},\ \gamma_b = \frac{|\phi^+| - |\phi^-|}{2} + \frac{\pi}{3},\ \gamma_c = \frac{|\phi^+| - |\phi^-|}{2} - \frac{\pi}{3} \tag{2.77}$$

where I_{pL} and I_{pS} are the values of the long and short axes of the active current ellipse; I_{qL} and I_{qS} are the values of the long and short axes of the reactive current ellipse; $\hat{I_m}$ represents the peak current in each phase; ϕ^+ and ϕ^- are the phase angles of the positive- and negative-sequence voltage respectively. If phase A is taken as an example, with (2.75)–(2.77) substituted into (2.74), the relationship of $\hat{I}_a$ with P^{ref} and Q^{ref} satisfies:

$$\begin{aligned}
0 = {} & Q^{ref2}\left[\frac{k_q^2\,|\mathbf{v}^-|^2 + (1-k_q)^2\,|\mathbf{v}^+|^2 - 2k_q(1-k_q)\cos 2\gamma_a\,|\mathbf{v}^-|\,|\mathbf{v}^-|}{|\mathbf{v}^+|^2\,|\mathbf{v}^-|^2}\right] \\
& - P^{ref}Q^{ref}\left[\frac{(2k_p + 2k_q - 4k_pk_q)|\,|\mathbf{v}^+|\,|\,|\mathbf{v}^-|\sin 2\gamma_a}{|\,|\mathbf{v}^+|^2\,|\,|\mathbf{v}^-|^2}\right] \\
& + P^{ref2}\left[\frac{k_p^2\,|\mathbf{v}^-|^2 + (1-k_p)^2\,|\mathbf{v}^+|^2 + 2k_p(1-k_p)\cos 2\gamma_a\,|\mathbf{v}^-|\,|\mathbf{v}^-|}{|\mathbf{v}^+|^2\,|\mathbf{v}^-|^2}\right] - \hat{I}_a^{\,2}
\end{aligned} \tag{2.78}$$

If the values of Q^{ref}, k_p and k_q are given, the relationship expressed in (2.78) can be regarded as a quadratic equation with P^{ref} as an unknown variable. The maximum permitted active power P_a^{limit} without violating the peak current limit in phase A is defined by the solution of this quadratic equation. If γ_a is changed to γ_b and γ_c respectively, the maximum permitted active power in phase B and phase C, namely P_b^{limit} and P_c^{limit}, can be obtained respectively with a similar procedure. Finally, if the currents in all phases are controlled within the limit, the active power will be restricted by:

$$P_{max} = \min\left\{P_a^{limit}, P_b^{limit}, P_c^{limit}\right\} \tag{2.79}$$

Corresponding to the simulations in Fig. 2.18–2.19, Fig. 2.20–2.21 illustrates the short circuit response of the VSC with the converter peak current limit. Under fault conditions, the VSC is able to inject active and reactive power simultaneously. The currents in all phases are restricted within 1.2 p.u. with curtailments in active power. This maximizes the utilization of the converter capacity. The more negative-sequence power is injected, the more active power has to be curtailed.

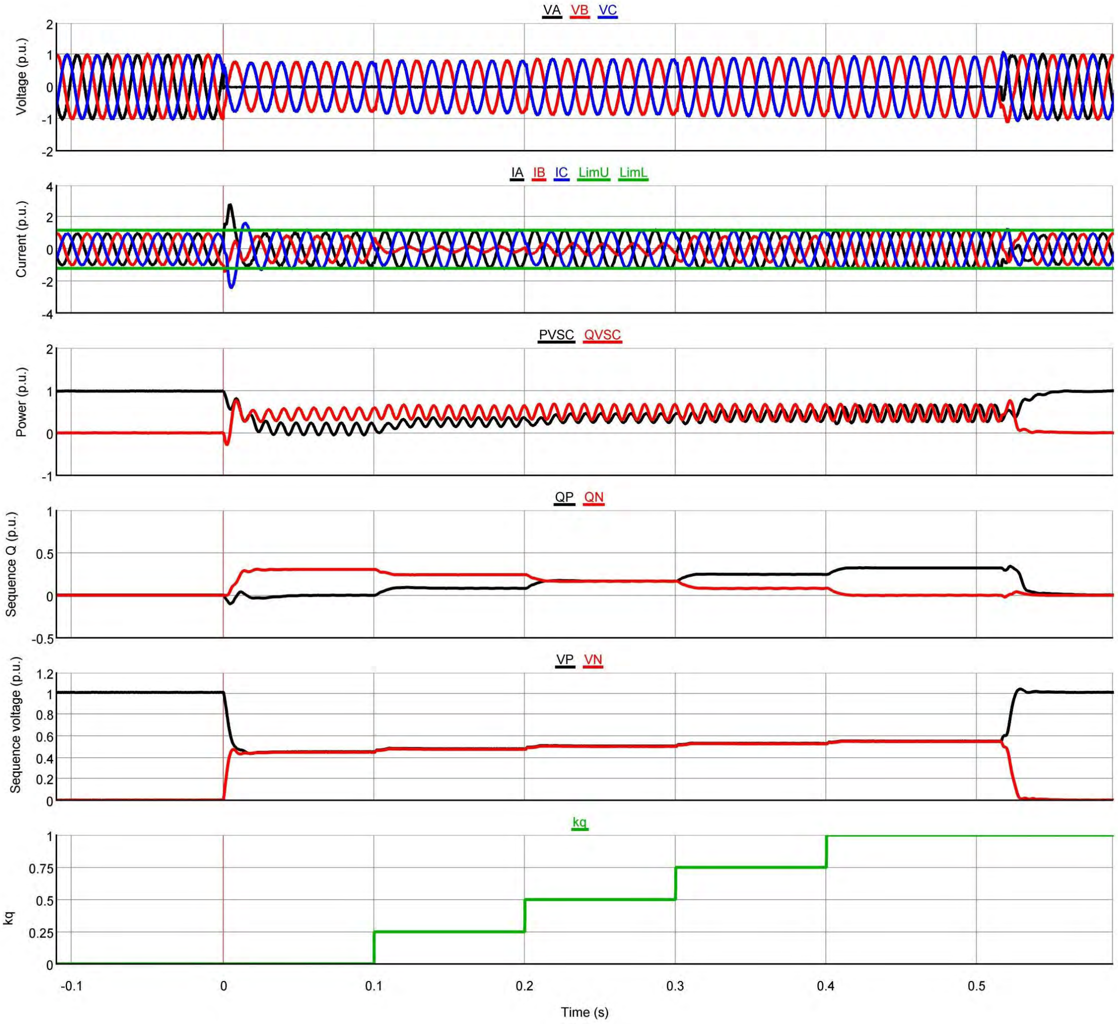

Figure 2.20: Short circuit response of a grid-connected VSC under A-B faults using FPNSPC for reactive power with converter current limit

Flexible oscillation power control

The method presented above is exclusively designed for FPNSPC since the current references (2.66)–(2.67) are used for the derivation. However, it can be extended to FOPC if (2.47)–(2.48) serve

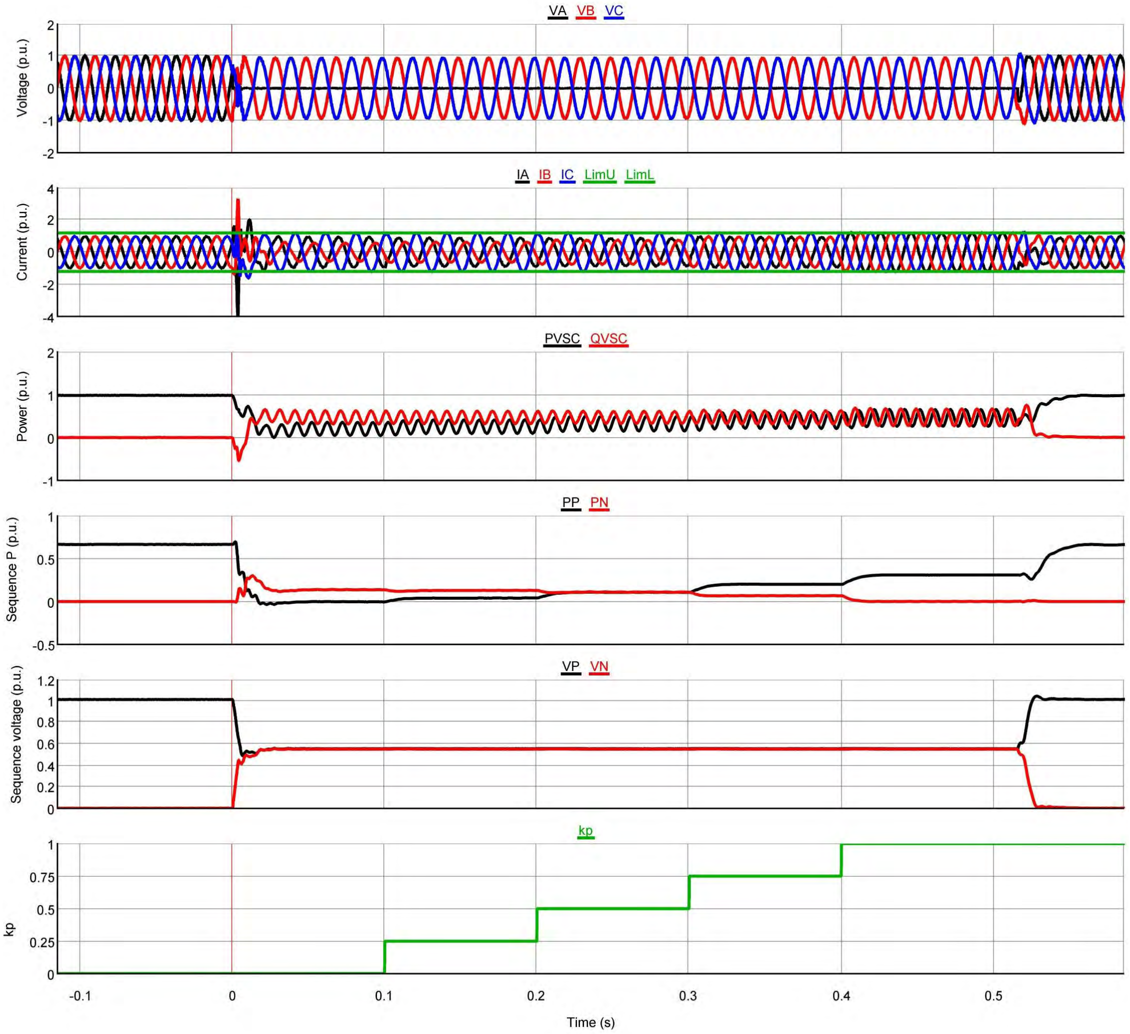

Figure 2.21: Short circuit response of a grid-connected VSC under A-B faults using FPNSPC for active power with converter current limit

as the current references. Equation (2.75)–(2.76) can be rewritten in terms of sequence powers as:

$$I_{pL} = \frac{P^+}{|\mathbf{v}^+|} + \frac{P^-}{|\mathbf{v}^-|}, \quad I_{pS} = \frac{P^+}{|\mathbf{v}^+|} - \frac{P^-}{|\mathbf{v}^-|} \tag{2.80}$$

$$I_{qL} = \frac{Q^+}{|\mathbf{v}_\perp^+|} + \frac{Q^-}{|\mathbf{v}_\perp^-|}, \quad I_{qS} = \frac{Q^+}{|\mathbf{v}_\perp^+|} - \frac{Q^-}{|\mathbf{v}_\perp^-|} \tag{2.81}$$

With (2.47)–(2.48) substituted into (2.15)–(2.16), the sequence active and reactive powers can be expressed by:

$$P^+ = \frac{P^{ref}\,|\mathbf{v}^+|}{|\mathbf{v}^+|^2 + k_p\,|\mathbf{v}^-|^2}, \quad P^- = \frac{k_p P^{ref}\,|\mathbf{v}^-|}{|\mathbf{v}^+|^2 + k_p\,|\mathbf{v}^-|^2} \tag{2.82}$$

$$Q^+ = \frac{Q^{ref}\,|\mathbf{v}^+|}{|\mathbf{v}^+|^2 + k_q\,|\mathbf{v}^-|^2}, \quad P^- = \frac{k_q Q^{ref}\,|\mathbf{v}^-|}{|\mathbf{v}^+|^2 + k_q\,|\mathbf{v}^-|^2} \tag{2.83}$$

Then, by substituting (2.82)–(2.83) into (2.80)–(2.81), the updated expressions for I_{pL}, I_{pS}, I_{qL} and I_{qS} become:

$$I_{pL} = P^{ref} \frac{\left(\left|\mathbf{v}^{+}\right| + k_p \left|\mathbf{v}^{-}\right|\right)}{\left|\mathbf{v}^{+}\right|^2 + k_p \left|\mathbf{v}^{-}\right|^2}, \quad I_{pS} = P^{ref} \frac{\left(\left|\mathbf{v}^{+}\right| - k_p \left|\mathbf{v}^{-}\right|\right)}{\left|\mathbf{v}^{+}\right|^2 + k_p \left|\mathbf{v}^{-}\right|^2} \tag{2.84}$$

$$I_{qL} = Q^{ref} \frac{\left(\left|\mathbf{v}^{+}\right| + k_q \left|\mathbf{v}^{-}\right|\right)}{\left|\mathbf{v}^{+}\right|^2 + k_q \left|\mathbf{v}^{-}\right|^2}, \quad I_{qS} = Q^{ref} \frac{\left(\left|\mathbf{v}^{+}\right| - k_q \left|\mathbf{v}^{-}\right|\right)}{\left|\mathbf{v}^{+}\right|^2 + k_q \left|\mathbf{v}^{-}\right|^2} \tag{2.85}$$

Finally, with (2.74), (2.77), (2.84) and (2.85) substituted into (2.74), the relationship of the peak current in phase A with P^{ref} and Q^{ref} can be obtained:

$$\begin{aligned} 0 = {} & Q^{ref2} \left(\left|\mathbf{v}^{+}\right|^2 + k_p \left|\mathbf{v}^{-}\right|^2\right)^2 \left(\left(\left|\mathbf{v}^{+}\right| + k_q \left|\mathbf{v}^{-}\right|\right)^2 \sin^2\gamma + \left(\left|\mathbf{v}^{+}\right| - k_q \left|\mathbf{v}^{-}\right|\right)^2 \cos^2\gamma\right) \\ & - 2P^{ref} Q^{ref} N \left(\left|\mathbf{v}^{+}\right|^2 + k_p \left|\mathbf{v}^{-}\right|^2\right) \left(\left|\mathbf{v}^{+}\right|^2 + k_q \left|\mathbf{v}^{-}\right|^2\right) \cos\gamma_a \sin\gamma_a \\ & + P^{ref2} \left(\left|\mathbf{v}^{+}\right|^2 + k_q \left|\mathbf{v}^{-}\right|^2\right)^2 \left(\left(\left|\mathbf{v}^{+}\right| + k_p \left|\mathbf{v}^{-}\right|\right)^2 \sin^2\gamma + \left(\left|\mathbf{v}^{+}\right| - k_p \left|\mathbf{v}^{-}\right|\right)^2 \cos^2\gamma\right) \\ & - \left(\left|\mathbf{v}^{+}\right|^2 + k_p \left|\mathbf{v}^{-}\right|^2\right)^2 \left(\left|\mathbf{v}^{+}\right|^2 + k_q \left|\mathbf{v}^{-}\right|^2\right)^2 \hat{I_a}^2 \end{aligned} \tag{2.86}$$

$$N = \left(\left|\mathbf{v}^{+}\right| + k_p \left|\mathbf{v}^{-}\right|\right)\left(\left|\mathbf{v}^{+}\right| + k_q \left|\mathbf{v}^{-}\right|\right) - \left(\left|\mathbf{v}^{+}\right| - k_p \left|\mathbf{v}^{-}\right|\right)\left(\left|\mathbf{v}^{+}\right| - k_q \left|\mathbf{v}^{-}\right|\right) \tag{2.87}$$

If P^{ref} is taken as an unknown variable, (2.86)–(2.87) become a quadratic equation whose solution is given by:

$$P^{ref} = \frac{-B + \sqrt{(B^2 - 4AC)}}{2A} \tag{2.88}$$

$$A = y^2 \left(m^2 \cos^2\gamma + n^2 \sin^2\gamma\right) \tag{2.89}$$

$$B = -2Qxy \sin\gamma \cos\gamma (mr - ns) \tag{2.90}$$

$$C = Q^2 x^2 \left(r^2 \sin^2\gamma + s^2 \cos^2\gamma\right) - x^2 y^2 \hat{I}_a^2 \tag{2.91}$$

$$m = \left|\mathbf{v}^{+}\right| + k_p \left|\mathbf{v}^{-}\right|, \ n = \left|\mathbf{v}^{+}\right| - k_p \left|\mathbf{v}^{-}\right| \tag{2.92}$$

$$r = \left|\mathbf{v}^{+}\right| + k_q \left|\mathbf{v}^{-}\right|, \ s = \left|\mathbf{v}^{+}\right| - k_q \left|\mathbf{v}^{-}\right| \tag{2.93}$$

$$x = \left|\mathbf{v}^{+}\right|^2 + k_p \left|\mathbf{v}^{-}\right|^2, \ y = \left|\mathbf{v}^{+}\right|^2 + k_q \left|\mathbf{v}^{-}\right|^2 \tag{2.94}$$

With the values of Q^{ref}, $\hat{I}_a$, k_p and k_q known in advance, the maximum permitted active power in phase A P_a^{limit} without exceeding the peak current limit in this phase can be determined. Similarly, the maximum permitted active power P_b^{limit} and P_c^{limit} can be calculated with (2.88)–(2.94) just by changing the value of γ to $(|\phi^{+}| - |\phi^{-}|)/2 + \pi/3$ and $(|\phi^{+}| - |\phi^{-}|)/2 - \pi/3$ respectively. As a result, the maximum permitted active power P^{limit} without violating the peak current limit in any phase is again decided by (2.79).

However, one assumption for the above equations is that injecting reactive power alone does not violate the peak current limit. This assumption can be eliminated by using a similar procedure of deriving P^{limit}. In this case, Q^{ref} is regarded as an unknown variable rather than P^{ref}. The value of P^{ref} is set to zero considering the priority of reactive power injection. Therefore, the reactive power limit is determined by:

$$Q^{limit} = \min\left\{Q_a^{limit}, Q_b^{limit}, Q_c^{limit}\right\} \tag{2.95}$$

Corresponding to the simulations in Fig. 2.16, Fig. 2.22 illustrates the short circuit response of the VSC with the converter peak current limit. Under fault conditions, the VSC is able to inject active and reactive power simultaneously. The currents in all phases are restricted within 1.2 p.u. with curtailments in active power.

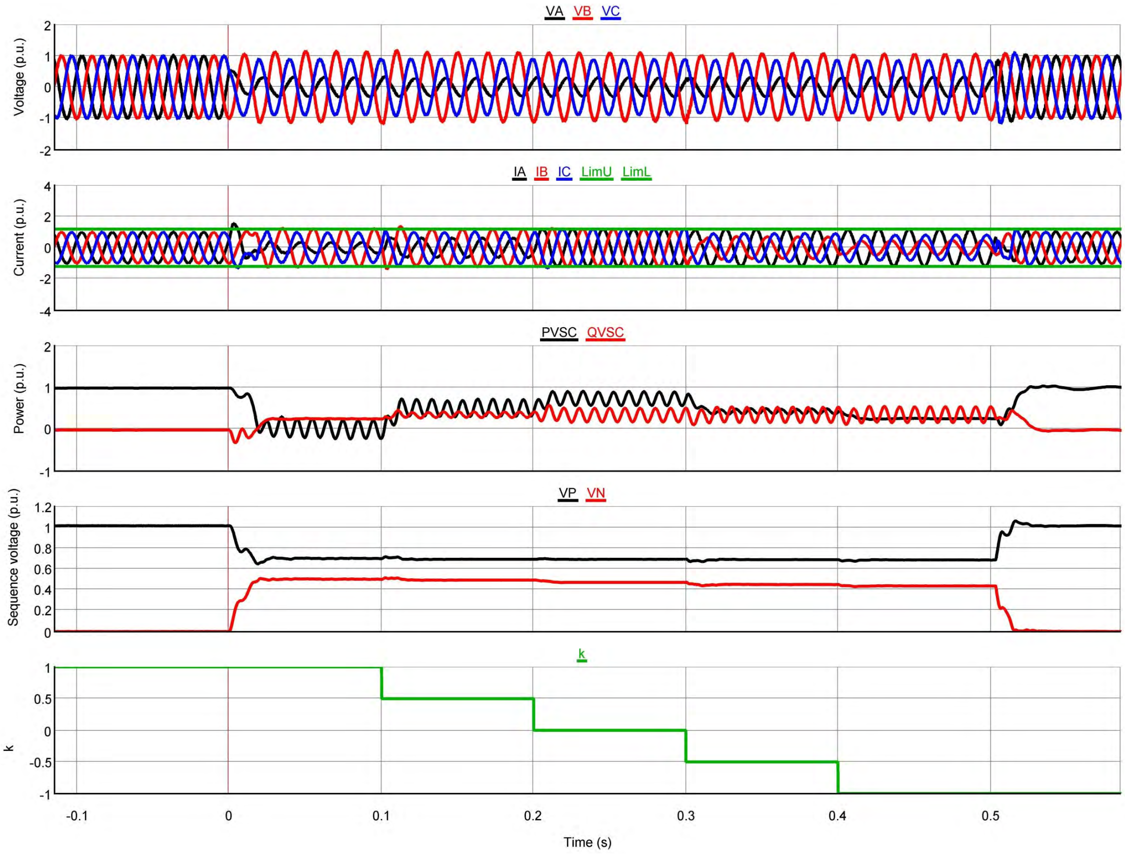

Figure 2.22: Short circuit response of a grid-connected VSC under A-g faults using FOPC with converter current limit

2.5 Discussion on dual-sequence current controls

As shown in Section 2.4, the short circuit response of a VSC under unbalanced faults can vary significantly depending on how the current references are formulated. The current references (2.47)–(2.48) for FOPC, (2.60)–(2.61) for semi-FPNSPC, and (2.66)–(2.67) for FPNSPC represent three groups of current references. The formations of the current references in each group share certain similarities, so that their differences can be characterized by the flexible scalars k_p and k_q. These current references are just formulated in a more general manner, which does not mean that a VSC has to use the exact formulation for dual-sequence current controls.

2.5.1 Relationship between FOPC and FPNSPC

Even though the current references of these dual-sequence current control strategies are different from each other, a common feature is that they can all be decomposed into positive- and negative-sequence components.

With the k_p and k_q replaced by k_{p1} and k_{q1} in (2.47)–(2.48) for FOPC, there are:

$$\mathbf{i}_P^{ref} = \frac{P^{ref}}{|\mathbf{v}^+|^2 + k_{p1}\,|\mathbf{v}^-|^2}(\mathbf{v}^+ + k_{p1}\mathbf{v}^-) \tag{2.96}$$

$$\mathbf{i}_Q^{ref} = \frac{Q^{ref}}{|\mathbf{v}^+|^2 + k_{q1}\,|\mathbf{v}^-|^2}(\mathbf{v}_\perp^+ + k_{q1}\mathbf{v}_\perp^-) \tag{2.97}$$

With the k_p and k_q replaced by k_{p2} and k_{q2} in (2.66)–(2.67) for FPNSPC, there are:

$$\mathbf{i}_P^{ref} = k_{p2}\frac{P^{ref}}{|\mathbf{v}^+|^2}\mathbf{v}^+ + (1-k_{p2})\frac{P^{ref}}{|\mathbf{v}^-|^2}\mathbf{v}^- \tag{2.98}$$

$$\mathbf{i}_Q^{ref} = k_{q2}\frac{Q^{ref}}{|\mathbf{v}^+|^2}\mathbf{v}_\perp^+ + (1-k_{q2})\frac{Q^{ref}}{|\mathbf{v}^-|^2}\mathbf{v}_\perp^- \tag{2.99}$$

Then, (2.96)–(2.97) can be rewritten as:

$$\begin{aligned}\mathbf{i}_P^{ref} &= \frac{P^{ref}}{|\mathbf{v}^+|^2 + k_{p1}|\mathbf{v}^-|^2}\mathbf{v}^+ + \frac{P^{ref}}{|\mathbf{v}^+|^2 + k_{p1}|\mathbf{v}^-|^2}k_{p1}\mathbf{v}^- \\ &= \frac{|\mathbf{v}^+|^2}{|\mathbf{v}^+|^2 + k_{p1}|\mathbf{v}^-|^2}\cdot\frac{P^{ref}}{|\mathbf{v}^+|^2}\mathbf{v}^+ + \frac{k_{p1}|\mathbf{v}^-|^2}{|\mathbf{v}^+|^2 + k_{p1}|\mathbf{v}^-|^2}\cdot\frac{P^{ref}}{|\mathbf{v}^-|^2}\mathbf{v}^- \\ &= k_{p2}\frac{P^{ref}}{|\mathbf{v}^+|^2}\mathbf{v}^+ + (1-k_{p2})\frac{P^{ref}}{|\mathbf{v}^-|^2}\mathbf{v}^-\end{aligned} \tag{2.100}$$

$$\begin{aligned}\mathbf{i}_Q^{ref} &= \frac{Q^{ref}}{|\mathbf{v}^+|^2 + k_{q1}|\mathbf{v}^-|^2}\mathbf{v}_\perp^+ + \frac{Q^{ref}}{|\mathbf{v}^+|^2 + k_{q1}|\mathbf{v}^-|^2}k_{q1}\mathbf{v}_\perp^- \\ &= \frac{|\mathbf{v}^+|^2}{|\mathbf{v}^+|^2 + k_{q1}|\mathbf{v}^-|^2}\cdot\frac{Q^{ref}}{|\mathbf{v}^+|^2}\mathbf{v}_\perp^+ + \frac{k_{q1}|\mathbf{v}^-|^2}{|\mathbf{v}^+|^2 + k_{q1}|\mathbf{v}^-|^2}\cdot\frac{Q^{ref}}{|\mathbf{v}^-|^2}\mathbf{v}_\perp^- \\ &= k_{q2}\frac{Q^{ref}}{|\mathbf{v}^+|^2}\mathbf{v}_\perp^+ + (1-k_{q2})\frac{Q^{ref}}{|\mathbf{v}^-|^2}\mathbf{v}_\perp^-\end{aligned} \tag{2.101}$$

This re-formulates FOPC in the form of FPNSPC. Therefore, the relationship between FOPC and FPNSPC can be characterized by:

$$k_{p2} = \frac{|\mathbf{v}^+|^2}{|\mathbf{v}^+|^2 + k_{p1}|\mathbf{v}^-|^2} \tag{2.102}$$

$$k_{q2} = \frac{|\mathbf{v}^+|^2}{|\mathbf{v}^+|^2 + k_{q1}|\mathbf{v}^-|^2} \tag{2.103}$$

which means constant active power control ($k_{p1} = -k_{q1} = -1$) will be realized in FPNSPC with:

$$k_{p2} = \frac{|\mathbf{v}^+|^2}{|\mathbf{v}^+|^2 - |\mathbf{v}^-|^2} \tag{2.104}$$

$$k_{q2} = \frac{|\mathbf{v}^+|^2}{|\mathbf{v}^+|^2 + |\mathbf{v}^-|^2} \tag{2.105}$$

and constant reactive power control will be achieved by flipping the values of k_{p2} and k_{q2} in (2.104)–(2.105). If there is the relationship $k_{p1} = -k_{q1}$ in (2.96)–(2.97), k_{p2} and k_{q2} in (2.102)–(2.103) will satisfy:

$$\frac{1}{k_{p2}} + \frac{1}{k_{q2}} = 2 \tag{2.106}$$

$$k_{p2},\ k_{p2} \in (0.5, +\infty) \tag{2.107}$$

which is illustrated by Fig. 2.23. As long as the k_p-k_q joint strategy is determined in one group of the flexible control strategies, the k_p-k_q relationship is also determined in the other group so that they are equivalent to each other. Therefore, the short circuit power from VSCs with different dual-sequence current control strategies under unbalanced faults can be characterized by the different combinations of the sequence powers (P^+, P^-, Q^+ and Q^-).

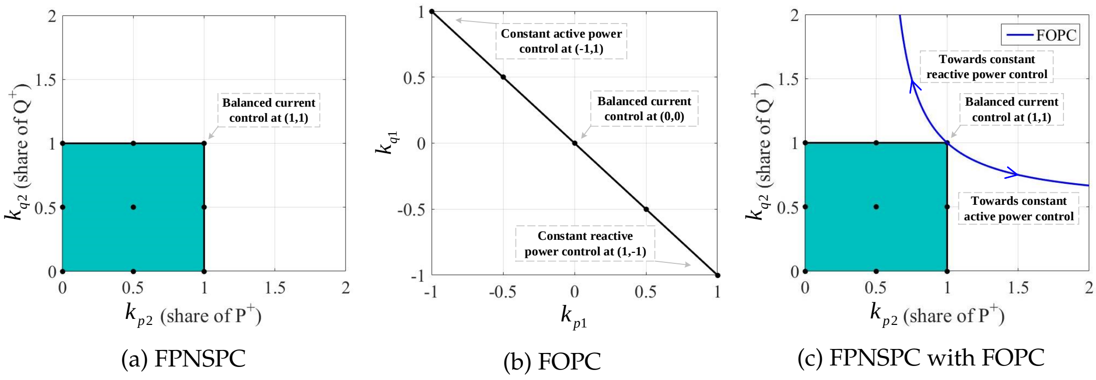

(a) FPNSPC (b) FOPC (c) FPNSPC with FOPC

Figure 2.23: Relationship between FOPC and FPNSPC

When there is $0 < k_{q2} < 1$, the VSC injects positive Q^+ and Q^- simultaneously ($Q^+ > 0$, $Q^- > 0$). If there is $k_{q2} > 1$ (e.g. control strategy moves from balanced current control to constant reactive power control), the VSC starts to inject negative Q^- and positive Q^+ at the same time ($Q^+ > 0$, $Q^- < 0$). Similarly, the VSC begins to inject negative P^- ($P^- < 0$) when there is $k_{p2} > 1$ (e.g. control strategy moves from balanced current control towards constant active power control). However, $P^+$and P^- have less effect on the PCC voltages for an inductive grid. Based on the voltage support concept in Section 2.4.3, the impact of the sequence powers on the sequence voltages at the PCC is summarized in Table. 2.1.

Table 2.1: Impact of sequence powers on the PCC voltage

Sequence reactive power	**Effect on an inductive grid**	**Sequence active power**	**Effect on a resistive grid**
Inject Q^+ ($Q^+ > 0$)	Increase $\lvert\mathbf{v}^+\rvert$	Inject P^+ ($P^+ > 0$)	Increase $\lvert\mathbf{v}^+\rvert$
Inject Q^- ($Q^- > 0$)	Decrease $\lvert\mathbf{v}^-\rvert$	Inject P^- ($P^- > 0$)	Increase $\lvert\mathbf{v}^-\rvert$
Absorb Q^+ ($Q^+ < 0$)	Decrease $\lvert\mathbf{v}^+\rvert$	Absorb P^+ ($P^+ < 0$)	Decrease $\lvert\mathbf{v}^+\rvert$
Absorb Q^- ($Q^- < 0$)	Increase $\lvert\mathbf{v}^-\rvert$	Absorb P^- ($P^- < 0$)	Decrease $\lvert\mathbf{v}^-\rvert$

2.5.2 Control objectives

Under grid unbalanced faults, a VSC with dual-sequence current controls is commonly controlled to provide three-phase balanced short circuit current. The design of the corresponding control system is relatively simple since there is no need to implement extra control logic to calculate the desired negative-sequence current. However, the provision of negative-sequence current from VSCs can provide extra benefits.

As shown in Fig. 2.22, the deployment of FOPC provides a flexible controllability over the oscillations in the short circuit power. Since the oscillations in active power can reflect the variation on the DC-side voltage, constant active power control helps maintain a constant DC-side voltage under unbalanced faults. However, the realization of constant active power is at the cost of active power curtailments because the unbalanced short circuit currents reduce the VSC operating margin. Therefore, the work in [131] proposes to apply a PI controller to regulate the flexible scalar $k_p = -k_q = k$. The value of k starts from 0 so that the active power delivery is maximized. If the oscillations on the DC-side voltage are beyond the acceptable limit, the PI controller will ramp up the value of k towards -1 to reduce the oscillations in the DC-side voltage.

With the deployment of FPNSPC, the work in [140] simply chooses the relationship $k_p = k_q = k$ or $k_p = 1 - k_q = k(0 \leq k \leq 1)$. The same-sign-scalar strategy reduces active and reactive power oscillations simultaneously when k moves towards 0; while for the complementary-scalar strategy, oscillation reduction in either active or reactive power will deteriorate the other. In [139], the average active and reactive power of each phase can be equalized by choosing:

$$k_p = k_q = \frac{1}{1 - \left|\mathbf{v}^+\right|^2 / \left|\mathbf{v}^-\right|^2} \tag{2.108}$$

In order to imitate the relationship between $\mathbf{i}^+$ and $\mathbf{i}^-$ of a synchronous condenser, the work in [150] maintains the relative amount between Q^+ and Q^- according to:

$$\frac{Q^+}{Q^-} = \frac{\left(V_{nom} - \left|\mathbf{v}^+\right|\right)\left|\mathbf{v}^+\right|}{\left|\mathbf{v}^-\right|^2} \tag{2.109}$$

where V_{nom} represents the nominal voltage of the grid. This means that k_q for FPNSPCis decided by:

$$k_q = \frac{Q^+}{Q^+ + Q^-} = \frac{\left(V_{nom} - \left|\mathbf{v}^+\right|\right)\left|\mathbf{v}^+\right|}{\left(V_{nom} - \left|\mathbf{v}^+\right|\right)\left|\mathbf{v}^+\right| + \left|\mathbf{v}^-\right|^2} \tag{2.110}$$

The control strategies mentioned above mainly pay attention the converter itself with less focus on the ancillary services that a VSC can provide. In [134], a modification is made to (2.60)–(2.61) in semi-FPNSPC by including the grid resistance in current references. This makes the flexible voltage support also effective for a resistive grid. However, the value of the flexible scalars are simply selected without justification. The work in [142] focuses on the voltage unbalance compensation using FPNSPC. The flexible scalars are generated by controlling the negative-sequence current from the VSC to be in phase with the grid negative-sequence current. With either semi-FPNSPC or FPNSPC, k_q together with Q^{ref} is calculated using on-line measurements [137, 148] so that the phase voltages at the PCC comply with:

$$\min\left\{V_a, V_b, V_c\right\} \geq V_L \tag{2.111}$$

$$\max\left\{V_a, V_b, V_c\right\} \leq V_H \tag{2.112}$$

where V_a, V_b and V_c are the magnitudes of the voltage in each phase; V_L and V_H correspond to the predefined lower and higher voltage boundary respectively.

The control strategies can also be designed based on multiple objectives. The studies in [147, 151, 152, 153, 154, 155] choose two or more objectives such as: DC-side voltage oscillation minimization, unbalance voltage compensation, phase voltage limit defined by (2.111)–(2.112), zero-sequence voltage compensation, maximizing active or reactive power delivery complying with converter peak current limit, or maximizing the lowest phase voltage. However, satisfying one objective may conflict with the other ones and a compromise among different objectives is needed.

It is worth mentioning that the control strategies in [142, 155] and studies considering (2.111)–(2.112) all require a good knowledge of the Thevenin equivalent impedance of the AC grid. Promising results are given in these studies for a simple system where the VSC is connected to a programmable source with source impedance, fault type, and location known in advance. However, the fault type and location cannot be predicted and the power system can integrate multiple VSCs with diverse short circuit responses. Therefore, it is quite challenging to estimate the Thevenin equivalent impedance as seen from the PCC during the fault accurately and fast enough for a large power system with high penetration of renewable-based generations. Therefore, the feasibility and applicability of these methods still need further investigation and validation regarding a larger power system.

2.6 Conclusion

This chapter compared the short circuit response of synchronous generators, synchronous condensers and grid-connected VSCs under different types of faults. Synchronous condensers, as synchronous machines in principle, share similar short circuit response with synchronous generators. They naturally provide fast short circuit power injection characterized by the short circuit current with a high magnitude.

In contrast, the quality and quantity of the short circuit current from VSCs are mainly governed by their control systems. Regarding three-phase balanced faults, VSCs can be controlled to inject three-phase balanced short circuit current. For a three-phase, three-wire VSC system, the short circuit current does not have DC offsets. However, due to the limited overload capability of semiconductors, the available short circuit current from VSCs is restricted by the converter peak current limit. As a result, the short circuit current provision from VSCs has to consider whether the priority of the current injection should be given to the active component or the reactive component.

The short circuit response of VSCs under grid balanced faults is more diverse than under three-phase balanced faults. With the conventional SRF control only for the positive-sequence component, VSCs exhibit undesirable performances such as distorted terminal voltage and short circuit current, which is due to the coupling between the positive-sequence SRF and negative-sequence SRF, and the limited bandwidth of PI controllers. Even though the voltage and current distortions can be eliminated by using only the positive-sequence components for the control loops, VSCs still lose their control over the converter peak current because of the uncontrolled negative-sequence current. Therefore, it is necessary for VSCs to have current control loops in both positive- and negative-sequence.

The inner current controllers of a VSC can be implemented in different reference frames but the short circuit response of a VSC under unbalanced faults mainly depends on how the current references are formulated. This chapter classified the dual-sequence current control strategies into two groups, namely power-characteristic-oriented control strategy, and voltage-support-oriented control strategy. Flexible scalars are included in the current references to generalize their formations. Various RTDS simulations are provided to illustrate the differences among various control strategies.

The complexity of a converter peak current limit increases as long as a VSC is controlled to provide both positive- and negative-sequence short circuit current. It has a close correlation with the deployed control strategy. Based on the converter peak current limit for flexible positive- and negative-sequence power control (FPNSPC), a genetic limit method is derived for flexible oscillating power control (FOPC). It is able to restrict the current in each individual phase within the limit when using FOPC.

The dual-sequence current references can be formulated in various ways but a common feature is that they can all be decomposed into positive- and negative-sequence component. As a result, the short circuit response of a VSC under unbalanced faults can be characterized by the different combinations of positive- and negative-sequence powers. The various control strategies are in principle an issue of how much active or reactive power is injected, and what is the share of the positive-sequence powers and the share of negative-sequence powers.

For an inductive grid, sequence reactive powers have more impact on the grid voltages rather than sequence active powers. The control strategies aiming to regulate the phase-voltages at the PCCs in compliance with pre-defined voltage constraints may not be feasible, in that they require a precise estimation of the Thevenin equivalent circuit as seen from the PCCs. This can become challenging for a large power system with multiple VSCs having dual-sequence current controls.

CHAPTER 3

Investigation on the Combined Effect of Voltage Source Converters and Synchronous Condensers

This chapter investigates the combined effect of VSC and SC by equipping an SC at the PCC of a VSC, and assesses the distance protection in low inertia power systems. Firstly, a simplified Western Danish Power System (DK1) with respect to a future scenario is modeled in RTDS. It includes detailed LCC-HVDC and VSC-HVDC systems, Type-III and Type-IV wind farms, and other electrical components together with their control systems. The model is validated by comparing its short circuit response with the real fault data. Next, a HIL test platform is developed integrating the RTDS model and protective relays into a closed loop. The platform is able to perform relay testing consecutively and automatically through the bi-directional communication between RTDS and MATLAB. In order to investigate the impact of the VSC dual-sequence current controls on distance protection, a commercial distance relay is tested systematically using the HIL test platform. Finally, the impact of equipping an SC at the PCC of a VSC-HVDC system is investigated through examining the combined short circuit current, the PCC voltage, the DC-side voltage, and the system frequency response under fault conditions, followed by suggestions on selecting the dual-sequence current control strategies for VSCs when incorporating SCs. The main results of this chapter were documented in [**Pub. A**], [**Pub. D**] and [**Pub. E**]

3.1 Western Danish power system

Figure 3.1 presents the single-line diagram of the simplified DK1 system being modeled through the SCAPP project. The model corresponds to the transmission system covering the geographical area of Jylland and Fyn in Denmark with newly planed lines. The data for the synchronous machines, transformers, transmission lines and the system topology are provided by the Danish TSO Energinet. In Fig. 3.1, each substation at the 400 kV level is assigned a three-letter name. The entire power system together with its control systems is modeled in RTDS with details. Some key components in the model are:

- Three LCC-HVDC links at TJE, VHA and FGD to Norway, Sweden and Sjælland (DK2), respectively;
- Two VSC-HVDC links at TJE and EDR to Norway and The Netherlands, respectively;

- Two Type-III wind farms at KAE and TRI, respectively;
- One Type-IV wind farm at EDR;
- Five SGs at EDR, NVV, SVS, TRI and FYO, respectively;
- Three SCs at TJE, VHA and FGD, respectively;

In order to validate the RTDS model of the DK1 system, the real fault data is compared to the simulated short circuit response subject to the same fault. The fault corresponds to a two-phase short circuit on the transmission line between ASR and REV in 2015 due to the storm ”Gorm“. Since this event occurred in 2015, the newly planned lines in Fig. 3.1 are disconnected so that the simulated system represents a past scenario in 2015.

Figure 3.2(a) presents the three-phase voltage and current in primary-side values recorded by the distance relay located at EDR looking into the line between EDR and REV. The real fault data is provided by the Danish TSO Energinet and re-plotted by MATLAB. Correspondingly, Fig. 3.2(b) is the RTDS simulation results subject to the same fault. The simulated short circuit response agrees with the real fault data and this helps validate the RTDS model of the DK1 system.

3.2 Hardware-in-the-loop test platform

3.2.1 Description of the platform

In the SCAPP project, a HIL test platform illustrated by Fig. 3.3 is developed integrating power system models and real protective relays into a closed loop. As shown in Fig. 3.3(a), the power system model is simulated in RTDS, which sends out the three-phase voltage and current signals needed by the protective relay through a Gigabit Transceiver Analogue Output Card (GTAO). Given the fact that the output voltage of the GTAO is restricted to +/-10 V, the signals measured from the secondary sides of the Current Transformer (CT) and Voltage Transformer (VT) in simulations have to be scaled down properly through the output scaling factor of the virtual GTAO component in the simulation model. Then, an amplifier scales up the signals measured from the physical GTAO terminal so that amplified signals reach the level as obtained from the CT and VT. The described relationship above can be described by:

$$RMS_a = \frac{5 \cdot RMS_i}{R_1} \cdot R_2 \tag{3.1}$$

where RMS_i refers to the Root Mean Square (RMS) value of the signal measured from the secondary side of CT or VT in simulations, which is also the input to the virtual GTAO; RMS_a refers to the RMS value of the amplified signal; R_1 represents the output scaling factor specified in the virtual GTAO while R_2 represents the amplification factor of the amplifier. This indicates that the relationship $5R_2 = R_1$ has to be maintained so that there is $RMS_a = RMS_o$.

The trip signal generated by the relay is sent back to RTDS through a Gigabit Transceiver Digital Input Card (GTDI). When there is no current driven through its terminal, the digital input read by the RTDS processor card will be a logic “0”. In order to have a logic “1”, an external 5 V DC signal is needed to drive a current into the physical GTDI terminal. Since the protective relays used in the SCAPP project have potential-free switches, a 5 V DC voltage source is connected in series

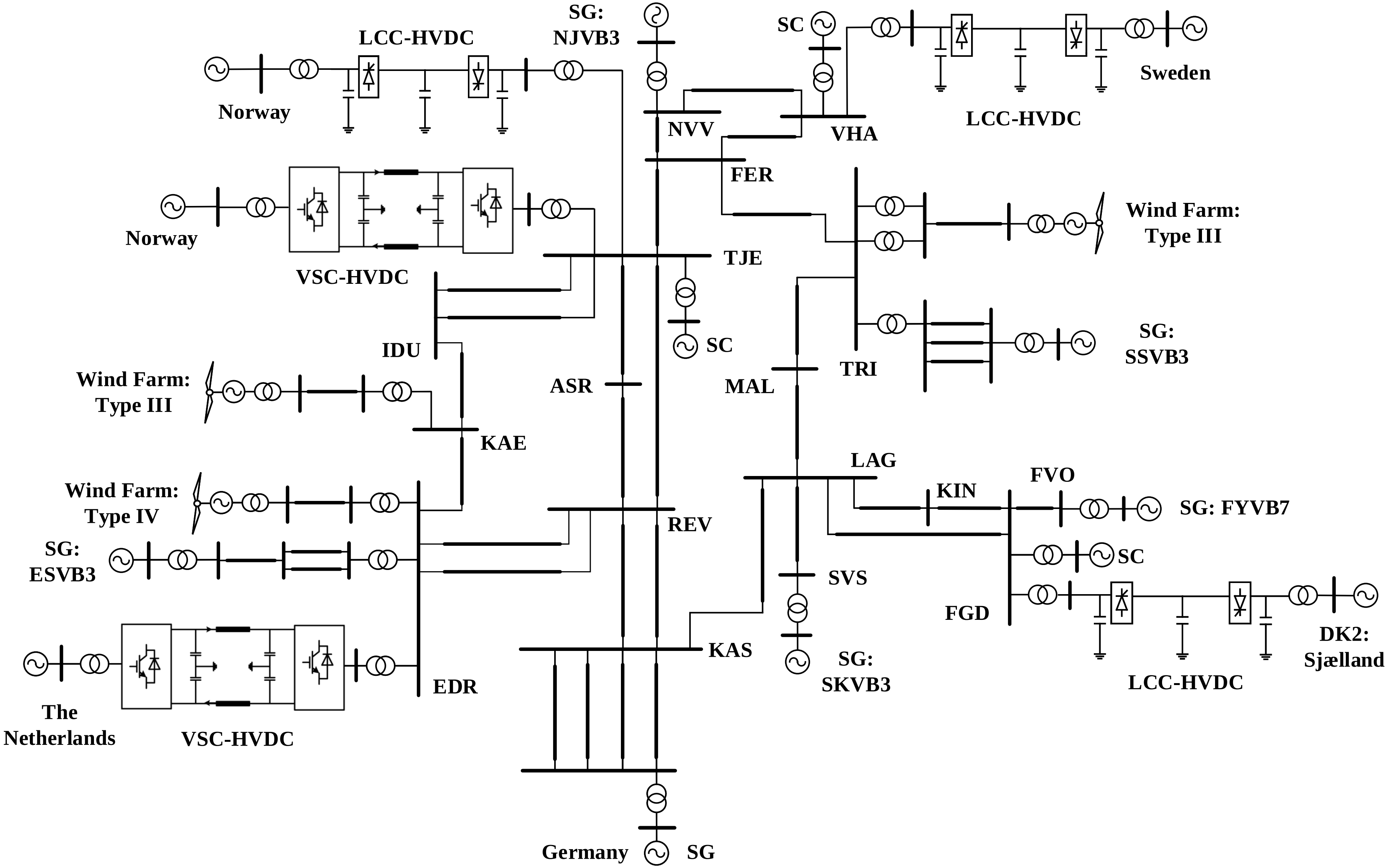

Figure 3.1: Single-line diagram of the simplified western Danish transmission system for a future scenario

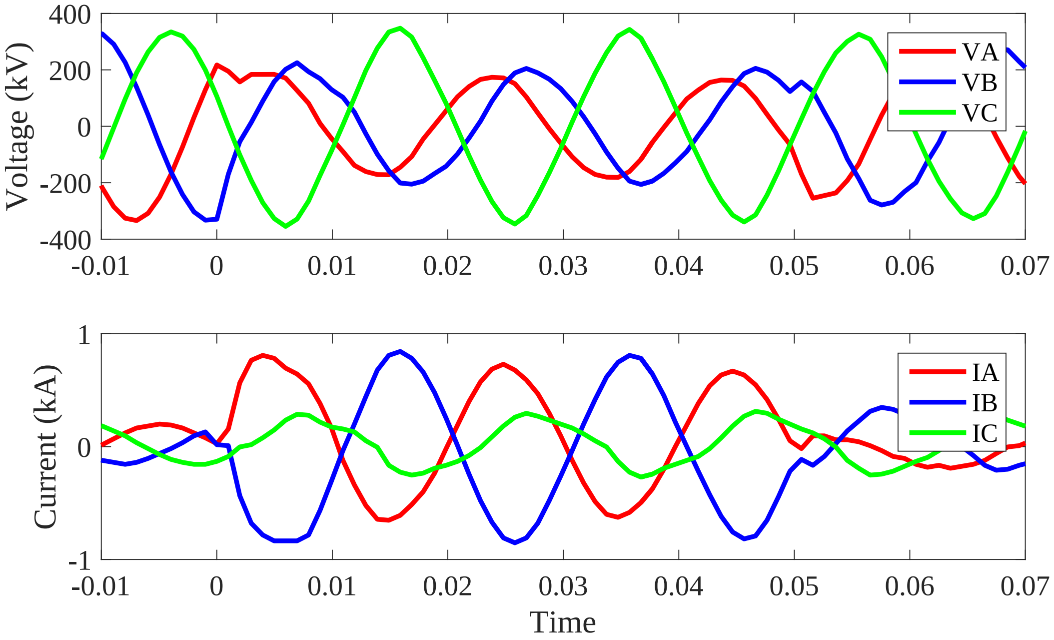

(a) Real fault data

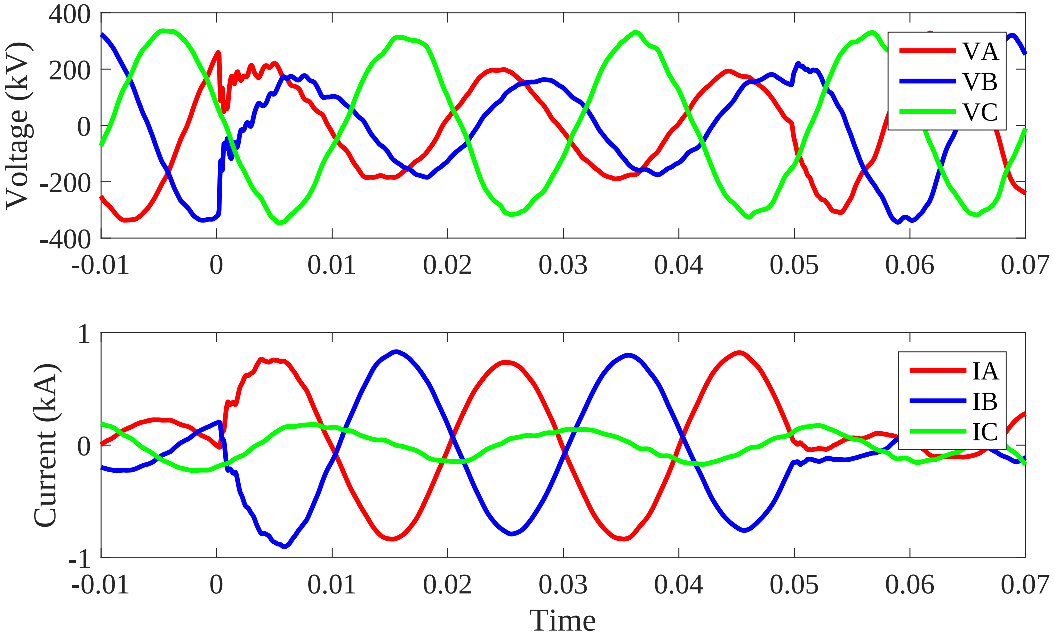

(b) RTDS simulation

Figure 3.2: RTDS model verification with real fault data

with the relay and the physical GTDI. Therefore, a logic “1” will be registered if the switch of the relay closes, meaning the trip signal is sent from the relay to the RTDS simulations.

In addition, the HIL test platform integrates a TCP/IP link between RTDS and MATLAB. This bi-directional communication [156, 157] enables to automate the simulations, the relay testing, and the data saving by executing RSCAD/Runtime and Matlab scripts [see Appendix C]. As a result, the platform can perform a large number of tests with various scenarios without the need of

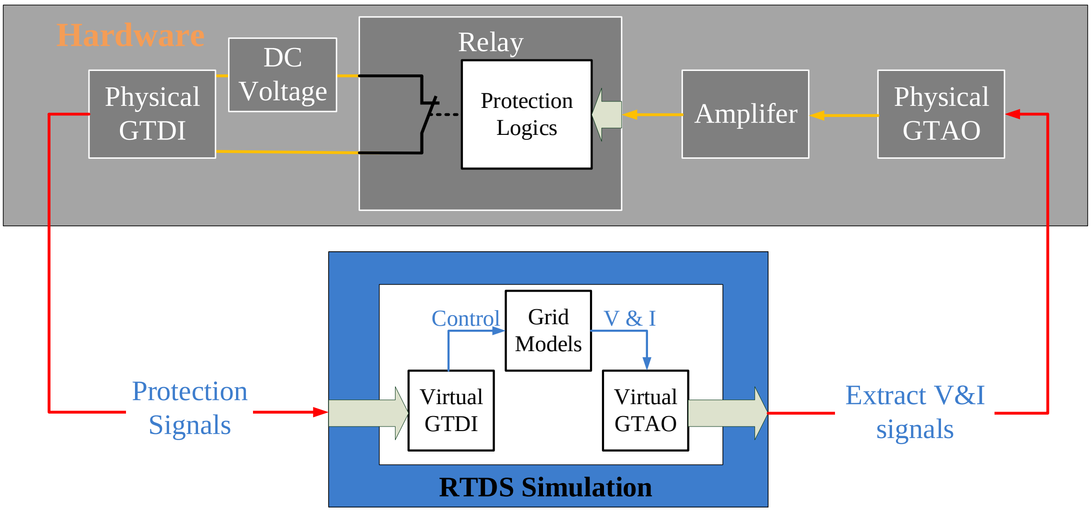

(a) RTDS simulation with hardware

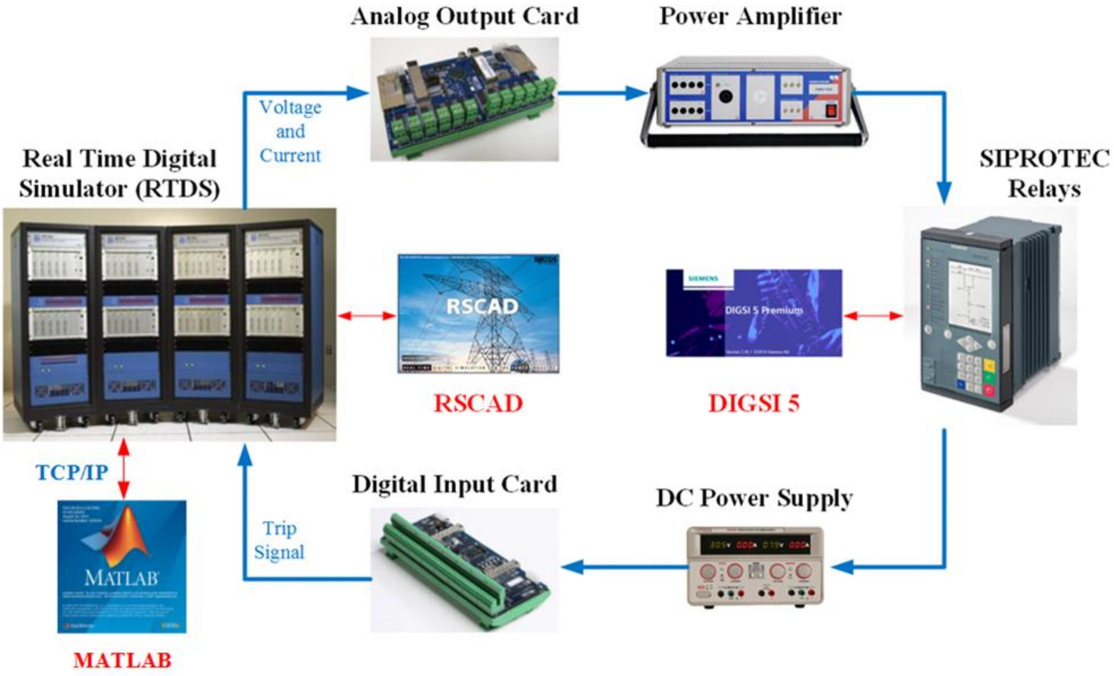

(b) Hardware and software communications

Figure 3.3: HIL test platform

manual controls.

3.2.2 Relay configuration

In the HIL test platform, the relay is configured through the SIPROTEC Relay kit software DIGSI 5. It acts as an interface between the user and the protective relay. The kit software is able to configure the routing of the relay inputs/outputs, select the protection schemes, specify the relay settings, monitor the device online, etc. The fault records are automatically saved in the relay and can be exported for further analysis. Some crucial aspects of the relay configuration are briefly described as follows.

- Select the correct device that matches with the physical relay from the library. Create the single-line diagram of the bay and associate the relay with the power system through the CT, the VT, and the circuit breaker [see Fig. 3.4]. This single-line diagram can also be configured to be shown on the relay display.
- Specify the measuring-points routing [see Fig. 3.5] and information routing [see Fig. 3.6]. This is to guarantee that the inputs/outputs of the relay are assigned correctly to the desired terminals.
- Select the desired protection function and specify the settings of the relay [see Fig. 3.7]. The "power system" setting mainly relates to the measurement supervision, while "Line 1" (distance protection in this case) relates to the actual setting of the protection schemes.

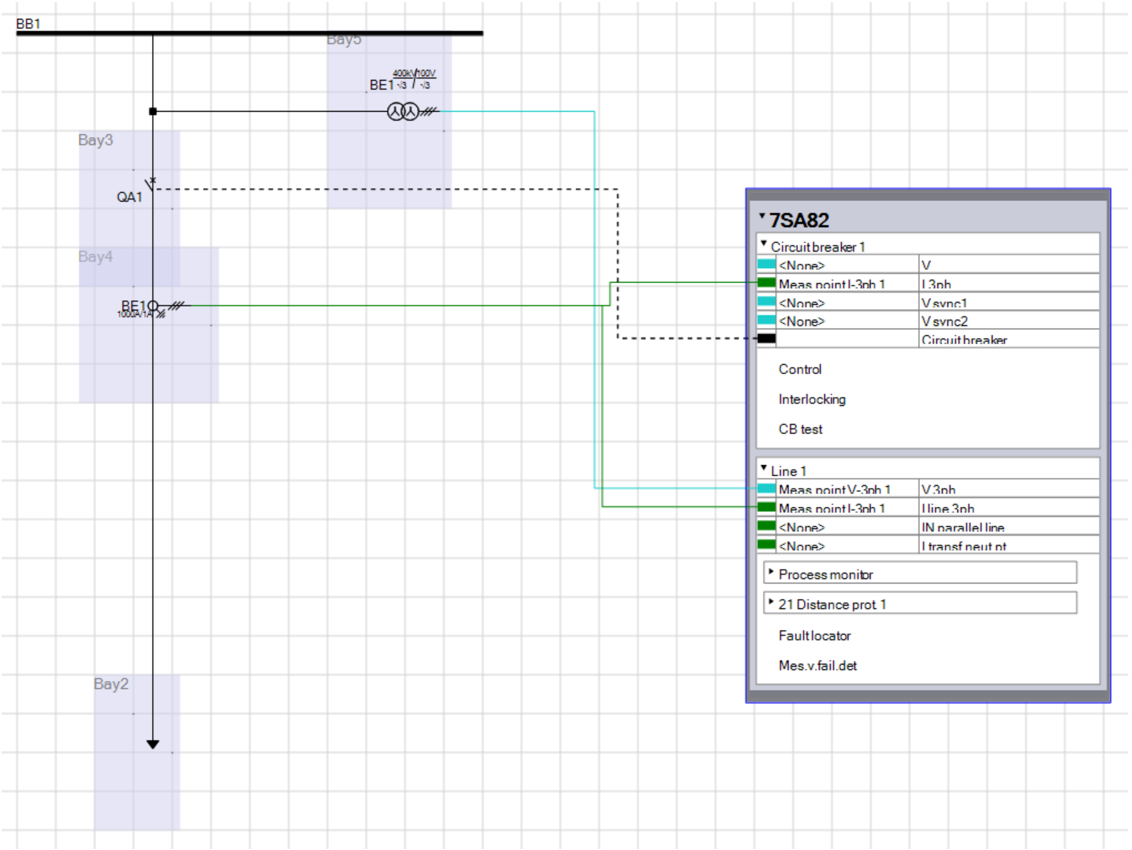

7SA82

Circuit breaker 1

🟦	<None>	V
🟩	Meas point I-3ph 1	I 3ph
🟦	<None>	V sync1
🟦	<None>	V sync2
■		Circuit breaker

Control

Interlocking

CB test

Line 1

🟦	Meas point V-3ph 1	V 3ph
🟩	Meas point I-3ph 1	I line 3ph
🟩	<None>	IN parallel line
🟩	<None>	I transf neut pt

Process monitor

21 Distance prot 1

Fault locator

Mes.v.fail.det

Figure 3.4: Single-line digram configuration

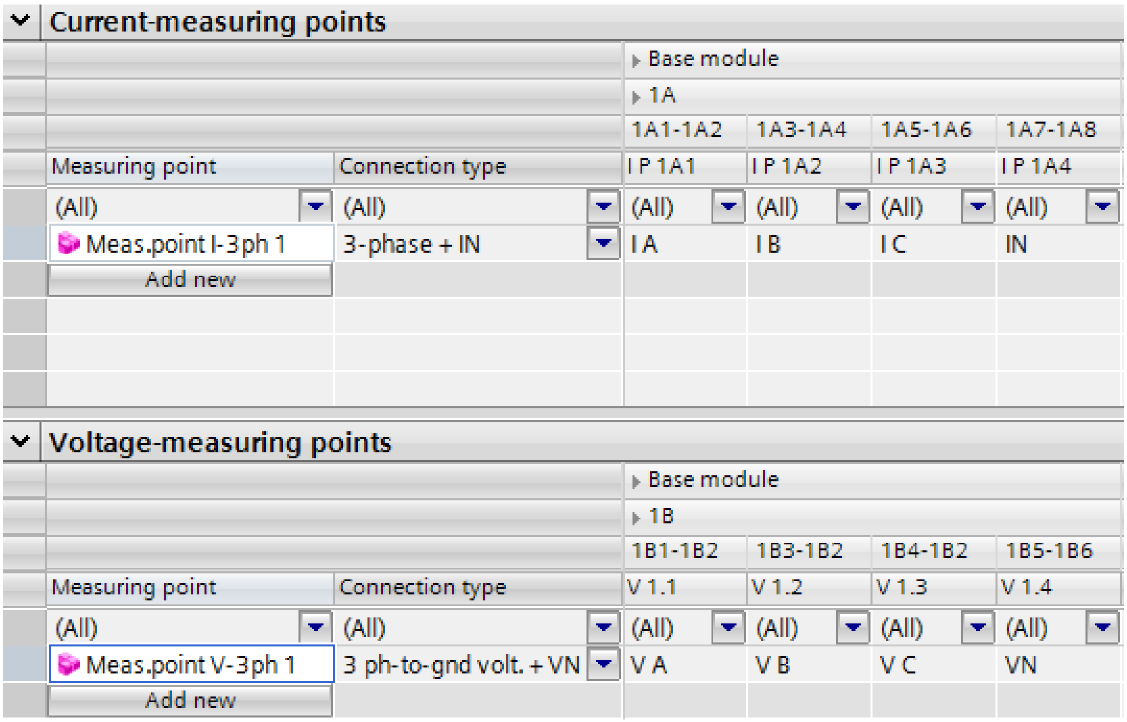

Current-measuring points

		Base module			
		1A			
		1A1-1A2	1A3-1A4	1A5-1A6	1A7-1A8
Measuring point	Connection type	I P 1A1	I P 1A2	I P 1A3	I P 1A4
(All)	(All)	(All)	(All)	(All)	(All)
Meas.point I-3ph 1	3-phase + IN	I A	I B	I C	IN
Add new					

Voltage-measuring points

		Base module			
		1B			
		1B1-1B2	1B3-1B2	1B4-1B2	1B5-1B6
Measuring point	Connection type	V 1.1	V 1.2	V 1.3	V 1.4
(All)	(All)	(All)	(All)	(All)	(All)
Meas.point V-3ph 1	3 ph-to-gnd volt. + VN	V A	V B	V C	VN
Add new					

Figure 3.5: Measuring-points routing

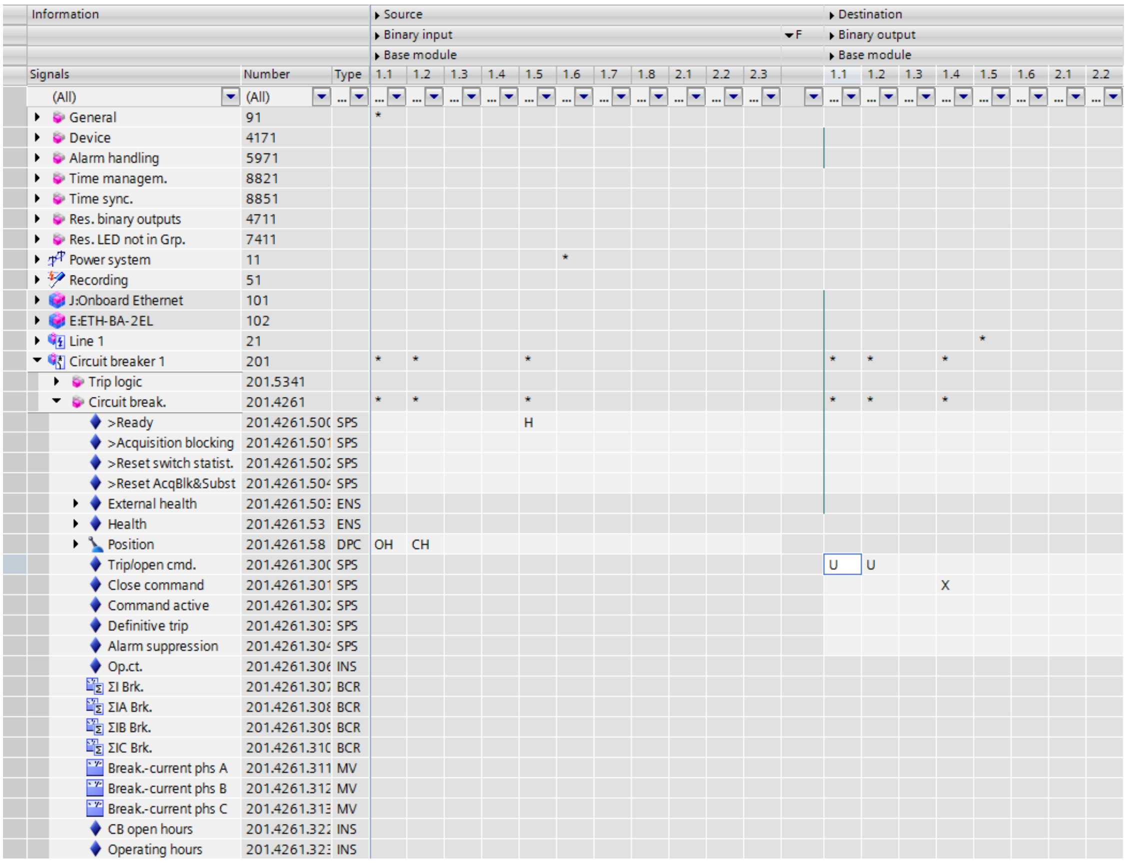

Information			Source												Destination							
			Binary input											F	Binary output							
			Base module												Base module							
Signals	Number	Type	1.1	1.2	1.3	1.4	1.5	1.6	1.7	1.8	2.1	2.2	2.3		1.1	1.2	1.3	1.4	1.5	1.6	2.1	2.2
(All)	(All)	...	...	...	...	...	...	...	...	...	...	...	...		...	...	...	...	...	...	...	...
General	91		*																			
Device	4171																					
Alarm handling	5971																					
Time managem.	8821																					
Time sync.	8851																					
Res. binary outputs	4711																					
Res. LED not in Grp.	7411																					
Power system	11							*														
Recording	51																					
J:Onboard Ethernet	101																					
E:ETH-BA-2EL	102																					
Line 1	21																		*			
Circuit breaker 1	201		*	*			*								*	*		*				
Trip logic	201.5341																					
Circuit break.	201.4261		*	*			*								*	*		*				
>Ready	201.4261.500	SPS					H															
>Acquisition blocking	201.4261.501	SPS																				
>Reset switch statist.	201.4261.502	SPS																				
>Reset AcqBlk&Subst	201.4261.504	SPS																				
External health	201.4261.503	ENS																				
Health	201.4261.53	ENS																				
Position	201.4261.58	DPC	OH	CH																		
Trip/open cmd.	201.4261.300	SPS													U	U						
Close command	201.4261.301	SPS																X				
Command active	201.4261.302	SPS																				
Definitive trip	201.4261.303	SPS																				
Alarm suppression	201.4261.304	SPS																				
Op.ct.	201.4261.306	INS																				
ΣI Brk.	201.4261.307	BCR																				
ΣIA Brk.	201.4261.308	BCR																				
ΣIB Brk.	201.4261.309	BCR																				
ΣIC Brk.	201.4261.310	BCR																				
Break.-current phs A	201.4261.311	MV																				
Break.-current phs B	201.4261.312	MV																				
Break.-current phs C	201.4261.313	MV																				
CB open hours	201.4261.322	INS																				
Operating hours	201.4261.323	INS																				

Figure 3.6: Information routing

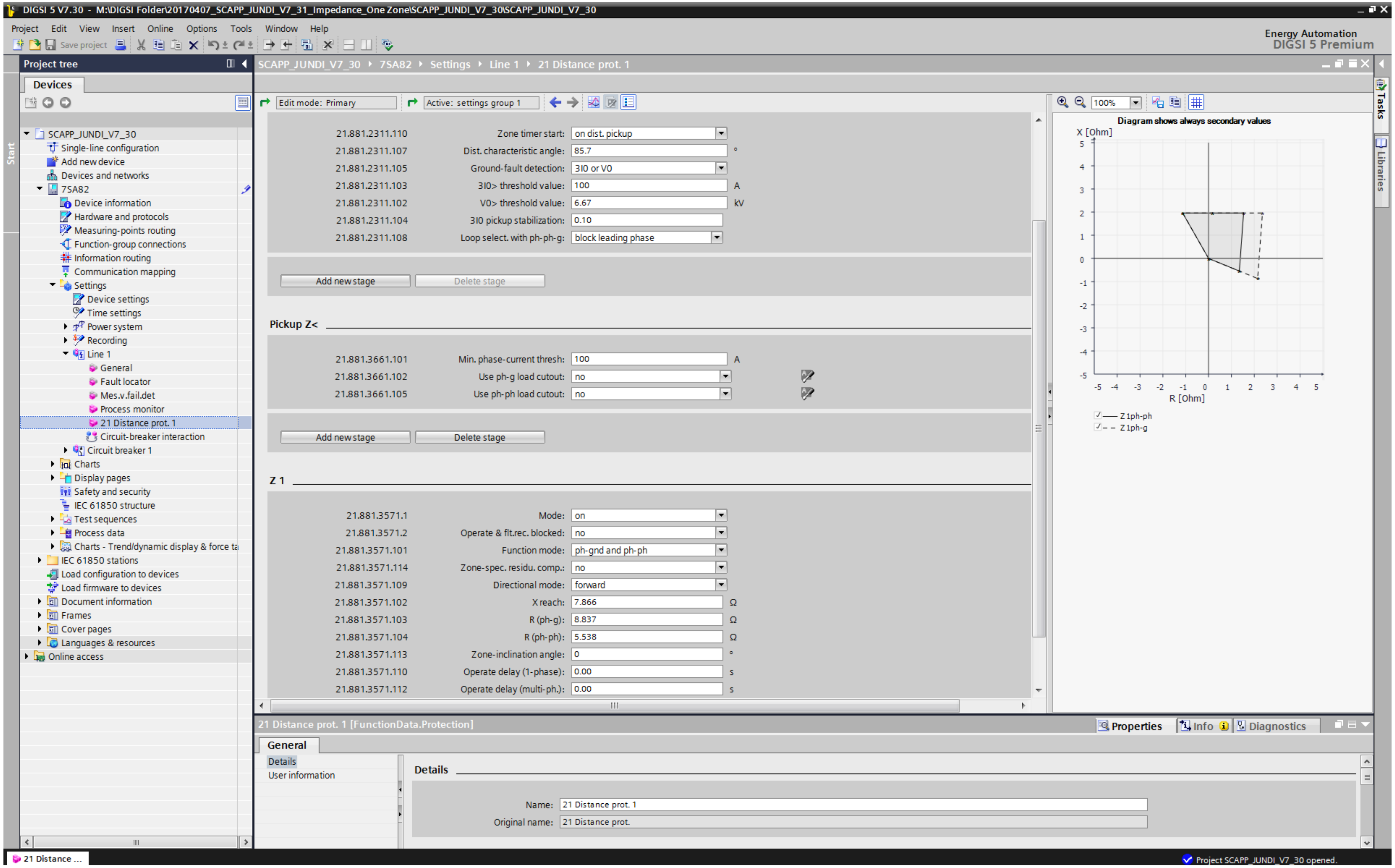

21.881.2311.110 Zone timer start: on dist. pickup
21.881.2311.107 Dist. characteristic angle: 85.7 °
21.881.2311.105 Ground-fault detection: 3I0 or V0
21.881.2311.103 3I0> threshold value: 100 A
21.881.2311.102 V0> threshold value: 6.67 kV
21.881.2311.104 3I0 pickup stabilization: 0.10
21.881.2311.108 Loop select. with ph-ph-g: block leading phase

Pickup Z<

21.881.3661.101 Min. phase-current thresh: 100 A
21.881.3661.102 Use ph-g load cutout: no
21.881.3661.105 Use ph-ph load cutout: no

Z 1

21.881.3571.1 Mode: on
21.881.3571.2 Operate & flt.rec. blocked: no
21.881.3571.101 Function mode: ph-gnd and ph-ph
21.881.3571.114 Zone-spec. residu. comp.: no
21.881.3571.109 Directional mode: forward
21.881.3571.102 X reach: 7.866 Ω
21.881.3571.103 R (ph-g): 8.837 Ω
21.881.3571.104 R (ph-ph): 5.538 Ω
21.881.3571.113 Zone-inclination angle: 0 °
21.881.3571.110 Operate delay (1-phase): 0.00 s
21.881.3571.112 Operate delay (multi-ph.): 0.00 s

Name: 21 Distance prot. 1
Original name: 21 Distance prot.

Figure 3.7: Relay configuration through DIGSI

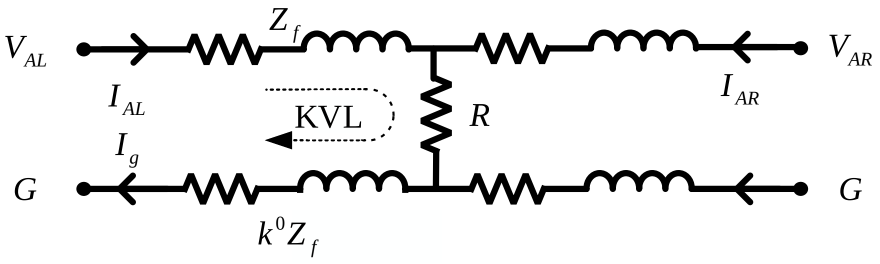

(a) A-g loop

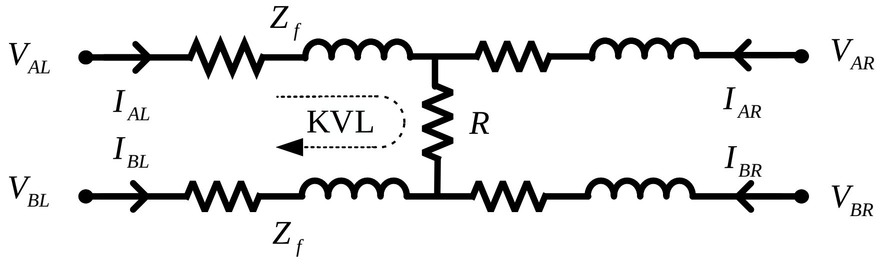

(b) A-B loop

Figure 3.8: Circuit diagrams for A-g and A-B faults

3.2.3 HIL tests on distance protection

Distance protection is widely used in high-voltage transmission systems and serves as the backbone for the line protection. It uses the measured local voltage and current to calculate the apparent impedance seen from the relay location to the fault to decided if a fault is internal or external with respect to a protective zone [158]. However, as presented in Chapter 2, the short circuit response of VSCs deviates significantly from SGs. This can bring up challenges and pose threat to the reliability of distance protection for a future low inertia power system, where VSCs become the main sources of the short circuit current. Even though the potential impact of VSCs on distance protection has raised much attention in recent years, less focus is given to unbalanced faults and the dual-sequence current controls of VSCs have been left unnoticed. This section presents the distance relay's possible maloperation for zone-1 unbalanced faults through HIL tests considering the power electronics control.

Distance protection for line unbalanced faults

A distance relay typically has six measurement loops (A-g, B-g, C-g, A-B, B-C, and C-A), which will start to calculate the impedance after being released by the pickup method. For example, the circuit diagrams of the A-g loop under an A-g fault and the A-B loop under an A-B fault is illustrated in Fig. 3.8. R refers to the fault resistance; Z_f is the positive-sequence apparent impedance from the relay location to the fault; k^0 is the zero-sequence compensation factor; L and R refer to the quantities related to the local and remote terminals respectively.

By applying the Kirchhoff's Voltage Law (KVL) to the left-side loop of Fig. 3.8(a) and Fig. 3.8(b)

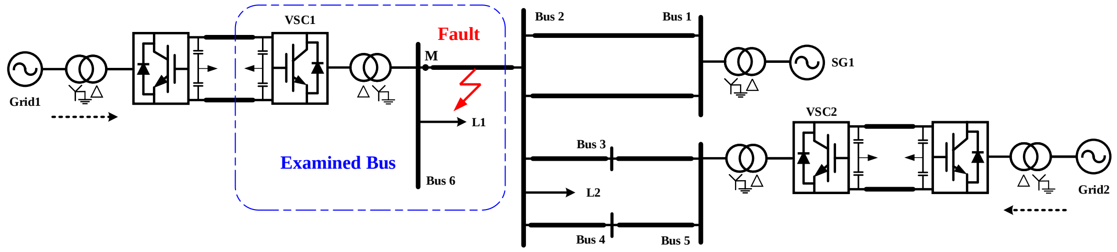

Figure 3.9: Single-line digram of the studied system

respectively, there are:

$$\dot{V}_{AL} = \dot{I}_{AL} Z_f + R(\dot{I}_{AL} + \dot{I}_{AR}) + k^0 \dot{I}_g Z_f \tag{3.2}$$

$$\dot{V}_{AL} - \dot{V}_{BL} = Z_f \dot{I}_{AL} - Z_f \dot{I}_{BL} + R(\dot{I}_{AL} + \dot{I}_{AR} - \dot{I}_{BL} - \dot{I}_{BR}) \tag{3.3}$$

Then the calculated line impedance from the relay location to the fault can be derived by re-arranging (3.2)–(3.3):

$$Z_{Ag} = \frac{\dot{V}_{AL}}{\dot{I}_{AL} + k^0 \dot{I}_g} = Z_f + R(1 + \frac{\dot{I}_{AR} - k^0 \dot{I}_g}{\dot{I}_{AL} + k^0 \dot{I}_g}) \tag{3.4}$$

$$Z_{AB} = \frac{\dot{V}_{AL} - \dot{V}_{BL}}{\dot{I}_{AL} - \dot{I}_{BL}} = Z_f + R(1 + \frac{\dot{I}_{AR} - \dot{I}_{BR}}{\dot{I}_{AL} - \dot{I}_{BL}}) \tag{3.5}$$

Both $\frac{\dot{I}_{AR} - k^0 \dot{I}_g}{\dot{I}_{AL} + k^0 \dot{I}_g}$ and $\frac{\dot{I}_{AR} - \dot{I}_{BR}}{\dot{I}_{AL} - \dot{I}_{BL}}$ are complex quantities and their imaginary part adds a factious reactance to Z_f. Therefore, the existence of the fault resistance R introduces an error to the measured impedance and thus affects the reach of the line protection. This measuring error mainly depends on the pre-fault power flow (phase displacement between the voltage at the local terminal and the remote terminal) in a conventional power system. It can be mitigated by adjusting the zone-inclination angle (tilting the reactance reach) [159]. However, with the presence of VSCs, whose short circuit current depends on the design of the control systems, the associated error can be enlarged and unpredictable so that the conventional compensation approach becomes insufficient.

Test system

Figure 3.9 presents the single-line diagram of the test system. This is a simplified version of the DK1 system in Fig. 3.1 with bus 1 corresponding to KAS, bus 5 corresponding to TJE and bus 6 corresponding to EDR. The line parameters remain the same as those in the DK1 system. In Fig. 3.9, a synchronous generator (SG1) is connected to the slack bus of the system bus 1. Two VSC-HVDC systems (VSC1 and VSC2) interface with the system at bus 6 and bus 5, respectively. On bus 6 and bus 2, there are two adjustable loads (L1 and L2).

In the following studies, VSC2 deploys balanced current control strategy. It has a converter peak current limit at 1 p.u. (2.7217 kA) with reactive current injection prioritized. In contrast, the FRT control strategy and the converter peak current limit of VSC1 are varied as different scenarios. It uses the current references (2.66)–(2.67) from FPNSPC with adjustable k_q, which means VSC1 is capable of providing positive- and negative-sequence reactive powers at the same time. The converter peak current limit is designed according to (2.74)–(2.79). The test scenarios are summarized in Table 3.1.

Prior to the fault, each VSC-HVDC system imports 500 MW active power at unity power factor. Three different pre-fault power flow conditions are examined according to Table 3.2. It is assumed that the reactive power references for both VSCs under fault conditions are generated using $Q^{ref} = |\mathbf{v}^{+}| \cdot I_Q$. The vaule of I_Q is obtained with respect to Fig. 1.4.

The HIL tests are with regard to the distance relay located at the point M. The relay protects the line 6-2 with a total length of 30 km. A-g or A-B faults are initiated at 75% (22.5 km) of line 6-2. The zone-1 protection of the distance relay is set to protect 80% (24 km) of the entire line using the classic method with impedance pick-up and a quadrilateral characteristic curve. The HIL test for each scenario is repeated 10 times.

Table 3.1: Test scenarios

Scenarios (VSC1)	**Converter Peak Current Limit (p.u.)**	**A-g fault resistance (Ω)**	**A-B fault resistance (Ω)**
Sx.1	1.00	0	0
Sx.2	1.00	5	1
Sx.3	1.25	5	1
Sx.4	1.50	5	1
Sx.5	1.25	10	2
x=1: prioritizing active current injection, $k_p = k_q$=1 x=2: prioritizing reactive current injection, k_p=1, k_q=1, 0.8, 0.6, 0.4, 0.2 or 0.0			

Table 3.2: Pre-fault power flow conditions

Load	**Power Flow 1 (MW) (power import)**	**Power Flow 2 (MW)**	**Power Flow 3 (MW) (power export)**
L1	1000	500	0
L2	0	500	1000

Test results

***(1)** Base case*

Firstly, the VSC-HVDC system at bus 6 is replaced by an SG with the same rating. Three different scenarios (denoted as S0.1, S0.2, and S0.5) with the same fault resistance as Sx.1, Sx.2, and Sx.5 respectively are tested. The measured fault distance for the A-g and A-B faults is summarized in Fig. 3.10. It can be observed that the error caused by the fault resistance and the different pre-fault power flow conditions are not significant for such a synchronous-generator-dominated system.

***(2)** Prioritizing active current injection*

Regarding the system in Fig. 3.9, Fig. 3.11 summarizes the measured fault distance under different scenarios when VSC1 prioritizes active current injection (x=1). It can be seen that the measured fault distance is accurate when there is no fault resistance (S1.1). However, when the fault resistance is present (S1.2-S1.5), the measuring error results in significant overreach problems (under-estimating the fault distance) for both A-g and A-B faults.

For A-g faults, the different converter peak current limit levels have less effect on the reach [see S1.2-S1.4 in Fig. 3.11(a)]. This is because the zero-sequence current from the neutral point of the

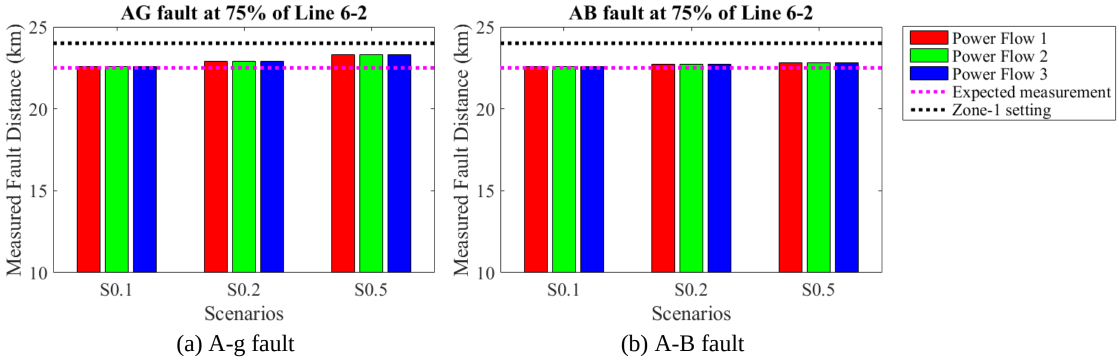

(a) A-g fault (b) A-B fault

Figure 3.10: Measured fault distance with VSC1 placed by an SG

interface transformer is not affected by the converter peak current limit. However, a lower peak current limit for A-B faults aggravates the overreach problem [see S1.2-S1.4 in Fig. 3.11(b)]. As explained by (3.4)–(3.5), larger measuring errors will occur with higher fault resistance, aggravating the overreach problem for both A-g and A-B faults [see S1.3 and S1.5 in Fig. 3.11(a)–(b)].

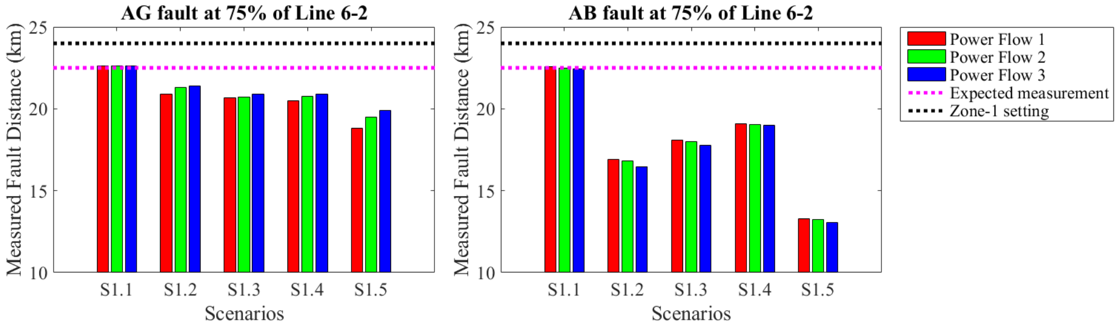

(a) A-g fault (b) A-B fault

Figure 3.11: Measured fault distance with with active current injection priority

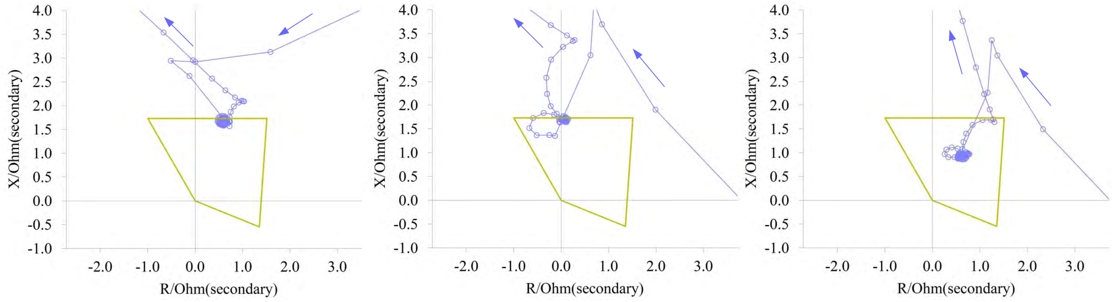

(a) S0.5, power flow 1 (b) S1.1, power flow 1 (c) S1.5, power flow 1

Figure 3.12: Impedance plane of the A-B element under the A-B fault

Corresponding to the scenarios S0.5, S1.1 and S1.5 with power flow 1, Fig. 3.12 presents the measured impedance locus under the A-B fault. It can be seen that the presence of VSC1 introduces more transients before the locus stabilizes at the indicated fault location. For the same fault condition, Fig. 3.12(a) gives relatively accurate measured impedance while a significant error appears in 3.12(c). This indicates that, for a low inertia power system, the measuring error caused by the fault resistance will be enlarged compared to the conventional system, which will degrade the reliability of distance protection.

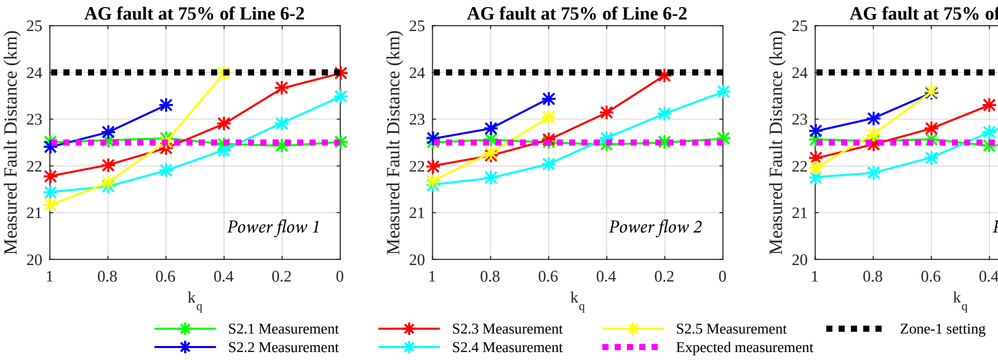

(a) A-g fault

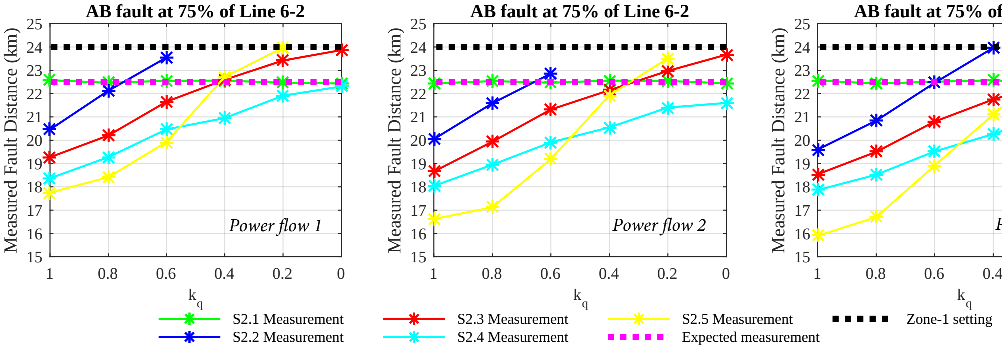

(b) A-B fault

Figure 3.13: Measured fault distance with reactive current injection priority

***(3)** Prioritizing reactive current injection*

Regarding the system in Fig. 3.9, Fig. 3.13 summarizes the measured fault distance when VSC1 prioritizes reactive current injection (x=2) with different values of k_q and pre-fault power flow conditions. When there is no fault resistance (S2.1), the measured fault distance is still accurate regardless of the value of k_q or the pre-fault power flow conditions. However, with the presence of the fault resistance (S2.2-S2.5), measuring errors start to exist. Underreach (over-estimating the fault distance) and overreach problems (under-estimating the fault distance) can both arise, and vary with the value of k_q, VSC1 peak current limit level, and the fault resistance.

Taking Fig. 3.13(a) with power flow 2 as an example, the measured fault distance for S2.2-S2.5 increases with k_q moving from 1 to 0. For S2.3, the fault resistance results in overreach problem with k_q=1 or 0.8. However, the fault resistance causes underreach with k_q below 0.6. When there is k_q=0, the relay fails to operate as the calculated impedance is beyond the zone-1 setting.

If the converter peak current limit of VSC1 increases from 1.25 p.u. (S2.3) to 1.5 p.u. (S2.4), the line S2.3 in Fig. 3.13(a) (power flow 2) moves downwards. This helps mitigate the underreach problem for k_q below 0.4, but aggravates the overreach problem for k_q above 0.6. Similarly, if the the peak current limit decreases from 1.25 p.u. to 1 p.u. (S2.2), the line S2.3 in Fig. 3.13(a) (power flow 2) is pushed further, resulting in overreach problem regardless the values of k_q. The relay fails to trip when k_q is below 0.6.

For the same peak current limit level, the value of k_q affects the the measuring error more if there is a higher fault resistance. The slope of the line S2.3 in Fig. 3.13(a) (power flow 2) increases as the fault resistance gets larger [see S2.3 and S2.5]. This aggravates the underreach problem for lower k_q, and also aggravates the overreach problem for higher k_q.

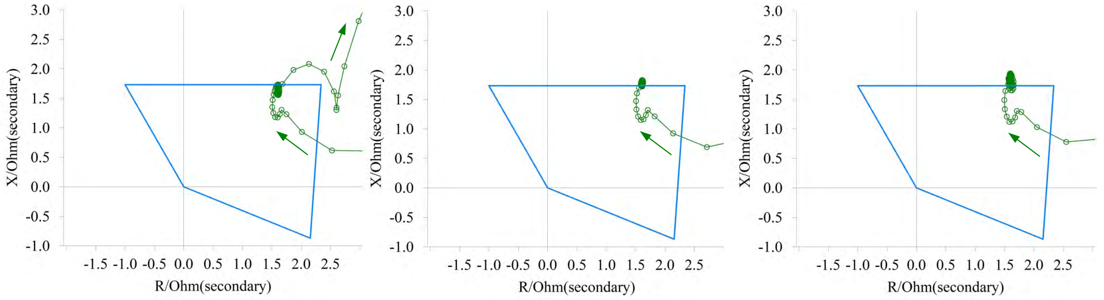

(a) S2.5, kq=1, power flow 3 (b) S2.4, kq=0.4, power flow 3 (c) S2.5, kq=0, power flow 3

Figure 3.14: Impedance plane of the A-g element under the A-g fault

Corresponding to S2.5 in Fig. 3.13(a) with power flow 3, Fig. 3.14 shows the measured impedance locus when VSC1 has different values k_q. The measured impedance locus stabilizes outside zone-1 and the relay fails to trip in Fig. 3.14(b)–(c).

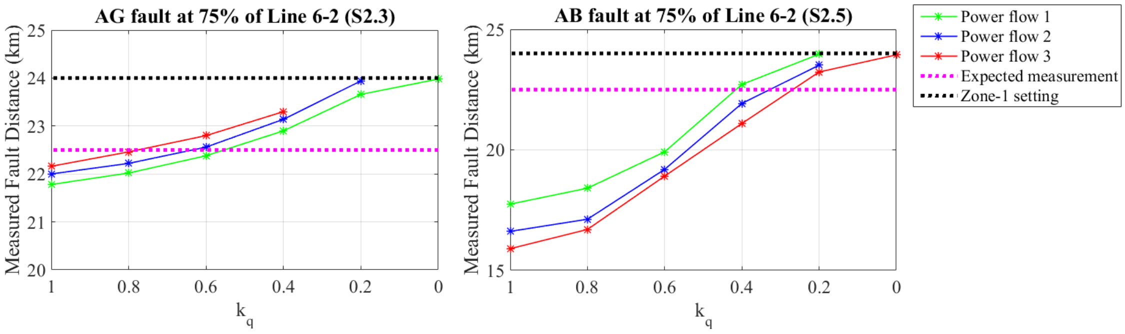

(a) A-g fault, S2.3 (a) A-B fault, S2.5

Figure 3.15: Measured fault distance under different pre-fault power flow conditions

For a distance relay using the classic method, the measuring error depends on pre-fault power flow conditions in such way that the power import tends to cause the underreach problem while the power export tends to cause the overreach problem [159]. This means the measured fault distance under a power import condition will be slightly larger than that of a power export condition. However, with the impact from VSCs, this may not be valid anymore for low inertia power systems.

Figure 3.15 compares the measured fault distance in two scenarios considering different pre-fault power flow conditions. In 3.15(b), “Power flow 1” (power import) is above “Power flow 3” (power export). This agrees with the reality of a conventional system. On the contrary, “Power flow 1” is below “Power flow 3” in Fig. 3.15(a), which is completely opposite to the common knowledge for the protection of a conventional system. This inconformity makes it even more challenging to decide whether an overreach problem or an underreach problem will appear. In this case, the conventional countermeasures such as adjusting the zone-inclination angle may become insufficient.

3.3 Combined effect of VSCs and synchronous condensers

Synchronous condensers have the advantages of contributing short circuit current and enhancing system frequency stability. It has been shown in [100, 101, 102] that there is a need of more SCs for a future low inertia power system. Even though the conventional power plants can be reimbursed into SCs, their locations may not be the optimal ones and newly-installed SCs can be anticipated at the PCC of a HVDC system or a wind power plant. This section investigates the combined effect of VSC and SC in terms of four different aspects, the combined short circuit current, the PCC voltage, the DC-side voltage, and the system frequency response under fault conditions. The VSC dual-sequence current control strategy and the capacity of the synchronous condenser are varied as different scenarios.

Figure 3.16 presents the studied system, which is the same as Fig. 3.9 except that two SCs (SC1 and SC2) are equipped bus 6 and bus 5 respectively. It is assumed that the active power delivered by Grid 1 and Grid 2 remains the same at all time. Both VSC-HVDC systems are equipped with a dynamic braking resistor system [see Fig. 3.17] on the DC-side to drain the excess electrostatic energy from the DC link into the resistor [160, 161]. SC2 has a capacity of 160 Mvar and VSC2 deploys balanced current control at all time.

In this study, the focus is given to the marked area around bus 6. The capacity of SC1 can be chosen from 50/150/250 Mvar as different scenarios. VSC1 can either use (2.47)–(2.48) from FOPC or (2.66)–(2.67) from FPNSPC under unbalanced faults. In the following, the flexible scalars k_p and k_q in (2.66)–(2.67) are represented by a and c respectively. The variations on the flexible scalars are summarized in Table 3.3.

Table 3.3: Variations on the flexible scalars

	FOPC [with (2.47)–(2.48)]	FPNSPC [with (2.66)–(2.67)]
Flexible scalars	$k_p = -k_q = k = \{\pm 1, \pm 0.5, 0\}$	$a = \{1, 0.5, 0\}$ $c = \{1, 0.5, 0\}$
Total scenarios	5	$3 \times 3 = 9$

The short circuit ratio at bus 6 is approximately 4.0 when SC1 is disconnected from the grid, and 5.8 when a 250 Mvar SC1 is connected. In order to guarantee identical pre-fault conditions, SC1

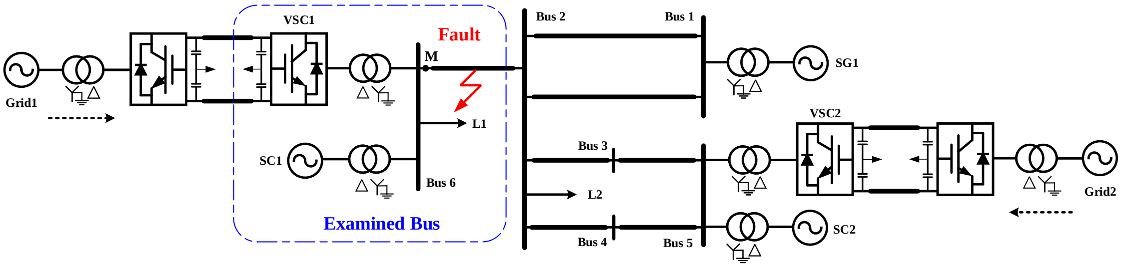

Figure 3.16: Single-line digram of the studied system with SCs

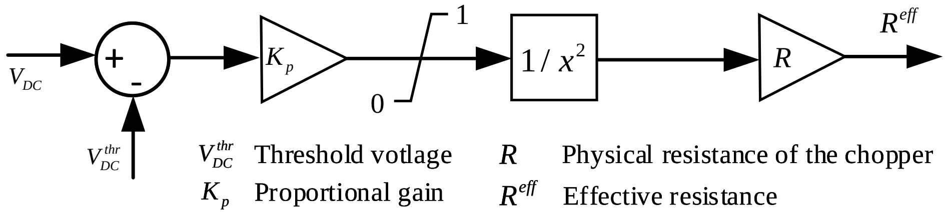

Figure 3.17: Dynamic braking resistor control system

is excited to exchange zero reactive power with the grid in the steady state. Prior to the fault, VSC1 and VSC2 deliver 500 MW and 350 MW active power respectively at unity power factor. The converter peak current limit is set to 1 p.u. (2.7217 kA) for both VSCs using the techniques presented in Section 2.4.4. It is assumed that both VSCs prioritize reactive current injection under fault conditions. The reactive power reference is generated using $Q^{ref} = |\mathbf{v}^{+}| \cdot I_Q$. The vaule of I_Q can be obtained in accordance to Fig. 1.4.

3.3.1 Short circuit current

Simulation results

For an A-B or an A-g fault at 50% of line 6-2, Fig. 3.18–3.19 compares the combined short circuit current (measured at the point M) in faulty phases with respect to different SC capacities when VSC1 deploys FOPC. In Fig. 3.18 for the A-B fault, when SC1 is not present (no SC), the phase relationship of the currents in phase A and phase B changes from nearly 180° out of phase [see Fig. 3.18(a)] to almost in phase [see Fig. 3.18(d)] as the control strategy moves from constant active power control ($k = -1$) to constant reactive power control ($k = 1$). SC1 helps to increase the combined short circuit current level but this advantage is gradually deteriorated with k moving from -1 to 1. In the worst case with $k = 1$, a 50 Mvar SC1 has almost no improvement on the amplitude of the phase A current [see "SC50 phase A" and "no SC phase A" in Fig. 3.18(d)]. This is because there is a phase discrepancy between the short circuit current provided by VSC1 and SC1. For VSC1, the phases of the short circuit current are mainly decided by the control strategy. For SC1, they are mainly consistent regarding a certain type of unbalanced faults. Therefore, this difference can cause the currents to cancel each other to some extent.

In contrast, for the A-g fault in Fig. 3.19, the current cancellation phenomenon is not significant. An SC1 of 50 Mvar is able to boost the short circuit current in the faulty phase. During the A-g fault, besides the short circuit currents from SC1 and VSC1, the step-up transformers of SC1 and VSC1 provide paths for the zero-sequence short circuit current to flow through the grounded neutral points. The zero-sequence current is relatively larger than the current contributed from VSC1 and thus the VSC1 control strategies have less effect on the combined short circuit current.

Figure 3.20 compares the combined short circuit current in faulty phases with respect to different values of k when SC1 has a capacity of 250 Mvar. It can be observed that the currents have relatively lower amplitudes with $k > 0$. This indicates that, with $k > 0$, a higher capacity of SC1 is needed to achieve the same short circuit level as with $-1 \leq k \leq 0$ when using FOPC.

The same investigation is repeated when VSC1 deploys FPNSPC with the different combinations of the flexible scalars specified in Table 3.3. In this case, the current cancellation phenomenon is not as significant as FOPC with $k > 0$ under A-B faults. The combined short circuit current

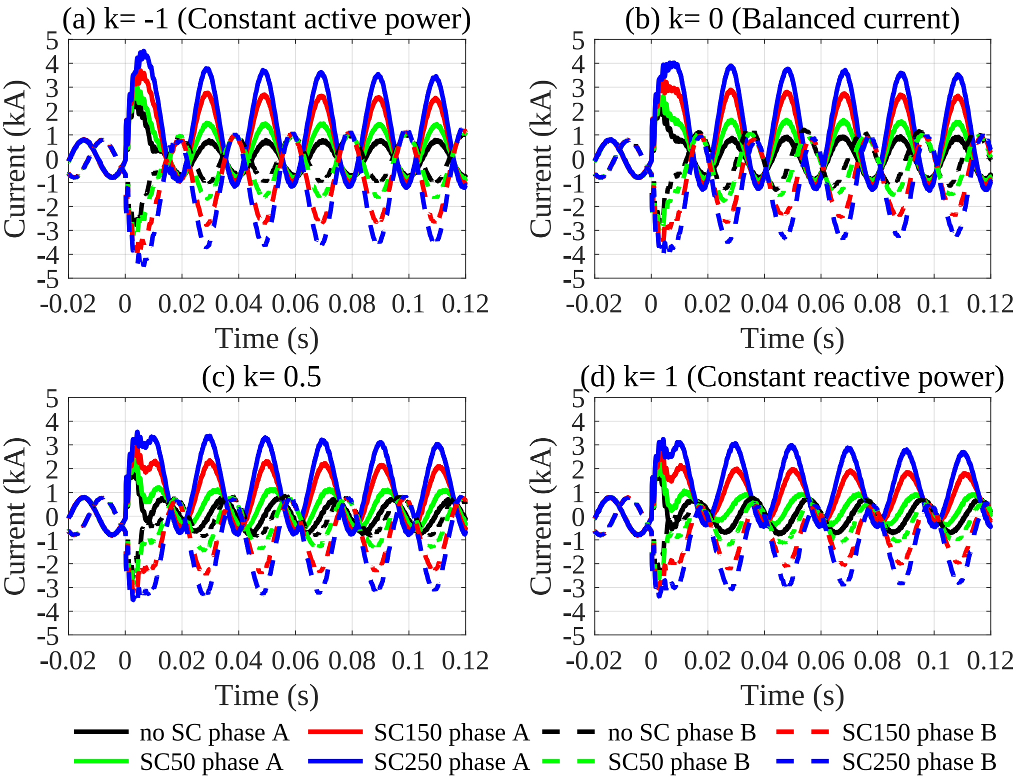

Figure 3.18: The combined short circuit current for the A-B fault with different capacities of SC1 when VSC1 deploys FOPC

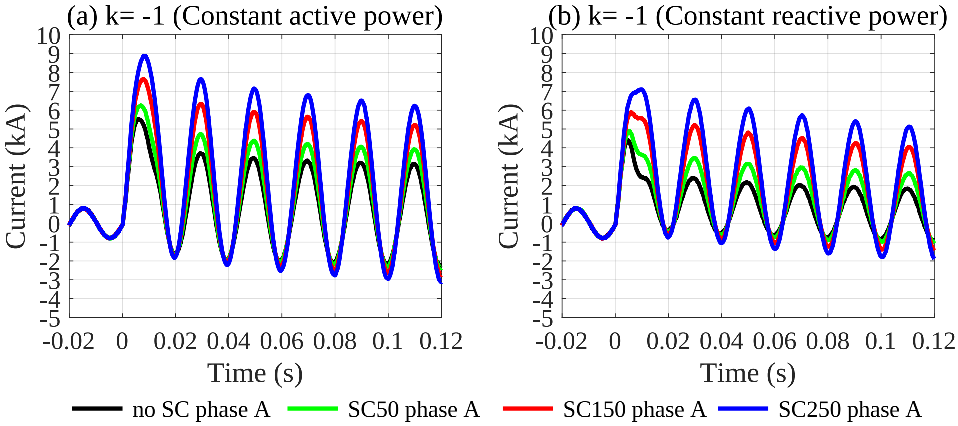

Figure 3.19: The combined short circuit current for the A-g fault with different capacities of SC1 when VSC1 deploys FOPC

in the faulty phases can all be increased with a 50 Mvar SC1, and the values of a (share of P^+) and c (share of Q^+) have less effect on the amplitudes of the combined short circuit current. The corresponding combined short circuit currents under different capacities of SC1 are similar to those in Fig. 3.18(b) for the A-B fault.

When there is the converter peak current limit in each phase, the short circuit current level drops significantly when it is only provided by a VSC. For all the examined control strategies, FOPC with $0 < k_p = -k_q = k \leq 1$ (absorbing Q^-) together with an SC should be avoided. It requires

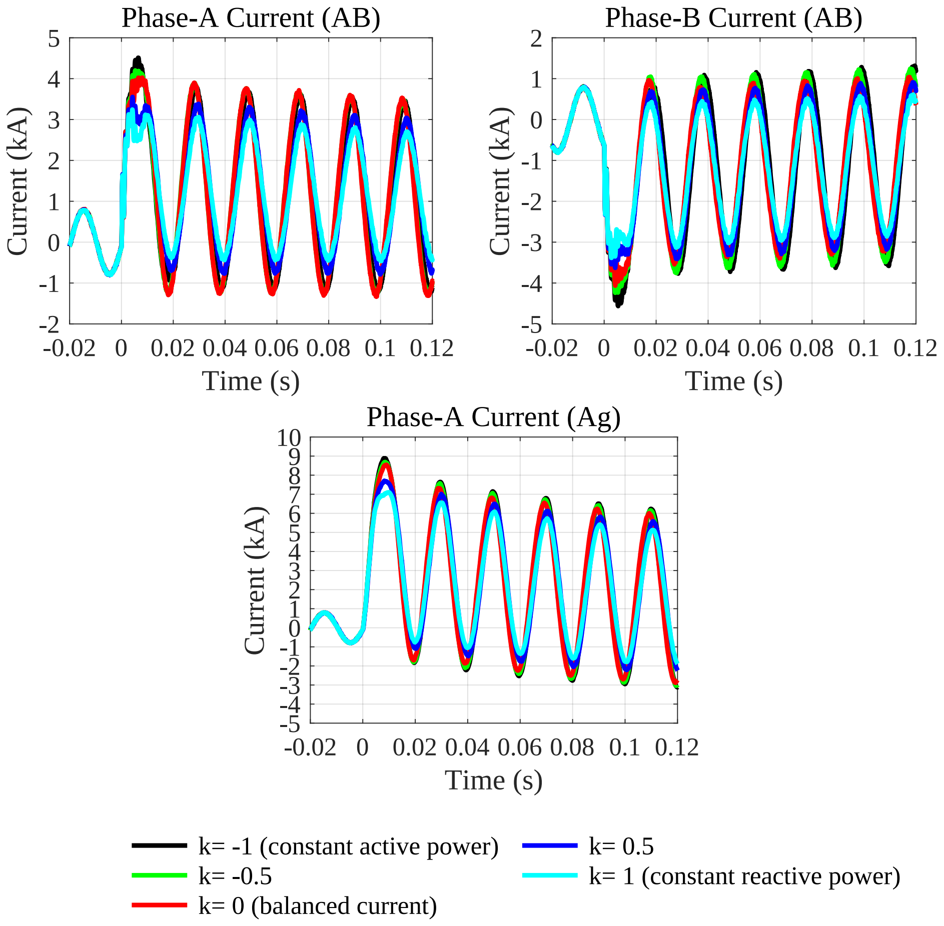

Figure 3.20: The combined short circuit current with different flexible scalar when VSC1 deploys FOPC

an SC with a higher capacity to achieve the same short circuit current level as the other control strategies. The advantage of SCs to contribute short circuit current can be deteriorated due to the current cancellation, which may even affect the reliability of the protection systems.

HIL tests on distance relay

This section investigates the impact of the current cancellation phenomenon on distance protection using HIL tests for the system in Fig. 3.16. The control strategy of VSC1 can be chosen from constant active power, balanced current, constant reactive power control. The capacity of SC1 can be chosen from 0/50/100/150/200/250 Mvar. The HIL tests are with regard to the distance relay located at point M protecting line 6-2. The test setup and the relay setting remain the same as Section 3.2.3. Three different unbalanced faults, A-g, A-B and A-B-g faults, are initiated at 25%, 50% and 75% of line 6-2. The zero time instant corresponds to the instant when the fault occurs. In the following, the response time of each test is defined as the time elapsed from the occurrence of the fault until the trip signal generated by the relay being registered in RTDS. Each HIL test is repeated 10 times for different scenarios. In order to ensure each test has the same pre-fault conditions, the faults are all initiated when the phase A voltage of bus 6 has a zero crossing from the negative to the positive.

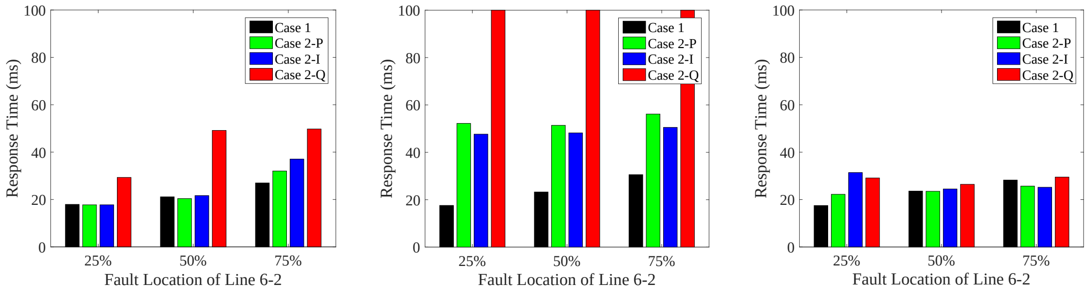

(a) A-g fault (b) A-B fault (c) A-B-g fault

Figure 3.21: Average response time of the distance relay for Case 1 and Case 2

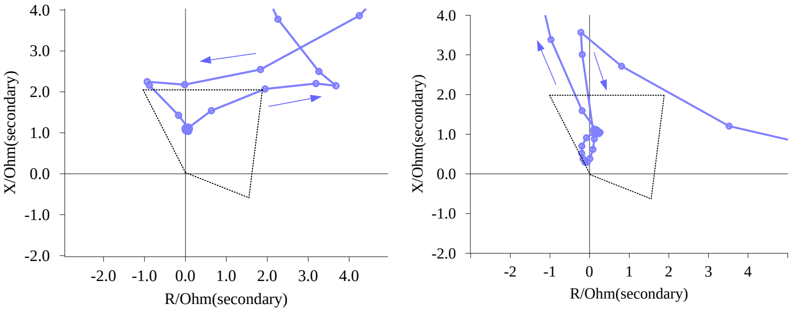

(a) Case 1 (b) Case-2P

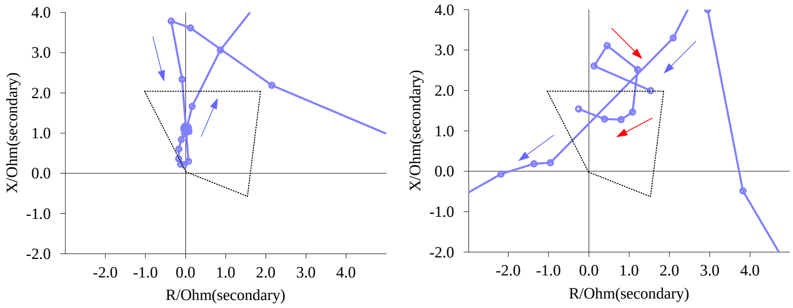

(c) Case-2I (d) Case-2Q

Figure 3.22: Impedance plane of the A-B element for the A-B fault at 50% of line 6-2

***Case 1**: SG solely*

This case, serving as the base case, considers a more traditional power system by replacing VSC1 with a 500 MVA synchronous generator and disconnecting SC1. Therefore, the short circuit current seen by the distance relay is only from the synchronous generator.

***Case 2**: Voltage source converter solely*

This case considers the system in Fig. 3.16 with SC1 disconnected so that the short circuit current seen by the relay is only from VSC1. As different scenarios, the control strategy of VSC1 under unbalanced faults can be chosen from constant active power (Case2–P), balanced current (Case2–I) and constant reactive power (Case2–Q) control.

For Case 1 and Case 2, Fig. 3.21 summarizes the average response time of the relay with respect to different fault types and locations. The response time in Case 2 generally increases when compared to Case 1, especially for A-B faults. This indicates that the speed of distance protection may be jeopardized due to the low short circuit current level in low inertia power systems. For the three examined control strategies, constant active power control and balanced current control yield similar performances when it comes to the response time. Nevertheless, with VSC1 using constant reactive power control, the speed of the relay is deteriorated to a large extent for A-g faults. The relay even fails to trip under A-B faults. Figure 3.22 presents the impedance plane given by the relay for the A-B fault at 50% of line 6–2 regarding Case 1 and Case 2. More transients are observed in Fig. 3.22(b)–(c) than Fig. 3.22(a) before the locus stabilizes at the indicated fault location inside the zone. In Fig. 3.22(d), the impedance locus exhibits unfavorable features. The locus enters zone-1 without clearly indicating a fault location. For the scenarios in Fig. 3.22, Fig. 3.23 presents the measured impedance versus time. For Case 1, Case2-P, and Case2-I, the curves enter and stay inside the effective zone stably after the fault. However, the curve for Case2-Q has discontinuous features.

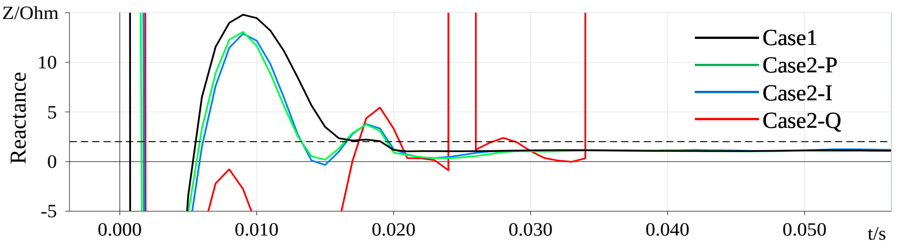

(a) Reactance

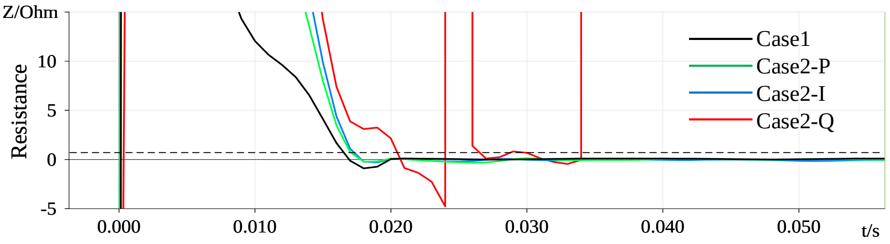

(b) Resistance

Figure 3.23: Measured impedance for the A-B fault at 50% of line 6-2

In order to investigate the phenomenon associated with Case2-Q, the three-phase voltage and current inputs to the relay are examined as shown in Fig. 3.24. The three-phase voltage (from the wye-winding side of the converter transformer) during the fault can be represented approximately by $\mathbf{v}_y$, which will become $\mathbf{v}_\Delta$ when referred to the delta-winding side.

$$\mathbf{v}_y = \begin{bmatrix} M_1 sin(\omega t) \\ M_1 sin(\omega t) \\ -M_2 sin(\omega t) \end{bmatrix}, \ \mathbf{v}_\Delta = \begin{bmatrix} M_3 sin(\omega t) \\ 0 \\ -M_3 sin(\omega t) \end{bmatrix} \tag{3.6}$$

where M_1, M_2 and $M_3 = (M_1 + M_2)/(\sqrt{3}N)$ refer to the magnitudes of the associated voltages. N is the transformer turns ratio from the wye-winding side to the delta-winding side. $\mathbf{v}_\Delta$ can be

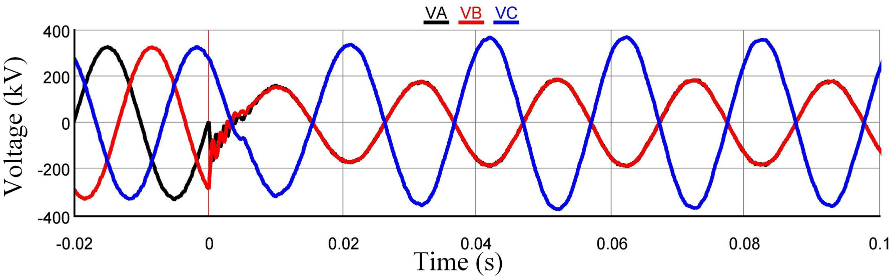

(a) Voltage

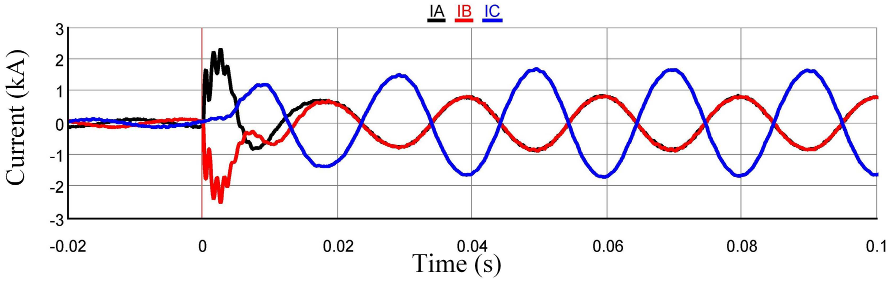

(b) Current

Figure 3.24: Inputs to the distance relay

further decomposed into:

$$\begin{bmatrix} v_a^+ \\ v_b^+ \\ v_c^+ \end{bmatrix} = \begin{bmatrix} M_4 sin(\omega t + \frac{\pi}{6}) \\ M_4 sin(\omega t - \frac{\pi}{6}) \\ M_4 sin(\omega t + \frac{5\pi}{6}) \end{bmatrix}, \begin{bmatrix} v_a^- \\ v_b^- \\ v_c^- \end{bmatrix} = \begin{bmatrix} M_4 sin(\omega t - \frac{\pi}{6}) \\ M_4 sin(\omega t + \frac{\pi}{6}) \\ M_4 sin(\omega t - \frac{5\pi}{6}) \end{bmatrix} \tag{3.7}$$

where $M_4 = (M_1 + M_2)/(3N)$ refers to the magnitudes of the associated voltages. Then, the orthogonal versions of the positive- and negative-sequence voltages can be written as:

$$\begin{bmatrix} v_{a\perp}^+ \\ v_{b\perp}^+ \\ v_{c\perp}^+ \end{bmatrix} = \begin{bmatrix} M_4 sin(\omega t - \frac{\pi}{3}) \\ M_4 sin(\omega t - \pi) \\ M_4 sin(\omega t + \frac{\pi}{3}) \end{bmatrix}, \begin{bmatrix} v_{a\perp}^- \\ v_{b\perp}^- \\ v_{c\perp}^- \end{bmatrix} = \begin{bmatrix} M_4 sin(\omega t + \frac{\pi}{3}) \\ M_4 sin(\omega t + \pi) \\ M_4 sin(\omega t - \frac{\pi}{3}) \end{bmatrix} \tag{3.8}$$

The current references (2.47) and (2.48) for FOPC indicate that, the phases of $\mathbf{i}_P^{ref}$ and $\mathbf{i}_Q^{ref}$ are determined by the phases of $\mathbf{v}^+$, $\mathbf{v}^-$, $\mathbf{v}_\perp^+$, $\mathbf{v}_\perp^-$, k_p, and k_q. As a result, with (3.7) and (3.8) substituted into (2.47) and (2.48), the current references for constant active power control strategy are:

$$\mathbf{i}_P^{ref} = \frac{P^{ref}}{|\mathbf{v}^+|^2 - |\mathbf{v}^-|^2} \begin{bmatrix} v_a^+ - v_a^- \\ v_b^+ - v_b^- \\ v_c^+ - v_c^- \end{bmatrix} = M_5 \begin{bmatrix} cos(\omega t) \\ -2cos(\omega t) \\ cos(\omega t) \end{bmatrix} \tag{3.9}$$

$$\mathbf{i}_Q^{ref} = \frac{Q^{ref}}{|\mathbf{v}^+|^2 + |\mathbf{v}^-|^2} \begin{bmatrix} v_a^+ + v_a^- \\ v_b^+ + v_b^- \\ v_c^+ + v_c^- \end{bmatrix} = M_6 \begin{bmatrix} sin(\omega t) \\ -2sin(\omega t) \\ sin(\omega t) \end{bmatrix} \tag{3.10}$$

while for constant reactive power control strategy, there are:

$$\mathbf{i}_P^{ref} = \frac{P^{ref}}{|\mathbf{v}^{+}|^2 + |\mathbf{v}^{-}|^2} \begin{bmatrix} v_{a\perp}^{+} + v_{a\perp}^{-} \\ v_{b\perp}^{+} + v_{b\perp}^{-} \\ v_{c\perp}^{+} + v_{c\perp}^{-} \end{bmatrix} = M_7 \begin{bmatrix} sin(\omega t) \\ 0 \\ -sin(\omega t) \end{bmatrix} \tag{3.11}$$

$$\mathbf{i}_Q^{ref} = \frac{Q^{ref}}{|\mathbf{v}^{+}|^2 - |\mathbf{v}^{-}|^2} \begin{bmatrix} v_{a\perp}^{+} - v_{a\perp}^{-} \\ v_{b\perp}^{+} - v_{b\perp}^{-} \\ v_{c\perp}^{+} - v_{c\perp}^{-} \end{bmatrix} = M_8 \begin{bmatrix} cos(\omega t) \\ 0 \\ -cos(\omega t) \end{bmatrix} \tag{3.12}$$

where M_5-M_8 refer to the magnitudes of the currents. If the currents expressed by (3.9)-(3.12) are referred back to the wye-winding side, the current in phase A and phase B will be out of phase with (3.9)–(3.10) (similiar to that of synchronous machines under A-B faults). However, for constant reactive power control with (3.11)–(3.12), the current in phase A and phase B will be in phase with the same magnitude [see Fig. 3.24(b)]. This is significantly different from that of a synchronous machine.

Typically, the A-B element of a distance relay calculate the impedance with [158]:

$$Z_{AB} = \frac{\dot{V}_A - \dot{V}_B}{\dot{I}_A - \dot{I}_B} \tag{3.13}$$

where $\dot{V}_A$, $\dot{V}_B$ and $\dot{I}_A$, $\dot{I}_B$ are the voltage and current inputs expressed in phasors. Therefore, if the currents are identical both in phase and in amplitude [see Fig. 3.24(b)], the denominator of (3.13) can become zero, which cause the distance relay to be unable to calculate the impedance reliably. This explains why the impedance locus in Case2-Q is discontinuous. The same phenomenon in the A-B element can also be observed for A-B-g faults when using constant reactive power control. The operation of the distance relay under A-B-g faults relies on A-g, B-g, and A-B elements. Even though the relay can still operate successfully through the A-g and B-g elements, the use of constant reactive power control still pose threats to the reliability of the distance relay.

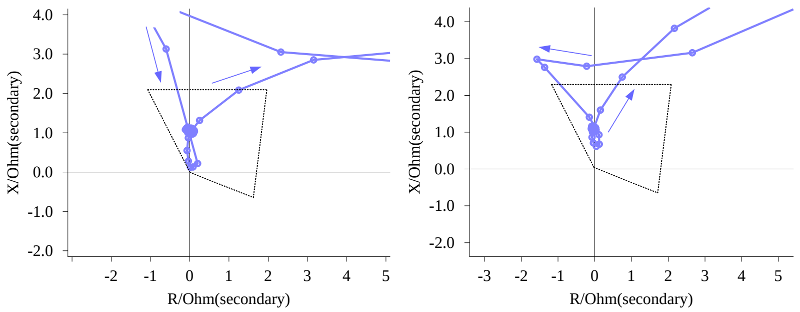

(a) SC1: 100 Mvar

(b) SC1: 200 Mvar

Figure 3.25: Impedance plane of the A-B element for the A-B fault at 50% of line 6-2 in Case 3 with constant reactive power control

***Case 3**: Incorporation of SCs*

In this case, the system in Fig. 3.16 is simulated with SC1 connected so that short circuit current seen by the relay is jointly provided by VSC1 and SC1. As different scenarios, the capacity of SC1 can be chosen from 50/100/150/200/250 Mvar. In each scenario, the excitation of SC1 is adjusted so that Case 3 has the same power flow results as Case 2 prior to the fault. This guarantees that Case 3 has the same pre-fault conditions as Case 2.

The measured impedance locus is generally improved with fewer transients in Case 3 with the application of SC1. With constant reactive power control for VSC1, Fig. 3.25 presents the impedance plane under A-B faults at 50% of line 6–2 with different capacities of SC1. Unlike Fig. 3.22(d), the locus in Fig. 3.25 is able to stabilize inside the zone and moves out of the zone only after the fault is cleared by the relay. This is because the currents in phase A and phase B are no longer identical with the help of SC1.

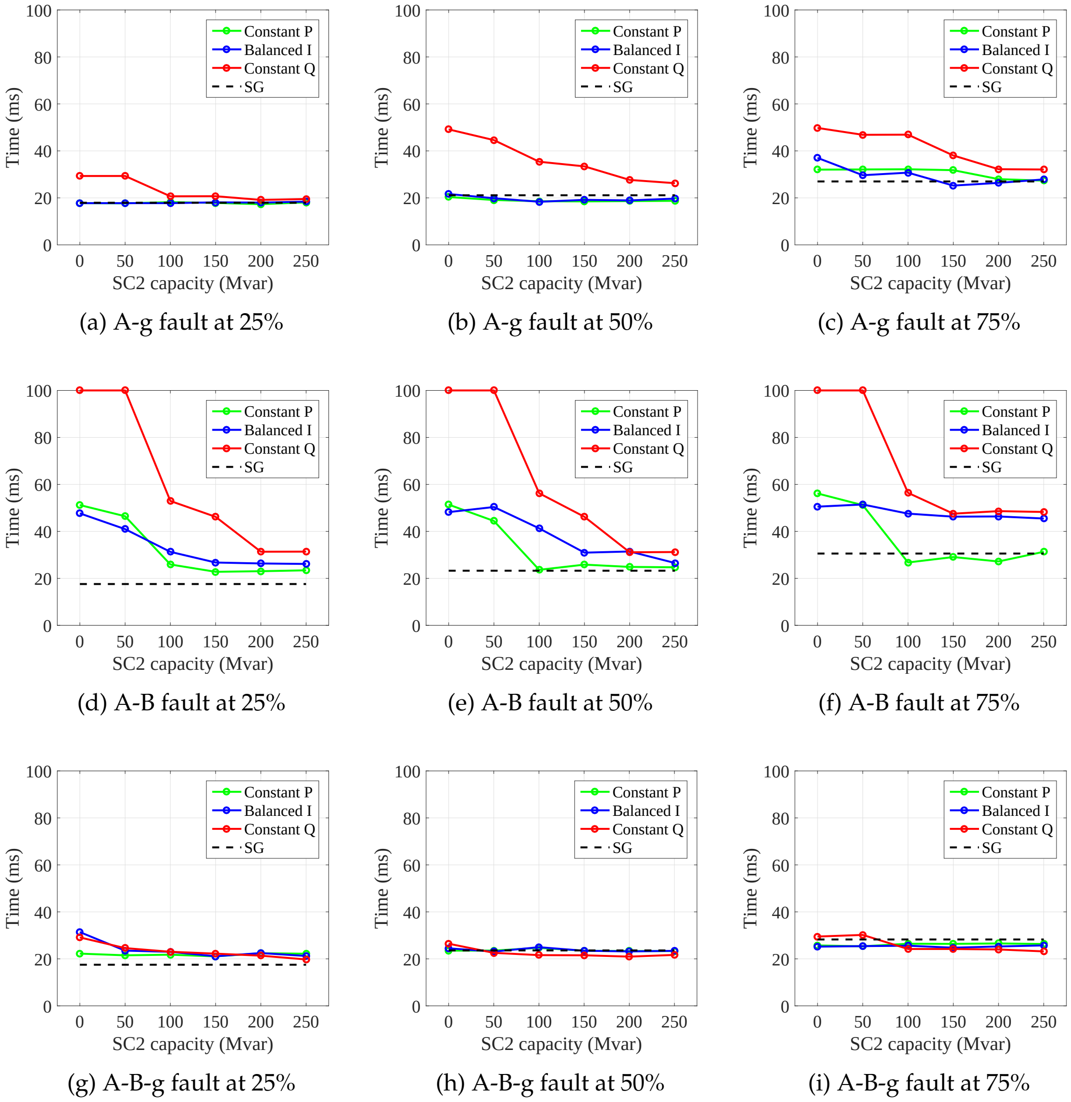

(a) A-g fault at 25%

(b) A-g fault at 50%

(c) A-g fault at 75%

(d) A-B fault at 25%

(e) A-B fault at 50%

(f) A-B fault at 75%

(g) A-B-g fault at 25%

(h) A-B-g fault at 50%

(i) A-B-g fault at 75%

Figure 3.26: Average response time of the distance relay for Case 3

Figure 3.26 summarized the average response time in Case 3 with respect to different SC1 capacities. It also includes the results from Case 1 (black dashed line) and Case 2 (points corresponding to 0 Mvar) for comparisons. When the capacity of SC1 increases from 0 to 250 Mvar, the speed of the distance relay improves generally and gets closer to Case 1. However, the relay still fails to trip with a 50 Mvar SC1 when constant reactive power control is used in VSC1. On the one hand, the short circuit current from a 50 Mvar SC1 is relatively small compared to that from the 500 MVA VSC1. On the other hand, as discussed above, there exists the current cancellation problem when using constant reactive power control strategy. As a result, the available short circuit current may be further reduced when using SC1 if the capacity of the SC and the control strategy of the VSC are not appropriate.

Figure 3.27 compares the combined short circuit currents of VSC1 and SC1 in phase A for the A-B fault at 50% of line 6–2 considering different capacities of SC1. Regarding constant active power control in Fig. 3.27(a), an increase in the capacity of SC1 helps boost the current. However, with constant reactive power control, the application of a 50 Mvar SC1 even reduces the available short circuit current when compared to the scenario without SC1 [see "IA(0)" and "IA(50)" in Fig. 3.27(b)]. This causes the combined short circuit current such small that it is not enough for the relay to activate impedance calculation. For the same size of SC1, the total available short circuit current with constant reactive power control is less than that with constant active power control. This further approves that the current cancellation problem associated with constant reactive power control will impair the advantages of synchronous condensers.

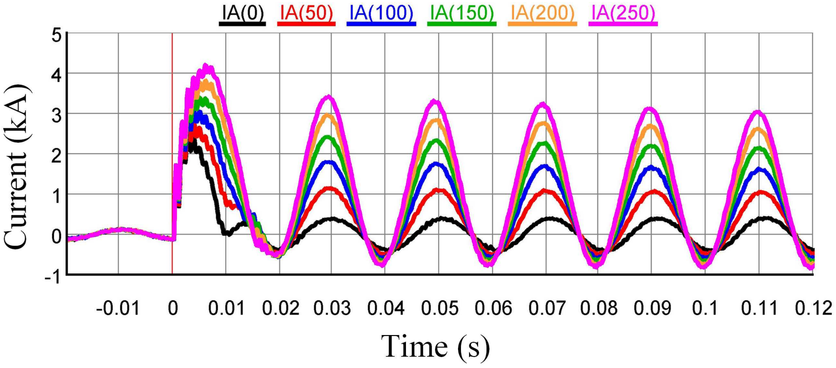

(a) Constant active power control for VSC1

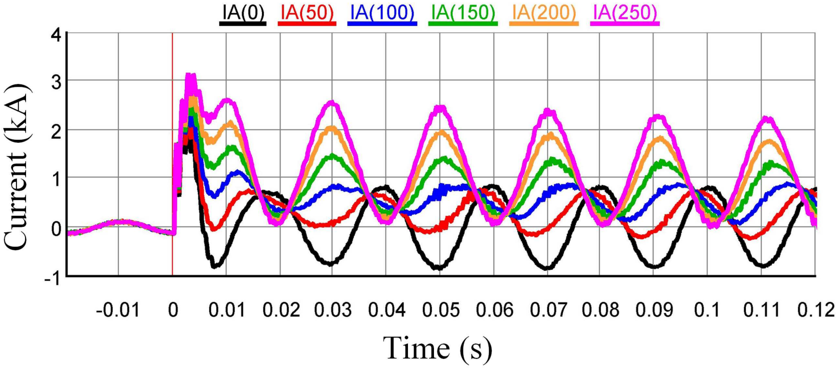

(b) Constant reactive power control for VSC1

Figure 3.27: Comparisons on the phase A short circuit current with different capacities of SC1 for the A-B fault at 50% of line 6-2

Case 4*: Limited zero-sequence current*

In Fig. 3.21(a) and (c), the relay performances under grounded faults are not affected as much as those under A-B faults. With the neutral point solidly grounded, the wye-winding side of the VSC1 interface transformer provides a path for the zero-sequence current under grounded faults. Therefore, as long as the zero-sequence current with a high amplitude is present for grounded

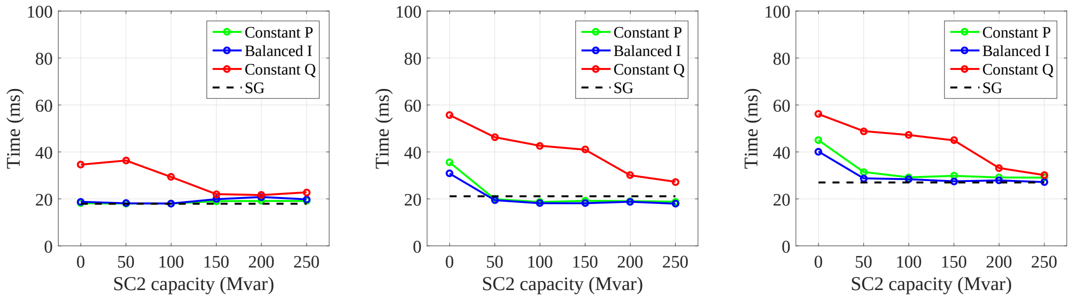

(a) A-g fault at 25% (b) A-g fault at 50% (c) A-g fault at 75%

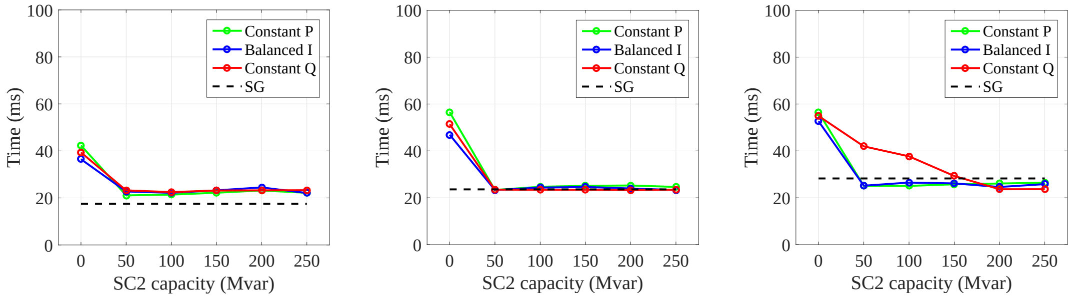

(d) A-B-g fault at 25% (e) A-B-g fault at 50% (f) A-B-g fault at 75%

Figure 3.28: Average response time of the distance relay for Case 4

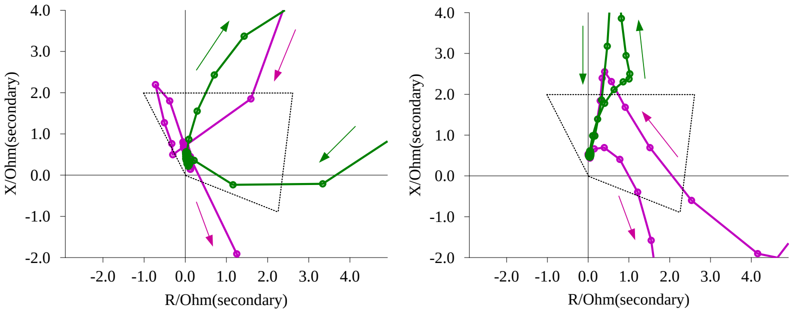

(a) A-g, B-g elements (no SC1) (b) A-g, B-g elements (50 Mvar SC1)

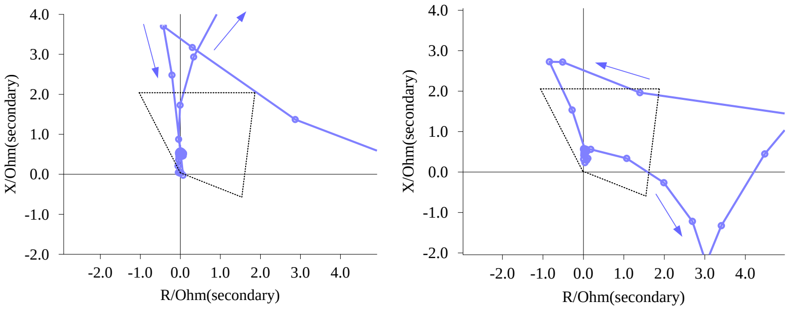

(c) A-B element (no SC1) (d) A-B element (50 Mvar SC1)

Figure 3.29: Impedance plane for the A-B-g fault at 25% of line 6-2 in Case 4

faults, the limited short circuit current and the control strategy of VSC1 will have less impact on the relay performances. In this case, a 300 Ω grounding resistance is added to the grounding branch of the VSC1 interface transformer to investigate the relay performances when there is a lack of zero-sequence current under A-g and A-B-g faults.

Figure 3.28 summarizes the average response time of the relay in Case 4. When SC1 is disconnected from the grid (0 Mvar), the response time of the relay increases if comparing Fig. 3.28(a)–(c) to Fig. 3.26(a)–(c) or comparing Fig. 3.28(d)–(f) to Fig. 3.26(g)–(i). When SC1 is re-connected to the system, the response time will be brought back for constant active power control and balanced current control. This is because the step-up transformer of SC1 also provides a path for the zero-sequence current to flow. Due to the current cancellation problem, constant reactive power control still has the worst performances. Figure 3.29 shows the impedance plane of the A-g, B-g and A-B elements for an A-B-g fault at 25% of line 6–2 without SC1 [see Fig. 3.29(a) and (c)] and with a 50 Mvar SC1 [see Fig. 3.29(b) and (d)]. It can be observed that, with limited zero-sequence current, the locus exhibits more transients in Fig. 3.29(a) than Fig. 3.29(b).

Based on the test results in Fig. 3.26 and Fig. 3.28, there is a correlation between the relay response time, the control strategy of VSC1, and the capacity of SC1. For the test system in Fig. 3.16, a 100 Mvar SC1 at bus 6 is a good choice when using constant active power control as the improvement in the speed starts to saturate if the capacity of SC1 further increases. Similarly, a 150 Mvar SC1 is an optimal choice when VSC1 uses balanced current control. However, for line-to-line faults, balanced current control does not perform as well as constant active power control [see Fig. 3.26(e)–(f)]. For constant reactive power control, it requires a synchronous condenser of at least 200 Mvar to achieve similar performances as the other two control strategies.

***Case 5**: Comparisons with other types of compensation*
In this case, another two types of compensation are considered for the system in Fig. 3.16. This is to illustrate the effect through a scenario instead of stemming from the reality.

Series compensation: with SC1 disconnected, a capacitor is connected in series with line 6–2 at the terminal near bus 6. The compensation factor is 40%. It is denoted as "SeriComp" in the following analysis.

STATCOM: with SC1 disconnected, a STATCOM rated at 250 Mvar is connected at bus 6. Typically, STATCOMs use current-controlled VSC technology. The different VSC dual-sequence current control strategies and converter peak current limit methods also apply to a STATCOM under unbalanced faults [162]. It is assumed that the STATCOM deploys constant active power control strategy and the reactive current injection is limited to 1 p.u. in each phase. Its reactive power reference is generated using the same rule as VSC1.

For an A-B fault at different locations of line 6–2, Fig. 3.30 compares the average response time of the relay with different compensation methods, where "NoComp" corresponds to Case 2 (without series/shunt compensation) and "SC" refers to Case 3 (with a 150 Mvar SC1 connected at bus 6). With either series compensation or STATCOM, the response time has no notable improvement compared to "NoComp" and the relay still fails to trip when VSC1 uses constant reactive power control. Even though the series-connected capacitor helps reduce the line impedance, the short circuit current is still solely provided by VSC1, having limited amplitudes and affected by the control strategies of VSC1 as Case 2. Correspondingly, Fig. 3.31(a) presents the measured impedance locus for an A-B fault at 75% of Line 6–2 when VSC1 deploys constant reactive power control.

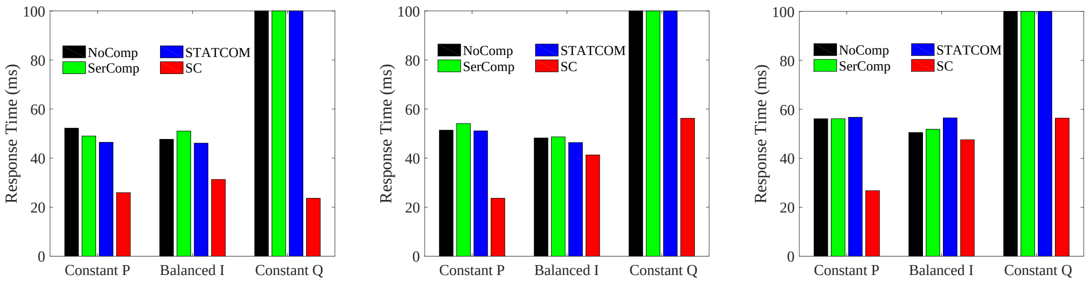

(a) A-B fault at 25%

(b) A-B fault at 50%

(c) A-B fault at 75%

Figure 3.30: Average response time of the distance relay with different compensation methods

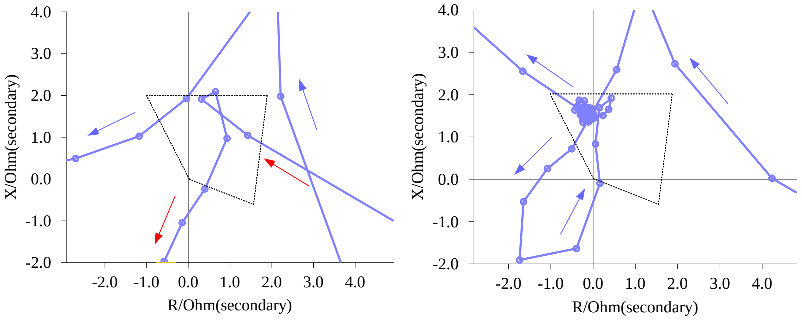

(a) With series compensation

(b) With STATCOM

Figure 3.31: Impedance plane of the A-B element for the A-B fault at 75% with series compensation or STATCOM

The locus still exhibits unfavourable features. When the STATCOM is shunt-connected at bus 6, the short circuit current is jointly provided by VSC1 and the STATCOM. Since both of them are current-controlled devices and have limited overload capability, the combined short circuit current is still low and does not notably help the relay operation. With constant reactive power control used in VSC1, the combined short circuit current of VSC1 and the STATCOM is not high enough to activate the relay impedance calculation and leads to a refuse-to-trip failure. In contrast, the application of the SC helps reduce the response time, and the relay successfully trips even when VSC1 uses constant reactive power control.

***Case 6**: Tests on DK1 system with different topologies*

In this case, the HIL tests on distance relay are further performed in the DK1 system. Figure 3.32 shows the examined area and the rest of the DK1 system is not shown here for brevity. In order to generate a future case, three SGs (ESVB3, NJVB3, and SKVB3) are assumed to be phased out and disconnected from the system. The tests are in regard to the distance relay located on L1 near bus EDR. It is set to protect 90% of L1. Table 3.4 lists five different topologies that will be examined. As an example, topology 2 (T2) represents the topology where L1 and SCEDR are present, while L2 and L3 are disconnected. It is assumed that the VSC-HVDC station connected at EDR has the possibility of using one of the three control strategies (constant active power, balanced current, and constant reactive power control).

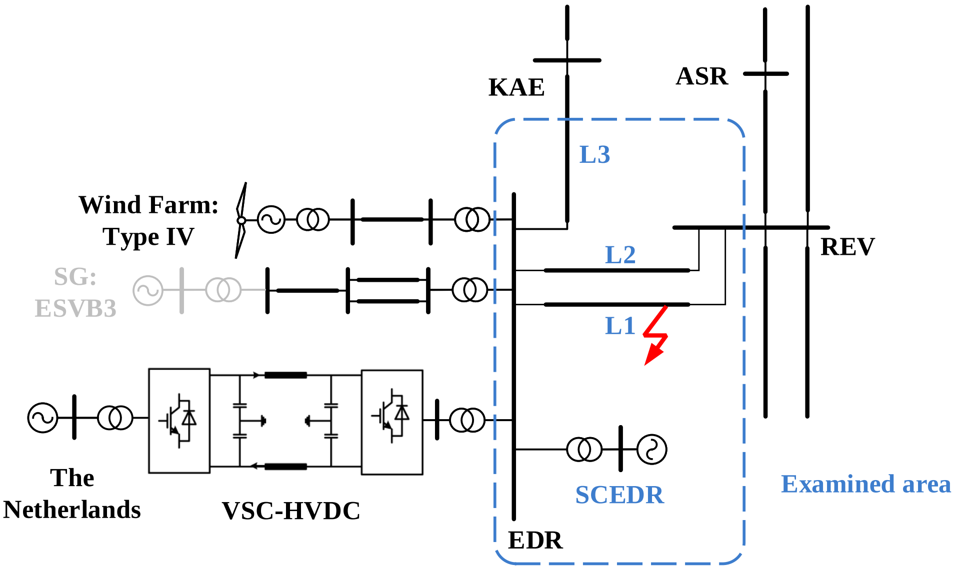

Figure 3.32: Single-line diagram of the western Danish power system around EDR

Table 3.4: Pre-fault topologies of the examined area

	Component			
Topology	L1	L2	L3	SCEDR
T1	Y	N	N	N
T2	Y	N	N	Y
T3	Y	N	Y	N
T4	Y	N	Y	Y
T5	Y	Y	Y	N

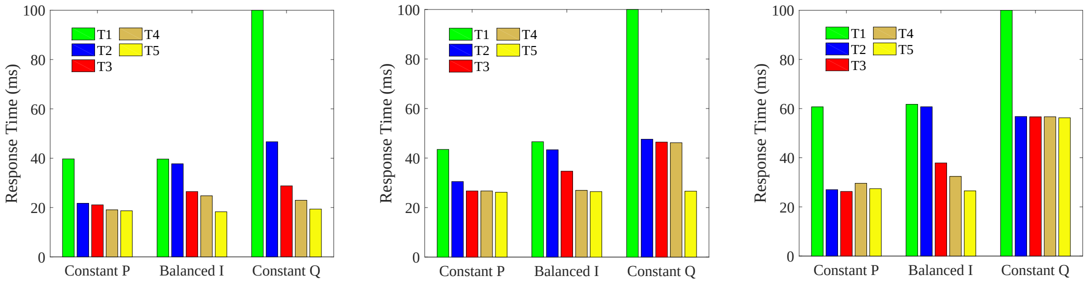

(a) 25 % of L1 (b) 50 % of L1 (c) 75 % of L1

Figure 3.33: Average response time of the distance relay for the A-B fault on L1 under different pre-fault topologies

Figure 3.33 summarizes the average response time of the relay for an A-B fault at different locations of L1. For T1, the short circuit current seen by the relay is mainly provided by the VSC and thus the relay has the slowest response. It fails to trip when the VSC deploys constant reactive power control. Figure 3.34(a)–(b) shows the impedance plane of the A-B element for A-B faults at 75% of L1. The locus in Fig. 18(a) still has discontinuous features so that the relay does not trip. For T2-T5, apart from the short circuit current from the VSC, there is additional short circuit current from SCDER, L2 or L3. This leads to fewer transients in the measured locus [see Fig. 3.34(c)–(d) and Fig. 3.34(b)], and helps to improve the relay speed. Regarding the relay performance with different VSC control strategies, constant active power control has slightly better performances than balanced current control, while constant reactive power control has the longest response time.

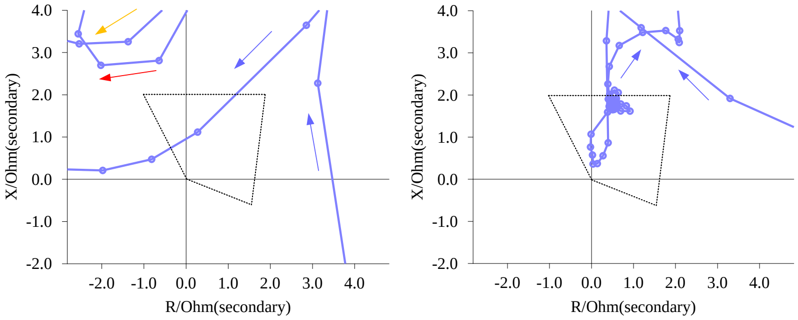

(a) T1, constant reactive power

(b) T1, balanced current

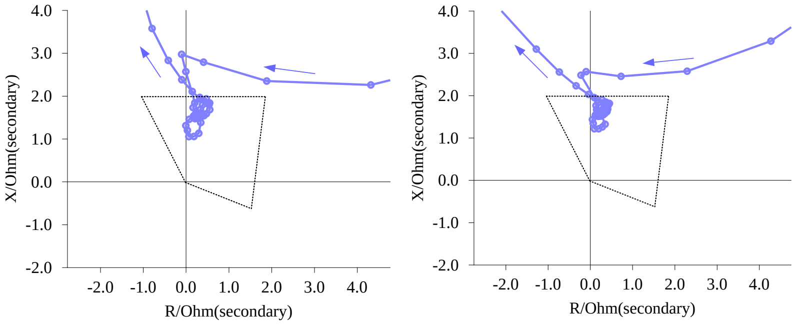

(c) T2, balanced current

(d) T5, balanced current

Figure 3.34: Impedance plane of the A-B element for the A-B fault at 75% of L1

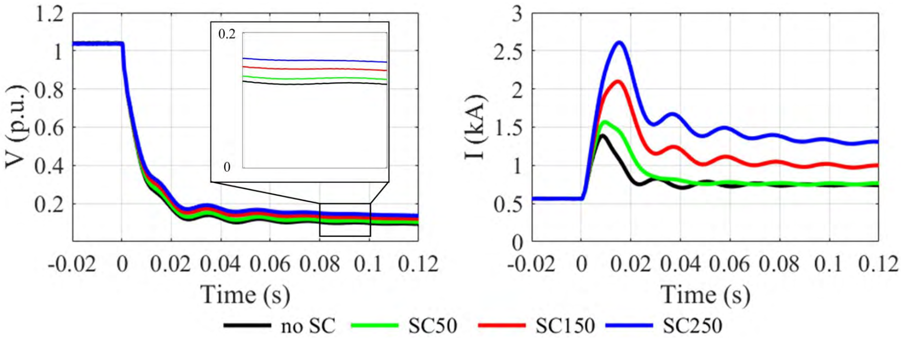

Figure 3.35: PCC voltage and short circuit current under three-phase balanced faults

3.3.2 PCC voltage

Regarding a three-phase balanced fault at 50% of line 6-2, Fig. 3.35 compares the RMS value of the PCC voltage and the short circuit current measured at point M with respect to different capacities of SC1. It can be seen that an SC1 with higher capacity helps increases the retained voltage during the fault by contributing more short circuit current.

Regarding a grid unbalanced fault, VSC1 can have different short circuit response depending on its control strategy. Here the capacity of SC1 is fixed and the flexible scalars of VSC1 are selected from Table 3.3. Figure 3.36–3.39 compares the sequence voltages at bus 6 and the sequence currents measured at point M for an A-B fault or an A-g fault at 50% of line 6-2. The capacity of SC1 is fixed at 250 Mvar, and the flexible scalars of FOPC and FPNSPC are varied as different scenarios.

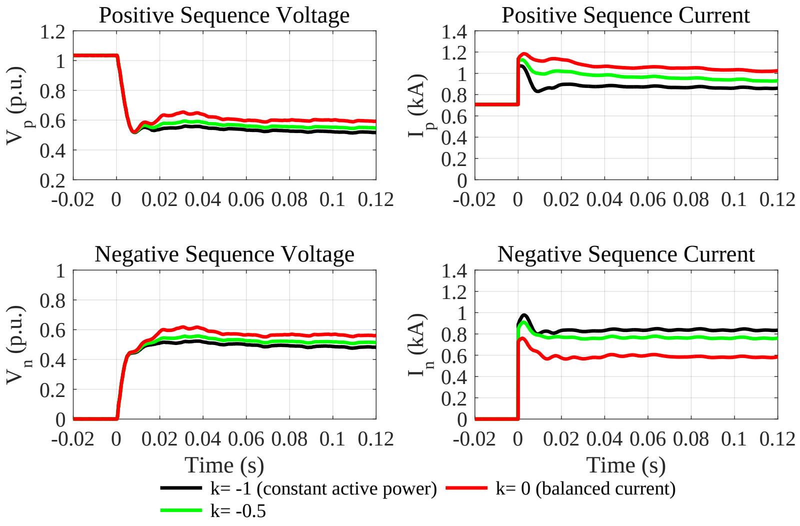

(a) FOPC with $-1 \leq k \leq 0$

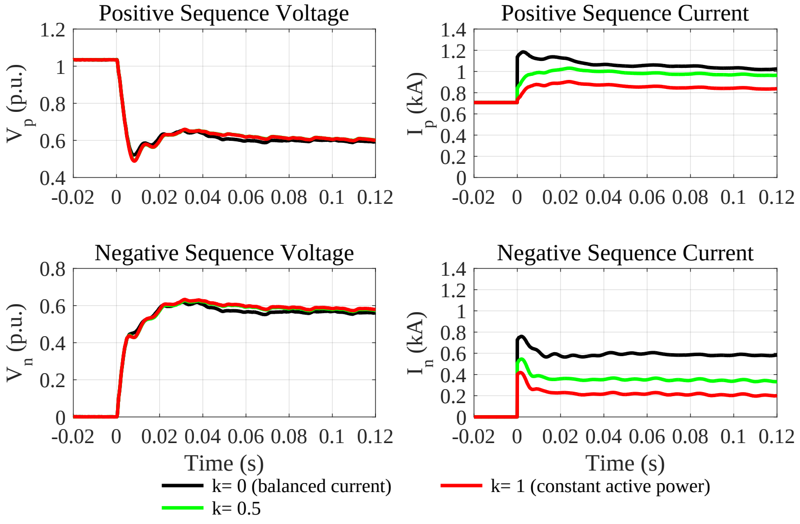

(b) FOPC with $0 \leq k \leq 1$

Figure 3.36: Sequence voltages at the PCC and combined short circuit currents under A-B fault when VSC1 deploys FOPC

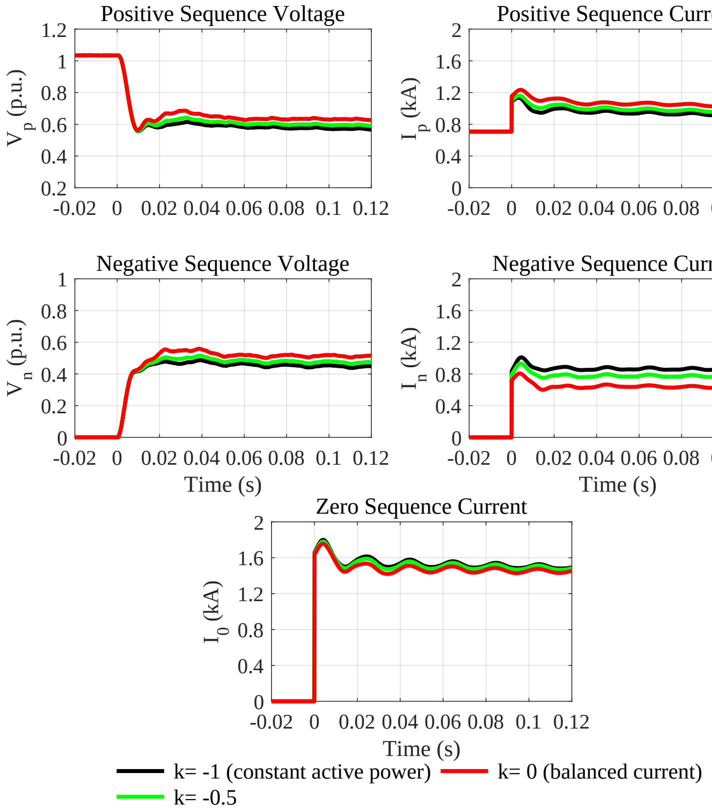

(a) FOPC with $-1 \leq k \leq 0$

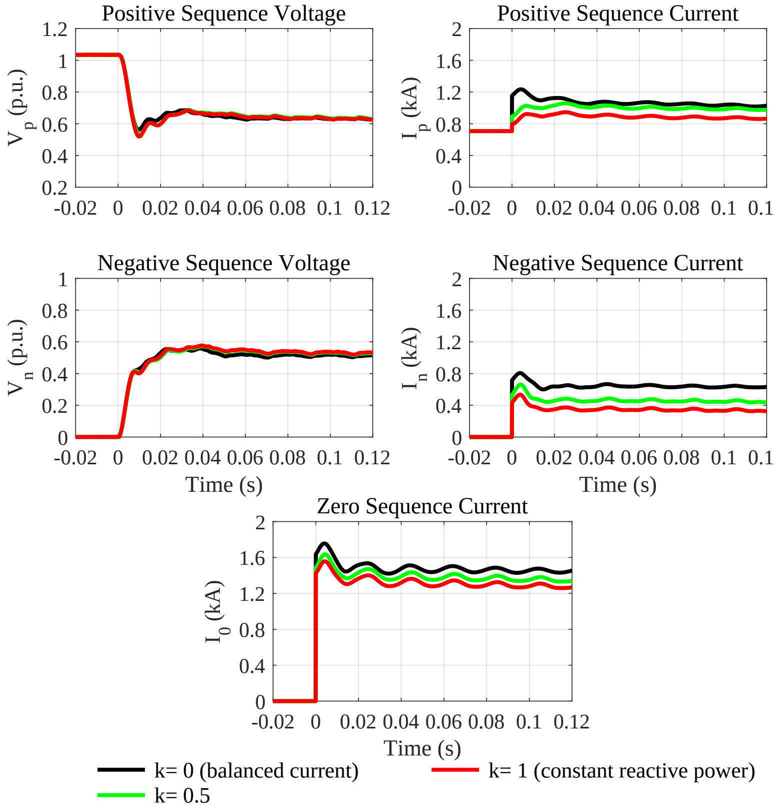

(b) FOPC with $0 \leq k \leq 1$

Figure 3.37: Sequence voltages at the PCC and combined short circuit currents under A-g fault when VSC1 deploys FOPC

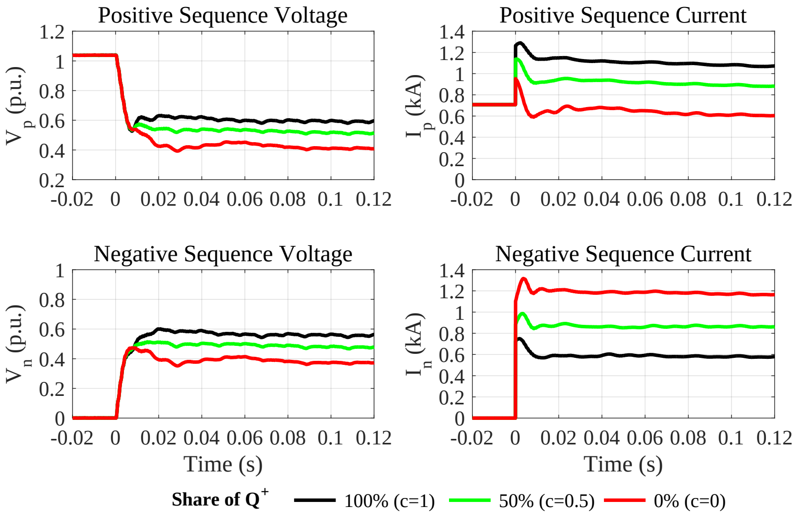

(a) FPNSPC with $0 \leq c \leq 1$

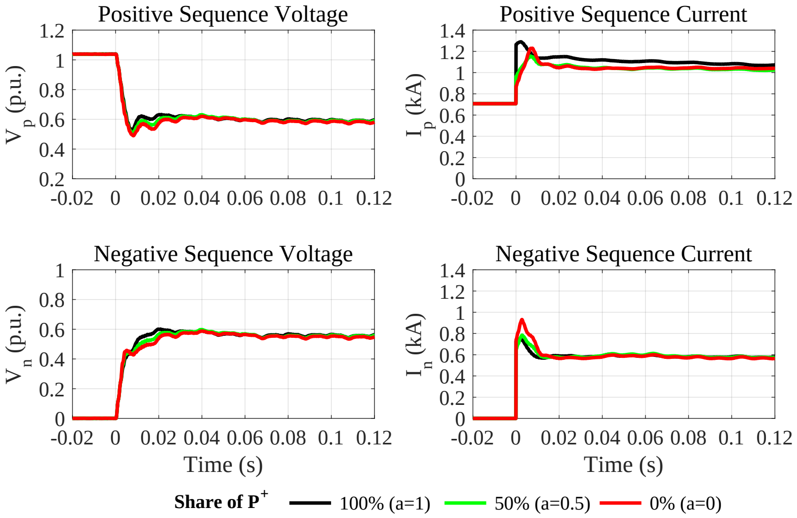

(b) FPNSPC with $0 \leq a \leq 1$

Figure 3.38: Sequence voltages at the PCC and combined short circuit currents under A-B fault when VSC1 deploys FPNSPC

It can be seen from Fig. 3.36(a) and Fig. 3.37(a) that, with the control strategy changing from constant active power control ($k = -1$) towards balanced current control ($k = 0$), both positive- and negative-sequence voltages increase. The positive-sequence current grows while the negative-sequence current reduces. In contrast, with the control strategy changing from balanced current to constant reactive power control ($k = 1$), both positive- and negative-sequence currents decrease in Fig. 3.36(b) and Fig. 3.37(b). This is the combined effect of the converter peak current limit and the current cancellation problem. Based on the voltage concept presented in Section 2.4.3, the increase of positive-sequence reactive current helps to improve positive-sequence voltage, and the increase of negative-sequence reactive current helps attenuate voltage unbalance. However, the voltage unbalance mitigation is also at the cost of reducing positive-sequence voltage. As a result, simultaneous increasing or decreasing the positive- and negative-sequence currents [see Fig. 3.36(b) and Fig. 3.37(b)] have less effect on the sequence voltages than the opposite trend [see Fig.

3.36(a) and Fig. 3.37(a)].

As shown in Fig. 3.38(a) and Fig. 3.39(a), with the share of Q^+ changing from 100% towards 0%, both positive- and negative-sequence voltages reduce. The changes in the positive- and negative-sequence currents have an opposite trend. For the inductive system in Fig. 3.16, the PCC voltage is mainly regulated through reactive current. Therefore, the PCC voltages in Fig. 3.38(b) and Fig. 3.39(b) almost remain the same with different values of a (the share of P^+).

Most grid codes have not imposed specific requirements on VSCs regarding the negative-sequence short circuit current injection. Under grid unbalanced faults, VSC-based sources are typically designed to provide short circuit current only in positive-sequence [63, 64]. Since there is no path for the negative-sequence current, VSCs behave as open circuits in the negative-sequence network. With the negative-sequence voltage not attenuated, this may lead to over-voltage problems in healthy phases. However, by moving the VSC control strategy from balanced current control to constant active power control with FOPC, or choosing c between 0 and 1 with FPNSPC, VSCs will have the potential to help attenuate negative-sequence voltages under grid unbalanced faults. The exact values of k or c can be generated using other control logic based on the needs of the grid.

Next, the impact of different SC1 capacities on the PCC voltages is investigated. With the control strategy of VSC1 fixed, the capacity of SC1 will be varied from 0 (disconnected from the grid) to 250 Mvar. Figure 3.40 presents the sequence voltages of bus 6 and the sequence currents measured at point M for an A-B or an A-g fault at 50% of line 6-2. The increase in the SC1 capacity leads to the increase in both positive- and negative-sequence short circuit current. For grid unbalanced faults, synchronous condensers inherently inject positive-sequence short circuit current and provide a path for negative-sequence short circuit current to flow. The simultaneous increase of the short circuit current in both sequences has less effect on the PCC voltages. As a result, compared to Fig. 3.38(a) and Fig. 3.39(a), SC1 does not alter the sequence voltages so much in Fig. 3.40. This indicates that the application of SC1 at the PCC has limited impact on the sequence voltages for grid unbalanced faults. SCs have a natural control over the sequence voltages mainly decided by their properties, while VSCs can actively participate in the control of sequence voltages through injecting positive- and negative-sequence reactive powers.

The voltage support from SCs under grid unbalanced faults is different from that under three-phase balanced faults. For three-phase balanced faults, only positive-sequence components are present and thus an increase in the positive-sequence reactive current is able to help boost the retained voltage. However, for unbalanced faults, there is a coupling between the positive- and negative-sequence networks and the voltage support depends on the combined effect of the positive- and negative-sequence reactive current. Based on the investigation, it can be observed that the dual-sequence current controls of VSCs have more effect on the PCC voltage than an SC for unbalanced faults.

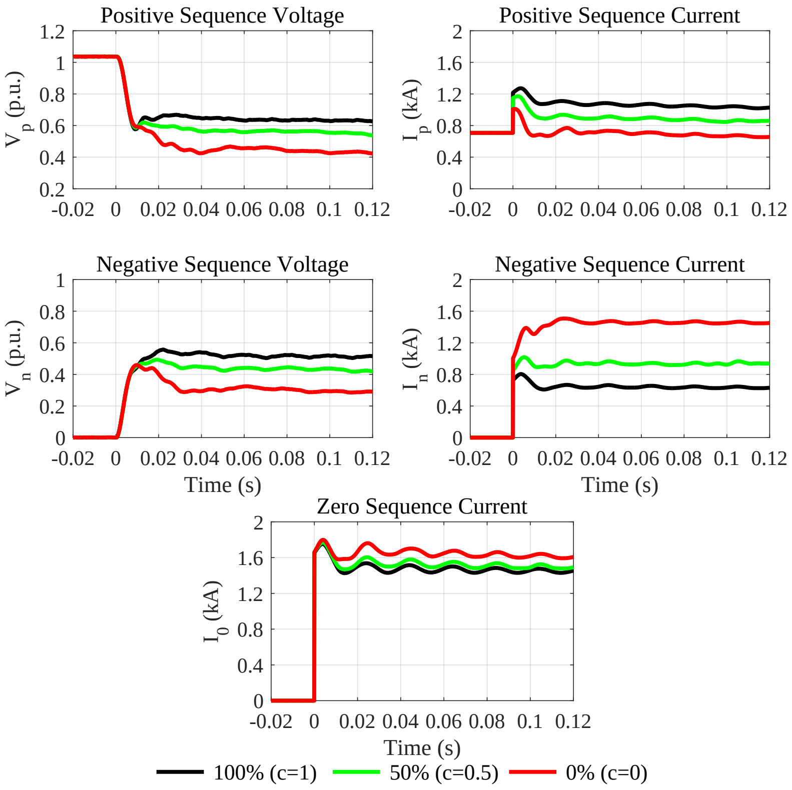

(a) FPNSPC with $0 \leq c \leq 1$

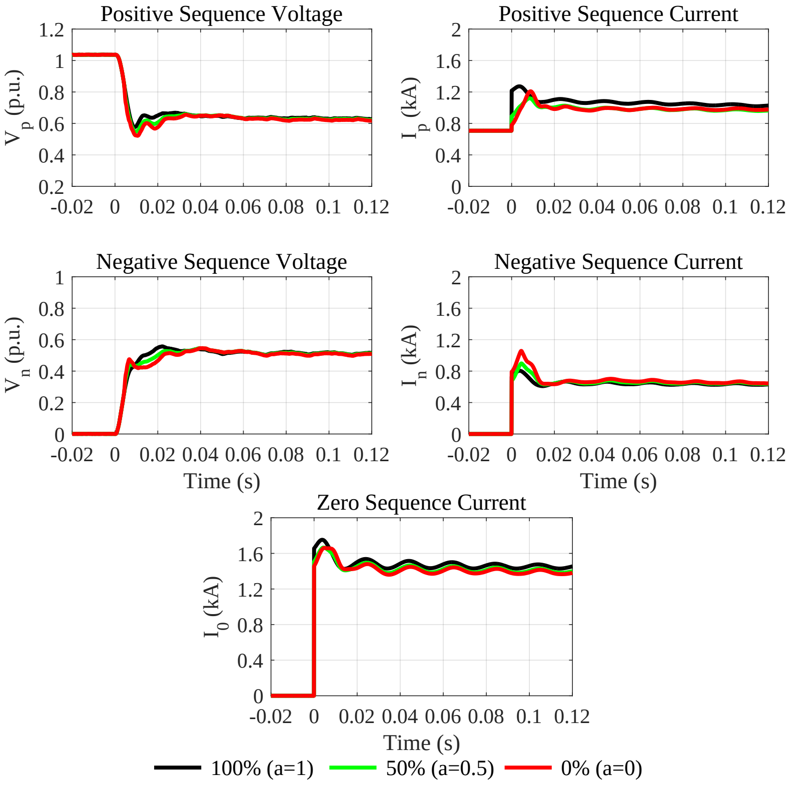

(b) FPNSPC with $0 \leq a \leq 1$

Figure 3.39: Sequence voltages at the PCC and combined short circuit currents under A-g fault when VSC1 deploys FPNSPC

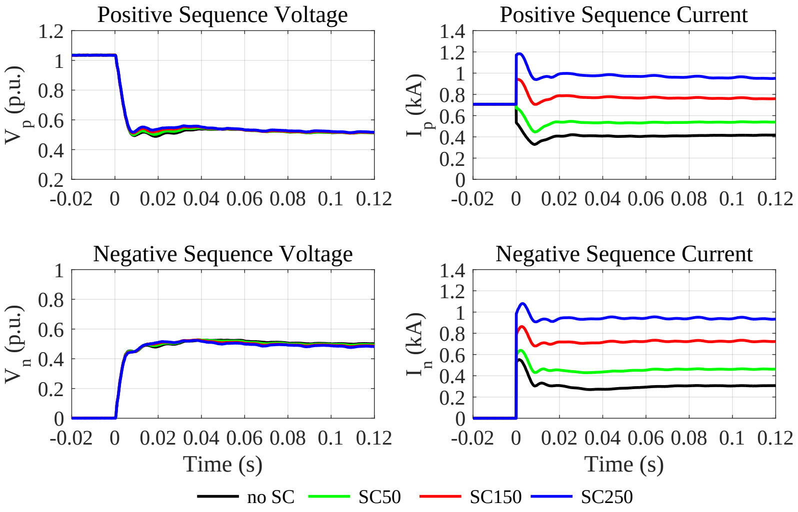

(a) A-B fault, FOPC with $k = 0$ (constant active power)

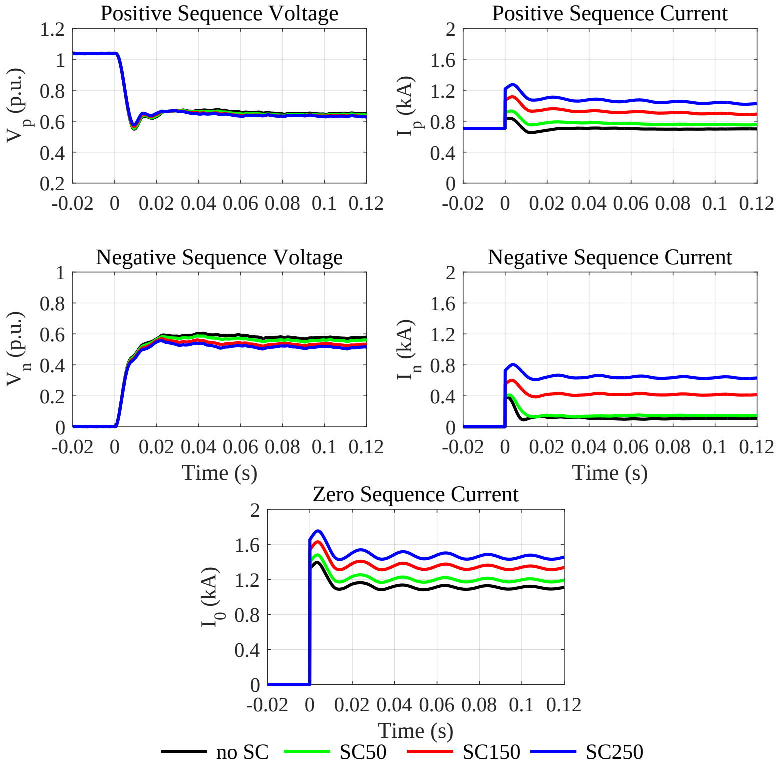

(b) A-g fault, FPNSPC with $k_p = k_q = 1$ (100% P^+ and Q^+)

Figure 3.40: Sequence voltages at the PCC and combined short circuit currents with different capacities of SC1

3.3.3 DC-side voltage

With the capacity of SC1 fixed, the effect of the control strategies on the DC-side voltage is investigated by varying the flexible scalars of VSC1. Figure 3.41 compares the DC-side voltages and the output active powers of VSC1 for an A-B fault at 50% of line 6-2. Due to the converter peak current limit and the reactive power priority, there is a curtailment in the active power from VSC1 under the faults, which causes the DC-side voltage to increase. It can be seen from Fig. 3.41(a) that, with the control strategy moving from constant active power control to constant reactive power control, there is an increase in the amplitudes of the DC-side voltage oscillations, as well as output active power oscillations.

The oscillations in Fig. 3.41(b) do not change notably with a variation on the share of P^+ when using FPNSPC. In contrast, with the share of Q^+ changing from 100% to 0% in Fig. 3.41(c), the amplitudes of the active power oscillations reduces first and then increases. The same trend also applies to the DC-side voltage oscillations. Therefore, a proper injection of positive Q^- helps reduce the DC-side voltage oscillations, while the impact from P^- is limited. In other words, the DC-side voltage oscillations can be reduced by moving the control strategy from balance current control to constant active power control with FOPC or choosing the share of Q^- between 100% ($c = 1$) to 50% ($c = 0.5$) with FPNSPC.

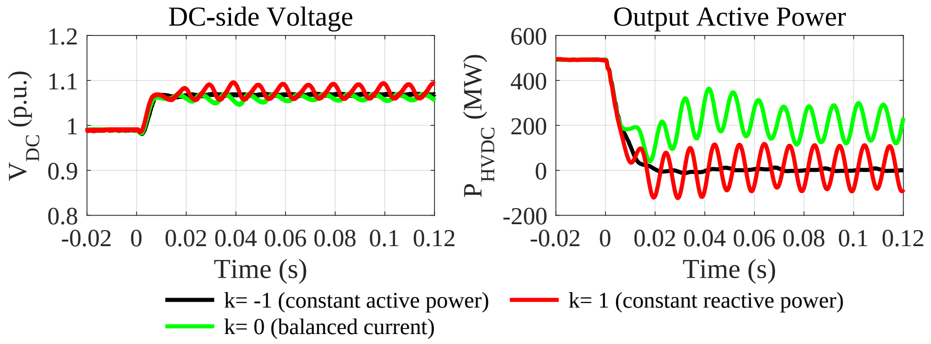

(a) A-B fault, FOPC with $-1 \leq k \leq 1$

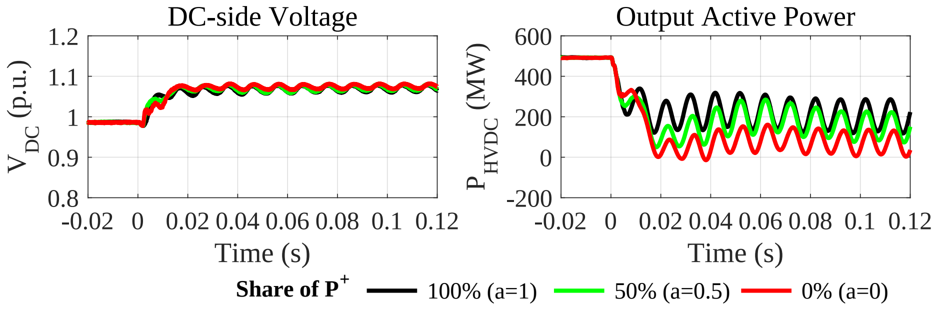

(b) A-B fault, FPNSPC with $a = 1$ and $0 \leq c \leq 1$

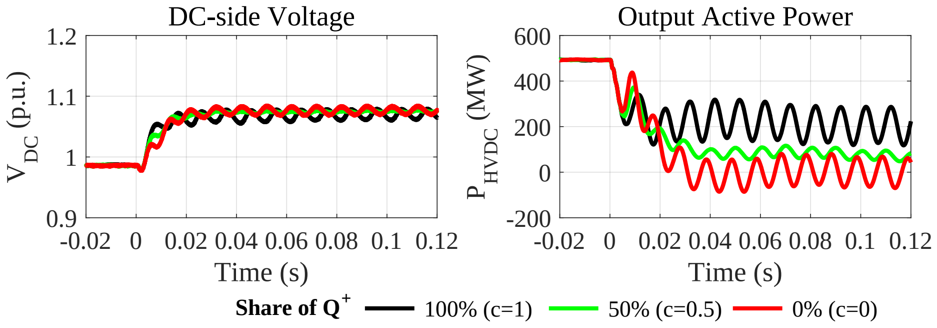

(c) A-B fault, FPNSPC with $c = 1$ and $0 \leq a \leq 1$

Figure 3.41: DC-side voltages and output active powers of VSC1 with different control strategies

Secondly, with the control strategy of VSC1 fixed, the impact of SCs on the DC-side voltage is investigated by varying the capacity of SC1. Figure 3.42 compares the DC-side voltages and the output active powers of VSC1 under different capacities of SC1 when VSC1 uses balanced current control. It shows that SC1 has no notable effect on the DC-side voltage under grid unbalanced faults regardless of the capacity of SC1.

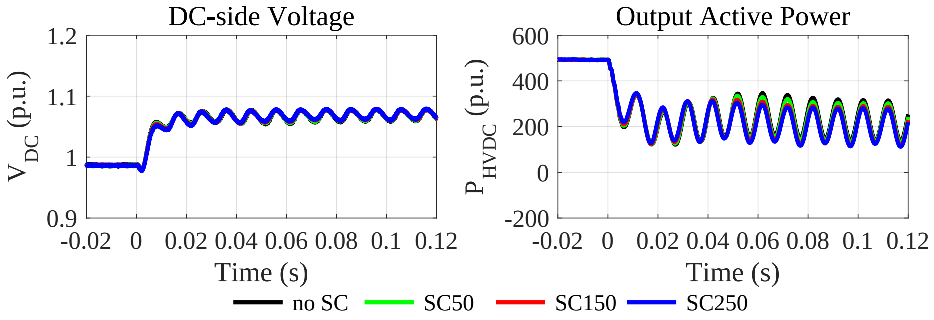

Figure 3.42: DC-side voltages and output active powers of VSC1 with different capacities of SC1

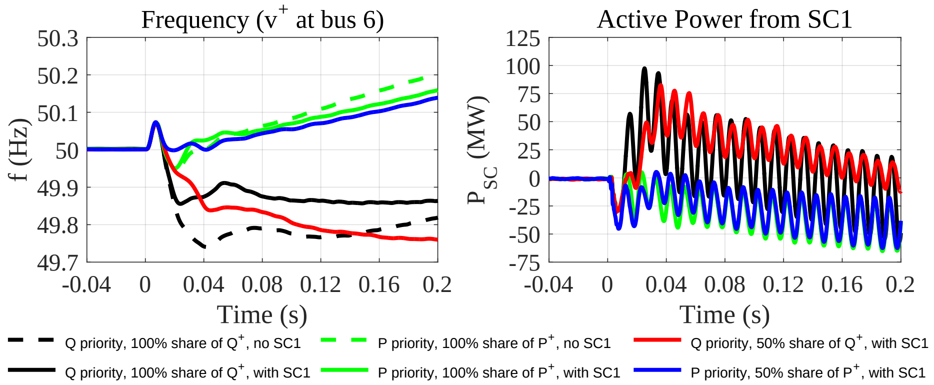

Figure 3.43: Frequency responses at the PCC and active powers of SC1 with different control strategies

3.3.4 System frequency

Here the combined effect of VSC1 control strategies and SC1 on the system frequency responses under unbalanced faults is investigated. With SC1 disconnected from the grid, the measured frequency at bus 6 (using the positive-sequence voltage) is plotted with dashed lines in Fig. 3.43 for an A-B fault at 50% of line 6-2. As the base cases, VSC1 is controlled to provide only positive-sequence short circuit powers. The green-dashed curve represents the case of active power priority while the black-dashed curve is for the case of reactive power priority. Then, a 250 Mvar SC1 is connected to the grid and corresponding measured frequency subject to the same fault is plotted in black- and green-solid curves in Fig. 3.43 for both cases. The synchronous condenser, as a rotating machine, provides inertia for the system so that there is less frequency deviation from 50 Hz when compared to the base cases. With the same SC1, VSC1 is controlled either to provide 50% Q^+ ($c = 0.5$) with Q priority, or to provide 50% P^+ ($a = 0.5$) with P priority. The corresponding measured frequency is plotted with the red- and blue-solid curves respectively in Fig. 3.43.

Figure 2.23(c) illustrates the relationship between FOPC and FPNSPC in an unified manner. The point $(a, c) = (1, 1)$ represents that VSC1 provides only positive-sequence short circuit power (P^+

and Q^+). As long as the point moves away from (1,1), there will be negative-sequence current flowing through the converter. The further (a, c) is away from (1,1), the more negative-sequence current flows through the converter, which also means the more active power has to be curtailed in order not to violate the converter peak current limit. In this sense, the impact of the VSC1 control strategy on the system frequency response can be considered as a question of how much active power is curtailed during the fault.

When there is under-frequency during the unbalanced fault, it is not recommended to have $a < 1$ because of two reasons. One is that the injection of positive P^- occupies the converter current margin, leading to more active power to be curtailed. The second is that P^- neither contributes to the voltage support for an inductive grid nor helps reduce the DC-side voltage oscillations. On the other hand, when there is over-frequency during unbalanced faults, the injection of P^- and Q^- in both directions can help reduce the frequency deviation because of the active power curtailment.

Table 3.5: Summary of the investigation

Aspects	VSC dual-sequence current control	Synchronous condensers
Short circuit current	Avoid $k > 0$ with FOPC (can raise current cancellation problem);	Help bring the phases and amplitudes of the short circuit currents close to those from synchronous sources;
PCC voltage	(1) Affected by Q^+ and Q^- rather than P^+ and P^- for inductive grids; (2) The injection of positive Q^- ($k < 0$ with FOPC or $c < 1$ with FPNSPC) helps attenuate negative-sequence voltage;	Natural control on sequence-voltages;
DC-side voltage	(1) The injection of positive Q^- ($k < 0$ with FOPC or $0.5 < c < 1$ with FPNSPC) helps reduce DC-side voltage oscillations; (2) P^- has no notable effect	No notable effect;
Frequency response	(1) Affected by how much active power is curtailed; (2) For under-frequency, avoid the injection of positive P^- ($k > 0$ with FOPC or $a < 1$ with FPNSPC); (3) For over-frequency, the injection of P^- and Q^- in both directions helps counter frequency deviation;	Provide inertia for the system;

3.4 Conclusion

This chapter introduced the modeling work on the western Danish power system (DK1) in RTDS, which includes detailed LCC-HVDC and VSC-HVDC systems, Type-III and Type-IV wind farms, other electrical components, and the corresponding control systems. The model was validated by comparing its short circuit response with real fault data. The retained grid voltage and the short circuit current in simulations agree with the fault record provided by the Danish TSO Energinet.

A hardware-in-the-loop (HIL) test platform was created integrating the RTDS model and protective relays into a closed loop. A bi-directional communication between RTDS and an external program MATLAB was also established. It enables to automate the relay testing and to perform a set of simulations without the need for manual controls. The simulation results under different scenarios can be automatically transferred to and saved in MATLAB for further comparisons.

With the HIL test platform, a commercial distance relay was tested under grid unbalanced faults considering the presence of a VSC-HVDC system and its dual-sequence current controls. When active current injection is prioritized, the distance relay exhibited significant overreach problems. In contrast, both underreach and overreach problems arose when the priority was given to the reactive current. This uncertainty not only depends on the share of the injected positive-sequence reactive power, but also on the converter peak current limit level, the fault resistance, and the pre-fault power flow conditions. The test results revealed that the measuring error from the distance relay caused by the fault resistance can be enlarged in a future low inertia power system. The impact of the pre-fault power flow conditions on the reach also disagreed with the common knowledge for a conventional power system. These indeterminacies can make it difficult to do the relay settings and can jeopardize the effectiveness of the conventional countermeasures. Therefore, the non-pilot distance protection using the classic method may not be sufficient for serving as the primary protection of transmission lines. Protection studies should not ignore the converter peak current limit and the power electronics control, especially the dual-sequence current controls.

The interaction between synchronous condensers and VSC-based sources was investigated by equipping a synchronous condenser at the PCC of a VSC-HVDC system. The different dual-sequence current control strategies of VSCs can raise problems such as non-conventional characteristics of the short circuit current, a lack of negative-sequence reactive current, DC-side voltage oscillations and excess active power curtailment under fault conditions. The application of a synchronous condenser at the PCC helps to increase the short circuit level and bring the phases of the combined short circuit current close to that from a synchronous source. By providing a path for the negative-sequence current to flow, synchronous condensers help to control sequence voltages naturally. As a rotating device, it can provide inertia for the system to counter the frequency deviation. The application of a synchronous condenser at the PCC is able to help mitigate the disadvantages of certain control strategies. For example, if the DC-side voltage oscillations or over-voltage in the healthy phases is a concern, the VSC can be controlled to inject a certain amount of positive Q^-. Even though this can lead to more active power from VSC being curtailed, the existence of the synchronous condenser provides inertia for the system to counter the frequency deviation. Table 3.5 provides a summary of the investigation and suggestions on selecting the dual-sequence current control strategies when incorporating a synchronous condenser under unbalanced faults.

The identified current cancellation problem was further investigated through HIL tests on distance protection with various systems and scenarios. The test results showed that the reliability and speed of distance protection can be jeopardized because of the low short circuit current level and the non-conventional characteristics of the short circuit current, especially when VSCs are the main sources of the short circuit current. The application of a synchronous condenser at the PCC can help improve the relay performances, but this also relies on the dual-sequence current controls of the VSCs. It confirmed that FOPC with $k > 0$, especially constant reactive power control, should not be used together with distance protection. The associated current cancellation problem can cause the distance relay malfunction or can even reduce the available short circuit current. With the incorporation of a synchronous condenser at the PCC, constant active power control can be considered for the VSCs as its use requires a smaller synchronous condenser than balanced current control and constant reactive power control to retain distance relay performances.

CHAPTER 4

Static Fault Analysis with the Presence of Voltage Source Converters

This chapter presents the development and the application of a static fault analysis method considering the dual-sequence short circuit current from multiple VSCs. Firstly, a static fault analysis method is developed taking the short circuit current contributions from VSCs into account. The method is able to integrate the VSC dual-sequence current controls and is verified through real-time simulations. Then, the fault analysis method is used to help explain a phenomenon that the system may not have a stable response under unbalanced faults due to the negative-sequence reactive power injection from the VSCs. Finally, the optimal allocation of SCs for improving the system SCRs is formulated into an optimization problem minimizing the total cost, where the developed analytical fault analysis method is applied to calculate the SCRs at the converter terminals. The allocation results indicate that there is a need of more SCs for the future DK1 system. The main results of this chapter were documented in [**Pub. C**] and [**Pub. G**].

4.1 Overview

In order to represent a VSC mathematically, the work in [163] proposes a sequence-component-based VSC model. Depending on the operation mode, the converter is either treated as an ideal voltage source or as a constant power source. The model is mainly for power flow analysis. It is not suitable for fault analysis considering the operation principles of VSCs under grid fault conditions. The work in [66] proposes the concept of fault current distribution-coefficients, which represents the fault current contribution of a specific VSC seen from the fault location. The method assumes constant grid voltages under fault conditions and hence it is solely used for small-scale grid-connected microgrids. In [67, 68, 69, 70], VSCs are considered as current sources in the phasor domain and the fault analysis is conducted by performing the power flow analysis of the faulted network using Gauss-Siedel or Newton-Raphson algorithms. These methods are developed based on the assumption that the main grid can be considered as an infinite bus whose voltage does not drop during a fault and thus the main grid can be identified as the slack bus. Therefore, power flow based methods are solely used in distribution networks where the above-mentioned assumption is valid. However, for transmission networks, such kind of infinite buses does not really exist and the slack bus for power flow analysis cannot be identified.

In addition, these power flow based methods are circumscribed for unbalanced fault analysis. In [69, 70], it is assumed that the VSCs do not contribute any negative-sequence short circuit current under unbalanced faults. As a result, the passive negative- and zero-sequence networks can be simply modeled as an equivalent impedance shunt-connected at the fault location. The same assumption is also made in [71], where VSCs are treated as constant current sources in the positive-sequence networks, and in [72, 73], where the positive-sequence bus impedance matrix is used for fault analysis. However, as long as VSCs are controlled to provide negative-sequence short circuit current, the assumption is not valid anymore and the above methods become insufficient.

4.2 Static fault analysis method

The conventional fault analysis method [60, 103] for three-phase balanced faults sees that, the voltage change caused by the fault is equivalent to the voltage change caused by a voltage source (with the pre-fault voltage level) at the fault location if all other voltages sources are short-circuited. The fault analysis for unbalanced cases typically connects the sequence networks according to the boundary conditions defined by the fault types. However, with the presence of VSCs, the conventional fault analysis method is not sufficient. Firstly of all, VSCs are not natural voltage sources and their short circuit current depends on the control systems. In addition, the negative-sequence current injection from VSCs under unbalanced faults turns the passive negative-sequence network into an active one. If a VSC deploys current references (2.66)–(2.67), the magnitudes and phases of the actual currents is actually a function of the grid voltage. Moreover, according to the voltage support concept presented in Section 2.4.3, the short circuit current from VSCs will also affect the grid voltage. This means the actual grid voltage is a function of the short circuit current from VSCs. The dependency of voltage and current on each other indicates that an iterative method is necessary to perform the fault analysis.

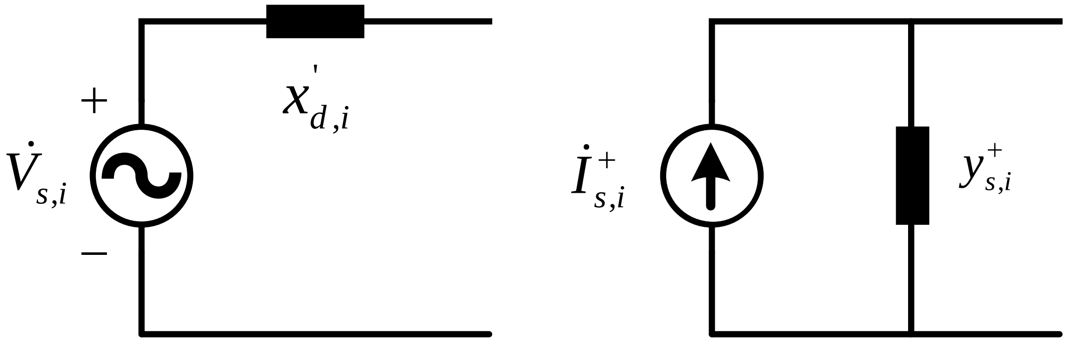

Figure 4.1: An ideal voltage source and its equivalent Norton's circuit.

4.2.1 Algorithm

The proposed fault analysis method takes the advantage of the relationship between the current injection and the bus impedance matrix. Firstly, based on Fig. 4.1, the ideal voltage source model of all SGs is converted to the equivalent Norton's circuits. $\dot{V}_{s,i}$ and $x'_{d,i}$ are the internal voltage and the direct transient reactance of the i-th SG; $\dot{I}^{+}_{s,i}$ is the current injection in the Norton's circuit, whose parallel admittance $y^{+}_{s,i}$ in the positive-sequence is:

$$\dot{I}^{+}_{s,i} = \frac{\dot{V}_{s,i}}{jx'_{d,i}} \quad y^{+}_{s,i} = \frac{1}{jx'_{d,i}} \tag{4.1}$$

Even though SGs do not inject negative-sequence current, they provides a path for the negative-sequence current to flow through its negative-sequence admittance. According to [164], this negative-sequence admittance can be approximated by:

$$y_{s,i}^{-} = \frac{2}{jx''_{d,i} + jx''_{q,i}} \tag{4.2}$$

where $x''_{d,i}$ and $x''_{q,i}$ are the direct and quadrature sub-transient reactance for the i-th SG, respectively.

Considering all the synchronous machines, transmission lines, and transformers of the system, the bus admittance matrices $\mathbf{Y}^{+}$, $\mathbf{Y}^{-}$ and $\mathbf{Y}^{0}$ for the positive-, negative- and zero-sequence networks are constructed using the conventional way. Then the corresponding bus impedance matrices $\mathbf{Z}^{+} = (\mathbf{Y}^{+})^{-1}$, $\mathbf{Z}^{-} = (\mathbf{Y}^{-})^{-1}$ and $\mathbf{Z}^{0} = (\mathbf{Y}^{0})^{-1}$ can be simply obtained.

Here it is assumed that the current references of a VSC under unbalanced faults are (2.66)–(2.67), which can be rewritten as:

$$\dot{I}_{c,j}^{+}(m) = a_j \frac{P_j^{ref}}{\left|\dot{V}_{c,j}^{+}(m-1)\right|^2} \dot{V}_{c,j}^{+}(m-1) + c_j \frac{Q_j^{ref}}{\left|\dot{V}_{c,j}^{+}(m-1)\right|^2} \dot{V}_{\perp c,j}^{+}(m-1) \tag{4.3}$$

$$\dot{I}_{c,j}^{-}(m) = (1-a_j) \frac{P_j^{ref}}{\left|\dot{V}_{c,j}^{-}(m-1)\right|^2} \dot{V}_{c,j}^{-}(m-1) + (1-c_j) \frac{Q_j^{ref}}{\left|\dot{V}_{c,j}^{-}(m-1)\right|^2} \dot{V}_{\perp c,j}^{-}(m-1) \tag{4.4}$$

where the subscript c, j represents the quantities related to the j-th converter; m denotes quantities after the m-th iteration; a_j and c_j are the flexible scalars for the j-th converter, which should be given prior to the fault analysis.

Next, the current injection vectors are constructed for both positive- and negative-sequence networks according to (4.5)–(4.6). A zero in the vector means that the associated bus does not have any current injection.

$$\mathbf{I}_{inj}^{+}(m) = \left[\dot{I}_{s,1}^{+}, ..., \dot{I}_{s,i}^{+}, \dot{I}_{c,1}^{+}(m), ..., \dot{I}_{c,j}^{+}(m), 0, ...0\right]^T \tag{4.5}$$

$$\mathbf{I}_{inj}^{-}(m) = \left[0, ...0, \dot{I}_{c,1}^{-}(m), ..., \dot{I}_{c,j}^{-}(m), 0, ...0\right]^T \tag{4.6}$$

During a fault, a system can be considered as a superposition of the normal network and the faulted network. In the normal network, there are the current injection vectors $\mathbf{I}_{inj}^{+}(m)$, $\mathbf{I}_{inj}^{-}(m)$, and the three independent bus impedance matrices $\mathbf{Z}^{+}$, $\mathbf{Z}^{-}$, $\mathbf{Z}^{0}$. As a result, the voltages of the normal network are raised by the current injections $\mathbf{I}_{inj}^{+}(m)$ and $\mathbf{I}_{inj}^{-}(m)$:

$$\mathbf{V}^{+}(m) = \mathbf{Z}^{+} \cdot \mathbf{I}_{inj}^{+}(m) \tag{4.7}$$

$$\mathbf{V}^{-}(m) = \mathbf{Z}^{-} \cdot \mathbf{I}_{inj}^{-}(m) \tag{4.8}$$

$$\mathbf{V}^{0}(m) = 0 \tag{4.9}$$

For the faulted network, different types of faults define the boundary conditions for the sequence networks: a single-phase-to-ground fault is characterized by series-connecting all three sequence networks; a two-phase fault is characterized by parallel-connecting positive- and negative-sequence networks; a two-phase-to-ground fault is characterized by parallel-connecting all three-sequence networks. Based on the voltages given by (4.7)–(4.8), the sequence voltages seen from the faulted bus f in the normal network can be identified as $\dot{V}_f^{+}(m)$ and $\dot{V}_f^{-}(m)$ after the m-th iteration. The self-impedance of the faulted bus f in each sequence network can be identified as Z_{ff}^{+}, Z_{ff}^{-} and

Z^0_{ff} from the bus impedance matrices $\mathbf{Z}^+$, $\mathbf{Z}^-$ and $\mathbf{Z}^0$. With all the related quantities identified, Fig. 4.2 illustrates the boundary conditions for the three types of unbalanced faults, where Z_f refers to the fault impedance. Compared to the conventional fault analysis method, the negative-sequence network in Fig. 4.2 becomes active. In this proposed method, the voltages $\dot{V}_f^+$ and $\dot{V}_f^-$ are considered as being raised by the current injections rather than natural voltage sources.

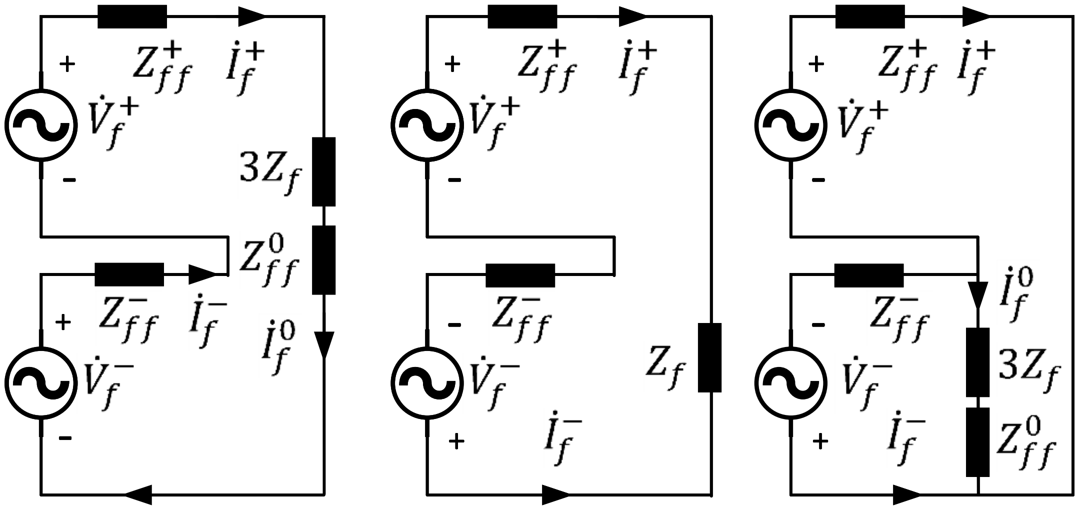

(a) Single-phase-to-ground fault (b) Two-phase fault (c) Two-phase-to-ground fault

Figure 4.2: Boundary condition of sequence networks under unbalanced faults

Then based on Fig. 4.2, the fault current after the m-th iteration for three types of unbalanced faults are:

Single-phase-to-ground fault:

$$\dot{I}^+_f(m) = \dot{I}^-_f(m) = \dot{I}^0_f(m) = \frac{\dot{V}^+_f(m) + \dot{V}^-_f(m)}{Z^+_{ff} + Z^-_{ff} + Z^0_{ff} + 3Z_f} \tag{4.10}$$

Two-phase faults:

$$\dot{I}^+_f(m) = -\dot{I}^-_f(m) = \frac{\dot{V}^+_f(m) - \dot{V}^-_f(m)}{Z^+_{ff} + Z^-_{ff} + Z_f} \tag{4.11}$$

Two-phase-to-ground faults:

$$\dot{I}^+_f(m) = \frac{\dot{V}^+_f(m) - \dot{V}^-_f(m) + \frac{Z^-_{ff}\dot{V}^-_f(m)}{Z^-_{ff}+Z^0_{ff}+3Z_f}}{Z^+_{ff} + \frac{Z^-_{ff}(Z^0_{ff}+3Z_f)}{Z^-_{ff}+Z^0_{ff}+3Z_f}} \tag{4.12}$$

$$\dot{I}^-_f(m) = \frac{\dot{V}^-_f(m) - \dot{V}^+_f(m) + Z^+_{ff}\dot{I}^+_f}{Z^-_{ff}} \tag{4.13}$$

$$\dot{I}^0_f(m) = -\dot{I}^+_f(m) - \dot{I}^-_f(m) \tag{4.14}$$

For a three-phase balanced fault, the negative- and zero-sequence networks are not involved in the fault analysis and the fault current after the m-th iteration can be simply obtained by:

$$\dot{I}^+_f(m) = \frac{\dot{V}^+_f(m)}{Z^+_{ff} + Z_f} \tag{4.15}$$

In the faulted network, the flowing of the fault current will cause the voltage to drop. As a result, the voltage change caused by the fault current in each sequence network can be expressed as:

$$\Delta \mathbf{V}^{+}(m) = \left[Z_{1f}^{+}, Z_{2f}^{+}, ..., Z_{Nf}^{+}\right]^{T} \cdot \dot{I}_{f}^{+}(m) \tag{4.16}$$

$$\Delta \mathbf{V}^{-}(m) = \left[Z_{1f}^{-}, Z_{2f}^{-}, ..., Z_{Nf}^{-}\right]^{T} \cdot \dot{I}_{f}^{-}(m) \tag{4.17}$$

$$\Delta \mathbf{V}^{0}(m) = \left[Z_{1f}^{0}, Z_{2f}^{0}, ..., Z_{Nf}^{0}\right]^{T} \cdot \dot{I}_{f}^{0}(m) \tag{4.18}$$

where N represents the total number of the buses.

Finally, with the superposition of the voltage raised by the current injections and the voltage changes caused by the fault, the sequence voltages of all buses after the m-th iteration can be obtained by:

$$\mathbf{V}^{+}(m) = \mathbf{V}^{+}(m) - \Delta \mathbf{V}^{+}(m) \tag{4.19}$$

$$\mathbf{V}^{-}(m) = \mathbf{V}^{-}(m) - \Delta \mathbf{V}^{-}(m) \tag{4.20}$$

$$\mathbf{V}^{0}(m) = -\Delta \mathbf{V}^{0}(m) \tag{4.21}$$

Based on (4.19)–(4.21), the sequence voltages of all converter terminals can be identified and will be substituted into (4.3)-(4.4). The updated current references will be compared with the previous iteration. Equation (4.3)–(4.21) represents one complete iteration and should be repeated until all the current references reach convergence. This is illustrated by the flow chart in Fig. 4.3.

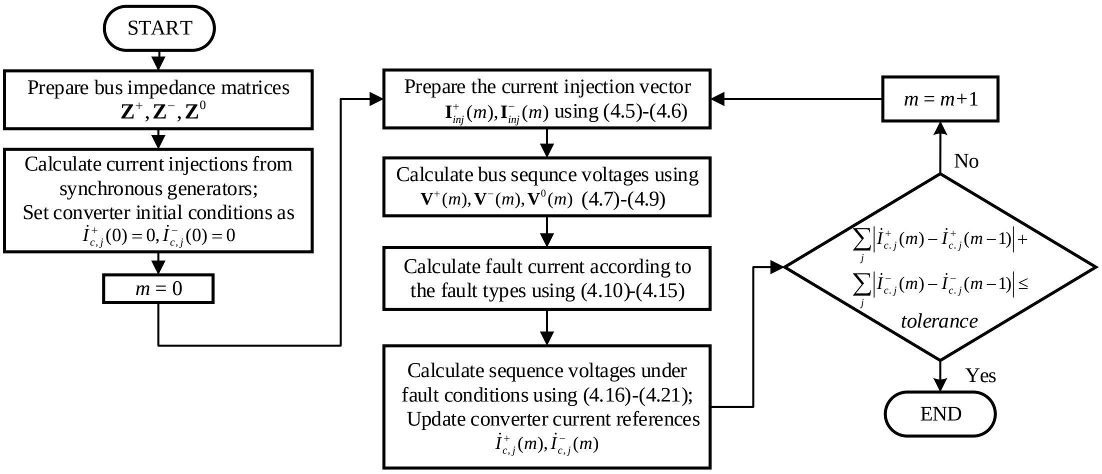

Figure 4.3: Flowchart of the proposed fault analysis method

4.2.2 Verification

In order to verify the proposed fault analysis method, the modified IEEE 9-bus system shown in Fig. 4.4, based on the original system [165], is firstly tested. The modifications are listed as follows:

(1) The system voltage level increases to 400 kV;

(2) The SGs at bus 6 and bus 10 are replaced by VSC1 and VSC2 respectively. It is assumed that both converters have the dual-sequence current controls with (2.66)–(2.67);

(3) A new bus (bus 2) is added compared to the original system;

(4) The parameters of the lines, transformers and machines are updated using the data from the DK1 system.

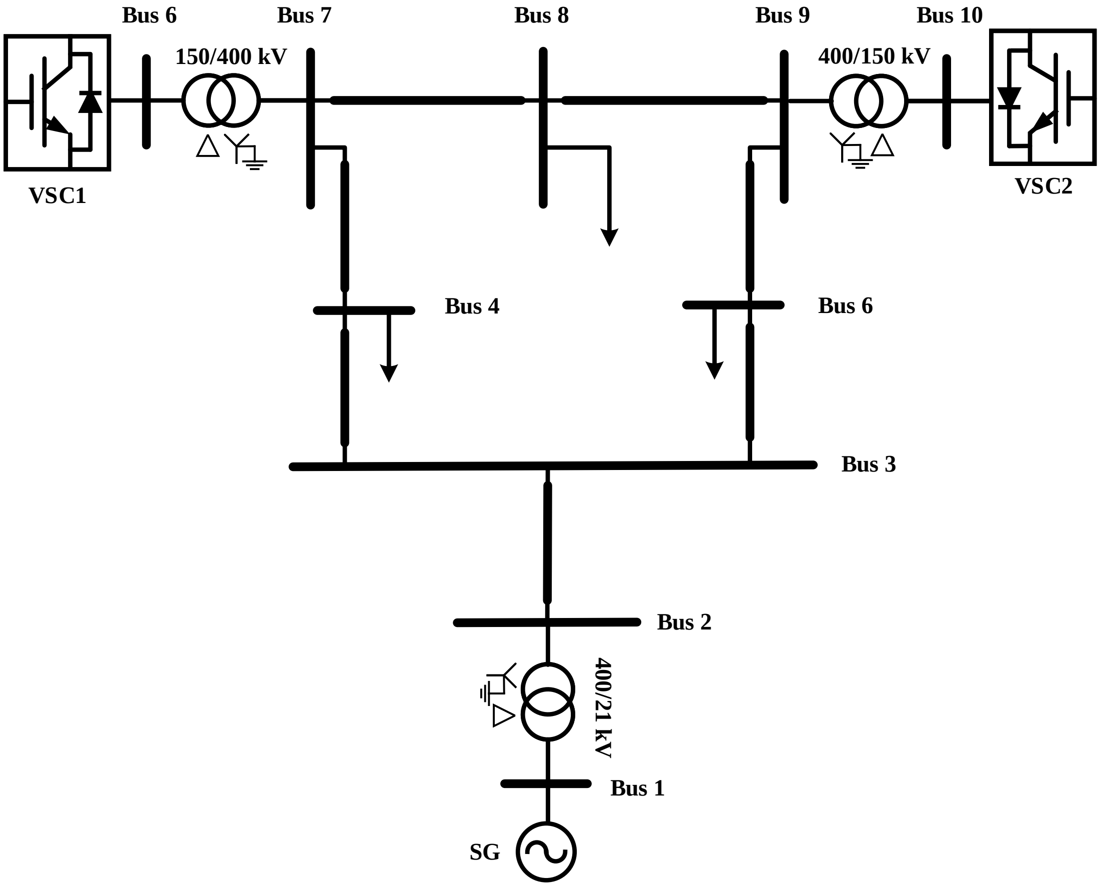

Figure 4.4: Single-line diagram of the modified IEEE 9-bus system

If there is a fault at bus *f*, Fig. 4.5 presents the current injections and the sequence networks for the system in Fig. 4.4. Three current injections $\dot{I}_{s,1}^{+}$ (from SG), $\dot{I}_{c,1}^{+}$ and $\dot{I}_{c,2}^{+}$ (from VSC1 and VSC2) are present for the positive-sequence network. Two current injections $\dot{I}_{c,1}^{-}$ and $\dot{I}_{c,2}^{-}$ (from VSC1 and VSC2) are present for the negative-sequence network. As a result, (4.5)–(4.6) can be expressed by:

$$\mathbf{I}_{inj}^{+}(m) = \left[\dot{I}_{s,1}^{+}, 0, 0, 0, 0, \dot{I}_{c,1}^{+}(m), 0, 0, 0, \dot{I}_{c,2}^{+}(m)\right]^{T} \tag{4.22}$$

$$\mathbf{I}_{inj}^{-}(m) = \left[0, 0, 0, 0, 0, \dot{I}_{c,1}^{-}(m), 0, 0, 0, \dot{I}_{c,2}^{-}(m)\right]^{T} \tag{4.23}$$

In the steady state, VSC1 and VSC2 has a power output of 165 MW and 75 MW respectively with unity power factor. The slack bus, bus 1, has the voltage at 1 p.u.. During the fault, besides feeding the active power, both VSCs are controlled to provide extra reactive power. There are $Q_{ref} = 50$ Mvar for VSC1 and $Q_{ref} = 250$ Mvar for VSC2. It is assumed that the dual-sequence current control strategy of VSC2 is fixed at $a_2 = c_2 = 1$ (providing P^+ and Q^+). In contrast, the dual-sequence current control strategy of VSC1, characterized by a_1 and c_1, will be varied according to Table 4.1 as different scenarios.

In order to verify the calculated results, the system shown in Fig. 4.4 is modeled with details in RTDS. The dual-sequence current controls shown in Fig. 2.11 are implemented for both VSCs with current references (2.66)–(2.67). The results calculated using the proposed method are compared with RTDS simulations for verification.

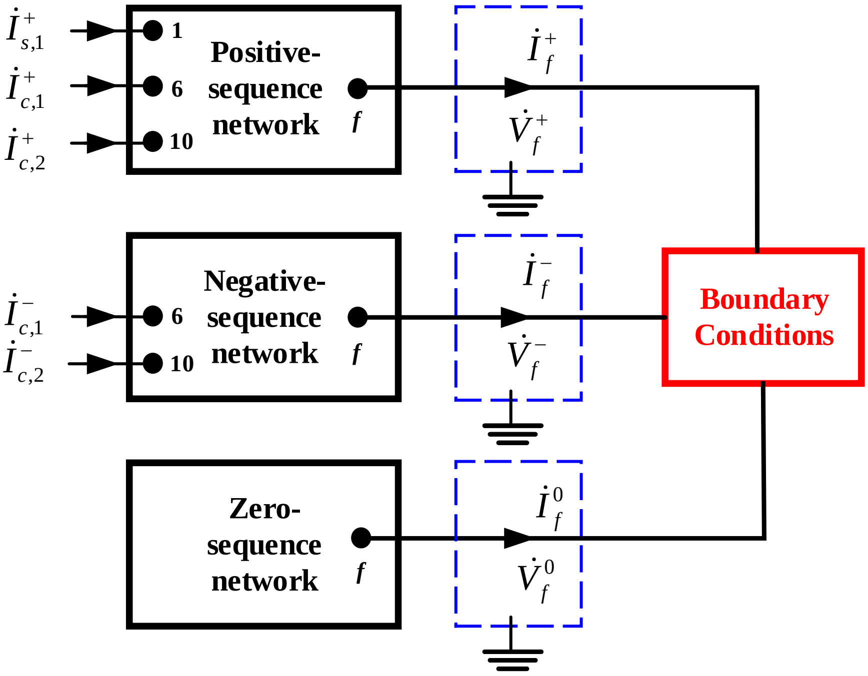

Figure 4.5: Sequence networks of the test system subject to a fault at f

Table 4.1: Different scenarios of VSC1 control strategies

Scenario	a_1	c_1	**Share of the sequence powers**
S1	1	1	P^+(100%), P^-(0%), Q^+(100%), Q^-(0%)
S2	1	0.5	P^+(100%), P^-(0%), Q^+(50%), Q^-(50%)
S3	1	0	P^+(100%), P^-(0%), Q^+(0%), Q^-(100%)
S4	0.5	1	P^+(50%), P^-(50%), Q^+(100%), Q^-(0%)

Here one example is given to show the effectiveness of the proposed method. For a solid A-B fault or A-g fault at bus 4, Fig. 4.6 shows the sequence voltages of bus 4, bus 6 and bus 10 obtained from the RTDS simulations. It corresponds to an A-g fault with S3 and an A-B fault with S4, in which the short circuit current from the VSCs are presented in Fig. 4.7–4.8. The measurements from the curves are compared with the calculation results. The RMS values of the sequence voltages and the sequence short circuit currents from VSCs are listed in Table 4.2 for the scenarios specified in Table 4.1. It can be seen that the calculation results agree with the simulation results, which proves that the developed method is capable of performing static fault analysis considering the presence of VSCs and their dual-sequence current controls.

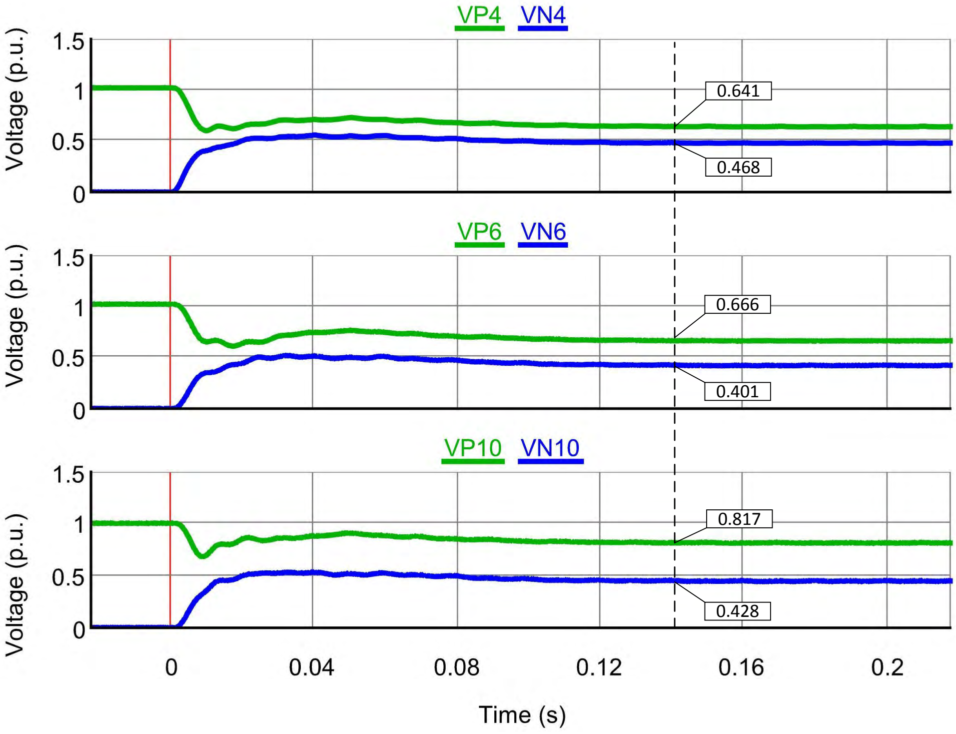

(a) S3, A-g fault

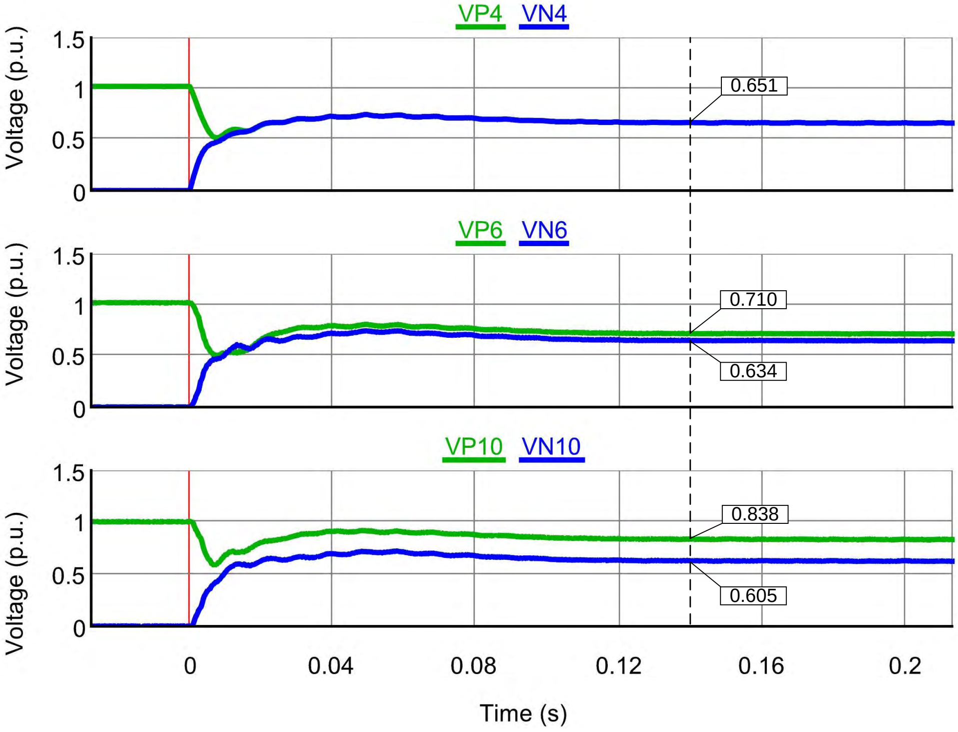

(b) S4, A-B fault

Figure 4.6: Sequence voltages in RTDS simulations subject to a fault at bus 4

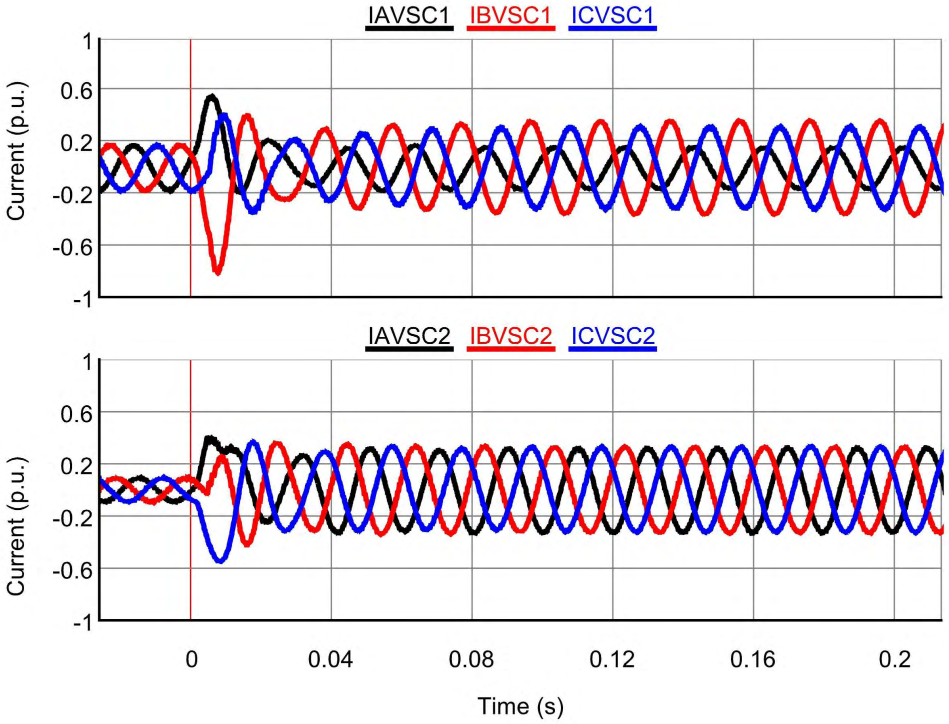

(a) S3, A-g fault

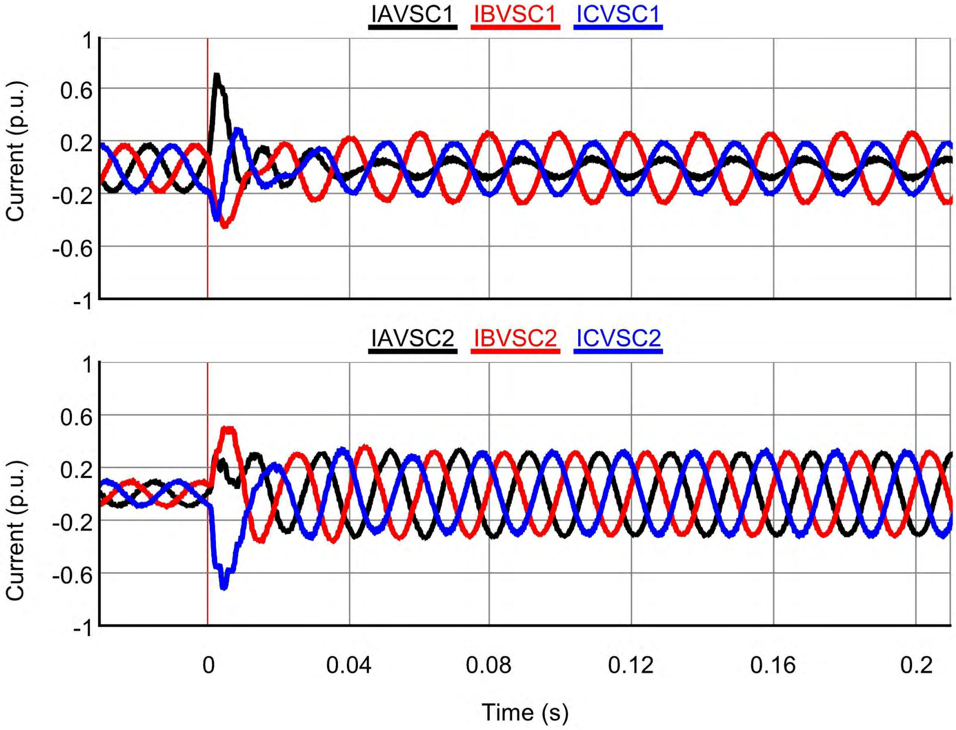

(b) S4, A-B fault

Figure 4.7: Three-phase short circuit current from VSCs in RTDS simulations subject to a fault at bus 4

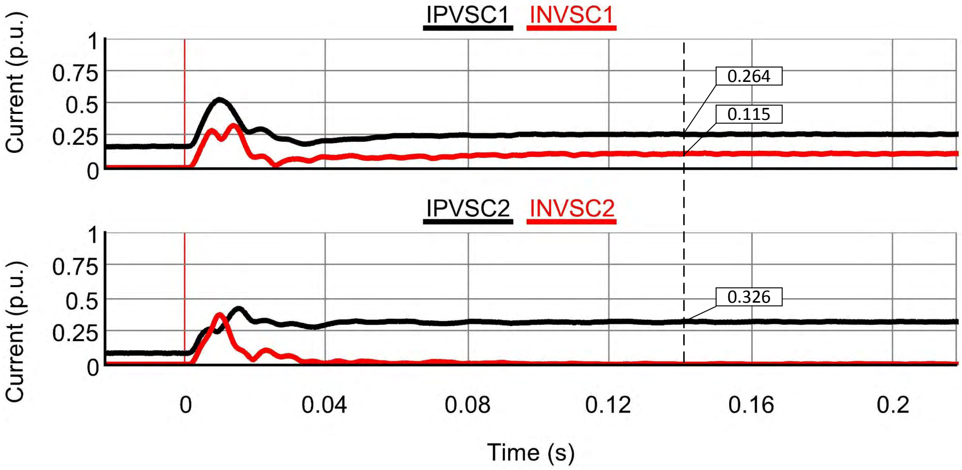

(a) S3, A-g fault

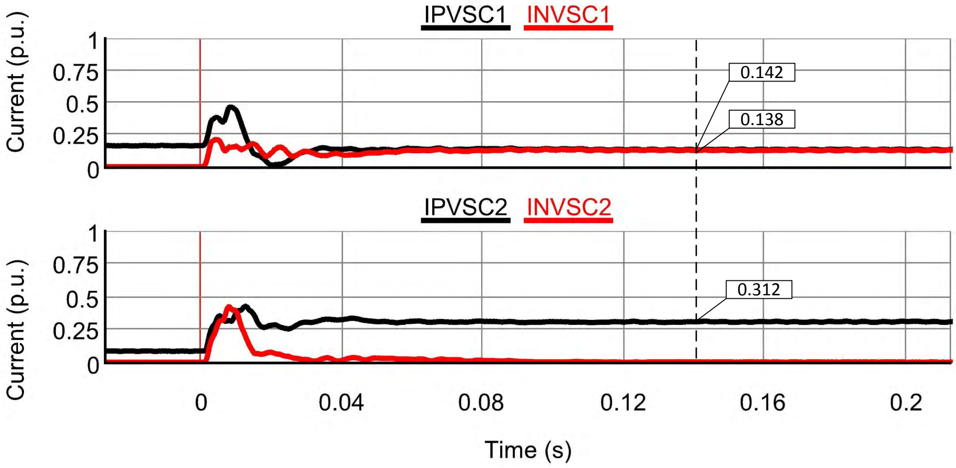

(b) S4, A-B fault

Figure 4.8: Sequence short circuit currents from VSCs in RTDS simulations subject to a fault at bus 4

The errors can originate from the fact that the short circuit impedance of a synchronous machine is a time-varying quantity. However, the calculation just uses the approximated value of a certain time period. In addition, the power system in RTDS is modeled with details and the simulations are performed in real time with all the system dynamics involved. As a result, when measuring the curves with the cursor in RTDS, it can be observed that the values are always varying with small changes because RTDS solves the whole system every time step (typically 50 μs). In contrast, the one-time measurements are the values with respect to a specific time instant and do not reflect the dynamics. However, the errors are not significant and are acceptable for static fault analysis and for planning studies.

The results in Table 4.2 also agree with the voltage support concept presented in Section 2.4.3. The changes in P^+ and P^- do not affect the voltage notably [see S1 and S4], while the different combinations of Q^+ and Q^- gives more differences in the retained voltages [see S1, S2, and S3].

Table 4.2: Comparison between calculations and simulations

Scenario		**A-B fault**				**A-g fault**			
1	Bus	$\lvert\dot{V}^{+}\rvert$ (p.u.)		$\lvert\dot{V}^{-}\rvert$ (p.u.)		$\lvert\dot{V}^{+}\rvert$ (p.u.)		$\lvert\dot{V}^{-}\rvert$ (p.u.)	
		Cal	RTDS	Cal	RTDS	Cal	RTDS	Cal	RTDS
	4	0.636	0.645	0.636	0.645	0.721	0.726	0.551	0.558
	6	0.692	0.699	0.619	0.625	0.773	0.780	0.536	0.542
	10	0.817	0.821	0.591	0.599	0.886	0.893	0.512	0.520
	Converter	$\lvert\dot{I}^{+}\rvert$ (p.u.)		$\lvert\dot{I}^{-}\rvert$ (p.u.)		$\lvert\dot{I}^{+}\rvert$ (p.u.)		$\lvert\dot{I}^{-}\rvert$ (p.u.)	
		Cal	RTDS	Cal	RTDS	Cal	RTDS	Cal	RTDS
	1	0.263	0.260	0	0	0.223	0.228	0	0
	2	0.320	0.317	0	0	0.279	0.282	0	0
2	Bus	$\lvert\dot{V}^{+}\rvert$ (p.u.)		$\lvert\dot{V}^{-}\rvert$ (p.u.)		$\lvert\dot{V}^{+}\rvert$ (p.u.)		$\lvert\dot{V}^{-}\rvert$ (p.u.)	
		Cal	RTDS	Cal	RTDS	Cal	RTDS	Cal	RTDS
	4	0.599	0.605	0.599	0.605	0.684	0.690	0.513	0.519
	6	0.640	0.646	0.564	0.570	0.723	0.727	0.477	0.485
	10	0.785	0.792	0.554	0.563	0.854	0.859	0.473	0.480
	Converter	$\lvert\dot{I}^{+}\rvert$ (p.u.)		$\lvert\dot{I}^{-}\rvert$ (p.u.)		$\lvert\dot{I}^{+}\rvert$ (p.u.)		$\lvert\dot{I}^{-}\rvert$ (p.u.)	
		Cal	RTDS	Cal	RTDS	Cal	RTDS	Cal	RTDS
	1	0.276	0.271	0.044	0.041	0.235	0.238	0.050	0.058
	2	0.332	0.034	0	0	0.298	0.297	0	0
3	Bus	$\lvert\dot{V}^{+}\rvert$ (p.u.)		$\lvert\dot{V}^{-}\rvert$ (p.u.)		$\lvert\dot{V}^{+}\rvert$ (p.u.)		$\lvert\dot{V}^{-}\rvert$ (p.u.)	
		Cal	RTDS	Cal	RTDS	Cal	RTDS	Cal	RTDS
	4	0.549	0.556	0.549	0.556	0.634	0.641	0.460	0.468
	6	0.571	0.580	0.491	0.499	0.658	0.666	0.394	0.401
	10	0.742	0.750	0.504	0.510	0.812	0.817	0.420	0.428
	Converter	$\lvert\dot{I}^{+}\rvert$ (p.u.)		$\lvert\dot{I}^{-}\rvert$ (p.u.)		$\lvert\dot{I}^{+}\rvert$ (p.u.)		$\lvert\dot{I}^{-}\rvert$ (p.u.)	
		Cal	RTDS	Cal	RTDS	Cal	RTDS	Cal	RTDS
	1	0.306	0.301	0.102	0.096	0.269	0.264	0.114	0. 115
	2	0.351	0.350	0	0	0.328	0.326	0	0
4	Bus	$\lvert\dot{V}^{+}\rvert$ (p.u.)		$\lvert\dot{V}^{-}\rvert$ (p.u.)		$\lvert\dot{V}^{+}\rvert$ (p.u.)		$\lvert\dot{V}^{-}\rvert$ (p.u.)	
		Cal	RTDS	Cal	RTDS	Cal	RTDS	Cal	RTDS
	4	0.645	0.651	0.645	0.651	0.725	0.732	0.558	0.564
	6	0.704	0.710	0.626	0.634	0.779	0.787	0.541	0.546
	10	0.834	0.838	0.599	0.605	0.890	0.899	0.518	0.525
	Converter	$\lvert\dot{I}^{+}\rvert$ (p.u.)		$\lvert\dot{I}^{-}\rvert$ (p.u.)		$\lvert\dot{I}^{+}\rvert$ (p.u.)		$\lvert\dot{I}^{-}\rvert$ (p.u.)	
		Cal	RTDS	Cal	RTDS	Cal	RTDS	Cal	RTDS
	1	0.143	0.142	0.140	0.138	0.123	0.124	0.152	0.149
	2	0.317	0.312	0	0	0.278	0.282	0	0

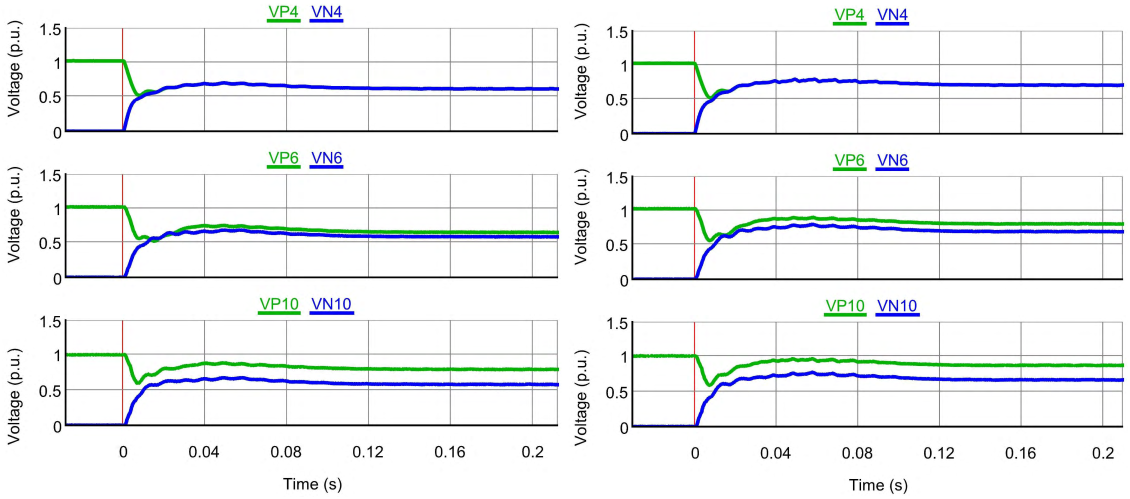

(a) $Q_{c,1}^{ref} = 50$ Mvar, $c_1 = 0.5$;
$Q_{c,2}^{ref} = 250$ Mvar, $c_2 = 1$;

(b) $Q_{c,1}^{ref} = 150$ Mvar, $c_1 = 0.5$;
$Q_{c,2}^{ref} = 250$ Mvar, $c_2 = 1$;

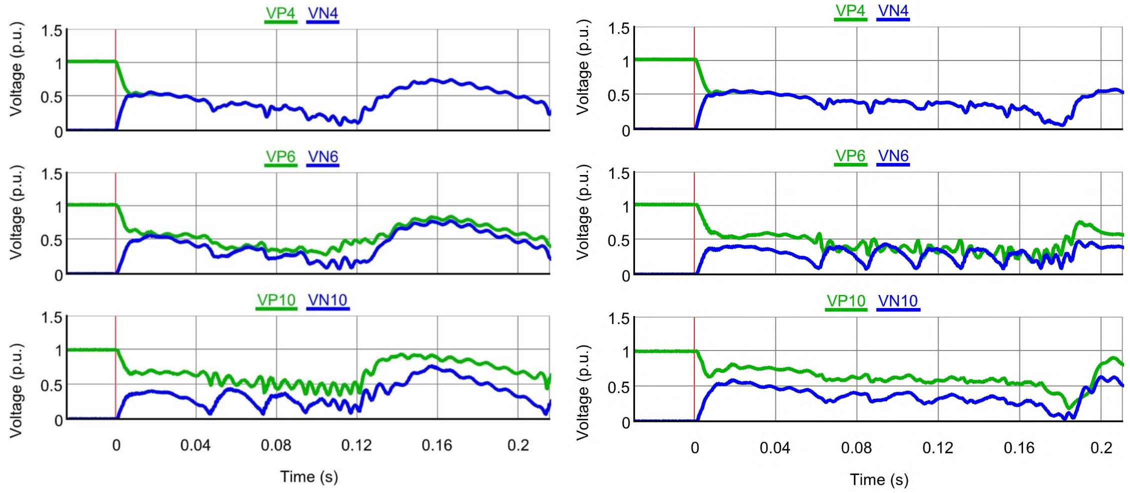

(c) $Q_{c,1}^{ref} = 50$ Mvar, $c_1 = 0.5$;
$Q_{c,2}^{ref} = 250$ Mvar, $c_2 = 0.5$;

(d) $Q_{c,1}^{ref} = 150$ Mvar, $c_1 = 0.5$;
$Q_{c,2}^{ref} = 250$ Mvar, $c_2 = 0.5$;

Figure 4.9: Sequence voltages in RTDS simulations subject to an A-B fault at bus 4

4.3 The impact of dual-sequence current controls

4.3.1 Problem description

When doing the simulations in RTDS with different combinations of Q^{ref}, c_1 and c_2, an interesting phenomenon is discovered that the system in certain scenarios does not have a stable response during unbalanced faults. Normally, the sequence voltages of the buses should be like Fig. 4.9(a)–(b), where the voltages retain at a certain level during the fault. The discovered phenomenon is illustrated in Fig. 4.9(c)–(d), where the voltages have oscillatory behavior and cannot stabilize at a certain level during the fault.

The only difference between Fig. 4.9(a)–(b) and Fig. 4.9(c)–(d) is the values of the reactive power references (Q^{ref1}, Q^{ref2}) or the share of Q^+ (c_1, c_2), which indicates that the provision of the negative-sequence reactive power (Q^-) may have an adverse impact on the system during unbalanced faults. If the proposed fault analysis method is applied regarding these unstable scenarios, the algorithm cannot converge even after a large number of iterations. Based on these observations and initial investigations, a hypothesis is made that the equation set defined by the fault analysis method does not have a solution mathematically. As a result, RTDS continues to look for a stable operating point that does not exist and yields oscillatory behavior.

4.3.2 Problem formulation

In order to further explore the reason for the phenomenon in Fig. 4.9(c)–(d) and find an theoretical explanation, the equations defined by the proposed fault analysis method are converted into an optimization problem, whose objective function is formulated as:

$$\begin{aligned} min\ Z = & \sum_j \left\{ [Q_{c,j}^{ref} - F_Q(\dot{V}_{c,j}^+)]^2 \right\} \\ & + \sum_j \left\{ \left\{ \Re(\dot{I}_{c,j}^+) - \Re[F^+(\dot{V}_{c,j}^+)] \right\}^2 \right\} + \sum_j \left\{ \left\{ \Re(\dot{I}_{c,j}^-) - \Re[F^-(\dot{V}_{c,j}^-)] \right\}^2 \right\} \\ & + \sum_j \left\{ \left\{ \Im(\dot{I}_{c,j}^+) - \Im[F^+(\dot{V}_{c,j}^+)] \right\}^2 \right\} + \sum_j \left\{ \left\{ \Im(\dot{I}_{c,j}^-) - \Im[F^-(\dot{V}_{c,j}^-)] \right\}^2 \right\} \end{aligned} \tag{4.24}$$

where the reactive power reference for the j-th conveter $Q_{c,j}^{ref}$, the real part $\Re(\dot{I}_{c,j}^+)$, $\Re(\dot{I}_{c,j}^-)$ and the imaginary part $\Im(\dot{I}_{c,j}^+)$, $\Im(\dot{I}_{c,j}^-)$ of current references are considered as the optimization variables; F^+ and F^- refer to the current references (4.3) and (4.4) respectively; while $\dot{V}_{c,j}^+$ and $\dot{V}_{c,j}^-$ are calculated using (4.5)–(4.21).

The reactive power support typically comes in the form of a profile of reactive current requirement versus the voltage at the PCC as shown in Fig. 1.4. As a result, the reactive power reference can be regarded as a function F_Q of the voltage (positive-sequence voltage) because power is a product of voltage and current. For the optimization problem defined by (4.24), all the quantities are converted into their per unit values. Mathematically speaking, the value of Z should be zero when the solution to the equation set, if existed, is substituted into (4.24). Therefore, the value of $min(Z)$ can serve as an indicator on if the equation set has a solution.

4.3.3 Problem investigation

Modified IEEE 9-bus system

In this investigation, the pre-fault conditions are kept the same as those in Section 4.2.2. The reactive power reference is generated by the function $F_Q(\dot{V}_{c,j}^+) = \left|\dot{V}_{c,j}^+\right| \cdot I_{Q,j}$. The value of $I_{Q,j}$ will be decided by the voltage based on Fig. 4.10. Here two different profiles are considered. The profile 1 can be expressed mathematically by:

$$I_{Q,j} = -2.5 \left|\dot{V}_{c,j}^+\right| + 2.25 \; (0 \le I_{Q,j} \le 1) \tag{4.25}$$

which is the same as Fig. 1.4. The profile 2 can be expressed by:

$$I_{Q,j} = -1.25 \left|\dot{V}_{c,j}^+\right| + 1.125 \; (0 \le I_{Q,j} \le 0.5) \tag{4.26}$$

Compared to profile 1, profile 2 refers to a case when the VSCs provide less reactive power support.

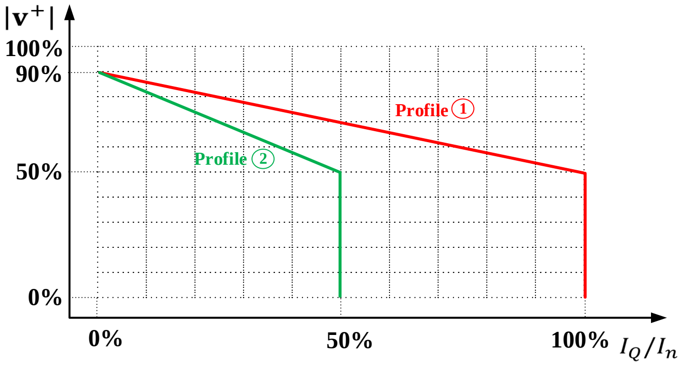

Figure 4.10: Reactive current profiles used to generate reactive power reference

In the following, the flexible scalars a_1 and a_2 are fixed at 1, which means both converters do not provide P^-. The flexible scalars c_1 and c_2 are varied between 0 and 1 with a 0.1 step, which means that the share of the Q^+ from each VSC can go from 0% to 100% with a 10% step. The optimization problem is actually a Non-Linear Programming (NLP) problem with (4.24) as the objective function, and with the proposed fault analysis method (4.1)-(4.21) as the constraints. Here the MATLAB optimation toolbox [166] with the Genetic Algorithm (GA) is used to perform the optimization, regarding a two-phase fault at bus 4 with all possible combinations of c_1 and c_2.

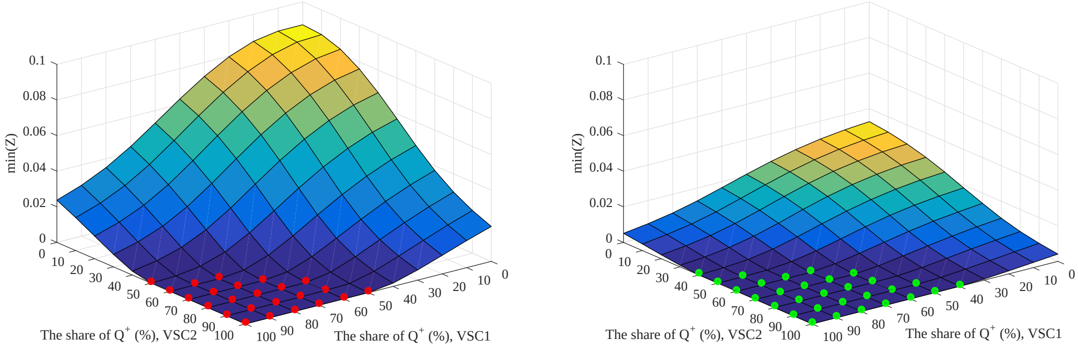

(a) With profile 1

(b) With profile 2

Figure 4.11: The values of *min(Z)* under different combinations of flexible scalars for an A-B fault at bus 4

Figure 4.11 presents the values of $min(Z)$ with respect to the different combinations of c_1 and c_2. The scenarios marked by a red or a green dot has the value of $min(Z)$ below 10^{-4}. The corresponding simulations in RTDS regarding these scenarios have a stable response like Fig. 4.9(a)–(b) during the fault. In contrast, with the rest of the combinations without being marked by a dot, the values of $min(Z)$ are above 10^{-4} and oscillatory behavior like Fig. 4.9(c)–(d) are observed in the RTDS simulations. It can be observed from Fig. 4.11 that, with the share of Q^+ gradually decreasing, $min(Z)$ gets further away from zero. This proves that the injection of Q^- can lead to unstable responses during unbalanced faults, which is because the system does not have a stable operating point fulfilling the reactive power support and (4.1)–(4.21).

If the VSCs are controlled to provide negative-sequence current, the negative-sequence network during a fault will become active. The simultaneous injection of Q^+ and Q^- can alter the positive- and negative-sequence voltages respectively at the PCC for an inductive grid. Since the current references of a VSC depend on the grid voltage, this will in return change the amplitudes and the phases of the current references. On top of that, the faulted network is also restrained by the boundary conditions. Therefore, the system may not have a stable operating point fulfilling all of these restrictions.

It can also be observed that, the surface in Fig. 4.11(b) is closer to zero and gives more stable scenarios than Fig. 4.11(a). The reason is that, with profile 2, the VSCs inject less reactive power during the fault compared to profile 1. As a result, the system with profile 2 is able to tolerate a higher share of Q^- (more stable scenarios) than with profile 1, as the total amount of the injected Q^- is smaller with profile 2 for the same combination of c_1 and c_2.

The western Danish power system

In this section, the same investigation is applied to the DK1 system [see Fig. 3.1] for a further verification. The two VSC-HVDC links at TJE and EDR and the Type-IV wind farm near EDR are assumed to have the dual-sequence current controls using (2.66)–(2.67). Their reactive power references are generated using the profile 1 in Fig. 4.10. Synchronous condensers are in principle synchronous machine and thus the Norton's circuit model (4.1)–(4.2) also applies to the three SCs at VHA, TJE and FGD. The two Type-III wind farms near KAE and TRI are treated as conventional induction motors for the static fault analysis [71, 167] and their Norton's circuit model for static fault analysis can be represented by:

$$\dot{I}_D = \frac{n_D \dot{V}_s}{X_s + X_r} \tag{4.27}$$

$$y_D = \frac{n_D}{j(X_s + X_r)} \tag{4.28}$$

where X_s and X_r refer to the stator reactance and rotor reactance respectively of a single Type-III wind generator; n_D is the number of the wind generators, which serves as a scale factor so that the model is equivalent to that of the whole wind farm.

Firstly, the proposed fault analysis method is applied to the DK1 system and the corresponding calculation results are compared with those obtained from the RTDS simulations. For example, with the flexible scalar a set to 1 (providing only P^+) for all the three VSC-based sources (two VSC-HVDC systems and one Type-IV wind farm), Table 4.3 compares the retained sequence voltages of certain buses subject to a solid A-B or A-g fault at IDU with different combinations of the flexible scalar *c*. It can be observed that the calculation results still agree with the simulation results from RTDS.

Similarly, under certain scenarios, the DK1 system does not have a stable fault response and exhibits oscillatory behavior. For example, Fig. 4.12 presents the three-phase voltage at IDU subject to an A-g fault at IDU with different values of *c*. In contrast with Fig. 4.12(a), the voltage in Fig. 4.12(b) exhibits unfavorable characteristics during the fault when both VSC-HVDC systems are controlled to inject reactive power with 50% in negative-sequence. Correspondingly, Fig. 4.13 shows the measured sequence voltages at certain buses. The voltages in Fig. 4.13(a) are retained at a certain level while oscillatory behavior is registered in Fig. 4.13(b).

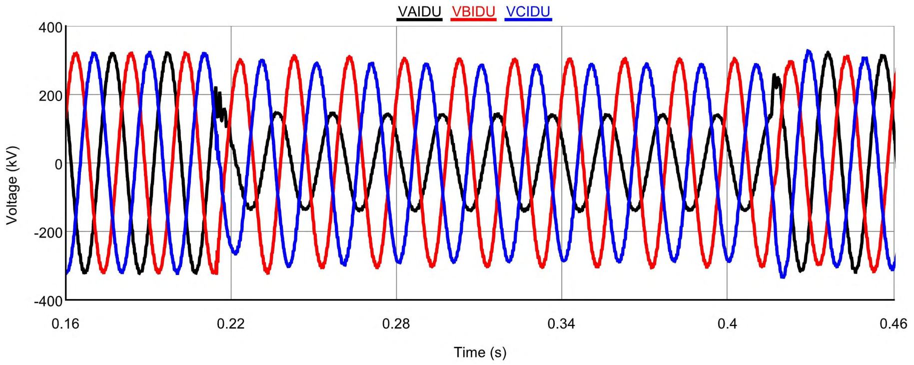

(a) c=1 for both VSC-HVDC

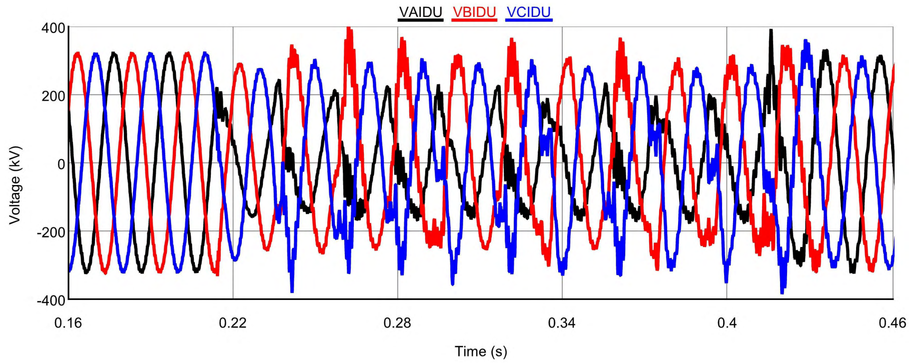

(b) c=0.5 for both VSC-HVDC

Figure 4.12: Three-phase voltage at IDU subject to an A-g fault at IDU

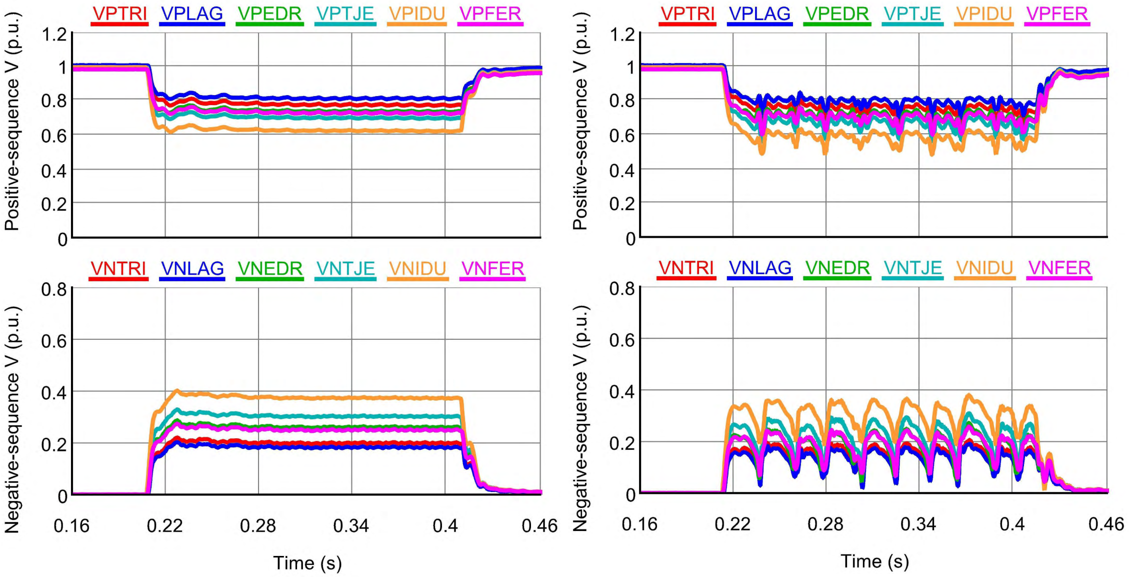

(a) c=1 for both VSC-HVDC (b) c=0.5 for both VSC-HVDC

Figure 4.13: Sequence voltages of certain buses subject to an A-g fault at IDU

Table 4.3: Comparison between calculations and simulations for the DK1 system

A-B fault, c=0.6 for both VSC-HVDC, c=1 for the Type-IV wind farm												
	$\lvert\dot{V}^{+}\rvert$ (p.u.)						$\lvert\dot{V}^{-}\rvert$ (p.u.)					
Bus	IDU	EDR	TJE	FER	TRI	LAG	IDU	EDR	TJE	FER	TRI	LAG
Cal	0.473	0.662	0.600	0.689	0.748	0.767	0.473	0.277	0.346	0.255	0.206	0.198
RTDS	0.462	0.653	0.590	0.678	0.739	0.753	0.461	0.278	0.343	0.253	0.215	0.200
A-g fault, c=0.8 for both VSC-HVDC, c=1 for the Type-IV wind farm												
	$\lvert\dot{V}^{+}\rvert$ (p.u.)						$\lvert\dot{V}^{-}\rvert$ (p.u.)					
Bus	IDU	EDR	TJE	FER	TRI	LAG	IDU	EDR	TJE	FER	TRI	LAG
Cal	0.608	0.722	0.687	0.732	0.774	0.849	0.320	0.300	0.227	0.271	0.226	0.209
RTDS	0.616	0.728	0.699	0.738	0.783	0.831	0.330	0.296	0.218	0.265	0.218	0.196

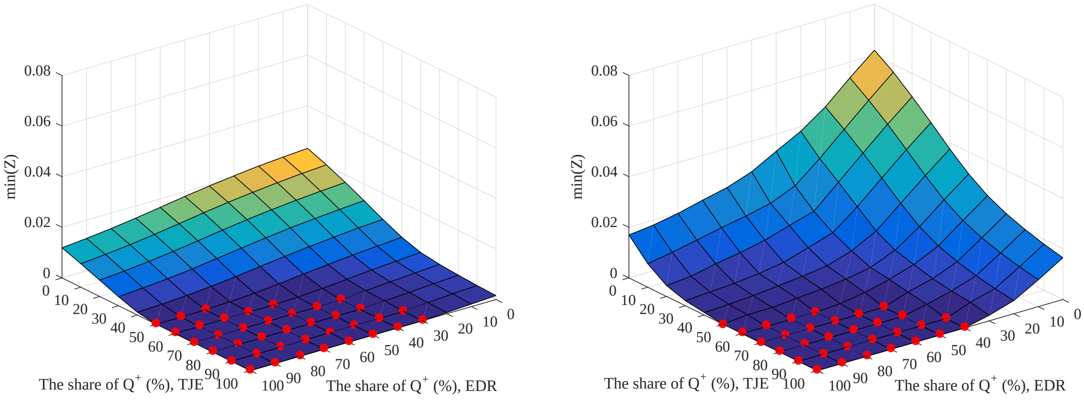

(a) The original system

(b) The system with three SGs phases out

Figure 4.14: The values of *min(Z)* under different combinations of flexible scalars subject to an A-B fault at IDU

Secondly, the investigation using (4.24) is applied to the DK1 system to help explore the solution of the system during an unbalanced fault. It is assumed that the Type-IV wind farm provides only P^+ and Q^+ during unbalanced faults. Here, the flexible scalar c of the two VSC-HVDC links is varied between 0 and 1 with a 0.1 step, which means that the share of Q^+ contributed by these two VSC-HVDC systems can go from 0% to 100% with a 10% step. Figure 4.14(a) presents the values of $min(Z)$ regarding a solid A–B fault at IDU. The scenarios marked by a dot have $min(Z)$ below 10^{-4}. Correspondingly, the simulations in RTDS have stable fault responses like Fig. 4.12(a) and Fig. 4.13(a). The rest of the scenarios have $min(Z)$ above 10^{-4} and the RTDS simulations exhibit oscillatory behavior.

For a further investigation, with three SGs (ESVB3, SKVB3, and NJVB3) disconnected from the grid, the optimization procedure is repeated for the same fault to get the values of $min(Z)$, which is presented in Figure 4.14(b). The surface in Fig. 4.14(b) is further away from zero and there exist fewer stable scenarios when compared to Fig. 4.14(a). In the case with the three SGs phased-out, the system has a lower short circuit power. This makes the reactive power from VSCs to have more impact on the system voltage so that the system tolerates less negative-sequence reactive power Q^{-}.

Based on the above investigation, the dual-sequence current control strategies of VSCs involving negative-sequence current injection should be re-evaluated for future low inertia power systems. If the amount of Q^{-} from VSCs is not restricted properly, the system may not have a stable response during unbalanced faults. The proposed fault analysis can serve as a tool to evaluate this issue.

4.4 Synchronous condenser allocation

This section presents the allocation of SCs using the proposed fault analysis method in Section 4.2. It aims to determine the optimal sizes and locations of the new SCs to improve the system SCRs for a future DK1 system. According to [168], the SCR at a converter terminal is defined as:

$$SCR = \frac{S}{P_d} \tag{4.29}$$

where S is the three-phase symmetrical short circuit power at the converter terminal, and P_d is the power rating of the corresponding converter. SCR is a common concern in power converter applications and is commonly used as an index on the AC/DC system strength. Typically, a system with SCR less than 3 is regarded as a weak system, where the AC system impedance is high relative to the DC power (from converters) at the PCC. When the SCR is insufficient, the system is more vulnerable to the disturbances and problems such as voltage instability and undesirable dynamic behavior of the converters can arise [169, 170, 171]. Therefore, specially designed control schemes of converters or reactive power compensation such as STATCOMs are needed for operating a power converter in low SCR systems.

4.4.1 Allocation method

Synchronous condensers, as synchronous machines in principle, can contribute large amount of short circuit current and improve the system SCRs. The allocation of SCs in this section is formulated into an optimization problem. It decides the optimal locations and sizes of the new SCs so that the SCR of each converter terminal is maintained above a certain level while minimizing the total cost. This can be formulated into a Mixed-Integer Non-Linear Programming (MINLP) problem:

$$minimize\ F(x_b, y_b) = \sum_{b=1}^{B} \left(C_{F,b} + C_{V,b} \cdot \frac{S_r}{y_b} \right) \cdot x_b \tag{4.30}$$

$$subject\ to\ \ SCR_j \geq M\ (j \in \pi_1) \tag{4.31}$$

$$\sum_{b=1}^{B} x_b = N\ (b \in \pi_2) \tag{4.32}$$

$$SCR_j = \frac{S''_{k,j}}{P_j} \tag{4.33}$$

$$S''_{k,j} = \sqrt{\frac{3}{2}} \cdot \left| \dot{I}_{f,j} \right| \cdot V_n \tag{4.34}$$

Table 4.4 lists the nomenclature for the optimization. $S''_{k,j}$ is the initial three-phase symmetrical short circuit power at the bus j, which is obtained based on the definition (2.2). $\dot{I}_{f,j}$ is the initial

Table 4.4: Nomenclature for the optimization

Category	Symbol	Explanation
Indices	j	index of converter terminals (PCCs)
	b	index of candidate locations for new SCs
Sets	π_1	set of the converter terminals (PCCs)
	π_2	set of the candidate locations for new SCs
Binary decision variables	x_b	status of the new SC at location *b* (1-installed; 0-not installed)
Integer decision variables	y_b	scale factor on the SC rating at location *b*
Intermediate variables	SCR_j	short circuit ratio at bus *j*
	$\left\lvert \dot{I}_{f,j} \right\rvert$	initial three-phase symmetrical short circuit current at bus *j*
	$S''_{k,j}$	initial three-phase symmetrical short circuit power at bus *j*
Parameters	$C_{F,b}$	fixed cost of installing a new SC at location *b*
	$C_{V,b}$	variable cost of installing a new SC at location *b*
	B	total number of the candidate locations
	N	maximum allowed number of SCs to be installed
	V_n	nominal line-line voltage of the system
	S_r	rated apparent power of the SC
	P_j	rated apparent power of the converters connected to bus *j*
	M	minimum required SCR at converter terminals;

three-phase symmetrical short circuit current at the bus *j* for a three-phase balanced fault the bus *j*. It is calculated using the proposed fault analysis method in Section 4.2 for three-phase balanced faults. Since the initial short circuit current is used here, sub-transient reactance x''_d of SGs and SCs is used in (4.1). The integer variable, y_b, is a scale factor controlling the rated apparent power of the SC at location *b*. Here two different ratings, 270 Mvar and 135 Mvar, are considered. If there is $S_r = 270$ Mvar, $y_b = 1$ will represent that a 270 Mvar SC is selected while $y_b = 2$ will represent a 135 Mvar SC is selected at location *b*. In this study, it is assumed that there is $C_{F,b} = 3$ million US dollars (M$) and $C_{V,b} = 1$ M$ per 100 Mvar. This MINLP problem is solved in MATLAB using the GA function of the optimization toolbox [166]. The SC allocation using the proposed fault analysis method is summarized by the flow chart in Fig. 4.15. The GA optimization provides the decision variables to the fault analysis method. With $\mathbf{Y}$ and $\mathbf{I}_{inj}$ obtained considering the existence of new SCs, the SCR of each converter PCC is calculated and the minimum SCR is returned to the GA optimization.

4.4.2 Allocation results

In this section, the SC allocation method described above is applied to the DK1 system in Fig. 3.1. In order to consider a future scenario, the following assumptions are made:

(1) The five SGs (ESVB3, NJVB3, SKVB3, FYVB7, and SSVB3) are phased out;
(2) The short circuit contribution from Germany is neglected;
(3) A new Type-IV wind farm is integrated at IDU;
(4) The installed capacity of the HVDC systems and wind farms is in accordance with Table 4.5;

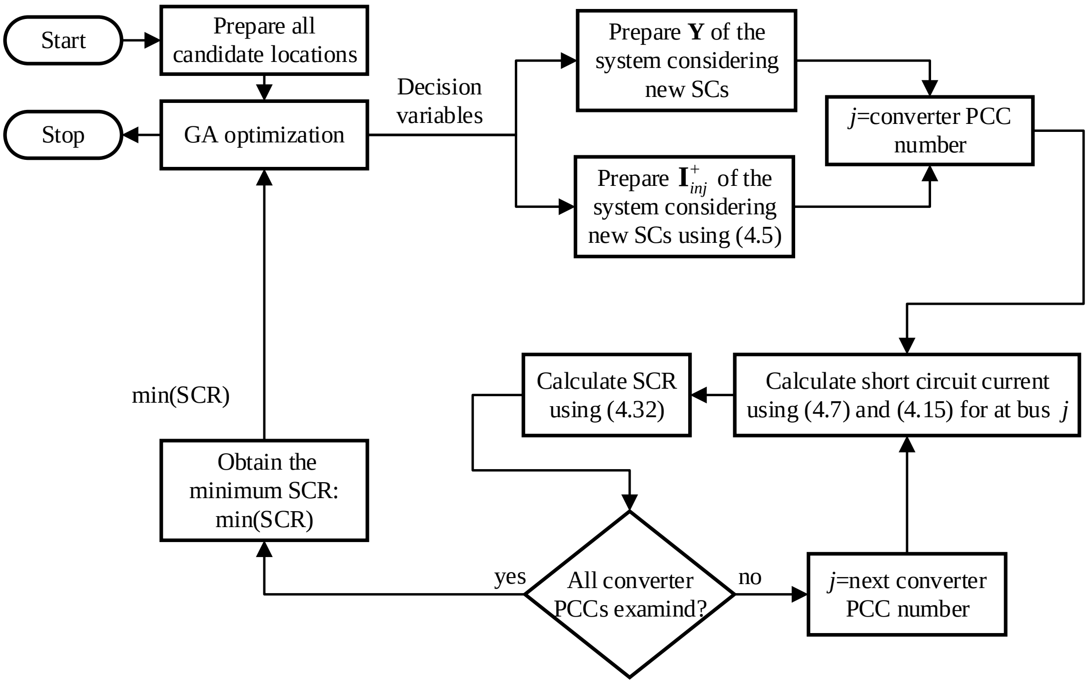

Figure 4.15: The flow chart for synchronous condenser allocation

Table 4.5: Installed capacity of HVDC systems and wind farms

Location	**Total installed capacity**
TJE	1000 MVA LCC-HVDC + 750 MVA VSC-HVDC
KAE	2×440 MVA Type-III wind farms
TRI	2×440 MVA Type-III wind farms
EDR	700 MVA VSC-HVDC + 3×400 MVA Type-IV wind farms
VHA	740 MVA LCC-HVDC
FGD	600 MVA LCC-HVDC
IDU	3×400 MVA Type-IV wind farms

Taking the short circuit contributions from VSC-based sources into account, it is assumed that all the VSC-HVDC systems and Type-IV wind farms inject 1 p.u. reactive current with respect to their own ratings under grid balanced faults while LCC-HVDC systems do not contribute any short circuit current under grid balanced faults.

For the optimal SC allocation, two different sets of candidate SC locations are considered:

Set 1: all 400 kV buses;
Set 2: only converter terminals (PCCs) at 400 kV level;

The GA optimization is repeated 50 times for each set of candidate locations. Table 4.6 summarizes the SC allocation results with the minimum SCR *M* in (4.31) set to 3 or 4.

Table 4.6: Synchronous condenser allocation plans

Minimum SCR	**Set**	**Plan**	**Location and Rating** [Mvar]	**Cost** [M$]	**Note**
3	1	1	EDR(270), REV(135)	14.15	with 270/135 Mvar SC
		2	EDR(135), REV(270)	14.15	
		3	EDR(270), ASR(135)	14.15	
		4	EDR(135), ASR(270)	14.15	
		5	EDR(270), KAE(135)	14.15	
		6	EDR(135), KAE(270)	14.15	
	2	5	EDR(270), KAE(135)	14.15	
		6	EDR(135), KAE(270)	14.15	
4	1	7	TJE(270), EDR(270), KAE(270), REV(270), ASR(270)	45.50	
		8	IDU(270), EDR(270), KAE(270), REV(270), ASR(270)	45.50	
	2	9	IDU(270), TJE(270), KAE(270), TRI(270), EDR(270), VHA(270), FGD(270)	63.70	with 270/135 Mvar SC, SCR at EDR is still below 4
		10	TJE(500), KAE(500), EDR(500), VHA(500), FGD(500)	80.00	with 500/250 Mvar SC

For the case with $M = 3$, no feasible solution can be found with $N = 1$ (one SC allowed) for set 1 and set 2. When there is $N = 2$ (two SCs allowed), the optimization successfully generates six different solutions (plan 1–6) with the same costs. Since set 2 is the subset of set 1, plan 5 and plan 6 for set 1 can also be obtained for set 2. Figure 4.16(a) shows the SCRs at the PCCs with plan 1–6. It can be seen that EDR and TJE are the weakest points in the original system and their SCRs are below 3. With the planned SCs, the SCRs at TJE and EDR increase to at least 3, fulfilling the constraint of $M = 3$.

For the case with $M = 4$, no feasible solution can be found with $N =$ 1–4 for set 1. When there is $N = 5$ (five SCs allowed), the optimization successfully generates two different solutions (plan 7–8) with the same costs. In contrast with set 2, no feasible solution can be found even when all the seven candidate locations are equipped with an SC of 270 Mvar (plan 9). The SCR at EDR is still below 4 as shown in Fig. 4.16(b). If the capacity of the available SCs increases to 500/250 Mvar, the optimization generated one solution (plan 10) when there is $N = 5$.

The results from plan 7–10 indicate that the converter terminals may not always be the optimal locations for new SCs. When an SC is located at the PCC, it mainly helps increase the PCC locally rather than the other PCCs if the SC is relatively far away from the other converters in terms of electrical distance. However, if an SC locates somewhere between two PCCs properly, the SCRs at both PCCs can be improved simultaneously. Otherwise, larger SCs or more SCs are in need if only converter terminals are the candidate locations, which will also result in a higher cost.

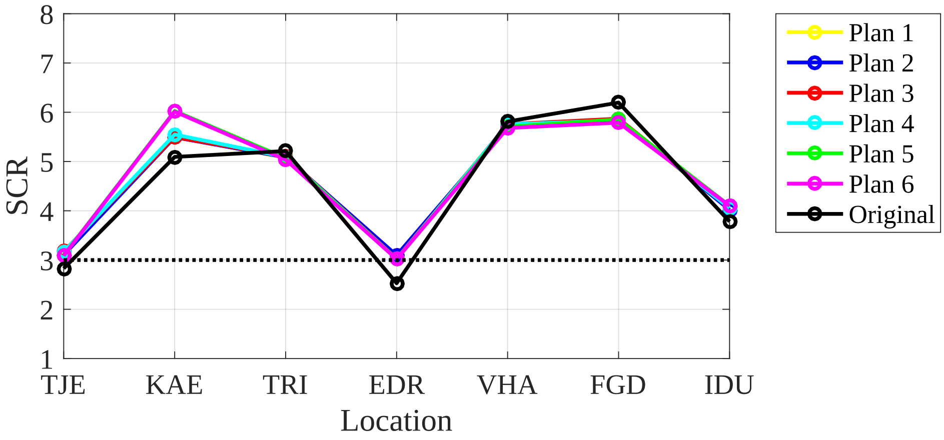

(a) with minimum SCR set to 3 (*M*=3)

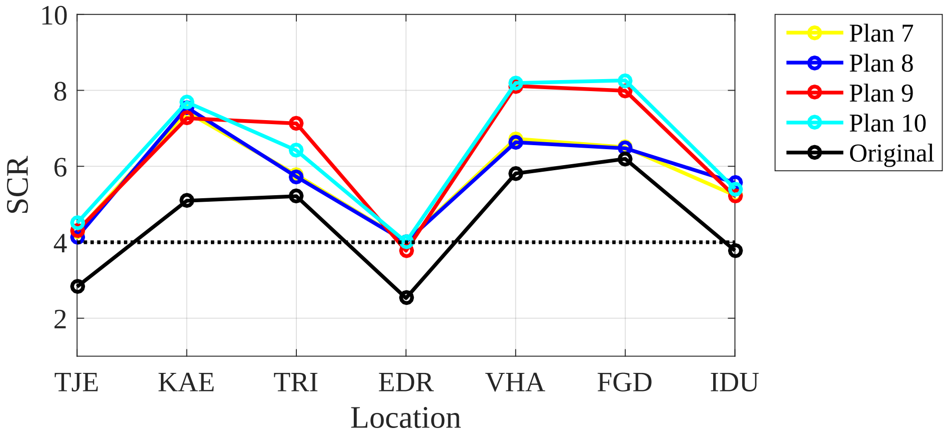

(b) with minimum SCR set to 4 (*M*=4)

Figure 4.16: Comparisons on system SCRs with different SC allocation plan

Table 4.7: Pre-fault conditions of the western Danish power system

Components	**Condition 1**	**Condition 2**
LCC-HVDC at TJE	Import 750 MW	Export 500 MW
VSC-HVDC at TJE	Import 500 MW	Export 500 MW
LCC-HVDC at VHA	Export 740 MW	Export 600 MW
LCC-HVDC at FGD	Export 600 MW	Export 400 MW
VSC-HVDC at EDR	Export 500 MW	Export 500 MW
Type-III wind farm at KAE	Generate 285 MW	Generate 570 MW
Type-III wind farm at TRI	Generate 285 MW	Generate 380 MW
Type-IV wind farm at EDR	Generate 360 MW	Generate 450 MW
The SG representing Germany	Generate 1070 MW	Generate 2150 MW

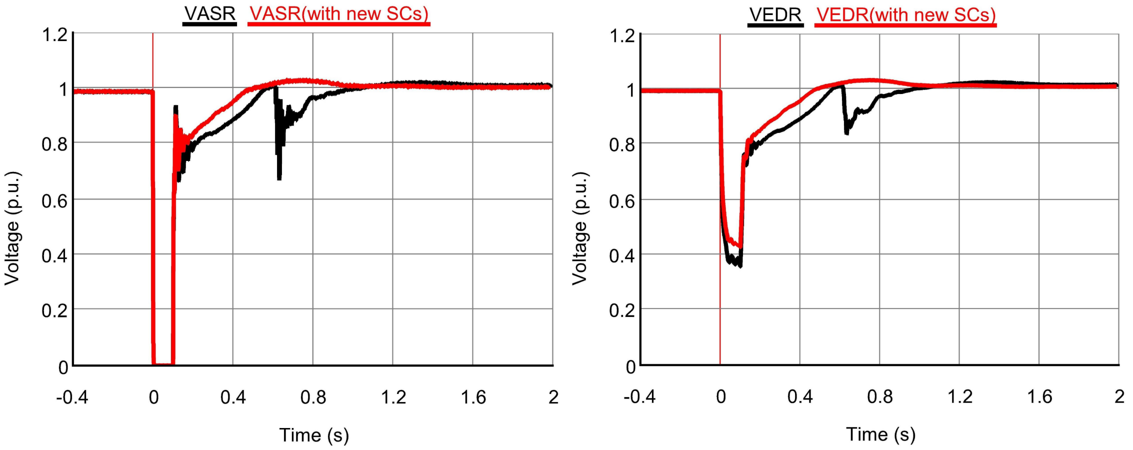

(a) ASR

(b) EDR

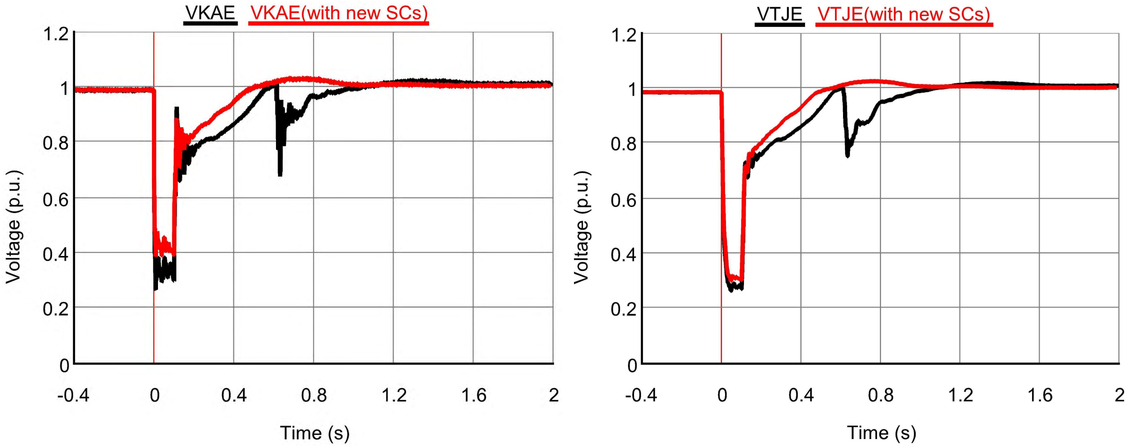

(c) KAE

(d) TJE

Figure 4.17: Comparisons on the voltage profiles for pre-fault condition 1

In order to illustrate the effect of synchronous condensers, the voltages of the DK1 system [see Fig. 3.1] are examined in RTDS without and with the new SCs from plan 5. Prior to the fault, all five SGs (ESVB3, NJVB3, SKVB3, FYVB7, and SSVB3) are disconnected from the grid and the grid in the German side is represented by an SG. All HVDC systems and wind farms are in operation according to the two different pre-fault conditions in Table 4.7. During the fault, VSC-HVDC systems and Type-IV wind farms are controlled to inject 1 p.u. reactive current with respect to their own ratings. At the zero time instant, a solid three-phase balanced is initiated at ASR and the fault lasts for 0.1 s. Figure 4.17–4.18 compares the voltages at ASR, EDR, KAE and TJE without and with the two SCs at EDR (270 Mvar) and KAE (135 Mvar).

It can be observed from Fig. 4.17–4.18 that system with two more SCs exhibits better fault-ride-through performances than the original system. With the help of the two more SCs, the system has higher retained voltages during the fault and has improved voltage profiles after the fault is cleared. For condition 2 where there is a higher power generation from the wind farms, the system is even not able to recover after the fault is cleared and the RTDS cannot run the whole system stably. In contrast, the added SCs help with the voltage recovery. The system maintains a stable operation after the fault is cleared.

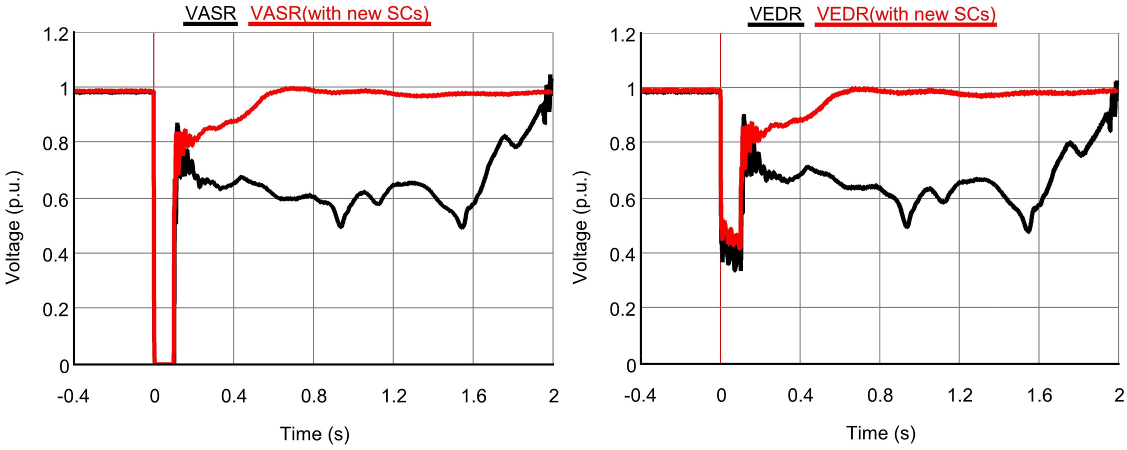

(a) ASR

(b) EDR

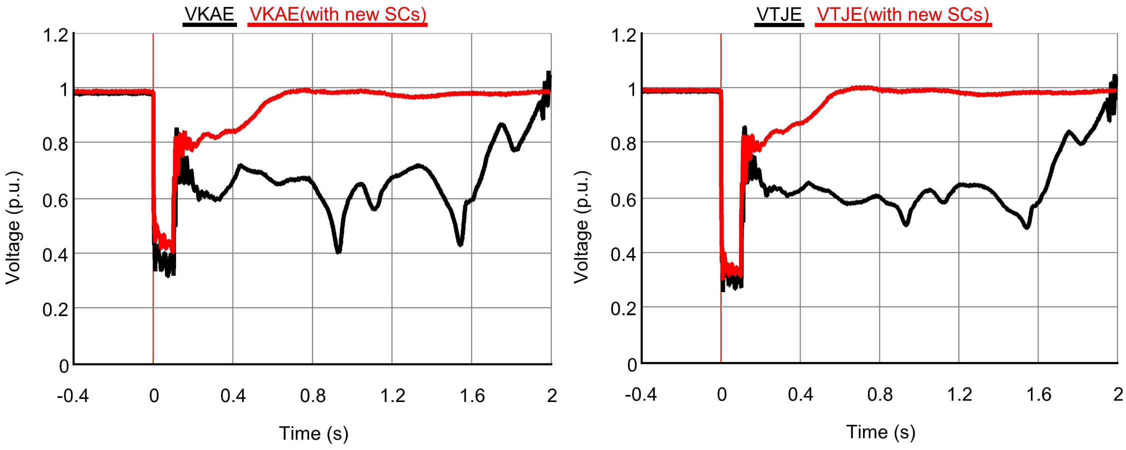

(c) KAE

(d) TJE

Figure 4.18: Comparisons on the voltage profiles for pre-fault condition 2

4.5 Conclusion

This chapter developed a static fault analysis method considering the short circuit current contributions from VSCs and the dual-sequence current controls of VSCs. The method uses the Norton's circuit model for synchronous sources and treats VSCs as voltage-dependent current sources. Flexible scalars were included in the method to reflect the various possible short circuit response of VSCs under unbalanced faults. Unlike the conventional fault analysis methods, both positive- and negative-sequence networks are active. The proposed method was verified through simulations with two different systems and can be applied to a system with multiple VSCs. It is able to analytically calculate the system retained voltages during different types of faults.

It was discovered through the RTDS simulations that the system may not have a stable response under unbalanced faults because of the negative-sequence reactive power injection from VSCs. In this case, the system voltages were not able to retain at a certain level during the fault but exhibited oscillatory behavior. This phenomenon has not been revealed by other studies and should raise people's attention regarding the evaluation of dual-sequence current controls of VSCs.

The proposed fault analysis method was used to help explain this phenomenon. Mathematically speaking, it turned out that the system did not have a solution to fulfill the dual-sequence current controls, the reactive power support requirement, and the boundary conditions of different sequence-networks defined by fault type. As a result, RTDS cannot find a stable operating point in such scenarios. This unstable phenomenon can occur when the share of negative-sequence reactive power from a single VSC or from multiple VSCs is high or when the system has a low short circuit power. The proposed fault analysis method provides a simple way to evaluate the impact of the negative-sequence reactive power injection from VSCs on the grid. It can help engineers to better understand the impact of multiple VSCs on a future low inertia power system. System operators can also take this as a reference to help define, evaluate, and reinforce the grid codes regarding the negative-sequence short circuit current injection from VSCs.

The static fault analysis method regarding three-phase balanced faults was further used to calculate the short circuit ratio (SCR) at converter terminals. The allocation of synchronous condensers was formulated into an optimization problem for improving the system SCRs while minimizing the total cost. Due to the simplicity of the proposed method, a power system does not need to have a detailed modeling to perform the fault analysis.

The optimization was applied to the simplified western Danish power system (DK1) of a future scenario. The allocation results showed that the DK1 system, with the retirement of the conventional power plants and the integration of more renewable energy, needs more synchronous condensers in the future to maintain the system SCRs at a certain level. It also showed that the points of common coupling may not always be the optimal locations for new synchronous condensers. If possible, the candidate locations should be expanded from the points of common coupling to all the buses at the transmission level.

CHAPTER 5

Microgrid – Case Study on Short Circuit Power Characterization

This chapter extends the use of the instantaneous power theory and the dual-sequence current controls presented in Chapter 2 to a typical microgrid setting to investigate the short circuit power characteristics in a grid with 100% penetration of renewable energy. The main results of this chapter were documented in [**Pub. H**].

5.1 Introduction

Conventional power systems have top-down structures where the centralized generation units deliver electric power to the users through transmission and distribution networks. However, such kind of power systems has limited resilience to transmission system failures, high power losses due to the long-distance transmission, and low levels of renewable energy penetration, etc. These deficiencies have given rise to the integration of Distributed Energy Resource (DER) in the distribution systems. With the DGs, energy storage devices, and electric vehicles, the conventionally passive distribution system is turning into an active one. Microgrid, as a special form of the distribution systems, has gained an increasing attention in recent years. It is an active low-voltage system, with controllable loads and DERs, that can either operate with the connection to the utility grids (grid-connected mode) or operate autonomously without the utility grids (islanded mode). The practice of microgrids has the advantages such as low greenhouse gas emission, high efficiency, continuous power supply, etc. [75]. It can be designed flexibly based on the actual needs and behaves like an aggregated, controllable load. However, most of the DERs interface with the microgrid through voltage source converters, which are not natural voltage sources. The characteristics of the short circuit power in microgrids will depend on not only the power electronics control but also the operation mode.

5.2 Islanded mode

Micrograds have two different operation modes, grid-connected mode and islanded mode. For grid-connected mode, VSCs are typically controlled as current sources to feed a certain amount active and reactive powers to the energized grid. The utility grid provides the voltage and frequency references to the VSCs so that the VSCs synchronize with the grid through PLL. All the content presented in Chapter 2 belongs to this type of VSCs (grid-feeding converters) and thus also applies to microgrids.

However, a microgrid will lose the support from the utility grid when operating in islanded mode. VSCs with the control systems shown in Fig. 2.11–2.13 can not work properly unless there is at least one reliable source such as local synchronous generators or energy storage devices that can provide the voltage and frequency references. This section focuses on the control aspects of a VSC to form the voltage amplitude and the frequency for an islanded microgrid (grid-forming converters).

5.2.1 Basic control structure

Figure 5.1 illustrates the configuration of a grid forming converter. It is usually fed by a reliable and stable DC voltage source such as batteries. In contrast with Fig. 2.6, the control system typically has two cascaded controllers and one voltage formation block. The voltage formation block, taking the desired amplitude of the voltage V_{ref} and the desired frequency f_{ref} as inputs, forms the voltage references for the voltage controller. The voltage controller is responsible for regulating the microgrid voltage (including the amplitude and the frequency) by generating current references for the inner current controller. Unlike 2.6 where the angle θ is provided by a PLL, the grid-forming converter obtains the angle from the voltage formation block. Therefore, the VSC is able to participate in the voltage amplitude and frequency regulation by controlling the active and reactive power injected to the grid [19].

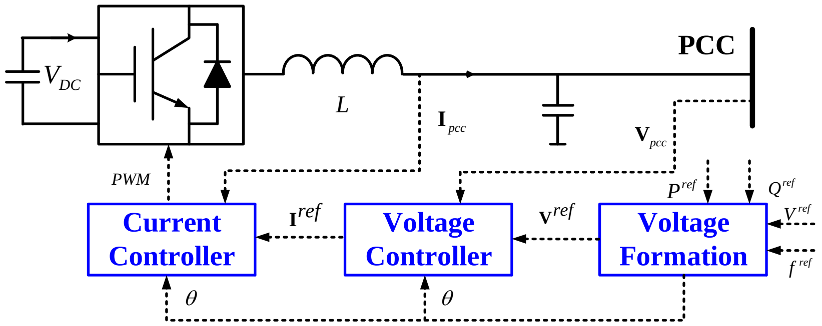

Figure 5.1: Configuration of a gird-forming VSC

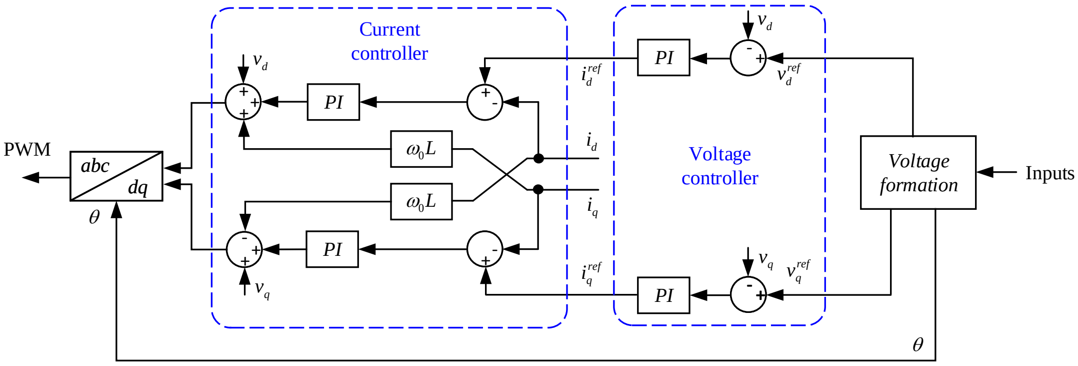

Figure 5.2: Control block diagram of a grid-forming converter

The detailed control block diagram of a grid-forming converter and three typical control structures of the voltage formation block are presented in Fig. 5.2 and Fig. 5.3, respectively. Figure 5.3(a) forms the voltage directly using the voltage and frequency references. In this way, the grid-forming converter emulates the role of an ideal AC source with a low-output impedance. This requires an extremely accurate synchronization system if more than one such kind of grid-forming converters operate in the islanded microgrid [19]. Figure 5.3(b) presents the application of the droop control in the voltage formation, which resembles a controlled AC source. The droop control typically has:

$$f^{ref'} = f^{ref} - m(P^{ref} - P^{meas}) \tag{5.1}$$

$$V^{ref'} = V^{ref} - n(Q^{ref} - Q^{meas}) \tag{5.2}$$

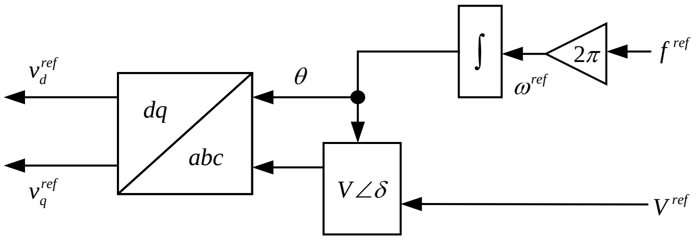

(a) Grid forming

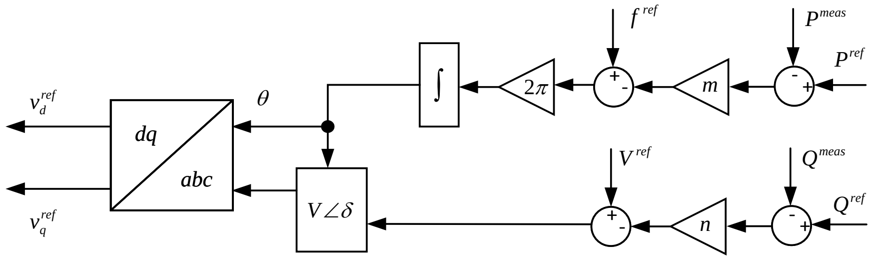

(b) Droop control

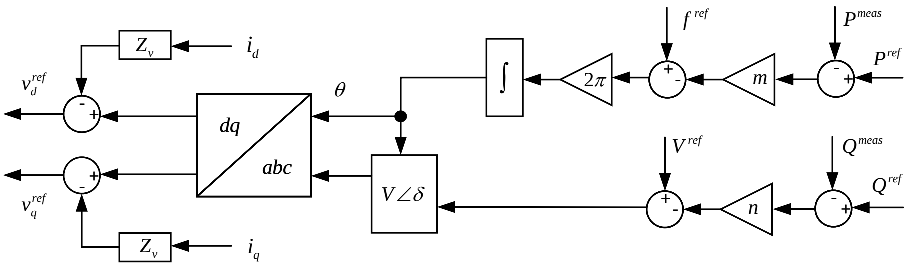

(c) Virtual impedance with droop control

Figure 5.3: Control block diagram of different voltage formations

where f^{ref} is frequency reference; V^{ref} is the voltage amplitude reference; m and n are the droops ($m < 0$, $n < 0$); P^{meas} and Q^{meas} are the measured output active and reactive powers of the converter. Figure 5.3(c) adds extra paths to the final voltage references using the concept of the virtual impedance to emulate the role of the impedance of a synchronous generator [172].

5.2.2 Dual-sequence current controls

It has been presented in Section 2.2.2 that the control system in Fig. 2.6 is not sufficient to control a VSC under unbalanced faults due to the coupling between the positive- and negative-sequence SRFs. This also applies to Fig. 5.2 for a grid-forming converter. In this study, to improve the performances of the grid-forming converter under unbalanced faults, the following modifications are made to the control systems shown in Fig. 5.2 and Fig. 5.3(c).

(1) Only positive-sequence component of the measurements are used in Fig. 5.2;
(2) Notch filters are used for the P_{meas} and Q_{meas} in Fig. 5.3(c) to filter out the oscillations at twice fundamental frequency under unbalanced faults;
(3) The negative-sequence current control loop in Fig. 2.11 is added to Fig. 5.2;

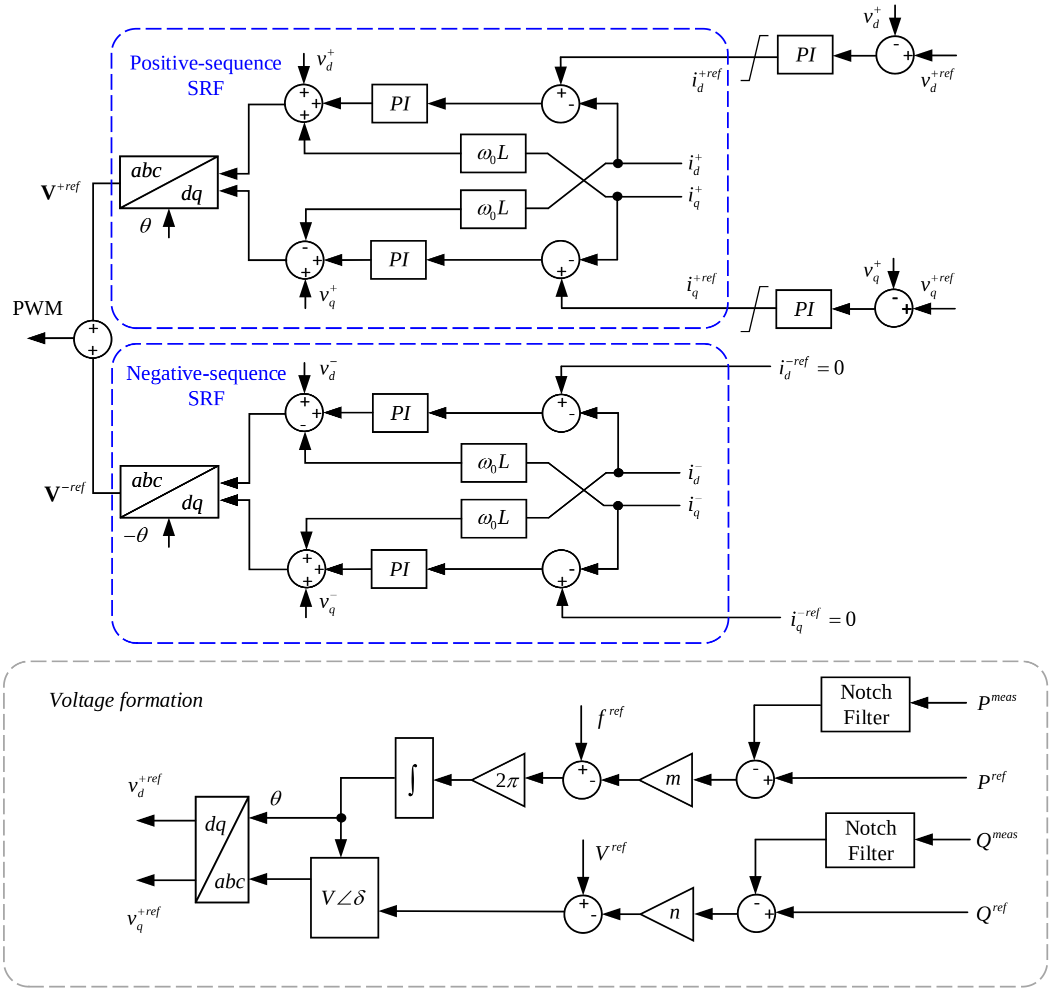

Figure 5.4: Control block diagram of a grid-forming VSC with negative-sequence current control

The grid-forming converter in a microgrid is responsible for providing the voltage and frequency references for the rest of the grid-feeding converters. The current references i_d^{+ref} and i_q^{+ref} are already determined by the voltage controller, which leaves only two variables i_d^{-ref} and i_q^{-ref} controllable. This means the various dual-sequence current control strategies in Chapter 2 cannot be easily and directly applied here. For simplicity, this case study sets the negative-sequence current references to zero, which means the grid-forming converter will inject three-phase balanced short circuit current under grid unbalanced faults. Therefore, the converter peak current limit (2.8) can be used in this case. Figure 5.4 presents the control block diagram of the grid-forming converter improved with a negative-sequence current control loop.

5.3 Short circuit current in microgrid

In this case study, the low voltage microgrid shown in Fig. 5.5 is modeled in RTDS. The utility grid feeds the microgrid through a 10 kV/0.4 kV transformer. Two VSC-interfaced DG units are connected to Bus 1 (solar array) and Bus 9 (Type IV wind turbine) respectively. One VSC-interfaced storage unit is connected to Bus 5. The three VSCs share the same parameters as listed in Table 5.1. When the microgrid is in grid-connected mode, the VSCs are operating as grid-feeding converters with the control system in Fig. 2.11. When the microgrid is in islanded mode, VSC 1 and VSC

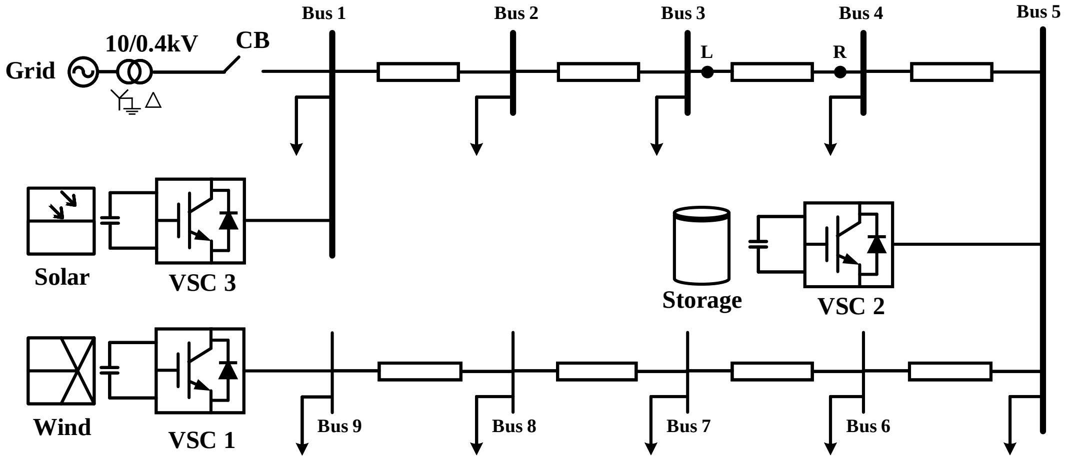

Figure 5.5: Single-line diagram of the microgrid

3 still act as grid-feeding converters while VSC 2 becomes the grid-forming converter with the control system in Fig. 5.4. The storage unit for VSC 2 is assumed to be large enough to provide the needed active power for the simulation time window. Each load (constant impedance type) has a power consumption at 8.07 kW when switched on. Table 5.2 lists line parameters of the feeder. The utility grid (10 kV, 50 Hz) has the short circuit power level at 300 kVA, and the R/X ratio at 5.

Table 5.1: VSC parameters of the microgrid

Type	**Nominal voltage** V_n	**Nominal capacity** S_n	**Peak current limit** I_{max}
Neutral-point clamped two level	400 V	60 MVA	163.3 A

Table 5.2: Feeder parameters of the microgrid

Line	1-2	2-3	3-4	4-5	5-6	6-7	7-8	8-9
R (Ω)	0.038	0.100	0.013	0.069	0.058	0.065	0.037	0.043
X (Ω)	0.007	0.012	0.002	0.008	0.007	0.008	0.005	0.004

Firstly, the operation of the microgrid in two different modes is examined by introducing disturbances to the microgrid. In grid-connected mode, VSCs 1-3 have the power output at 10 kW, 40 kW and 30 kW with unity power factor receptively. The utility grid imports around 4.5 kW active power from the microgrid. Then VSC 2 is switched off at 0.2 s time instant. Figure 5.6 shows that, VSC 1 and VSC 3 keep the same power output while the utility grid starts to export power to the microgrid at 0.2 s. Figure 5.7 shows the three-phase voltage and the frequency of Bus 5 during the transition.

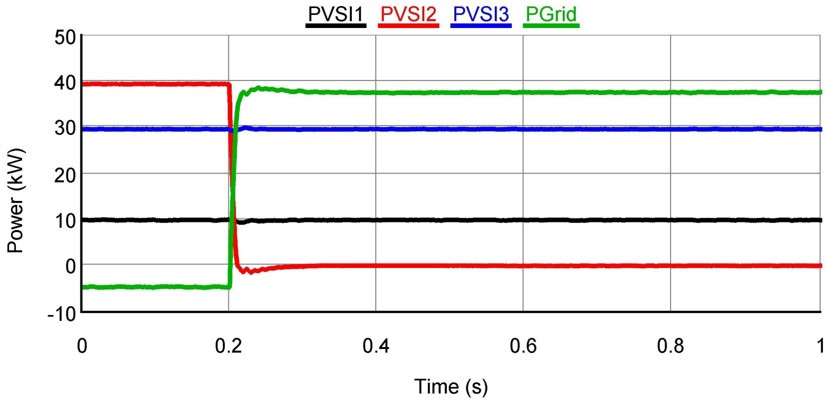

Figure 5.6: Power generations of the VSCs and the utility grid in grid-connected mode

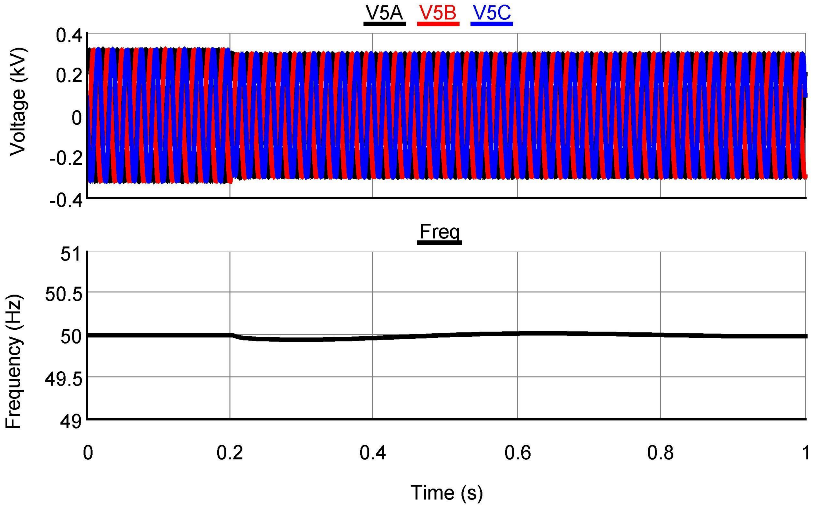

Figure 5.7: Three-phase voltage and frequency measured at Bus 5 in grid-connected mode

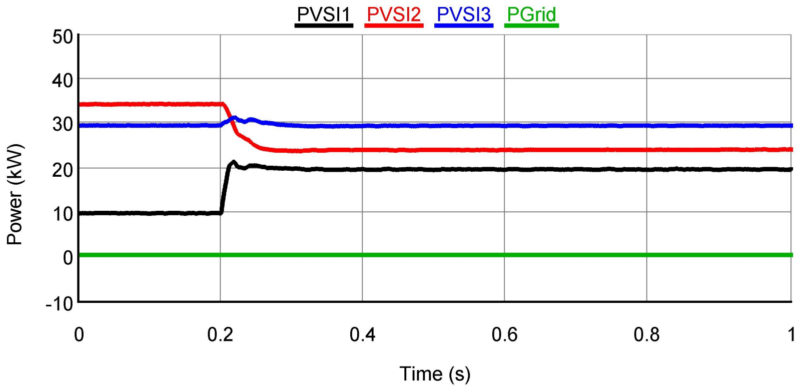

Figure 5.8: Power generations of the VSCs and the utility grid in islanded mode

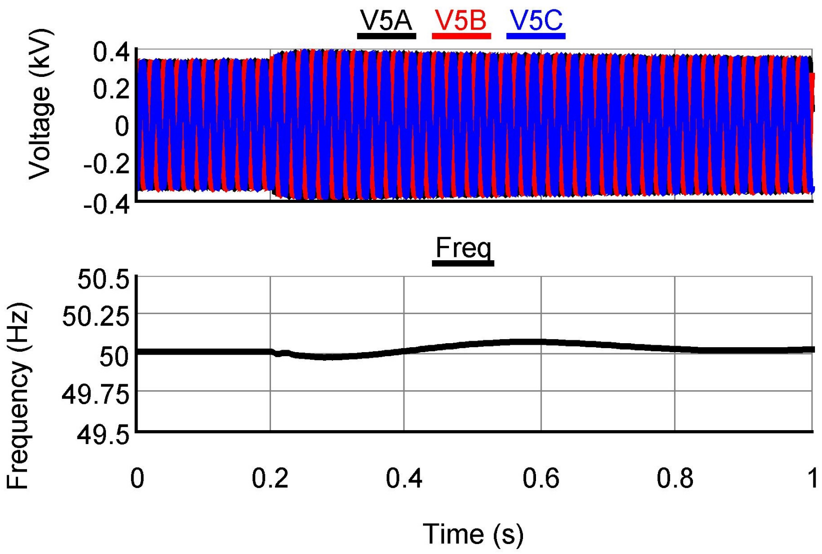

Figure 5.9: Three-phase voltage and frequency measured at Bus 5 in islanded mode

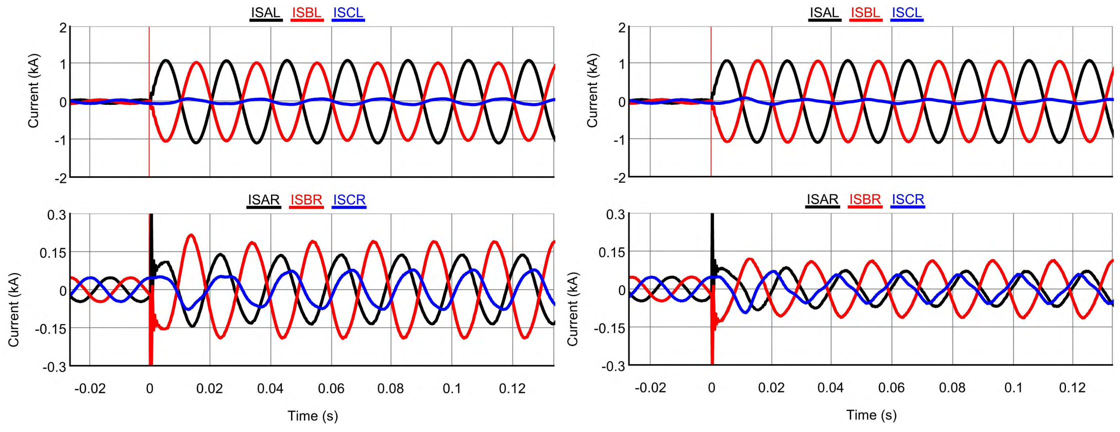

(a) A-B fault, constant active power control

(b) A-B fault,constant reactive power control

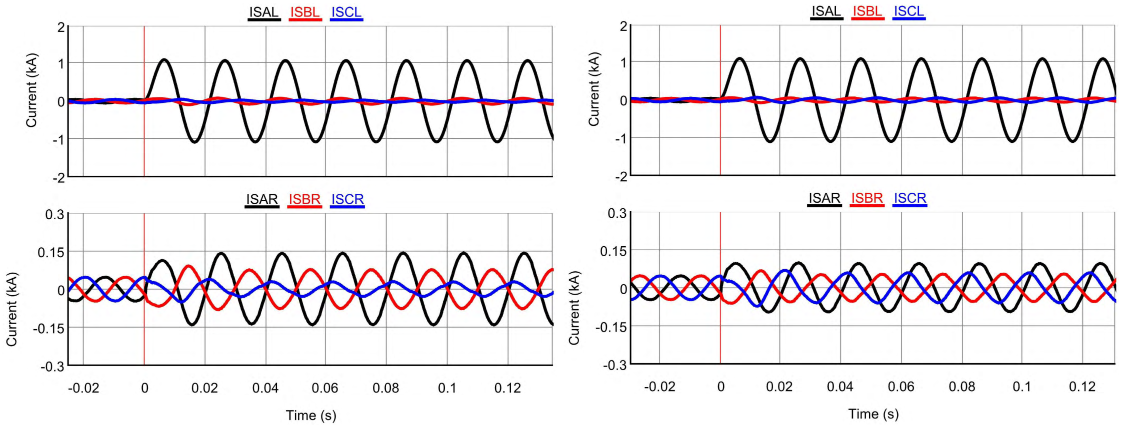

(c) A-g fault, constant active power control

(d) A-g fault, constant reactive power control

Figure 5.10: Short circuit current on line 3-4 subject to an unbalanced fault in the middle of line 3-4 in grid-connected mode

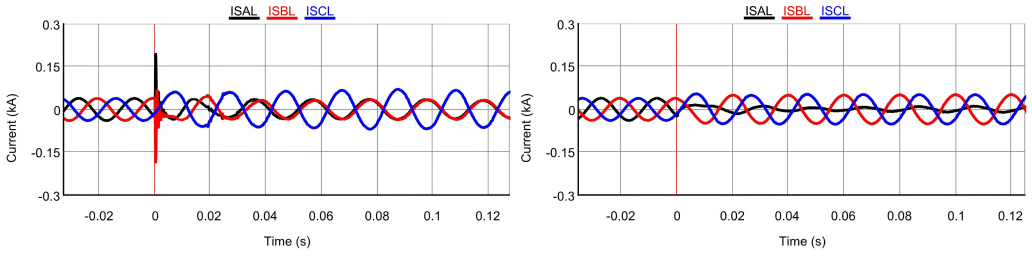

(a) Constant reactive power control, A-B fault (b) Constant reactive power control, A-g fault

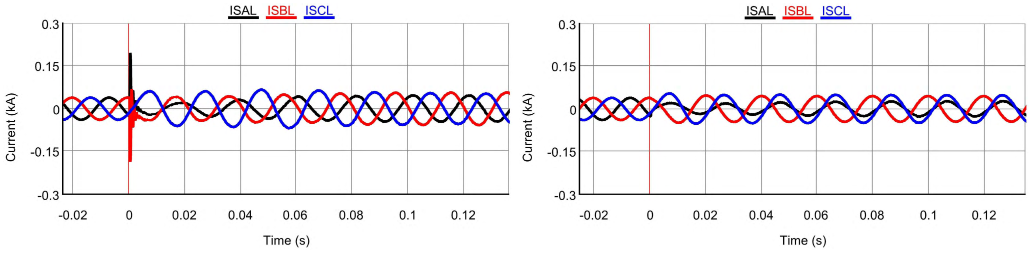

(c) Balanced current control, A-B fault (d) Balanced current control, A-g fault

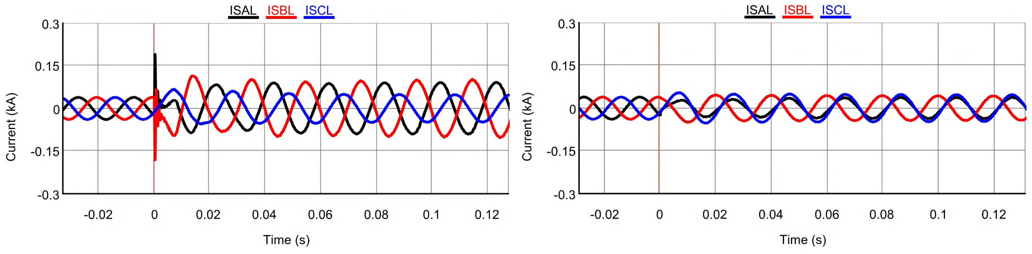

(e) Constant active power control, A-B fault (f) Constant active power control, A-g fault

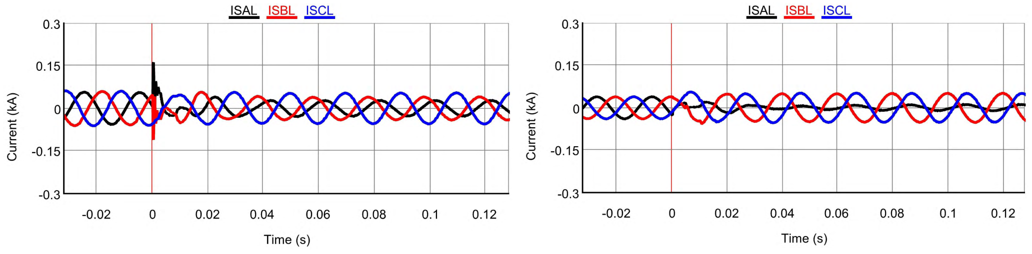

(g) FPNSPC ($k_p = 0.7$, $k_q = 0$), A-B fault (h) FPNSPC ($k_p = 0.7$, $k_q = 0$), A-g fault

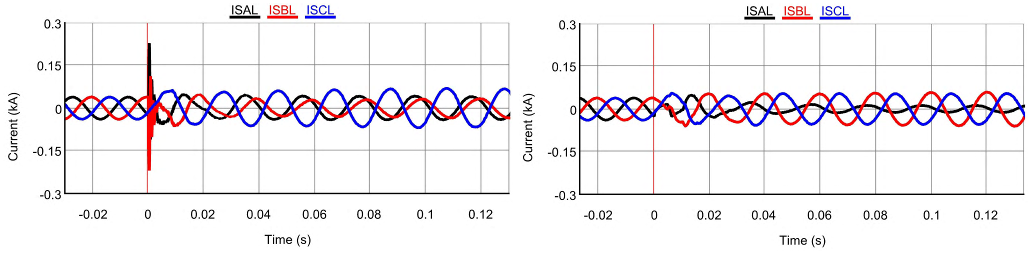

(i) FPNSPC ($k_p = 0.3$, $k_q = 0$), A-B fault (j) FPNSPC ($k_p = 0.3$, $k_q = 0$), A-g fault

Figure 5.11: Short circuit current at the point L subject to an unbalanced fault in the middle of line 3-4 with pre-fault condition (1)

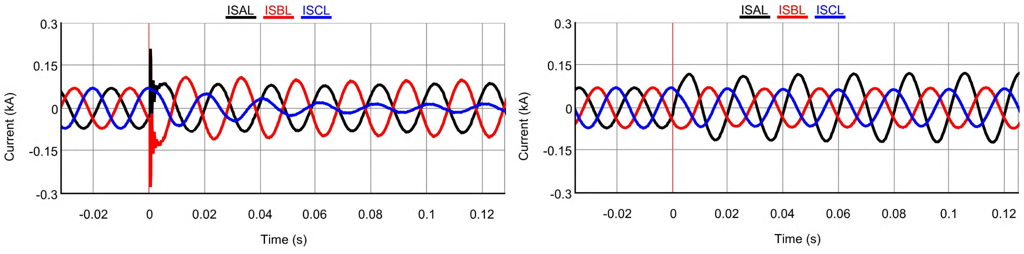

(a) A-B fault (b) A-g fault

Figure 5.12: Short circuit current at the point L subject to an unbalanced fault in the middle of line 3-4 with pre-fault condition (2)

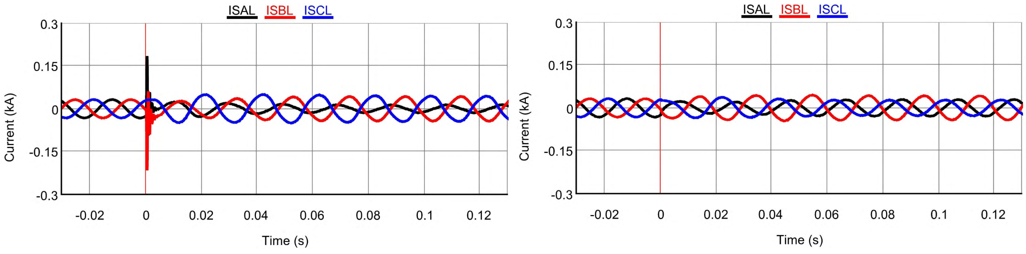

(a) A-B fault (b) A-g fault

Figure 5.13: Short circuit current at the point L subject to an unbalanced fault in the middle of line 3-4 with pre-fault condition (3)

With the circuit breaker CB switched off, the microgrid operates in islanded mode. The grid-feeding converters, VSC 1 and VSC 3, have the power output at 10 kW and 30 kW respectively with unity power factor. The grid-forming converter, VSC2, takes the responsibility to form the voltage and frequency reference for the microgrid. Then the power output from VSC 1 suddenly increases to 20 kW. Figure 5.8 shows that, VSC 3 keeps the same power output while VSC 2 reduces its power output to keep the voltage and frequency stable, which are presented in Fig. 5.9.

In the following simulations it is assumed that, under fault conditions, all VSCs only provide active short circuit current. The active power will be curtailed if the converter peak current limit is reached in any phase. For an A-B or an A-g fault in the middle of line 3-4 at 0 s time instant, Fig. 5.10 shows the short circuit current measured at the two ends of line 3-4 (point R and point L). In grid-connected mode, the short circuit current at the point L (ISAL, ISBL, and ISCL) is mainly contributed by the utility grid. It is much higher than the short circuit current at the point R (ISAR, ISBR, and ISCR). Therefore, the dual-sequence current control strategies have no notable impact on the short circuit current from the utility grid.

In contrast, the three VSCs become the sole sources of the short circuit current in islanded mode. Here three different pre-fault power flow conditions are considered:

(1) $P_{VSC1} = 10$ kW, $P_{VSC3} = 30$ kW, all loads equal to 8.07 kW;
(2) $P_{VSC1} = 60$ kW, $P_{VSC3} = 10$ kW, all loads equal to 8.07 kW;
(3) $P_{VSC1} = 10$ kW, $P_{VSC3} = 30$ kW, all loads equal to 8.07 kW (loads on bus 1, 2 and 3 are disconnected);

For each scenario, VSC 2, as the grid-forming converter, provides the remaining needed power to keep the load-generation balance. Figure 5.11 shows the short circuit current at the point L regarding an unbalanced fault in the middle of the line 3-4 for condition (1) with a variation on the dual-sequence current control strategies for VSC 1 and VSC 3. Figure 5.12–5.13 presents the short circuit current at the point L for condition (2) and (3) when both VSC 1 and VSC 3 use balanced current control. The short circuit current at the point R is also examined for these three conditions. The short circuit current on this side does not change notably with the variation on the control strategy. The reason is that, in terms of the electrical distance, VSC 1 is relatively far from the fault location. As a result, the short circuit power from VSC 1 during the fault tends to flow to the loads nearby rather than the fault location. The short circuit current at point R mainly comes from VSC 2, whose control strategy is fixed at balanced current control.

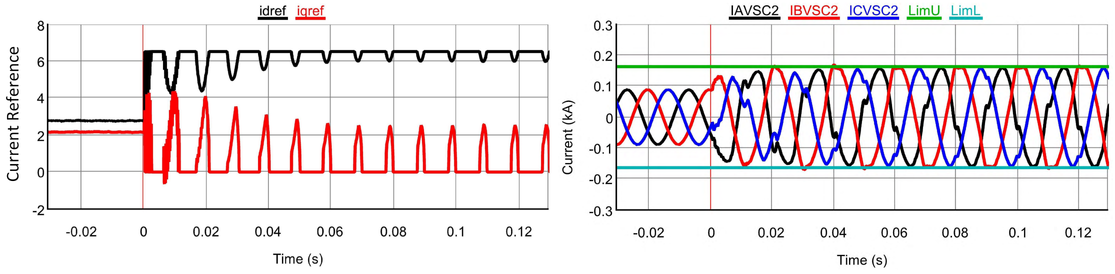

(a) Current references (without negative-sequence current control)

(b) Three-phase short circuit current (without negative-sequence current control)

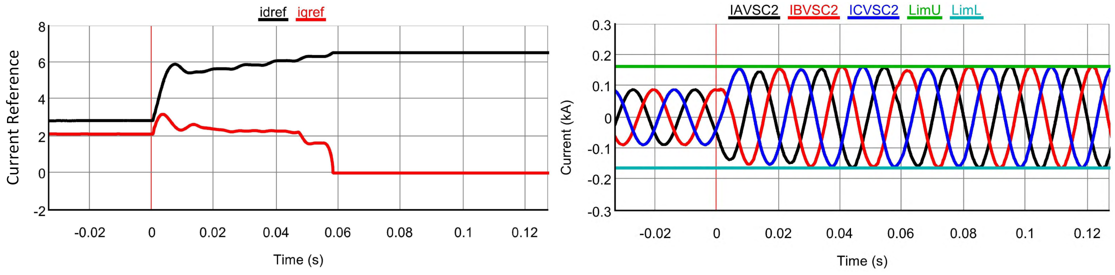

(c) Current references (with negative-sequence current control)

(d) Three-phase short circuit current (with negative-sequence current control)

Figure 5.14: Short circuit response of VSC 2 subject to an A-B fault at Bus 5 with pre-fault condition (1)

For an A-B fault at Bus 5, Fig. 5.14 compares the short circuit response of VSC 2 without the negative-sequence current control and with the negative-sequence current control. When there is no negative-sequence current control, the current references in Fig. 5.14(a) are mixed with oscillations at twice fundamental frequency and are "chopped" by the converter peak current limit. Correspondingly, the three-phase short circuit current shown in Fig. 5.14(b) does not have sinusoidal waveforms. In contrast, the response shown in Fig. 5.14(c)–(d) is improved by the negative-sequence current control.

5.4 Discussion

For the same fault type and location, the short circuit current in grid-connected mode differs significantly from that in islanded mode. Without the utility grid support, the short circuit current level in islanded mode drops drastically compared to grid-connected mode. Therefore, if the microgrid uses over-current protection with unique settings, the relays will not function as expected since they are not capable to distinguish the two different operation modes. In grid-connected mode, the faulty phase can be identified based on the current amplitude. For example, in Fig. 5.10(a)–(b), the currents in the faulty phases (phase A and phase B) are much higher than that in the healthy phase (phase C). Such kind of logic agrees with that for a conventional power system.

However, in islanded mode, the short circuit current can have diverse characteristics. Firstly, due to the converter peak current limit, the short circuit current level drops significantly. Secondly, the phases of the short circuit current are not consistent regarding a certain type of unbalanced faults. For example, for an A-B fault, the current in phase C has the highest amplitude in Fig. 5.11(a) rather than phase A and phase B. In Fig. 5.11(h), for an A-g fault, the current in phase A is even lower than the pre-fault current level. Typically, an over-current relay has the setting to operate at 2-10 times the full load current [76]. As a result, for an islanded microgrid, it is not possible to identify the faulty phases by just using the amplitude of the current. The difference between the current amplitudes in normal conditions and in fault conditions is not significant enough to distinguish the load current from the short circuit current.

It can be seen by comparing Fig. 5.12-5.13 to Fig. 5.11(c)–(d) that, the short circuit current characteristics also vary with the pre-fault power flow conditions for the same fault. Typically, the topology of a microgrid and the generation from DERs are dynamic, resulting in variations on the direction, the amplitude, and the phase angle of the short circuit current. This means that the non-directional or directional over-current relays with fixed setting are not sufficient for microgrid protection. It is reported in [173] that the directional over-current relay can even fail to identify the fault current direction in a microgrid environment.

The short circuit response of DERs is significantly different from that of synchronous sources. It varies very much with the deployed dual-sequence current control strategies. The conventional protection schemes based only on local measurement may not be appropriate for microgrids. Therefore, microgrid protection and power electronics control are in close correlation with each other for the future low inertia or zero inertia power systems. In order to develop a fast, selective and reliable protection system, the trend can turn to the application of adaptive relays, new protection schemes, high-speed communications or smart devices that consider the control aspects of the converters, to fill the gap between power system protection and power electronics control.

CHAPTER 6

Conclusion and future work

This Ph.D. project, as part of the larger project “Synchronous Condenser Application in Low Inertia Systems (SCAPP)”, concerned the assessment of short circuit power and protection systems for future low inertia power systems. For that purpose, the project classified, evaluated, and improved the short circuit response of voltage source converters considering the converter peak current limit and reactive power support capability; The performances of distance relays were evaluated through the developed hardware-in-the-loop test platform. Possible malfunctions of distance relays in low inertia power systems were discovered and identified; Synchronous condensers were considered as a key component for the future low inertia power systems. The effect of applying synchronous condensers at the point of common couplings of converters was investigated by examining different system properties. Based on the investigation, suggestions on how voltage source converters should be controlled during faults were provided for a better incorporation of synchronous condensers; To analytically perform the fault analysis in low inertia power systems, a static fault analysis method was developed considering the presence of voltage source converts and their dual-sequence current controls. The proposed method was used to explain a new unstable phenomenon in low inertia power systems, and to optimally allocate synchronous condensers for the future western Danish power system.

The presented work has touched the areas of: power electronics control, static and dynamic fault analysis, power system protection and relay testing, shunt compensation for transmission networks, system planning, and microgrid.

6.1 Conclusion

In this section, the conclusions of this dissertation will be presented in terms of the following four aspects.

6.1.1 Short circuit power in low inertia power systems

Low inertia power systems introduce not only changes in frequency characteristics, but also changes in short circuit power characteristics. In a conventional power system, synchronous generators are the main sources of short circuit power, whose characteristics are mainly decided by the physical properties and operating principles of the machines. In contrast, voltage source converters, which may become the main sources of short circuit power in converter-dominated power systems, have significantly different short circuit response from synchronous generators and synchronous condensers.

Voltage source converters do not provide short circuit current naturally and their response cannot be characterized by the conventional method. Firstly, the available short circuit current is limited in terms of magnitude. Due to the limited semiconductor overload capability, the magnitude of the short circuit current has to be controlled within the limit. As a result, there exists a competition between the active power injection and the reactive power injection. Even though the priority does not affect the short circuit current level, this competition creates a coupling between the frequency and voltage for low inertia power systems. For a transmission network, the reactive short circuit power helps increase the system retained voltage during fault conditions. However, the reactive power injection will in turn reduce the current margin left for active power injection. Since low inertia power systems are more vulnerable to frequency changes, significant reductions in the active power from converters may degrade the system frequency stability even though the duration of grid faults is typically short.

Secondly, being programmable is another crucial feature of the short circuit power from voltage source converters. For three-phase balanced faults where only positive-sequence components exist, voltage source converters (three-phase, three-wire types) can contribute a set of three-phase balanced short circuit current. The control freedom is dedicated to the active component or the reactive component priority, and the amount of the current (within the converter peak current limit).

However, the short circuit response of voltage source converters under grid unbalanced faults can be quite diverse. The conventional synchronous reference frame control only in positive-sequence is not sufficient for unbalanced faults. It results in distorted voltage and current outputs, and uncontrollable converter peak current due to the coupling between the positive- and negative-sequence synchronous reference frames, and the uncontrolled negative-sequence current. Therefore, it is necessary for voltage source converters to have current controls in both positive- and negative-sequence. This enables the converters to provide positive- and negative-sequence short circuit currents at the same time.

Regarding the dual-sequence current controls, even though the control system can be designed in different ways, it is how the current references are formulated in both sequences that mainly decides the characteristics of the short circuit power. This work has classified the dual-sequence current control strategies into two groups, one concerning the converters themselves, and one concerning the services that the converters can provide. Even though the control objectives and the current references vary significantly, the short circuit response of voltage sources converters under grid unbalanced faults can be regarded as an issue of how much active power and reactive power is injected, and what is the share of the positive-sequence powers or the share of the negative-sequence powers.

The provision of negative-sequence short circuit current can bring a variety of benefits to both the converters and the power systems. However, the different control objectives cannot be achieved at the same time as the control freedom is limited to positive- and negative-sequence current (magnitudes and phases). In addition, the complexity of the converter peak current limit increases when the converters are controlled to provide short circuit current in both sequences. A stiff current limiter that simply chops the current cannot effectively control the current or maximize the utilization of the converter rating. Instead, it is more straightforward to calculate how much power can be injected without violating the converter peak current. The short circuit current level can be increased, even though not too much, by fully utilizing the current margin.

Therefore, the existing grid codes regarding the short circuit response of power park modules should be reinforced considering the aspects of:

- Priority of active/reactive power/current injection

- How much power/current is injected
- What is the share of positive/negative-sequence power/current in case of unbalanced faults
- Fully utilizing of the converter rating
- The rising time of the power/current
- How the power/voltage/current should be measured/calculated

The relevant power system simulation software can also come up with generic models of converters with these aspects customizable. This will help system operators and researchers to better understand and utilize the programmable short circuit power from voltage source converters.

6.1.2 Distance protection in low inertia power systems

Considering the significant differences of the short circuit power in conventional power systems and low inertia power systems, this work has evaluated the performances of a commercial distance relay through hardware-in-the-loop tests taking the different short circuit response of voltage source converters into account. It is found that the speed and the reliability of distance protection will be degraded in low inertia power systems.

Firstly, due to the low short circuit current level, the distance relay requires a longer operation time in low inertia power systems. Even though the tested distance relay deploys impedance pick-up as the pick-up method, it still relies on the magnitude of the phase-current to active the impedance calculation. In addition, due to the possible phase discrepancy between the short circuit current from voltage source converters and synchronous sources under unbalanced faults, the combined short circuit current can even be too low to activate the distance relay for a two-phase fault within the protective zone, deteriorating the reliability of distance protection. Due to the absence of zero-sequence current, protection against two-phase faults is becoming critical. Therefore, phase-current monitoring is no longer sufficient to guarantee the speed and the reliability of distance protection.

Secondly, the present distance protection scheme can be strongly affected by the dual-sequence current controls of voltage source converters. This fact was left unnoticed by both power electronics engineers and protection engineers. This work has identified the possible malfunctions of distance relays under certain scenarios. When the short circuit current is solely provided by a voltage source converter, the deployment of constant reactive power control strategy will result in a refuse-to-trip failure of the distance relay for two-phase faults. The reason is that the short circuit currents in faulty phases become identical both in phase and in amplitude. This results in a zero value in the denominator of the impedance calculation equation for two-phase faults so that the relay cannot clearly identify the fault location.

In addition, the measuring error of distance relays caused by fault resistance will be enlarged in low inertia power systems under unbalanced faults. Significant overreach problem will arise if the converter prioritizes active power injection, while both overreach and underreach problems can occur if the converter prioritizes reactive power injection. This indeterminacy is a combined effect of the limited short circuit current level and the dual-sequence current control strategies, of which the distance protection is supposed to be independent. The effect of the pre-fault power conditions on the reach in conventional power systems will no longer hold true in low inertia power systems. This may invalidate the conventional countermeasures for underreach and overreach problems.

Therefore, non-pilot distance protection is not sufficient for the primary protection of transmission lines in low inertia power systems. From the author’s point of view, the above problems should be solved through the upgrading of the current distance protection scheme such as using the quantities of the remote terminal for impedance calculation, rather than through the converter controls. This is because the control system has to give consideration to the different converter constraints and the short circuit power provision already. There is not enough control freedom left to achieve another objective. Most importantly, the assessment of the protection systems in low inertia power systems should not ignore the control aspects of power electronics, especially the dual-sequence current control strategies and the converter peak current limit under unbalanced faults.

6.1.3 Synchronous condenser application in low inertia power systems

Even though it is a well-known fact that a synchronous condenser has short circuit contributions and adds inertia to a system as a synchronous generator does, it is still important to investigate the effect of synchronous condenser application in low inertia power systems considering the power electronics controls, for the better utilization of the advantages of synchronous condensers. Given the limited ancillary services that voltage source converters can provide, synchronous condensers are likely to be installed at the points of common coupling of wind power plants, photovoltaic power plants, storage units, and VSC-HVDC stations. This work has investigated the combined effect of voltage sources converters and synchronous condensers.

Firstly, synchronous condensers help retain relay performances with their short circuit contributions. However, there potentially exists a short circuit current cancellation problem under unbalanced faults when equipping a synchronous condenser at the point of common coupling. The phases of the short circuit current from voltage source converters and synchronous condensers can differ from each other significantly. As a result, the combined short circuit current in faulty phases is possible to be lowered down with the application of a synchronous condenser. This phenomenon is in particular critical for two-phase faults, where the zero-sequence short circuit current is not present. The problem can be avoided by not using the range between constant reactive power control and balanced current control in flexible oscillating power control strategy for the voltage source converters. Instead, with the same size of the synchronous condenser, constant active power control gives a higher short circuit level. In another word, constant active power control requires a smaller synchronous condenser to achieve the same short circuit current level compared to other control strategies.

Secondly, the effect of synchronous condensers on the grid voltages is different between during unbalanced faults and during three-phase balanced faults. For three-phase balanced faults, with only positive-sequence components present, the application helps increase the retained grid voltage during faults. However, synchronous condensers have less effect on the grid voltage than the control strategies of voltage sources converters during unbalanced faults. This is because synchronous condensers can only provide paths for negative-sequence current to flow, rather than actively provide negative-sequence short circuit current like voltage source converters. This work has shown the effect of different control strategies on the grid voltage and DC-side voltage under unbalanced faults with fully utilizing the converter rating.

Thirdly, due to the limited semiconductor overload capability, the effect of different voltage source converter control strategies on system frequency can be regarded as an issue of how much active power is curtailed during faults. The flowing of the negative-sequence active or reactive current can reduce the current margin for active power delivery. Even though the duration of a fault is typically short, frequency stability is still a crucial aspect in low inertia power systems. Therefore, the negative-sequence short circuit current from voltage source converters has the potential for frequency control during faults. The reduction of negative-sequence short circuit current is beneficial for under-frequency situations, while the increase of negative-sequence short circuit current is beneficial for over-frequency situations.

The different dual-sequence current control strategies of voltage source converters can raise problems such as non-conventional characteristics of short circuit current, a lack of negative-sequence voltage attenuation, DC-side voltage oscillations and excess active power curtailments under fault conditions. Synchronous condensers are able to mitigate these disadvantages if coordinated with the voltages source converters properly. This work has pointed out how the control of voltage source converters should be selected when incorporating synchronous condensers.

6.1.4 Fault analysis in low inertia power systems

With the presence of voltage source converters and their capability of negative-sequence short circuit current contributions, the conventional static fault analysis method becomes insufficient. In order to analytically perform the fault analysis in low inertia power systems, this work has developed a new static fault analysis method considering the short circuit contributions from voltage source converters and their dual-sequence current control strategies. The method can help estimate the retained voltages and the fault currents under different types of faults.

This work has also discovered a phenomenon that a low inertia power system may not have a stable response during unbalanced faults. This can happen when voltage source converters are controlled to provide too much negative-sequence reactive power, and when the short circuit power level of the system is low. The phenomenon was investigated and explained with the developed fault analysis method, which shows that the system does not have a solution mathematically so that it cannot operate stably during faults.

One the one hand, the developed method can be used for planning the future low inertia power systems. The system operators can gather the information from converter manufactures on how the converters are controlled during different types of faults, and in which way the converters participate in negative-sequence short circuit current contributions. Then an off-line study can be performed to see if the system has a solution mathematically for all types of fault at all buses. This examines the impact of multi-converters on the grid from a system level. Therefore, the system operator can determine the limit on the share of the negative-sequence reactive power each converter can provide. The developed method helps researchers and engineers to understand the short circuit response of a low inertia power system. It has the potential to be used for reinforcing the next generation of grid codes. The relevant power system simulation software can also improve this concept into an integrated function.

On the other hand, from the author's point of view, it may not be suitable anymore to keep the present form of grid codes regarding reactive current injection during voltage dips. Synchronous generators provide short circuit current naturally, not relying on any input. However, the present grid codes manually introduce a coupling between the grid retained voltage and the short circuit current from converters, which does not exist in a conventional power system. This coupling can potentially cause the power system not able to find a stable operating point, or an equilibrium, for low inertia power systems under fault conditions.

The proposed fault analysis method was further used to optimally allocate synchronous condensers for the western Danish power system of a future scenario. The allocation was formulated into an optimization problem minimizing the total cost while maintaining the system short circuit ratios above a certain level. The developed method is simple to use and does not require a detailed power system model for simulations. The results showed that, if possible, all buses should be considered as the candidate locations for new synchronous condensers rather than only the points of common coupling for converters. It also showed that there is a need of more synchronous condensers for the future western Danish power system to maintain the system short circuit ratios.

6.2 Future work

In the following, an outlook on future work and research challenges will be listed.

- The modeling of a detailed voltage converter together with its control system is time-consuming and the model has to occupy several processors in Real Time Digital Simulator. This limits the number of the converters that can be simulated. Therefore, it is necessary to develop a simplified model of voltage source converters while preserving the same short circuit response.

- The short circuit response of voltage source converters under grid unbalanced faults in this dissertation assumed that the reactive power references were generated based on a pre-defined profile. Since the available grid codes lack specific statements regarding power park modules under unbalanced faults, it would be necessary to investigate how grid codes should be formulated and what criteria should be used when doing the evaluations.

- In the literature, a variety of control strategies for voltage source converters under grid unbalanced faults requires the Thevenin equivalent impedance of the remaining network. The conventional methods to estimate the Thevenin equivalent impedance were developed based on the characteristics of synchronous generators. Nevertheless, how the Thevenin equivalent impedance should be obtained in a fast and accurate manner for a converter-dominated power system still remains a challenge.

- The distance relay testing in this dissertation was only in regard to the distance protection with classic method. It would also be interesting to see how the relay will response in low inertia power systems when distance protection with reactance method (RMD) is used.

- The distance relay testing in this dissertation did not consider any coordination or communication. It is also necessary to examine different pilot protection schemes of transmission lines such as permissive overreach transfer trip, direction comparison blocking, current differential, etc.

- The simulations and testing in this study assumed that the synchronous condensers always remains connected to the grid under fault conditions. However, the dynamics of the synchronous condenser should also be considered. It is important to integrate the generator protection into the hardware-in-the-loop tests to validate the settings of the generator relay such as reverse power protection, under- and over-excitation protection, under- and over-frequency protection, etc. The settings should guarantee that the synchronous condenser will not be tripped unnecessarily by the protection under grid faults or transients.

- The adverse impact from voltage source converters on distance protection was revealed in this dissertation. It would be useful to investigate, from the relay point of view, what can be improved in the protection algorithm to avoid or mitigate the impact. In addition, it can be observed from the literature that there is a gap between the areas of power electronics control and power system protection. These two areas will correlate strongly with each other for future low inertia power systems.

- The proposed fault analysis method used an iterative method. Therefore, an optimization approach was used to explore the solution of the defined equation set. However, the method can be further improved with more advanced computing techniques to efficiently decide if the system has a solution. It would be even more useful to determine the boundary between the unstable scenarios and the stable scenarios proactively rather than to examine each scenario passively.

- The allocation of synchronous condensers in this dissertation considered the advantage of synchronous condensers on short circuit contributions. It can be further improved by taking frequency issues into consideration so that the optimization distributes not only short circuit power but also inertia.

Bibliography

[1] "Energinet's RUS plan 2017," Energinet, Fredericia, Denmark, Rep. 2017. [Online]. Available: https://en.energinet.dk/About-our-reports/Reports/Rus-plan-2017-summary

[2] *Technical regulation 3.2.5 for wind power plants with a power output above 11 kW*, Energinet, Fredericia, Denmark, Jul. 2016. [Online]. Available: https://en.energinet.dk/Electricity/Rules-and-Regulations/Regulations-for-grid-connection

[3] "Energy and climate change," International Energy Agency, Paris, France, 2015. [Online]. Available: https://www.iea.org/publications/freepublications/publication/WEO2015SpecialReportonEnergyandClimateChange.pdf

[4] (2018, May) ABB, HVDC-what and why. [Online]. Available: http://www.abb.com/cawp/seitp202/3542d8666d0032d0c1257368002af3b6.aspx

[5] A. Korompili, Q. Wu, and H. Zhao, "Review of VSC HVDC connection for offshore wind power integration," *Renewable and Sustainable Energy Reviews*, vol. 59, pp. 1405 – 1414, Jun. 2016.

[6] "Energy strategy 2050-from coal, oil and gas to green energy," The Danish Ministry of Climate and Energy, Copenhagen, Denmark, Feb. 2011. [Online]. Available: http://www.danishwaterforum.dk/activities/Climate%20change/Dansk_Energistrategi_2050_febr.2011.pdf

[7] "Energi-til et grønt danmark," Energi-, Forsynings- og Klimaministeriet, Copenhagen, Denmark, Apr. 2018. [Online]. Available: https://efkm.dk/media/11859/energiudspil_2018.pdf

[8] (2018, May) Energinets anlaegsprojekter. [Online]. Available: https://energinet.dk/Anlaeg-og-projekter/Projektliste

[9] "Plan for støtte under forskel-udbud 2016," Energinet, Fredericia, Denmark, 2018. [Online]. Available: https://energinet.dk/Analyse-og-Forskning/ForskEL-og-ForskVE/ForskEL-og-ForskVE-doks/Plan-for-stoette-2016

[10] B. Kroposki, B. Johnson, Y. Zhang, V. Gevorgian, P. Denholm, B. M. Hodge, and B. Hannegan, "Achieving a 100% renewable grid: operating electric power systems with extremely high levels of variable renewable energy," *IEEE Power and Energy Mag.*, vol. 15, no. 2, pp. 61–73, Mar. 2017.

[11] F. Milano, F. Dörfler, G. Hug, D. J. Hill, and G. Verbič, "Foundations and chanllenges of low-inertia systems," in *Proc. 20th Power Syst. Computation Conf. (PSCC)*, Dublin, Ireland, 11-15 Jun. 2018, pp. 1–25.

[12] "Impact of inverter based generation on bulk power system dynamics and short-circuit performance," IEEE, Piscataway, NJ, USA, Tech. Rep., PES-TR68, Jul. 2018.

[13] K. Prasertwong, N. Mithulananthan, and D. Thakur, "Understanding low frequency oscillation in power systems," *Int. J. Elect. Eng. Educ.*, vol. 47, no. 3, pp. 248–262, Oct. 2012.

[14] "Fault current contributions from wind plants," in *Proc. 68th Annu. Conf. for Protective Relay Engineers*, College Station, TX, USA, 30 Mar.-2 Apr. 2015, pp. 137–227.

[15] "Black system South Australia 28 september 2016-final report," Australian Energy Market Operator Limited, Melbourne, Australia, Tech. Rep., Rep. Mar. 2017.

[16] B. Chen, A. Shrestha, F. A. Ituzaro, and N. Fischer, "Addressing protection challenges associated with Type 3 and Type 4 wind turbine generators," in *Proc. 68th Annu. Conf. for Protective Relay Engineers*, College Station, TX, USA, 30 Mar.-2 Apr. 2015, pp. 335–344.

[17] S. M. Holder, L. Hang, and B. K. Johnson, "Investigation of transmission line protection performance in an electric grid with electronically coupled generation," in *Proc. North Amer. Power Symp. (NAPS)*, Manhatan, KS, USA, 22-24 Sep. 2013.

[18] M. Nagpal and C. Henville, "Impact of power-electronic sources on transmission line ground fault protection," *IEEE Trans. Power Del.*, vol. 33, no. 1, pp. 62–70, Feb. 2018.

[19] J. Rocabert, A. Luna, F. Blaabjerg, and P. Rodríguez, "Control of power converters in AC microgrids," *IEEE Trans. Power Electron.*, vol. 27, no. 11, pp. 4734–4749, Nov. 2012.

[20] H. P. Beck and R. Hesse, "Virtual synchronous machine," in *Proc. 9th Int. Conf. on Elect. Power Quality and Utilisation*, Barcelona, Spain, 9-11 Oct. 2007, pp. 1–6.

[21] Q. C. Zhong and G. Weiss, "Synchronverters: inverters that mimic synchronous generators," *IEEE Trans. Ind. Electron.*, vol. 58, no. 4, pp. 1259–1267, Apr. 2011.

[22] (2018, May) The massive integration of power electronic devices. [Online]. Available: https://www.h2020-migrate.eu

[23] (2018, May) Prosmart, KPN-project ENERGIX. [Online]. Available: http://www.ntnu.edu/prosmart

[24] (2018, May.) Operation of low-inertia power systems. [Online]. Available: https://www.qub.ac.uk/schools/eeecs/Research/PhDStudy/Studentships-Dec2017/phd2018-66/

[25] P. C. Sen, *Principles of Electric Machines and Power Electronics*. New York, NY, USA: Wiley, 1989.

[26] (2018 May.) The stable way–synchronous condenser solutions. [Online]. Available: https://www.energy.siemens.com/hq/pool/hq/power-transmission/FACTS/Synchronous%20Condenser/Synchronous_Condenser.pdf

[27] (2018, May) Application of synchronous condensers. [Online]. Available: http://www.scapp.dk

[28] *COMMISSION REGULATION (EU) 2016/631 establishing a network code on requirements for grid connection of generators*, ENTSO-E, Brussels, Belgium, Apr. 2016. [Online]. Available: https://eur-lex.europa.eu/legal-content/EN/TXT/PDF/?uri=CELEX:32016R0631&from=EN

[29] *COMMISSION REGULATION (EU) 2016/1447 establishing a network code on requirements for grid connection of high voltage direct current systems and direct current-connected power park modules*, ENTSO-E, Brussels, Belgium, Aug. 2016. [Online]. Available: https://eur-lex.europa.eu/legal-content/EN/TXT/PDF/?uri=CELEX:32016R1447&from=EN

[30] M. Mohseni and S. M. Islam, "Review of international grid codes for wind power integration: diversity, technology and a case for global standard," *Renewable and Sustainable Energy Reviews*, vol. 16, no. 6, pp. 3876–3890, Apr. 2012.

[31] *Technical regulation 3.2.2 for PV power plants above 11 kW*, Energinet, Fredericia, Denmark, Jul. 2016. [Online]. Available: https://en.energinet.dk/Electricity/Rules-and-Regulations/Regulations-for-grid-connection

[32] M. Curzi, R. Sharma, and F. Martin, "In fault ride through reactive current rise time requirements of various European grid codes-analysis based on a full-converter wind turbine," *Wind Energy*, vol. 19, no. 6, pp. 1121–1133, Jun. 2016.

[33] J. Fortmann, R. Pfeiffer, E. Haesen, F. V. Hulle, F. Martin, H. Urdal, and S. Wachtel, "Fault-ride-through requirements for wind power plants in the ENTSO-E network code on requirements for generators," *IET Renewable Power Gener.*, vol. 9, no. 1, pp. 18–24, Jan. 2015.

[34] B. Weise, "Impact of K-factor and active current reduction during fault-ride-through of generating unit connected via voltage-sourced converters on power system stability," *IET Renewable Power Gener.*, vol. 9, no. 1, pp. 25 – 36, Jan. 2015.

[35] *The Grid Code Issue 5 Revision 22*, Nationalgrid, London, UK, May 2018. [Online]. Available: https://www.nationalgrid.com/sites/default/files/documents/00_FULL_GRID_CODE_I5R22_1.pdf

[36] *VDE Technische Anschlussbedingungen Hochspannung*, VDE, Berlin, Germany, Jan. 2015.

[37] *EirGrid Grid Code Version 6.0*, EirGrid Plc., Dublin, Ireland, Jul. 2015. [Online]. Available: http://www.eirgridgroup.com/site-files/library/EirGrid/GridCodeVersion6.pdf

[38] *Requisitos Técnicos de las Instalaciones Eólicas, Fotovoltaicas y Todas Aquellas Instalaciones de Producción Cuya Tecnología no Emplee un Generador Síncrono Conectado Directamente a La Red*, Red Eléctrica de España, Madrid, Spain, Oct. 2008.

[39] *Fault current contribution from PPMs and HVDC converters-ENTSO-E guidance document for national implementation for network codes on grid connection*, ENTSO-E, Brussels, Belgium, Nov. 2016. [Online]. Available: https://docstore.entsoe.eu/Documents/Network%20codes%20documents/NC%20RfG/161116_IGD_Fault%20Current%20Contribution%20from%20PPMs%20%20HVDC_for%20consultation_for%20publication.pdf

[40] E. Muljadi, N. Samaan, V. Gevorgian, J. Li, and S. Pasupulati, "Different factors affecting short circuit behavior of a wind power plant," *IEEE Trans. Ind. Appl.*, vol. 49, no. 1, pp. 284–292, Jan. 2013.

[41] E. Farantatos, U. Karaagac, H. Saad, and J. Mahseredjian, "Short circuit current contribution of converter interfaced wind turbines and the impact on system protection," in *Proc. 9th Bulk Power Syst. Dynamics and Control Symp. (IREP)*, Rethymnon, Greece, 25-30 Aug. 2013, pp. 1–9.

[42] H. Ahuja, G. Bhuvaneswari, and R. Balasubramanian, “Ride through of grid faults for PMSG based wind energy conversion systems,” in *Proc. IEEE 7th Int. Conf. on Ind. and Inform. Syst. (ICIIS)*, Chennai, India, 6-9 Aug. 2012, pp. 1–6.

[43] M. B. C. Salles, A. P. Grilo, and J. R. Cardoso, “Doubly fed induction generator and conventional synchronous generator based power plants: Operation during grid fault,” in *Proc. Int. Conf. on Renewable Energies and Power Quality (ICREPQ)*, Las Palmas de Gran Canaria, Spain, 13-15 Apr. 2011, pp. 1–5.

[44] Y. Jiang-Hafner, M. Hyttinen, and B. Paajarvi, “On the short circuit current contribution of HVDC light,” in *Proc. IEEE PES Transm. Distrib. Conf. and Exhibition*, Yokohama, Japan, 6-10 Oct. 2002, pp. 1926–1932.

[45] R. Li, C. D. Booth, A. Dyśko, A. J. Roscoe, and J. Zhu, “Development of models to study VSC response to AC system faults and the potential impact on network protection,” in *Proc. 49th Int. Universities Power Engineering Conf. (UPEC)*, Cluj-Napoca, Romania, 2-5 Sep. 2014, pp. 1–6.

[46] R. Devarapalli and R. K. Pandey, “HVDC converter control performance during faults (icaesm),” in *Proc. IEEE Int. Conf. on Advances in Eng., Sci. and Manage.*, Nagapattinam, Tamil Nadu, India, 30-31 Mar. 2012, pp. 386–392.

[47] P. Rioual, H. Pouliquen, and J. P. Louis, “Regulation of a PWM rectifier in the unbalanced network state using a generalized model,” *IEEE Trans. Power Electron.*, vol. 11, no. 3, pp. 495–502, 1996.

[48] G. Saccomando, J. Svensson, and A. Sannino, “Improving voltage disturbance rejection for variable-speed wind turbines,” *IEEE Trans. Energy Convers.*, vol. 17, no. 3, pp. 422–428, Nov. 2002.

[49] S. Ahn and D. Hyun, “New control scheme of three-phase PWM AC/DC converter without phase angle detection under the unbalanced input voltage conditions,” *IEEE Trans. Power Electron.*, vol. 17, no. 5, pp. 616–622, Nov. 2002.

[50] H. Song and K. Nam, “Dual current control scheme for PWM converter under unbalanced input voltage conditions,” *IEEE Trans. Ind. Electron.*, vol. 45, no. 5, pp. 722–729, Oct. 1998.

[51] H. Akagi, E. H. Watanabe, and M. Aredes, *Instantaneous power theory and applications to power conditioning*. Hoboken, NJ, USA: John Wiley & Sons, Inc., 2006.

[52] A. V. Timbus, P. Rodriguez, R. Teodorescu, M. Liserre, and F. Blaabjerg, “Control strategies for distributed power generation systems operating on faulty grid,” in *Proc. IEEE Int. Symp. on Ind. Electron.*, vol. 2, Montreal, Que., Canada, 9-13 Jul. 2006, pp. 1601–1607.

[53] P. Rodríguez, A. V. Timbus, R. Teodorescu, M. Liserre, and F. Blaabjerg, “Independent PQ control for distributed power generation systems under grid faults,” in *Proc. IEEE 32rd Annu. Conf. Ind. Electron. (IECON)*, Paris, France, 6-10 Nov. 2006, pp. 5185–5190.

[54] R. Teodorescu, M. Liserre, and P. Rodríguez, *Grid converters for photovoltaic and wind power systems*. Chichester, UK: John Wiley & Sons, Ltd., 2011.

[55] H. D. Tafti, A. I. Maswood, Z. Lim, G. H. P. Ooi, and P. H. Raj, "A review of active/reactive power control strategies for PV power plants under unbalanced grid faults," in *Proc. IEEE Innovative Smart Grid Technologies-Asia (ISGT)*, Bangkok, Thailand, 3-6 Nov. 2015.

[56] M. P. Kazmierkowski and L. Malesani, "Current control techniques for three-phase voltage-source PWM converters: a survey," *IEEE Trans. Ind. Electron.*, vol. 45, no. 5, pp. 691–703, Oct. 1998.

[57] A. Yazdani and R. Iravani, *Voltage-sourced converters in power systems: modeling, control, and applications*. Hoboken, NJ, USA: John Wiley & Sons, Inc., 2010.

[58] A. Timbus, M. Liserre, R. Teodorescu, P. Rodríguez, and F. Blaabjerg, "Evaluation of current controllers for distributed power generation systems," *IEEE Trans. Power Electron.*, vol. 24, no. 3, pp. 654–664, Mar. 2009.

[59] F. Blaabjerg, R. Teodorescu, M. Liserre, and A. V. Timbus, "Overview of control and grid synchronization for distributed power generation systems," *IEEE Trans. Ind. Electron.*, vol. 53, no. 5, pp. 1398–1409, Oct. 2006.

[60] J. D. Glover, M. S. Sarma, and T. J. Overbye, *Power system analysis and design, 5th Edition*. Stamford, CT, USA: Cengage Learning, 2015.

[61] *DIgSILENT PowerFactory user manual*, DIgSILENT GmbH, Gomaringen, Germany, Oct. 2015.

[62] *IEC 60909 Short circuit currents in three phase a.c. systems calculation of currents*, International Electrotechnical Commission, Geneva, Switzerland, Jul. 2001.

[63] Ö. Göksu, R. Teodorescu, C. L. Bak, F. Iov, and P. C. Kjær, "Impact of wind power plant reactive current injection during asymmetrical grid faults," *IET Renewable Power Gener.*, vol. 7, no. 5, pp. 484–492, Sep. 2013.

[64] T. Neumann, T. Wijnhoven, G. Deconinck, and I. Erlich, "Enhanced dynamic voltage control of Type 4 wind turbines during unbalanced grid faults," *IEEE Trans. on Energy Convers.*, vol. 30, no. 4, pp. 1650–1659, Dec. 2015.

[65] T. Wijnhoven, G. Deconinck, T. Neumann, and I. Erlich, "Control aspects of the dynamic negative sequence current injection of Type 4 wind turbines," in *Proc. IEEE PES General Meeting Conf. Expo.*, National Harbor, MD, USA, 27-31 Jul. 2014, pp. 1–5.

[66] D. M. Bui, "Simplified and automated fault-current calculation for fault protection system of grid-connected low-voltage AC microgrids," *Int. J. of Emerging Electric Power Syst.*, vol. 18, no. 2, pp. 1–24, Mar. 2017.

[67] B. Dağ, A. R. Boynueğri, Y. Ateş, A. Karakaş, A. Nadar, and M. Uzunoğlu, "Static modeling of microgrids for load flow and fault analysis," *IEEE Trans. Power Syst.*, vol. 32, no. 3, pp. 1990–2000, May 2017.

[68] C. A. Plet and T. C. Green, "Fault response of inverter interfaced distributed generators in grid-connected applications," *Electric Power Syst. Research*, vol. 106, pp. 21 – 28, Jan. 2014.

[69] A. Mathur, B. Das, and V. Pant, "Fault analysis of unbalanced radial and meshed distribution system with inverter based distributed generation (IBDG)," *Int. J. of Elect. Power and Energy Syst.*, vol. 85, pp. 164 – 177, Feb. 2017.

[70] D. V. Tu, S. Chaitusaney, and A. Yokoyama, "Maximum-allowable distributed generation considering fault ride-through requirement and reach reduction of utility relay," *IEEE Trans. Power Del.*, vol. 29, no. 2, pp. 534–541, Apr. 2014.

[71] "Wind power plant short-circuit modeling guide," Sandia National Laboratories, Albuquerque, NM and Livermore, CA, Tech. Rep., SAND2012-6664, Aug. 2012.

[72] A. P. Moura, J. P. Lopes, A. A. de Moura, J. Sumaili, and C. Moreira, "IMICV fault analysis method with multiple PV grid-connected inverters for distribution systems," *Electric Power Syst. Research*, vol. 119, pp. 119 – 125, Feb. 2015.

[73] H. Hooshyar and M. E. Baran, "Fault analysis on distribution feeders with high penetration of PV systems," *IEEE Trans. Power Syst.*, vol. 28, no. 3, pp. 2890–2896, Aug. 2013.

[74] P. T. Manditereza and R. Bansal, "Renewable distributed generation the hidden challenges a review from the protection perspective," *Renewable and Sustainable Energy Reviews*, vol. 58, pp. 1457–1465, May 2016.

[75] S. A. Hosseini, H. A. Abyaneh, S. H. H. Sadeghi, F. Razavi, and A. Nasiri, "An overview of microgrid protection methods and the factors involved," *Renewable and Sustainable Energy Reviews*, vol. 64, pp. 174–186, Oct. 2016.

[76] A. A. Memon and K. Kauhaniemi, "A critical review of AC microgrid protection issues and available solutions," *Electric Power Syst. Research*, vol. 129, pp. 23–31, Dec. 2015.

[77] R. Li, C. Booth, A. Dyśko, A. Roscoe, H. Urdal, and J. Zhu, "Protection challenges in future converter dominated power systems: demonstration through simulation and hardware tests," in *Proc. IET Int. Conf. Renewable Power Gener. (RPG)*, Beijing, China, 17-18 Oct. 2015.

[78] C. C. Teixeira and H. Leite, "The influence of a VSC based HVDC link on distance protection relay assessed by CAPE software," in *Proc. IEEE PowerTech Conf.*, Manchester, UK, 18-22 Jun. 2017, pp. 1–4.

[79] L. He, C. Liu, A. Pitto, and D. Cirio, "Distance protection of AC grid with HVDC-connected offshore wind generators," *IEEE Trans. Power Del.*, vol. 29, no. 2, pp. 493–501, Apr. 2014.

[80] F. Iov, A. D. Hansen, P. Sørensen, and N. A. Cutululis, "Mapping of grid faults and grid codes," Risø Nat. Lab., Roskilde, Denmark, Tech. Rep., Risø-R-1617(EN), Jul. 2007.

[81] A. D. Hansen, N. A. Cutululis, H. Markou, P. Sørensen, and F. Iov, "Grid fault and design-basis for wind turbines-final report," Risø Nat. Lab., Roskilde, Denmark, Tech. Rep., Risø-R-1714(EN), Jan. 2010.

[82] A. Roy and B. K. Johnson, "Transmission side protection performance with Type-IV wind turbine system integration," in *Proc. North Amer. Power Symp. (NAPS)*, Pullman, Washington, USA, 7-9 Sep. 2014.

[83] A. Hooshyar, M. A. Azzouz, and E. F. El-Saadany, "Distance protection of lines emanating from full-scale converter-interfaced renewable energy power plants part I: problem statement," *IEEE Trans. Power Del.*, vol. 30, no. 4, pp. 1770–1780, Aug. 2015.

[84] M. M. Alam, H. Leite, J. Liang, and A. D. S. Carvalho, "Effects of VSC based HVDC system on distance protection of transmission lines," *Int. J. of Elect. Power and Energy Syst.*, vol. 92, pp. 245–260, Nov. 2017.

[85] M. M. Alam, H. Leite, N. Silva, and A. da Silva Carvalho, "Performance evaluation of distance protection of transmission lines connected with VSC-HVDC system using closed-loop test in RTDS," *Electric Power Syst. Research*, vol. 152, pp. 168 – 183, 2017.

[86] R. Li, C. Booth, A. Dyśko, A. Roscoe, H. Urdal, and J. Zhu, "A systematic evaluation of network protection responses in future converter-dominated power systems," in *Proc. IET 13th Int. Conf. on Develop. in Power Syst. Protection (DPSP)*, Edinburgh, UK, 7-10 Mar. 2016, pp. 1–7.

[87] A. Hooshyar, M. A. Azzouz, and E. F. El-Saadany, "Distance protection of lines emanating from full-scale converter-interfaced renewable energy power plants part II: solution description and evaluation," *IEEE Trans. Power Del.*, vol. 30, no. 4, pp. 1781–1791, Aug. 2015.

[88] I. Erlich, T. Neumann, F. Shewarega, P. Schegner, and J. Meyer, "Wind turbine negative sequence current control and its effect on power system protection," in *Proc. IEEE PES General Meeting*, Denver, CO, USA, 21-25 Jul. 2013, pp. 1–5.

[89] P. E. Marken, A. C. Depoian, J. Skliutas, and M. Verrier, "Modern synchronous condenser performance considerations," in *Proc. IEEE PES General Meeting*, San Diego, CA, USA, 24-29 Jul. 2011, pp. 1–5.

[90] M. Nambiar and Z. Konstantinovic, "Impact of using: synchronous condensers for power system stability and improvement of short-circuit power in mining projects," *Mining Eng.*, vol. 67, no. 1, pp. 38–44, Jan. 2015.

[91] F. B. K. Mahmood, S. Ahmad, G. Mukit, M. T. I. Shuvo, S. Razwan, M. N. I. Maruf, and F. M. Albatsh, "Weakest location exploration in IEEE-14 bus system for voltage stability improvement using STATCOM, synchronous condenser and static capacitor," in *Proc. Int. Conf. on Elect. Comput. and Commun. Eng. (ECCE)*, Cox's Bazar, Bangladesh, 16-18 Feb. 2017, pp. 623–629.

[92] M. Nedd, Q. Hong, K. Bell, C. Booth, and P. Mohapatra, "Application of synchronous compensators in the GB transmission network to address protection challenges from increasing renewable generation," in *Proc. Cigre Study Committee B5 Colloq.*, Auckland, New Zealand, 11-15 Sep. 2016, pp. 1–6.

[93] S. Kynev, G. Pilz, and H. Schmitt, "Comparison of modern STATCOM and synchronous condenser for power transmission systems," in *Proc. IEEE Elect. Power and Energy Conf. (EPEC)*, Ottawa, Canada, 12-14 Oct. 2016, pp. 1–6.

[94] Y. Liu, S. Yang, S. Zhang, and F. Z. Peng, "Comparison of synchronous condenser and STATCOM for inertial response support," in *Proc. IEEE Energy Convers. Congr. and Expo. (ECCE)*, Pittsburgh, PA, USA, 14-18 Sep. 2014, pp. 2684–2690.

[95] H. Zhang, J. P. Hasler, N. Johansson, L. Ängquist, and H. P. Nee, "Frequency response improvement with synchronous condenser and power electronics converters," in *Proc. IEEE 3rd Int. Future Energy Electron. Conf. (IFEEC) and ECCE Asia*, Kaohsiung, Taiwan, 3-7 Jun. 2017, pp. 1002–1007.

[96] Nahid-Al-Masood, R. Yan, T. K. Saha, and N. Modi, “Frequency response and its enhancement using synchronous condensers in presence of high wind penetration,” in *Proc. IEEE PES General Meeting*, Denver, CO, USA, 26-30 Jul. 2015, pp. 1–5.

[97] P. E. Marken, D. LaForest, R. D’Aquila, D. Wallace, E. Kronbeck, and J. Skliutas, “Dynamic performance of the next generation synchronous condenser at VELCO,” in *Proc. IEEE PES Power Syst. Conf. Expo.*, Seattle, WA, USA, 15-18 Mar. 2009, pp. 1–5.

[98] F. O. Igbinovia, G. Fandi, Z. Müller, J. Švec, and J. Tlustý, “Optimal location of the synchronous condenser in electric-power system networks,” in *Proc. 2016 17th Int. Scientific Conf. on Electric Power Eng. (EPE)*, Prague, Czech Republic, 16-18 May 2016, pp. 1–6.

[99] Y. Singh, P. Chopra, and R. Singh., “Optimal placement of synchronous condensers for power quality improvement in transmission system by using etap power station,” *J. of Elect. and Electron. Engineering*, vol. 11, no. 4, pp. 63–73, Jul./Aug. 2016.

[100] N. Masood, R. Yan, T. K. Saha, and S. Bartlett, “Post-retirement utilisation of synchronous generators to enhance security performances in a wind dominated power system,” *IET Gener., Transm. Distrib.*, vol. 10, no. 13, pp. 3314–3321, Oct. 2016.

[101] Z. H. Rather, Z. Chen, P. Thøgersen, and P. Lund, “Dynamic reactive power compensation of large-scale wind integrated power system,” *IEEE Trans. Power Syst.*, vol. 30, no. 5, pp. 2516–2526, Sep. 2015.

[102] E. Marrazi, G. Yang, and P. Weinreich-Jensen, “Allocation of synchronous condensers for restoration of system short-circuit power,” *J. of Modern Power Syst. and Clean Energy*, vol. 6, no. 1, pp. 17–26, Jan. 2018.

[103] H. Saadat, *Power system analysis, 3rd Edition*. Arlington, VA, USA: PSA Publishing LLC, 2010.

[104] K. R. Padiyar and N. Prabhu, “Modelling, control design and analysis of VSC based HVDC transmission systems,” in *Proc. Int. Conf. on Power Syst. Technology (PowerCon)*, Singapore, 21-24 Nov. 2004, pp. 774–779.

[105] T. Nakajima and S. Irokawa, “A control system for HVDC transmission by voltage sourced converters,” in *Proc. IEEE PES Summer Meeting Conf.*, Edmonton, Alta., Canada, 18-22 Jul. 1999, pp. 1113–1119.

[106] N. P. W. Strachan and D. Jovcic, “Stability of a variable-speed permanent magnet wind generator with weak AC grids,” *IEEE Trans. Power Del.*, vol. 25, no. 4, pp. 2779–2788, Oct. 2010.

[107] M. Reyes, P. Rodríguez, S. Vazquez, A. Luna, R. Teodorescu, and J. M. Carrasco, “Enhanced decoupled double synchronous reference frame current controller for unbalanced grid-voltage conditions,” *IEEE Trans. Power Electron.*, vol. 27, no. 9, pp. 3934–3943, Sep. 2012.

[108] S. Fukuda and T. Yoda, “A novel current-tracking method for active filters based on a sinusoidal internal model for PWM invertors,” *IEEE Trans. Ind. Appl.*, vol. 37, no. 3, pp. 888–895, May 2001.

[109] A. V. Timbus, M. Ciobotaru, R. Teodorescu, and F. Blaabjerg, “Adaptive resonant controller for grid-connected converters in distributed power generation systems,” in *Proc. IEEE Appl. Power Electron. Conf. Expo. (APEC)*, Dallas, TX, USA, 19-23 Mar. 2006, pp. 1601–1606.

[110] D. N. Zmood and D. G. Holmes, “Stationary frame current regulation of pwm inverters with zero steady-state error,” *IEEE Trans. Power Electron.*, vol. 18, no. 3, pp. 814–822, May 2003.

[111] E. Twining and D. G. Holmes, “Grid current regulation of a three-phase voltage source inverter with an LCL input filter,” *IEEE Trans. Power Electron.*, vol. 18, no. 3, pp. 888–895, May 2003.

[112] D. N. Zmood, D. G. Holmes, and G. H. Bode, “Frequency-domain analysis of three-phase linear current regulators,” *IEEE Trans. Ind. Appl.*, vol. 37, no. 2, pp. 601–610, Mar./Apr. 2001.

[113] R. Ottersten and J. Svensson, “Vector current controlled voltage source converter-deadbeat control and saturation strategies,” *IEEE Trans. Power Electron.*, vol. 17, no. 2, pp. 279–285, Mar. 2002.

[114] Y. Zhang, W. Xie, and Y. Zhang, “Deadbeat direct power control of three-phase pulse-width modulation rectifiers,” *IET Power Electron.*, vol. 7, no. 6, pp. 1340–1346, Jun. 2014.

[115] J. Eloy-Garcia, S. Arnaltes, and J. L. Rodriguez-Amenedo, “Direct power control of voltage source inverters with unbalanced grid voltages,” *IET Power Electron.*, vol. 1, no. 3, pp. 395–407, Sep. 2008.

[116] Y. Zhang and C. Qu, “Table-based direct power control for three-phase AC/DC converters under unbalanced grid voltages,” *IEEE Trans. Power Electron.*, vol. 30, no. 12, pp. 7090–7099, Dec. 2015.

[117] A. Yazdani and R. Iravani, “A unified dynamic model and control for the voltage-sourced converter under unbalanced grid conditions,” *IEEE Trans. Power Del.*, vol. 21, no. 3, pp. 1620–1629, Jul. 2006.

[118] P. Xiao, K. A. Corzine, and G. K. Venayagamoorthy, “Multiple reference frame-based control of three-phase PWM boost rectifiers under unbalanced and distorted input conditions,” *IEEE Trans. Power Electron.*, vol. 23, no. 4, pp. 2006–2017, Jul. 2008.

[119] Y. Liu, N. Li, Y. Fu, J. Wang, and Y. Ji, “Stationary-frame-based generalized control diagram for PWM AC-DC front-end converters with unbalanced grid voltage in renewable energy systems,” in *Proc. IEEE Appl. Power Electron. Conf. Expo. (APEC)*, Charlotte, NC, USA, 15-19 Mar., 2015, pp. 678–683.

[120] K. Ma, W. Chen, M. Liserre, and F. Blaabjerg, “Power controllability of a three-phase converter with an unbalanced AC source,” *IEEE Trans. on Power Electron.*, vol. 30, no. 3, pp. 1591–1604, Mar. 2015.

[121] N. B. Lai and K. Kim, “An improved current control strategy for a grid-connected inverter under distorted grid conditions,” *Energies*, vol. 9, no. 3, Mar. 2016.

[122] P. Rodríguez, A. V. Timbus, R. Teodorescu, M. Liserre, and F. Blaabjerg, “Flexible active power control of distributed power generation systems during grid faults,” *IEEE Trans. Ind. Electron.*, vol. 54, no. 5, pp. 2583–2592, Oct. 2007.

[123] Z. R. Ivanović, E. M. Adžić, M. S. Vekić, S. U. Grabić, N. L. Čelanović, and V. A. Katić, "HIL evaluation of power flow control strategies for energy storage connected to smart grid under unbalanced conditions," *IEEE Trans. Power Electron.*, vol. 27, no. 11, pp. 4699–4710, Nov. 2012.

[124] S. Alepuz, S. Busquets-Monge, J. Bordonau, J. A. MartÃnez-Velasco, C. A. Silva, J. Pontt, and J. RodrÃguez, "Control strategies based on symmetrical components for grid-connected converters under voltage dips," *IEEE Trans. Ind. Electron.*, vol. 56, no. 6, pp. 2162–2173, Jun. 2009.

[125] C. H. Ng, L. Ran, and J. Bumby, "Unbalanced-grid-fault ride-through control for a wind turbine inverter," *IEEE Trans. Ind. Appl.*, vol. 44, no. 3, pp. 845–856, May/Jun. 2008.

[126] P. RodrÍguez, A. Timbus, R. Teodorescu, M. Liserre, and F. Blaabjerg, "Current control reference calculation issues for the operation of renewable source grid interface VSCs under unbalanced voltage sags," *IEEE Trans. Power Electron.*, vol. 26, no. 12, pp. 3744–3753, Dec. 2011.

[127] P. Rodríguez, A. Timbus, R. Teodorescu, M. Liserre, and F. Blaabjerg, "Reactive power control for improving wind turbine system behavior under grid faults," *IEEE Trans. Power Electron.*, vol. 24, no. 7, pp. 1798–1801, Jul. 2009.

[128] P. Rodríguez, G. Medeiros, A. Luna, M. C. Cavalcanti, and R. Teodorescu, "Safe current injection strategies for a STATCOM under asymmetrical grid faults," in *Proc. IEEE Energy Convers. Congr. and Expo. (ECCE)*, Atlanta, GA, USA, 12-16 Sep. 2010, pp. 3929–3935.

[129] R. Kabiri, D. G. Holmes, and B. P. McGrath, "Control of active and reactive power ripple to mitigate unbalanced grid voltages," *IEEE Trans. Ind. Appl.*, vol. 52, no. 2, pp. 1660–1668, Mar./Apr. 2016.

[130] F. Wang, J. L. Duarte, and M. A. M. Hendrix, "Design and analysis of active power control strategies for distributed generation inverters under unbalanced grid faults," *IET Gener. Transm. Distrib.*, vol. 4, no. 8, pp. 905–916, Aug. 2010.

[131] F. Wang, J. L. Duarte, and M. Hendrix, "Pliant active and reactive power control for grid-interactive converters under unbalanced voltage dips," *IEEE Trans. Power Electron.*, vol. 26, no. 5, pp. 1511–1521, May 2011.

[132] P. Rodríguez, R. Teodorescu, I. Candela, A. V. Timbus, M. Liserre, and F. Blaabjerg, "New positive-sequence voltage detector for grid synchronization of power converters under faulty grid conditions," in *Proc. IEEE 37th Power Electron. Specialists Conf.*, Jeju, South Korea, 18-22 Jun. 2006, pp. 1–7.

[133] M. M. da Oliveira, "Power electronics for mitigation of voltage sags and improved control of AC power systems," in *Ph.D. dissertation*, Royal Institute of Technology, Stockholm, Sweden. 2010.

[134] X. Guo, X. Zhang, B. Wang, W. Wu, and J. M. Guerrero, "Asymmetrical grid fault ride-through strategy of three-phase grid-connected inverter considering network impedance impact in low-voltage grid," *IEEE Trans. Power Electron.*, vol. 29, no. 3, pp. 1064–1068, Mar. 2014.

[135] M. Castilla, J. Miret, A. Camacho, J. Matas, E. Alarcón-Gallo, and L. G. D. Vicuña, "Coordinated reactive power control for static synchronous compensators under unbalanced voltage sags," in *Proc. IEEE Int. Symp. on Ind. Electron.*, Hangzhou, China, 28-31 May 2012, pp. 987–992.

[136] A. Camacho, M. Castilla, J. Miret, J. C. Vasquez, and E. Alarcón-Gallo, "Flexible voltage support control for three-phase distributed generation inverters under grid fault," *IEEE Trans. Ind. Electron.*, vol. 60, no. 4, pp. 1429–1441, Apr. 2013.

[137] J. Miret, A. Camacho, M. Castilla, L. G. D. Vicuña, and J. Matas, "Control scheme with voltage support capability for distributed generation inverters under voltage sags," *IEEE Trans. Power Electron.*, vol. 28, pp. 5252–5262, Nov. 2013.

[138] M. Castilla, J. Miret, A. Camacho, J. Matas, and L. G. D. Vicuña, "Voltage support control strategies for static synchronous compensators under unbalanced voltage sags," *IEEE Trans. Ind. Electron.*, vol. 61, no. 2, pp. 808–820, Feb. 2014.

[139] A. Camacho, M. Castilla, J. Miret, A. Borrell, and L. G. D. Vicuña, "Active and reactive power strategies with peak current limitation for distributed generation inverters during unbalanced grid faults," *IEEE Trans. Ind. Electron.*, vol. 62, no. 3, pp. 1515–1525, Mar. 2015.

[140] M. A. Fotouhi, Z. Vale, R. Castro, S. F. Pinto, and F. A. Silva, "Flexible operation of grid-interactive converters under unbalanced grid conditions," *Advanced Sci. and Tech. Lett.*, vol. 97, pp. 1–9, 2015.

[141] X. Guo, W. Liu, X. Zhang, X. Sun, Z. Lu, and J. M. Guerrero, "Flexible control strategy for grid-connected inverter under unbalanced grid faults without PLL," *IEEE Trans. Power Electron.*, vol. 30, no. 4, pp. 1773–1778, Jul. 2014.

[142] F. Nejabatkhah, Y. Li, and B. Wu, "Control strategies of three-Phase distributed generation inverters for grid unbalanced," *IEEE Trans. Power Electron.*, vol. 31, no. 7, pp. 5228–5241, Jul. 2016.

[143] O. Ojo and Z. Wu, "A new controller for three-phase boost rectifiers lacking balance in source votages and impedances," in *Proc. IEEE Appl. Power Electron. Conf. Expo.*, Austin, Texas, USA, 6-10 Mar. 2005, pp. 508–514.

[144] C. Lee, C. Hsu, and P. Cheng, "A low-voltage ride-through technique for grid-connected converters of distributed energy resources," *IEEE Trans. Ind. Appl.*, vol. 47, no. 4, pp. 1821–1832, Jul./Aug. 2011.

[145] J. Miret, M. Castilla, A. Camacho, L. G. D. Vicuña, and J. Matas, "Control scheme for photovoltaic three-phase inverters to minimize peak currents during unbalanced grid-voltage sags," *IEEE Trans. Power Electron.*, vol. 27, no. 10, pp. 4262–4271, Oct. 2012.

[146] Z. Ivanović, M. Vekić, S. Grabić, and V. Katić, "Control of multilevel converter driving variable speed wind turbine in case of grid disturbances," in *Proc. 12th Int. Power Electron. and Motion Control Conf.*, Portoroz, Slovenia, 30 Aug.-1 Sep. 2006, pp. 1569–1573.

[147] A. Milicua, G. Abad, and M. Á. R. Vidal, "Online reference limitation method of shunt-connected converters to the grid to avoid exceeding voltage and current limits under

unbalanced operation part I: theory," *IEEE Trans. Energy Convers.*, vol. 30, no. 3, pp. 852–863, Sep. 2015.

[148] A. Camacho, M. Castilla, J. Miret, R. Guzman, and A. Borrell, "Reactive power control for distributed generation power plants to comply with voltage limits during grid faults," *IEEE Trans. Power Electron.*, vol. 29, no. 11, pp. 6224–6234, Nov. 2014.

[149] P. Rodríguez, A. Luna, J. R. Hermoso, I. Etxeberria-Otadui, R. Teodorescu, and F. Blaabjerg, "Current control method for distributed generation power generation plants under grid fault conditions," in *Proc. IEEE 37th Annu. Conf. Ind. Electron. (IECON)*, Melbourne, Australia, 7-10 Nov. 2011, pp. 1262–1269.

[150] S. Revelo and C. A. Silva, "Current reference strategy with explicit negative sequence component for voltage equalization contribution during asymmetric fault ride through," *Int. Trans. Elect. Energ. Syst.*, vol. 25, no. 12, pp. 3449–3471, Dec. 2015.

[151] J. Lu, F. Nejabatkhah, Y. Li, and B. Wu, "Dg control strategies for grid voltage unbalance compensation," in *Proc. IEEE Energy Convers. Congr. and Expo. (ECCE)*, Pittsburgh, PA, USA, 14-18 Sep. 2014, pp. 2932–2939.

[152] M. M. Shabestary and Y. A. R. I. Mohamed, "Advanced voltage support and active power flow control in grid-connected converters under unbalanced conditions," *IEEE Trans. Power Electron.*, vol. 33, no. 2, pp. 1855–1864, Feb. 2018.

[153] ——, "Analytical expressions for multiobjective optimization of converter-based DG operation under unbalanced grid conditions," *IEEE Trans. Power Electron.*, vol. 32, no. 9, pp. 7284–7296, Sep. 2017.

[154] H. C. Chen, C. T. Lee, P. T. Cheng, R. Teodorescu, and F. Blaabjerg, "A low-voltage ride-through technique for grid-connected converters with reduced power transistors stress," *IEEE Trans. Power Electron.*, vol. 31, no. 12, pp. 8562–8571, Dec. 2016.

[155] A. Camacho, M. Castilla, J. Miret, L. G. de Vicuña, and G. L. M. Andrés, "Control strategy for distribution generation inverters to maximize the voltage support in the lowest phase during voltage sags," *IEEE Trans. Ind. Electron.*, vol. 65, no. 3, pp. 2346–2355, Mar. 2018.

[156] *Connecting RSCAD/Runtime with external applications*, RTDS Technologies Inc., Winnipeg, Canada, Jun. 2018.

[157] *Script language reference manual*, RTDS Technologies Inc., Winnipeg, Canada, Jun. 2018.

[158] S. H. Horowitz and A. G. Phadke, *Power system relaying, third edition*. Chichester, UK: John Wiley & Sons, Ltd., 2006.

[159] *SIPROTEC 5 Distance Protection, Line Differential Protection, and Breaker Management for 1-Pole and 3-Pole Tripping-Manual V7.00 and higher*, Siemens, Nov. 2017.

[160] A. A. van der Meer, R. L. Hendriks, and W. L. Kling, "Combined stability and electro-magnetic transients simulation of offshore wind power connected through multi-terminal VSC-HVDC," in *Proc. IEEE PES General Meeting*, Providence, RI, USA, 25-29 Jul. 2010, pp. 1–7.

[161] A. A. van der Meer, M. Ndreko, M. Gibescu, and M. A. M. M. van der Meijden, "The effect of FRT behavior of VSC-HVDC-connected offshore wind power plants on AC/DC system dynamics," *IEEE Trans. Power Del.*, vol. 31, no. 2, pp. 878–887, Apr. 2016.

[162] P. Rodríguez, G. Medeiros, A. Luna, M. C. Cavalcanti, and R. Teodorescu, "Safe current injection strategies for a statcom under asymmetrical grid faults," in *Proc. IEEE Energy Conv. Congr. and Expo. (ECCE)*, Atlanta, GA, USA, 12-16 Sep. 2010, pp. 3929–3935.

[163] M. Z. Kamh and R. Iravani, "A unified three-phase power-flow analysis model for electronically coupled distributed energy resources," *IEEE Trans. Power Del.*, vol. 26, no. 2, pp. 899–909, Apr. 2011.

[164] ——, "Unbalanced model and power-flow analysis of microgrids and active distribution systems," *IEEE Trans. Power Del.*, vol. 25, no. 4, pp. 2851–2858, Oct. 2010.

[165] P. M. Anderson and A. A. Fouad, *Power System Control and Stability, 2nd Edition*. Hoboken, NJ, USA: Wiley-IEEE Press, 2002.

[166] (2018, May) Mathworks global optimization toolbox functions. [Online]. Available: https://www.mathworks.com/help/gads/ga.html

[167] T. N. Boutsika and S. A. Papathanassiou, "Short-circuit calculations in networks with distributed generation," *Electric Power Syst. Research*, vol. 78, no. 7, pp. 1181 – 1191, Jul. 2008.

[168] *IEEE Guide for Planning DC Links Terminating at AC Locations Having Low Short-Circuit Capacities IEEE Std 1204-1997(R2003)*, New York, NY, USA, The Institute of Electrical and Electronics Engineers, Inc., Dec. 2003.

[169] Y. Zhang, S. H. F. Huang, J. Schmall, J. Conto, J. Billo, and E. Rehman, "Evaluating system strength for large-scale wind plant integration," in *Proc. IEEE PES General Meeting Conf. Expo.*, National Harbor, MD, USA, 27-31 Jul. 2014, pp. 1–5.

[170] J. Z. Zhou and A. M. Gole, "VSC transmission limitations imposed by AC system strength and AC impedance characteristics," in *Proc. 10th IET Int. Conf. on AC and DC Power Transm.*, Birmingham, UK, 4-5 Dec. 2012, pp. 1–6.

[171] J. Z. Zhou, H. Ding, S. Fan, Y. Zhang, and A. M. Gole, "Impact of short-circuit ratio and phase-locked-loop parameters on the small-signal behavior of a VSC-HVDC converter," *IEEE Trans. Power Del.*, vol. 29, no. 5, pp. 2287–2296, Oct. 2014.

[172] J. M. Guerrero, L. Hang, and J. Uceda, "Control of distributed uninterruptible power supply systems," *IEEE Trans. Ind. Electron.*, vol. 55, no. 8, pp. 2845–2859, Aug. 2008.

[173] A. Hooshyar and R. Iravani, "Microgrid protection," *Proceedings of the IEEE*, vol. 105, no. 7, pp. 1332–1353, Jul. 2017.

Appendix A Instantaneous Power Theory for Power Electronics Controls

If the instantaneous three-phase voltage and current measured at the PCC are denoted by $[v_a \;\; v_b \;\; v_c]^T$ and $[i_a \;\; i_b \;\; i_c]^T$ respectively, the application of Clark Transformation on the three-phase quantities gives:

$$\begin{bmatrix} v_0 \\ v_\alpha \\ v_\beta \end{bmatrix} = \frac{\sqrt{2}}{\sqrt{3}} \begin{bmatrix} 1/\sqrt{2} & 1/\sqrt{2} & 1/\sqrt{2} \\ 1 & -1/2 & -1/2 \\ 0 & \sqrt{3}/2 & \sqrt{3}/2 \end{bmatrix} \begin{bmatrix} v_a \\ v_b \\ v_c \end{bmatrix} \tag{1}$$

$$\begin{bmatrix} i_0 \\ i_\alpha \\ i_\beta \end{bmatrix} = \frac{\sqrt{2}}{\sqrt{3}} \begin{bmatrix} 1/\sqrt{2} & 1/\sqrt{2} & 1/\sqrt{2} \\ 1 & -1/2 & -1/2 \\ 0 & \sqrt{3}/2 & \sqrt{3}/2 \end{bmatrix} \begin{bmatrix} i_a \\ i_b \\ i_c \end{bmatrix} \tag{2}$$

where α and β represent the two phases in the stationary reference frame.

For a three-phase, three-wire VSC system, zero-sequence components are not present. As a result, the instantaneous active power p and the instantaneous reactive power q can be defined as:

$$p = \mathbf{v} \cdot \mathbf{i} = v_\alpha i_\alpha + v_\beta i_\beta \tag{3}$$

$$q = \mathbf{v}_\perp \cdot \mathbf{i} = v_\beta i_\alpha - v_\alpha i_\beta \tag{4}$$

where $\mathbf{v} = [v_\alpha \;\; v_\beta]^T$ and $\mathbf{i} = [i_\alpha \;\; i_\beta]^T$ are the voltage and current vectors in the stationary reference frame, respectively. The operator "$\cdot$" represents the dot product of vectors. The subscript "$\perp$" denotes an orthogonal version of the original vector:

$$\mathbf{v}_\perp = \begin{bmatrix} 0 & 1 \\ -1 & 0 \end{bmatrix} \mathbf{v} = \begin{bmatrix} 0 & 1 \\ -1 & 0 \end{bmatrix} \begin{bmatrix} v_\alpha \\ v_\beta \end{bmatrix} = \begin{bmatrix} v_\beta \\ -v_\alpha \end{bmatrix} \tag{5}$$

Since the voltage and current can be regarded the superposition of symmetrical components, (3)–(4) can be further expressed by:

$$p = v_\alpha i_\alpha + v_\beta i_\beta = (v_\alpha^+ + v_\alpha^-)(i_\alpha^+ + i_\alpha^-) + (v_\beta^+ + v_\beta^-)(i_\beta^+ + i_\beta^-) \tag{6}$$

$$q = v_\beta i_\alpha - v_\alpha i_\beta = (v_\beta^+ + v_\beta^-)(i_\alpha^+ + i_\alpha^-) - (v_\alpha^+ + v_\alpha^-)(i_\beta^+ + i_\beta^-) \tag{7}$$

where the superscripts "+" and "-" represent the positive- and negative-sequence components, respectively.

By expanding (6)–(7) and rearranging different terms, there are:

$$p = \underbrace{v_\alpha^+ i_\alpha^+ + v_\beta^+ i_\beta^+ + v_\alpha^- i_\alpha^- + v_\beta^- i_\beta^-}_{\mathbf{v}^+ \cdot \mathbf{i}^+ + \mathbf{v}^- \cdot \mathbf{i}^-} + \underbrace{v_\alpha^+ i_\alpha^- + v_\alpha^- i_\alpha^+ + v_\beta^+ i_\beta^- + v_\beta^- i_\beta^+}_{\mathbf{v}^+ \cdot \mathbf{i}^- + \mathbf{v}^- \cdot \mathbf{i}^+} \tag{8}$$

$$q = \underbrace{v_\beta^+ i_\alpha^+ - v_\alpha^+ i_\beta^+ + v_\beta^- i_\alpha^- - v_\alpha^- i_\beta^-}_{\mathbf{v}_\perp^+ \cdot \mathbf{i}^+ + \mathbf{v}_\perp^- \cdot \mathbf{i}^-} + \underbrace{v_\beta^+ i_\alpha^- + v_\beta^- i_\alpha^+ - v_\alpha^+ i_\beta^- - v_\alpha^- i_\beta^+}_{\mathbf{v}_\perp^+ \cdot \mathbf{i}^- + \mathbf{v}_\perp^- \cdot \mathbf{i}^+} \tag{9}$$

where voltage and current vectors in the stationary reference frame are:

$$\mathbf{v}^+ = \begin{bmatrix} v_\alpha^+ \\ v_\beta^+ \end{bmatrix} \quad \mathbf{v}_\perp^+ = \begin{bmatrix} v_\beta^+ \\ -v_\alpha^+ \end{bmatrix} \quad \mathbf{v}^- = \begin{bmatrix} v_\alpha^- \\ v_\beta^- \end{bmatrix} \quad \mathbf{v}_\perp^- = \begin{bmatrix} v_\beta^- \\ -v_\alpha^- \end{bmatrix} \tag{10}$$

$$\mathbf{i}^+ = \begin{bmatrix} i_\alpha^+ \\ i_\beta^+ \end{bmatrix} \quad \mathbf{i}^- = \begin{bmatrix} i_\alpha^- \\ i_\beta^- \end{bmatrix} \tag{11}$$

With only fundamental frequency components considered, the voltage and current expressed in the stationary reference frame can be transformed into the synchronous reference frame using Park Transformation:

$$\begin{bmatrix} v_d^+ \\ v_q^+ \end{bmatrix} = \begin{bmatrix} \cos(\omega t) & \sin(\omega t) \\ -\sin(\omega t) & \cos(\omega t) \end{bmatrix} \begin{bmatrix} v_\alpha^+ \\ v_\beta^+ \end{bmatrix} \quad \begin{bmatrix} v_d^- \\ v_q^- \end{bmatrix} = \begin{bmatrix} \cos(-\omega t) & \sin(-\omega t) \\ -\sin(-\omega t) & \cos(-\omega t) \end{bmatrix} \begin{bmatrix} v_\alpha^- \\ v_\beta^- \end{bmatrix} \tag{12}$$

$$\begin{bmatrix} i_d^+ \\ i_q^+ \end{bmatrix} = \begin{bmatrix} \cos(\omega t) & \sin(\omega t) \\ -\sin(\omega t) & \cos(\omega t) \end{bmatrix} \begin{bmatrix} i_\alpha^+ \\ i_\beta^+ \end{bmatrix} \quad \begin{bmatrix} i_d^- \\ i_q^- \end{bmatrix} = \begin{bmatrix} \cos(-\omega t) & \sin(-\omega t) \\ -\sin(-\omega t) & \cos(-\omega t) \end{bmatrix} \begin{bmatrix} i_\alpha^- \\ i_\beta^- \end{bmatrix} \tag{13}$$

where the subscripts *"d"* and *"q"* denote the *d*-axis and the *q*-axis in the synchronous reference frame, respectively.

By substituting (12)–(13) into (8)–(9), the instantaneous power can be expressed by:

$$p = \overbrace{\underbrace{P^+ + P^-}_{\mathbf{v}^+ \cdot \mathbf{i}^+ + \mathbf{v}^- \cdot \mathbf{i}^-}}^{\overline{P}} + \overbrace{\underbrace{P_{c2}\cos(2\omega t) + P_{s2}\sin(2\omega t)}_{\mathbf{v}^+ \cdot \mathbf{i}^- + \mathbf{v}^- \cdot \mathbf{i}^+}}^{\widetilde{P}} \tag{14}$$

$$q = \overbrace{\underbrace{Q^+ + Q^-}_{\mathbf{v}_\perp^+ \cdot \mathbf{i}^+ + \mathbf{v}_\perp^- \cdot \mathbf{i}^-}}^{\overline{Q}} + \overbrace{\underbrace{Q_{c2}\cos(2\omega t) + Q_{s2}\sin(2\omega t)}_{\mathbf{v}_\perp^+ \cdot \mathbf{i}^- + \mathbf{v}_\perp^- \cdot \mathbf{i}^+}}^{\widetilde{Q}} \tag{15}$$

where

$$\overline{P} = \frac{3}{2}(v_d^+ i_d^+ + v_q^+ i_q^+ + v_d^- i_d^- + v_q^- i_q^-) \tag{16}$$

$$P_{c2} = \frac{3}{2}(v_d^- i_d^+ + v_q^- i_q^+ + v_d^+ i_d^- + v_q^+ i_q^-) \tag{17}$$

$$P_{s2} = \frac{3}{2}(v_q^- i_d^+ - v_d^- i_q^+ - v_q^+ i_d^- + v_d^+ i_q^-) \tag{18}$$

$$\overline{Q} = \frac{3}{2}(v_q^+ i_d^+ - v_d^+ i_q^+ + v_q^- i_d^- - v_d^- i_q^-) \tag{19}$$

$$Q_{c2} = \frac{3}{2}(v_q^- i_d^+ - v_d^- i_q^+ + v_q^+ i_d^- - v_d^+ i_q^-) \tag{20}$$

$$Q_{s2} = \frac{3}{2}(-v_d^- i_d^+ - v_q^- i_q^+ + v_d^+ i_d^- + v_q^+ i_q^-) \tag{21}$$

$\overline{P}$ and $\overline{Q}$ are constant power terms consisting of positive-sequence power P^+ and Q^+, and negative-sequence power P^- and Q^-. $\widetilde{P}$ and $\widetilde{Q}$ are the power terms oscillating at twice fundamental frequency.

Appendix B Voltage Support Concept

A set of zero-, positive- and negative-sequence voltages can be expressed by:

$$\begin{pmatrix} \dot{V}^0 \\ \dot{V}^+ \\ \dot{V}^- \end{pmatrix} = \begin{pmatrix} \sqrt{2}V^0 \sin(\omega t + \angle\varphi_0) \\ \sqrt{2}V^+ \sin(\omega t + \angle\varphi_+) \\ \sqrt{2}V^- \sin(\omega t + \angle\varphi_-) \end{pmatrix} \tag{22}$$

where V^0, V^+, and V^- are the RMS values of the sequence voltages. ϕ_0, ϕ_+ and ϕ_- are the corresponding phase angles.

With the inverse of the symmetrical-component transformation, the three-phase voltage becomes:

$$\begin{pmatrix} \dot{V}_a \\ \dot{V}_b \\ \dot{V}_c \end{pmatrix} = \begin{pmatrix} 1 & 1 & 1 \\ 1 & \alpha^2 & \alpha \\ 1 & \alpha & \alpha^2 \end{pmatrix} \begin{pmatrix} \dot{V}^0 \\ \dot{V}^+ \\ \dot{V}^- \end{pmatrix} = \begin{pmatrix} 1 & 1 & 1 \\ 1 & \alpha^2 & \alpha \\ 1 & \alpha & \alpha^2 \end{pmatrix} \begin{pmatrix} \sqrt{2}V^0 \sin(\omega t + \angle\varphi_0) \\ \sqrt{2}V^+ \sin(\omega t + \angle\varphi_+) \\ \sqrt{2}V^- \sin(\omega t + \angle\varphi_-) \end{pmatrix} \tag{23}$$

By expanding (23), the three-phase instantaneous voltage can be futher expressed by:

$$\begin{pmatrix} v_a \\ v_b \\ v_c \end{pmatrix} = \begin{pmatrix} \sqrt{2}V^0 \sin(\omega t + \varphi_0) + \sqrt{2}V^+ \sin(\omega t + \varphi_+) + \sqrt{2}V^- \sin(\omega t + \varphi_-) \\ \sqrt{2}V^0 \sin(\omega t + \varphi_0) + \sqrt{2}V^+ \sin(\omega t + \varphi_+ - \frac{2\pi}{3}) + \sqrt{2}V^- \sin(\omega t + \varphi_- + \frac{2\pi}{3}) \\ \sqrt{2}V^0 \sin(\omega t + \varphi_0) + \sqrt{2}V^+ \sin(\omega t + \varphi_+ + \frac{2\pi}{3}) + \sqrt{2}V^- \sin(\omega t + \varphi_- - \frac{2\pi}{3}) \end{pmatrix} \tag{24}$$

Then the voltage expressed in the stationary reference frame can be obtained by using Clark Transformation:

$$\begin{pmatrix} v_0 \\ v_\alpha \\ v_\beta \end{pmatrix} = \frac{\sqrt{2}}{\sqrt{3}} \begin{bmatrix} 1/\sqrt{2} & 1/\sqrt{2} & 1/\sqrt{2} \\ 1 & -1/2 & -1/2 \\ 0 & \sqrt{3}/2 & \sqrt{3}/2 \end{bmatrix} \begin{pmatrix} v_a \\ v_b \\ v_c \end{pmatrix} = \begin{pmatrix} \sqrt{6}V^0 \sin(\omega t + \varphi_0) \\ \underbrace{\sqrt{3}V^+ \sin(\omega t + \varphi_+)}_{v_\alpha^+} + \underbrace{\sqrt{3}V^- \sin(\omega t + \varphi_-)}_{v_\alpha^-} \\ \underbrace{-\sqrt{3}V^+ \cos(\omega t + \varphi_+)}_{v_\beta^+} + \underbrace{\sqrt{3}V^- \cos(\omega t + \varphi_-)}_{v_\beta^-} \end{pmatrix} \tag{25}$$

The current in the stationary reference frame can be derived in the same way:

$$\begin{pmatrix} i_0 \\ i_\alpha \\ i_\beta \end{pmatrix} = \begin{pmatrix} \sqrt{6}I^0 \sin(\omega t + \delta_0) \\ \underbrace{\sqrt{3}I^+ \sin(\omega t + \delta_+)}_{i_\alpha^+} + \underbrace{\sqrt{3}I^- \sin(\omega t + \delta_-)}_{i_\alpha^-} \\ \underbrace{-\sqrt{3}I^+ \cos(\omega t + \delta_+)}_{i_\beta^+} + \underbrace{\sqrt{3}I^- \cos(\omega t + \delta_-)}_{i_\beta^-} \end{pmatrix} \tag{26}$$

where I^0, I^+, and I^- are the RMS values of the sequence currents. δ_0, δ_+ and δ_- are the corresponding phase angles.

For the system shown in Fig. 2.17, if the grid resistance is ignored, the relationship between the grid voltage $\mathbf{v}_g$ and the PCC voltage $\mathbf{v}$ can be given by:

$$\mathbf{v} = \mathbf{v}_g + L_g \frac{\mathrm{d}\mathbf{i}}{\mathrm{d}t} \tag{27}$$

Equation (27) can be further decomposed into (28)–(29) in the stationary reference frame:

$$v_\alpha = v_{g\alpha} + L_g \frac{di_\alpha}{dt} \tag{28}$$

$$v_\beta = v_{g\beta} + L_g \frac{di_\beta}{dt} \tag{29}$$

By applying the voltage and current decomposition (25)–(26) to both sides of (28)–(29), there are:

$$\begin{aligned} \sqrt{3}V^+ \sin(\omega t + \varphi_+) + \sqrt{3}V^- \sin(\omega t + \varphi_-) = \\ \sqrt{3}V_g^+ \sin(\omega t + \varphi_{g+}) + \sqrt{3}V_g^- \sin(\omega t + \varphi_{g-}) + \\ \omega L_g \sqrt{3}I^+ \cos(\omega t + \delta_+) + \omega L_g \sqrt{3}I^- \cos(\omega t + \delta_-) \end{aligned} \tag{30}$$

$$\begin{aligned} -\sqrt{3}V^+ \cos(\omega t + \varphi_+) + \sqrt{3}V^- \cos(\omega t + \varphi_-) = \\ -\sqrt{3}V_g^+ \cos(\omega t + \varphi_{g+}) + \sqrt{3}V_g^- \cos(\omega t + \varphi_{g-}) + \\ \omega L_g \sqrt{3}I^+ \sin(\omega t + \delta_+) - \omega L_g \sqrt{3}I^- \sin(\omega t + \delta_-) \end{aligned} \tag{31}$$

Next, by adding (30) to (31) on both sides of the equation, there is:

$$\begin{aligned} V^+[\sin(\omega t + \varphi_+ - \frac{\pi}{4})] + V^-[\cos(\omega t + \varphi_- - \frac{\pi}{4})] = \\ V_g^+[\sin(\omega t + \varphi_{g+} - \frac{\pi}{4})] + V_g^-[\cos(\omega t + \varphi_{g-} - \frac{\pi}{4})] \\ -\omega L_g I^+[\sin(\omega t + \delta_+ - \frac{3\pi}{4})] - \omega L_g I^-[\cos(\omega t + \delta_- - \frac{3\pi}{4})] \end{aligned} \tag{32}$$

Since the grid resistance is ignored, the angle between the sequence voltage at the PCC and the sequence current is given by:

$$\varphi_+ - \delta_+ = \frac{\pi}{2} \tag{33}$$

$$\varphi_- - \delta_- = \frac{-\pi}{2} \tag{34}$$

With (33)–(34) substituted into (32), the different terms on both sides of (32) can be categorized by the table below.

Finally, as all the terms within the same sequence are in phase with each other, there are:

$$V^+ = V_g^+ + \omega L_g I^+ \tag{35}$$

$$V^- = V_g^- - \omega L_g I^- \tag{36}$$

	Left-side term	**=**	**Right-side term 1**	**+**	**Right-side term 2**
Positive sequence	$V^+[\sin(\omega t + \varphi_+ - \frac{\pi}{4})]$	=	$V_g^+[\sin(\omega t + \varphi_{g+} - \frac{\pi}{4})]$	+	$\omega L_g I^+[\sin(\omega t + \delta_+ - \frac{\pi}{4})]$
Negative sequence	$V^-[\cos(\omega t + \varphi_- - \frac{\pi}{4})]$	=	$V_g^-[\cos(\omega t + \varphi_{g-} - \frac{\pi}{4})]$	+	$\omega L_g I^-[\cos(\omega t + \delta_- - \frac{\pi}{4})]$

On the other hand, for a resistive grid with L_g replaced by R_g, (27) can be rewritten as:

$$\mathbf{v} = \mathbf{v}_g + R_g\mathbf{v} \tag{37}$$

By using a similar derivation procedure, (38)–(39) can be obtained.

$$V^{+} = V_g^{+} + R_g I^{+} \tag{38}$$

$$V^{-} = V_g^{-} + R_g I^{-} \tag{39}$$

Appendix C Hardware-in-the-loop Test Automation

In RTDS, the RSCAD/Runtime offers a script function for automating the simulations. This enables RTDS to perform a series of simulations as well as relay testing under different scenarios without the need of manual controls.

The script executed by the RSCAD/Runtime is:

```
string temp_string;
fprintf(stdmsg, "Initialization of RTDS simulation");
ListenOnPort(4575,"true");
fprintf(stdmsg, "Execution of script is done\n");
```

The "ListenOnPort()" command enables RSCAD/Runtime to become a Transmission Control Protocol (TCP) server. After the "ListenOnPort()" command is executed, RSCAD/Runtime listens to a port with a designated number, waiting for a connection request from MATLAB. The external program, MATLAB, serves as the socket client. Once the connection is established, a TCP streams commences between MATLAB and RSCAD/Runtime. Therefore, the simulations can be controlled by executing a .m file in MATLAB that contains the necessary commands to be sent to the TCP server. The .m file requires an external library file "JTCP.m" for the TCP communications.

The connection request sent from MATLAB is realized with the script:

```
portnum = 4575;
JTCPOBJ = jtcp('REQUEST','127.0.0.1', portnum);
```

where "portnum" is the port number. It should match with the port number in the RSCAD/Runtime script. The Internet Protocol (IP) address specifies the IP address of the TCP server. The HIL test platform in Fig. 3.3 has RSCAD/Runtime (server) and MATLAB (client) running on the same computer and thus the local host IP address is used. The termination of the connection is achieved by the script:

```
portnum = 4575;
msg1 = sprintf('ClosePort(%d);', portnum);
jtcp('writes',JTCPOBJ,msg1);
disp('Simulation finished.');
```

The RSCAD/Runtime script function will not execute the remaining scripts after the "ListenOnPort()" command until the TCP/IPcommunication is terminated.

The other MATLAB scripts necessary for controlling the HIL tests are:

- Start and stop the RTDS simulation:

```
% Start simulation
     jtcp('writes',JTCPOBJ,'Start;');
% Stop simulation
     jtcp('writes',JTCPOBJ,'Stop;');
```

- Change the value of a slider (for changing parameters of a component in RTDS, specifying fault locations, etc.):

```
msg1 = sprintf('SetSlider "Subsystem #x: CTLs: Inputs: y"=%f;',z);
jtcp('writes', JTCPOBJ, msg1);
```

- Set a switch on and off (for turning on/off a component in RTDS, specifying fault types and locations, sending signals to the external hardware):

```
% Set the switch on
msg1 = sprintf('SetSwitch "Subsystem #x: CTLs: Inputs: y"=%f;',1);
jtcp('writes', JTCPOBJ, msg1);
% Set the switch off
msg1 = sprintf('SetSwitch "Subsystem #x: CTLs: Inputs : y"=%f;',0)
    ;
jtcp('writes', JTCPOBJ, msg1);
```

- Push and release a push button (for making a short circuit event):

```
msg1 = sprintf('PushButton "Subsystem #x: CTLs: Inputs: y";');
jtcp('writes', JTCPOBJ, msg1);
msg1 = sprintf('WAIT 0.001;');
jtcp('writes', JTCPOBJ, msg1);
msg1 = sprintf('ReleaseButton "Subsystem #x: CTLs: Inputs: y";');
```

  where "x" refers to the number of the subsystem in the RTDS model; "y" represents the name of the slider, the switch or the push button specified in the RTDS model; "z" is the desired value for the slider.

Besides feeding commands from MATLAB to RSCAD/Runtime, the data can also be transferred in a reverse direction. This enables MATLAB to save the data from RTDS within a time window, making it convenient for comparing the simulation results under various scenarios. In order to realize the bi-directional communication, the "ListenOnPortHandshake()" command is used in the .m file as:

```
jtcp('writes',JTCPOBJ,'temp_string = "sequence1";');
jtcp('writes',JTCPOBJ,'ListenOnPortHandshake(temp_string);');
rmsg  = jtcp('read',JTCPOBJ);
rmsg2 = char(rmsg);
while (isempty(strfind(rmsg2, 'sequence1')) == 1)
    rmsg = jtcp('read',JTCPOBJ);
    rmsg2 = char(rmsg);
end
```

Since the executing of a .m file in MATLAB is extremely faster than the real-time simulation in RTDS, the above scripts are inserted in the .m file wherever MATLAB needs to wait for RTDS. This ensures the synchronism between RSCAD/Runtime and MATLAB by changing the token string "Sequence1". At the same time, the captured RTDS simulation results can be imported into the Workspace of MATLAB by using:

```
filename=strcat('name1');
msg1 = sprintf('SavePlot "name2", "%s";',filename);
jtcp('writes', JTCPOBJ, msg1);
outfile=strcat(filename,'.out');
eval([filename '= outimp(outfile,2,inf);']);
```

where "name1" is the variable name in Workspace; "name2" is the plot name specified in RSCAD/Runtime.

In general, the steps to perform a series of simulations, as well as relay testing under different scenarios, are:

(1) Create sliders, switches and push buttons in RSCAD/Draft to define the inputs;
(2) Compile RSCAD/Draft with no error;
(3) Execute the script in RSCAD/Runtime;
(4) Specify the scenarios to be run by RTDS in the .m file;
(5) Execute the .m file in MATLAB;
(6) The simulations and HIL tests are automated. The corresponding results are imported into MATLAB with the bi-directional communication;

Department of Electrical Engineering
Center for Electric Power and Energy (CEE)
Technical University of Denmark
Elektrovej, Building 325
DK-2800 Kgs. Lyngby
Denmark

www.elektro.dtu.dk/cee
Tel: (+45) 45 25 35 00
Fax: (+45) 45 88 61 11
E-mail: cee@elektro.dtu.dk